Studies of the Dissociation and Energetics of Ions

Simon-John King

A thesis submitted to

University College London

for the degree of Doctor of Philosophy

2008

ProQuest LLC
789 East Eisenhower Parkway
P.O. Box 1346
Ann Arbor, MI 48106-1346

To my Mum and Dad who gave me everything

dissociations of $C_2F_6^{2+}$, $SiCl_4^{2+}$, $C_2H_2^{2+}$, CO_2^{2+} and H_2O^{2+}. Estimates of the dication precursor state energies for forming ion pairs are derived, and are shown to be in good agreement with existing experimental and theoretical data. The measurements presented in this thesis include the first estimates of the electronic state energies of the $C_2F_6^{2+}$ and $SiCl_4^{2+}$ dications. A breakdown scheme for $C_2H_2^{2+}$ is derived, which in combination with the relative PICS for ion pair formation, yields branching ratios for primary two-body charge separating dissociation. Comparison of this scheme with recent theoretical calculations suggests that below 75 eV, $C_2H_2^{2+}$ dissociates predominantly on the ground triplet potential energy surface ($^3\Sigma_g^-$). By contrast, the dissociations of the $C_2F_6^{2+}$ dication are postulated to be predominantly impulsive in nature, for which fast-sequential decay mechanisms are proposed for forming ion pairs.

Acknowledgements

Sincere thanks are due to Professor Stephen Price, without whom none of the experimental work presented in this thesis would have been possible. His great enthusiasm for Physical Chemistry, and extreme professionalism in all areas of life, has been a source of inspiration during my postgraduate years. I must also thank Steve, as a friend, for the patience he has shown during the preparation of this thesis.

I would also like to express here my most heartfelt thanks to my Mum and Dad, for their unconditional love during four years of joy, despair, optimism and turmoil.

Contents

Chapter 1 Introduction 1

Chapter 2 Experimental Details 35

Appendices

Chapter 1 Introduction

1.1 Background

This thesis presents the results of experimental investigations on the dissociative electron ionization of a number of small gaseous molecules, with applications to plasma processing technologies[1] and/or atmospheric and interstellar chemistry[2,3]. In highly energised media such as industrial plasmas and planetary atmospheres, collisions between ionizing electrons and neutral molecules may result in the formation of a variety of positively charged ionic products. These products typically include ions formed *via* non-dissociative and dissociative electron ionization processes, involving both single and multiple ionization. Thus, the accurate modelling of these environments, where dissociative ionization can occur, requires reliable information on the formation efficiency of both the parent ion and the various ionic fragments. Such information is commonly provided in the form of partial ionization cross sections (PICS).[4]

The determination of the PICS requires a mass spectrometric experiment, to provide information on the identity and the abundance of the various ionic products formed following electron ionization events. Therefore, when using a mass spectrometer to produce accurate and reliable PICS measurements, the apparatus must be able to detect all positive ions, regardless of their mass or initial kinetic energy, with equal efficiency. As highlighted in a number of recent reviews, the main technical difficulty in measuring accurate PICS is caused by the initial kinetic energy of ions formed by dissociative ionization processes.[5-7] Many earlier experiments used to determine PICS, for example, involving quadrupole mass spectrometers[8,9] or magnetic sector instruments[10-12], do not ensure the complete collection of such fragment ions formed with considerable kinetic energy, particularly those fragments formed *via* dissociative multiple ionization processes.[13,14] Thus, for many molecules these earlier PICS measurements obtained by different research groups are found not to agree within the stated experimental uncertainties and often exhibit markedly different energy dependencies.[1,6] This discrepancy amongst the available PICS data has prompted the development of new experimental techniques for the accurate determination of PICS, for which the complete collection of energetic fragment ions can be demonstrated.[15,16]

In this thesis, time-of-flight mass spectrometry coupled with a 2-D ion coincidence technique is used to investigate the electron ionization of C_2F_6, $SiCl_4$, C_2H_2, CO_2 and H_2O, in the ionizing electron energy range 30-200 eV. This experimental method enables fragment ions formed *via* dissociative single, double, and triple ionization processes to be distinguished and quantified, and hence, provides detailed information on the various ionization processes that take place following electron-molecule collisions. The key aspects of the apparatus design, experimental setup, and data sets produced by the experiment are described in Chapter 2. The various analysis procedures by which the experimental data is processed to derive relative partial ionization cross sections and precursor specific relative PICS, are presented in Chapter 3. Also presented in Chapter 3, is a description of the methods used for analysing the peaks produced from the 2-D ion coincidence data, to derive information concerning the dynamics and energetics involved in the charge-separating dissociations of small molecular dications. The remainder of this thesis (Chapters 4-8) presents the results of the experimental work, and a discussion of the results for each target molecule.

1.2 Laboratory Techniques for Forming Positive Ions

If sufficient energy is transferred to a neutral molecule (AB), an electron may be ejected, resulting in the formation of a positively charged ion. The minimum energy that is required for this process is termed the ionization energy, and may be transferred to the molecule by one of a number of different methods, including:

$e^- + AB \rightarrow AB^+ + e^- + e^-$	Electron ionization	1.i
$h\nu + AB \rightarrow AB^+ + e^-$	Photoionization	1.ii
$C^+ + AB \rightarrow AB^+ + C$	Electron Transfer	1.iii
$M + AB^+ \rightarrow AB^{2+} + M + e^-$	Charge-stripping	1.iv
$M^* + AB \rightarrow AB^+ + M + e^-$	Penning Ionization	1.v

The methods of ionization listed above are classified as follows: Interaction with an electron (1.i); Absorption of a photon (1.ii); Collisions involving positively charged species (1.iii and 1.iv); Collisions involving excited neutral species (1.v). It is noted that this list is by no means exhaustive. The mechanism of the ionization process and the identity of the products formed depend on the ionization technique that is used. In this Section, the main ionization techniques that are used in mass spectrometry to generate positively charged ions, are briefly discussed.

1.2.1 Electron Ionization

Electron ionization generally involves the formation of ions following inelastic collisions between electrons and neutral gas species. The electrons are commonly produced by thermionic emission from a filament, with subsequent acceleration and focusing to form a collimated beam of ionizing electrons. Electrons can therefore be easily generated with any desired energy and in high abundance, and hence electron ionization is a technique widely used in experiments to investigate the formation and fragmentation of positively charged ions.[5]

If the energy of the electron beam is greater than the ionization energy of the target molecule, then a small proportion of the target species will be ionized. However, not all inelastic collisions between an electron and a neutral molecule will result in the formation of a positively charged ion, since there is no restriction on the proportion of electron energy that may be transferred to the target molecule during such collisions. This situation can be contrasted to the absorption of a photon, whereby the energy transferred to the target molecule must exactly match the photon energy (Section 1.2.2). The majority of the ions formed following electron ionization of a neutral molecule are singly charged, and for most molecular systems these ions include singly charged parent ions, also called parent monocations (1.ia), and singly charged ionic fragments formed by dissociative single ionization (1.ib).[4] For ionizing electron energies in excess of the single ionization threshold energy, usually by a factor of around 2.5, doubly charged ions may also be formed by multiple electron ionization (1.ic). As will be described in Section 1.3.2, the majority of such doubly charged ions are unstable with respect to dissociation and rapidly fragment to form a pair of singly charged fragment ions.

$e^- + AB \rightarrow AB^+ + 2e^-$	Parent Ion Formation	1.ia
$e^- + AB \rightarrow A^+ + B + 2e^-$	Dissociative Single Ionization	1.ib
$e^- + AB \rightarrow AB^{2+} + 3e^-$	Multiple Electron Ionization	1.ic

The ionization of target molecules at electron energies close to the ionization threshold proceeds predominantly *via* direct ionization processes, that is, where the ejected electron and the scattered electron leave the target molecule within 10^{-16}s of one another.[4] Direct ionization is a non-resonant process because the ejected electron is released into a continuum and therefore can accommodate any excess kinetic energy. The behaviour of the single ionization cross section ($\sigma_{\rm ion}$) close to the ionization threshold is described by the classical Wannier theory of direct ionization processes (Eqn 1.1).[17,18] This theory considers the motion of the two outgoing electrons upon single electron ionization to be collinear, which, if long range interactions and correlations between these outgoing electrons are taken into account, leads to the proportionality relationship:

$$\sigma_{ion} \propto E^{1.127} \qquad 1.1$$

where E represents the excess energy of the molecule above the ionization threshold. Indeed, the Wannier threshold law has been shown to be in good accord with experimental measurements of the energy dependence of the single ionization cross section of small molecules within a few electron Volts of the single ionization threshold.[17]

For the general case involving the formation of a multiply charged ion involving the loss of n-1 electrons, Wannier theory predicts that in the absence of long range correlations between the outgoing n electrons, the ionization cross section should increase as the $(n-1)^{th}$ power of the excess energy E.[19] An obvious consequence of this relationship is that for single electron ionization, yielding two outgoing electrons, the ionization cross section has an approximately linear onset with a value of zero at threshold, while for double electron ionization the cross section increases approximately proportional to E^2. However, while this energy dependence of the double ionization cross section may be true close to the double ionization threshold, it is noted that at higher ionizing electron energies, direct processes are not the main means of multiple ionization.[20]

Another mechanism by which a positively charged ion may be formed following a collision with an electron is autoionization.[4,21] Autoionization is an indirect process, whereby the scattered electron and the ejected electron leave the molecule sequentially on a much longer time scale than 10^{-16}s, and can be described by the following scheme:

$$e^- + AB \rightarrow AB^* + e^- \rightarrow AB^+ + e^- + e^- \qquad 1.id$$

Initially the target molecule is excited to a super-excited neutral electronic state, AB^*, involving the promotion of one or a number of electrons to high-lying molecular orbitals. Once the super-excited state has been formed, it can decay in a number of ways, for example, by predissociation to form a pair of neutral fragments, or by fluorescence to a lower neutral electronic state. Alternatively, the molecule may undergo autoionization *via* a conversion of excess electronic energy (and perhaps excess vibrational and rotational energy) into kinetic energy of an electron occupying a high-lying orbital. Typically, this process will involve two electrons, where one electron falls into an orbital hole formed by the initial excitation of a non-valence electron, while a second electron is ejected from the molecule. Autoionization is therefore a resonance process, since the energy transferred to the molecule by the electron (or photon or other means of excitation) must match the energy of a transition involving the excitation of the non-valence electron.

1.2.2 Photoionization

Photoionization is the process by which the ionization of a target species occurs following the absorption of a photon (1.iia). Such photons are most commonly provided by a discharge lamp, laser, or by storage rings emitting synchrotron radiation.[22] The increased availability of synchrotron radiation sources in recent decades, providing a pulsed source of ionizing photons of variable wavelength and high intensity, and improving laser technology, means that photoionization is now a method widely used for the generation of gas phase ions.

$$h\nu + \mathrm{AB} \rightarrow \mathrm{AB}^{n+} + n\mathrm{e}^- \qquad 1.\mathrm{id}$$

The absorption of a photon below the ionization threshold energy is a resonant process, most commonly involving a single electron transition from one electronic state to another. Selection rules apply to these transitions, which arise due to the requirements of conservation of quantum variables such as angular momentum, spin and parity.[23] However, direct photoionization is non-resonant, since the outgoing electron is released into the continuum and can accommodate any excess kinetic energy. There are also no strict selection rules for photoionization, since the outgoing photoelectron may take on any value of angular momentum (l) in order to satisfy the conservation law:

$$\Delta l = \pm 1 \qquad 1.2$$

Therefore, the nature of the orbital from which an electron is removed can be found by studying the angular distribution of the photoelectrons. Such information can be provided by photoelectron imaging experiments.[24-28]

For direct photoionization processes involving the loss of n electrons, the threshold behaviour of the ionization cross section (σ) is described by the Wigner equation[29]:

$$\sigma \propto E^{n-1} \qquad 1.3$$

This means that the onset of the single photoionization cross section (n=1) at threshold is a step function, while for double photoionization (n=2) the onset of the ionization cross section is predicted to increase linearly with excess energy E. If long range interactions are also considered between the two outgoing electrons formed upon double photoionization, the energy dependence of the ionization cross section can be derived as:

$$\sigma_{ion} \propto E^{1.056} \qquad 1.4$$

which is the Wannier threshold law for double photoionization.[19] As described previously, such threshold laws produce their most accurate predictions of the ionization cross section within a small range of energies lying close to the ionization threshold. Of course, indirect processes may also contribute to the photoionization cross section, particularly at photon energies high above the ionization threshold.[30]

A considerable advantage offered by the photoionization method, in comparison with electron ionization, is that the amount of energy transferred to the target molecule is, in most cases, precisely known. For single photoionization, this means that if the energy of an ejected photoelectron can be measured accurately, it is possible to define exactly the state of the molecular ion that is populated by the photoionization event, and forms the basis of photoelectron spectroscopy (PES).[21] If the energy analysed electron is detected in coincidence with a photoion (PEPICO), the breakdown products from molecular ions formed with a single internal energy can be observed directly. Such measurements enable the state-selective fragmentation dynamics of singly charged ions formed by photoionization to be examined in detail.[31] Another form of experiment involves the detection of a photoelectron in coincidence with a fluorescence photon (PEFCO) and can be used to determine whether an excited electronic state of the molecular ion decays *via* a radiative process.[32] For some molecular systems such coincidence measurements have led to the observation of isolated electronic states, for which decomposition occurs without transformation of excess electronic energy into vibrational energy of the molecular ion.[33-35] In recent years, these coincidence studies have been extended to investigate the electronic states of molecular dications formed by double photoionization[22], and are discussed in later chapters.

1.2.3 Interactions with Positive Ions

The energy required to ionize a target species may be provided by collisions between positively charged ions and a neutral species. Here we consider two techniques that can be used for the generation of gas phase dications: Double charge transfer (DCT)[36,37] and Charge-stripping[38,39]. Experiments involving these ionization techniques can provide detailed information on the electronic states of doubly charged ions, and hence, can be compared to measurements described in this thesis of the energetics of small molecular dications.

$$C^+ + AB \rightarrow AB^{2+} + C^- \qquad \text{Double Charge Transfer (DCT)} \qquad 1.\text{iiia}$$

$$AB^+ + M \rightarrow AB^{2+} + M + e^- \qquad \text{Charge-stripping} \qquad 1.\text{iv}$$

In the double charge transfer process, a fast-moving positively charged projectile ion (C^+) acquires two electrons *via* a double electron-capture reaction with a neutral molecule of interest (AB). Such a reaction, as illustrated in (1.iiia), is endoergic since, in general, the energy required to doubly ionize AB is greater than the energy released in the charge inversion of C^+.[36,40] The additional energy required for the DCT reaction is supplied by the translational energy of the projectile ion C^+. Therefore, by measuring the translational energy lost by the fast moving ion following charge inversion, information on the double ionization energies of the neutral can be found.[41-43] If the product anions C^- are detected within a small angle of the original projectile direction, the recoil energy of the AB^{2+} dication can be ignored, and hence, the change in translational energy of the projectile ΔE can be expressed as:

$$\Delta E = \mathrm{IE}_2(\mathrm{AB}) - E(\mathrm{C}^+ \rightarrow \mathrm{C}^-) \qquad 1.5$$

where $\mathrm{IE}_2(\mathrm{AB})$ is the double ionization energy of AB (assumed to be initially in its ground electronic state), and $E(\mathrm{C}^+ \rightarrow \mathrm{C}^-)$ is the energy made available from charge inversion of the projectile ion. Long-range double charge transfer between the projectile ion and the neutral takes place in the Born-Oppenheimer approximation, and so the double ionization energies recorded by a DCT spectrometric experiment represent the vertical double ionization energies of the neutral molecule AB from the ground state. Such measurements are particularly useful in measuring the energies of dicationic electronic states which do not exist as stable species.[44,45] In addition, the total electron spin angular momentum must be conserved during the course of a collision involving DCT. Therefore, by choosing a suitable projectile ion for the DCT reaction, it is possible to populate exclusively electronic states of the AB^{2+} dication with a single electron spin multiplicity.[36,46]

In the charge-stripping reaction (1.iv) a fast-moving projectile ion of interest (AB^+) is ionized in a collision with a neutral species (M), resulting in the formation of a dication AB^{2+}. The energy required to ionize the projectile ion AB^+ is taken from the translational energy of the projectile ion itself, and so a careful measurement of the translational energy loss in a charge-stripping experiment gives information on the vertical ionization energy of the cation.[38] This information indirectly allows the double ionization energy of the neutral molecule (AB) to be evaluated. One major limitation of the charge-stripping technique is that the doubly charged ions formed must have a lifetime of at least several microseconds in order to be detected in a typical charge-stripping experiment. Despite this, the technique has been used successfully to study the low-lying electronic states of a number of small molecular dications.[38,39] In some instances, the charge-stripping process enables the electronic states of a molecular dication to be accessed, that are inaccessible *via* a vertical transition at the geometry of the neutral molecule in its ground state. Thus, the charge-stripping technique can be used to prepare a number of stable molecular dications that cannot be prepared directly by ionization involving single photons or by collisions with electrons.[39,47]

1.2.4 Penning Ionization

Penning ionization involves the ionization of a target molecule following collisions with excited neutral species (1.v).[48,49] For ionization to occur, the electronic energy of the excited neutral must exceed the ionization energy of the target molecule. Most commonly, the excited neutral species used are excited rare gas atoms, as such metastable atoms may be long lived and are formed with a well defined energy.[49-51] Indeed, the majority of ionization studies employing Penning ionization involve metastable He ($1s^12s^1$) atoms, which have an energy of either 19.818 or 20.614 eV, depending on whether the $^3S_1$ or $^1S_0$ spin state is formed.[52,53]

Following Penning ionization the ejected electron can be detected and energy analysed. To a good approximation, the energy of the ejected electron corresponds to the energy difference between the electronic energy of the metastable atom and the molecular orbital energy.[49] Thus, Penning ionization can provide detailed information on the electronic structure of a molecule of interest, and hence, may produce results analogous to those obtainable by photoelectron spectroscopy.

1.3 Product Ions

Following the electron ionization of small gas phase molecules, a number of different product ions are formed. For the target molecules investigated in this thesis, these product ions generally consist of ions formed by both dissociative and non-dissociative ionization. Such product ions are singly or doubly charged, and for many product ion fragments formed *via* dissociative ionization, contributions to the yields of these ions may be from single, double or triple ionization. In this section, the different types of ions formed following an electron-molecule collision are examined in more detail. A particular emphasis is placed on the stability and ultimate fate of singly, doubly and triply charged parent ions formed upon direct single or multiple electron ionization. In addition, the ion coincidence methodology used in this thesis to distinguish fragment ions formed *via* dissociative single, double and triple ionization, is briefly reviewed.

1.3.1 Product Ions from Single Ionization

The direct single ionization of a neutral gas phase molecule involves a transition between two well-defined electronic states of the molecule and the molecular ion. In this process, an electron is removed from the neutral molecule and released into a continuum, resulting in the formation of a singly charged ion. Depending on the amount of energy that is transferred to the molecule during the electron-molecule collision, vibrational and rotational excitation may also accompany this transition, although one notes that the energy transferred into vibration and rotation is much smaller than the energy transfer during electronic excitation. Direct single ionization obeys the Franck-Condon principle, since the electronic transition takes place on a timescale much faster than nuclear motion. Therefore, the transition from the ground electronic state of the neutral to the electronic state of the molecular ion is vertical with respect to the interatomic distance r, as shown in schematically in Figure 1.1. In this Section the Franck-Condon principle is discussed for the generic diatomic molecule A—B, but, of course, it also true for polyatomic molecules comprising of N atoms (N>2), for which the potential curves shown in Figures 1.1-1.2 represent cuts through the 3N-6 dimensional potential energy surface.

Upon ionization, a number of different monocation electronic states may be accessed, depending on the relative shapes of the neutral and cationic potential energy curves of the molecular system under investigation, and the energy deposited by the electron collision. As shown in Figure 1.1(a), the parent ion may be formed *via* a vertical transition from the ground state of the neutral to a bound region of a cationic potential curve. This bound region is typically a deep potential energy well supporting a number of vibrational and rotational energy levels. For some molecular systems, the bound region of a cationic state cannot be accessed *via* a vertical transition from the ground electronic state of the neutral molecule. This results in the population of the cation potential curve at an energy above the dissociation asymptote, as shown in Figure 1.1(b), and hence, the monocation will dissociate to form a fragment monocation (A^+) and a neutral (1.ib). Of course, the cationic state accessed *via* a vertical transition may be a repulsive state. Once this state is populated the nuclei A^+ and B rapidly move apart and the excess potential energy of the system above the dissociation limit is converted into kinetic energy.

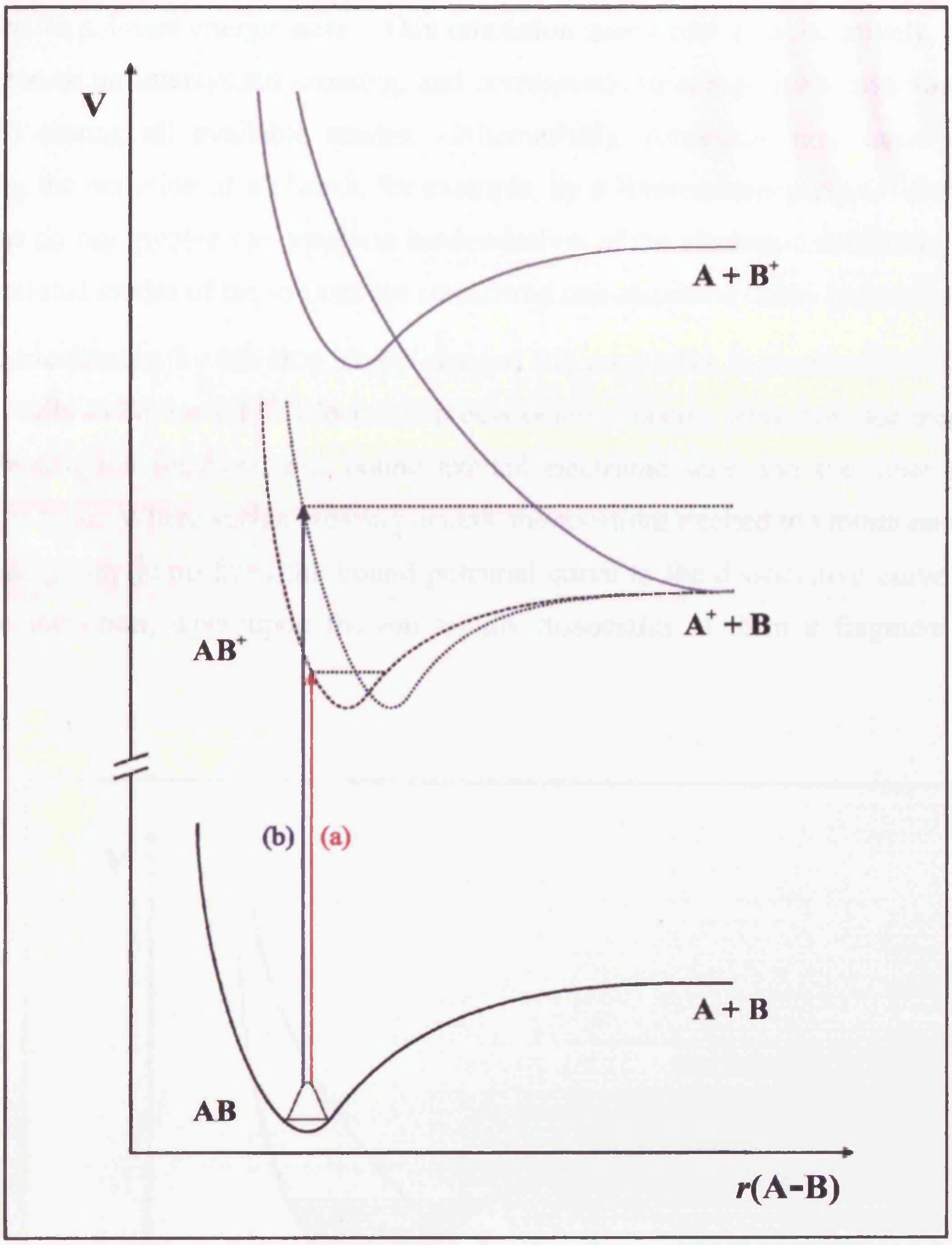

Figure 1.1 Schematic potential energy curves for the generic diatomic molecule A–B. Process (a) represents a vertical transition from the ground electronic state of the neutral to a bound region of a cationic potential curve, while process (b) corresponds to a transition to a cationic potential energy curve at an energy above the dissociation asymptote, and hence dissociates to form a singly charged fragment ion and a neutral.

For the ionizing electron energies investigated in this thesis (30-200 eV), singly charged ions are produced in a wide range of highly excited electronic and vibrational energy levels. If this cationic state is not the ground state of the monocation, the ion will, in general, undergo relaxation to a lower-energy state. This relaxation may occur non-radiatively, *via* internal conversion or an intersystem crossing, and corresponds to energy randomisation within the molecule among all available modes. Alternatively, relaxation may occur radiatively, involving the emission of a photon, for example, by a fluorescence process. Such radiative processes do not involve the complete randomisation of the electronic excitation energy into the vibrational modes of the ion and are considered non-statistical decay processes.

Another mechanism by which a singly charged ion may relax is predissociation, as shown schematically in Figure 1.2.[54] Electronic predissociation occurs when two potential curves of the molecular ion intersect; one bound excited electronic state and the other a repulsive electronic state. Where such a crossing occurs, monocations excited to vibrational levels near the crossing may jump from the bound potential curve to the dissociative curve *via* a non-radiative transition, whereupon the ion rapidly dissociates to form a fragment ion and a neutral.

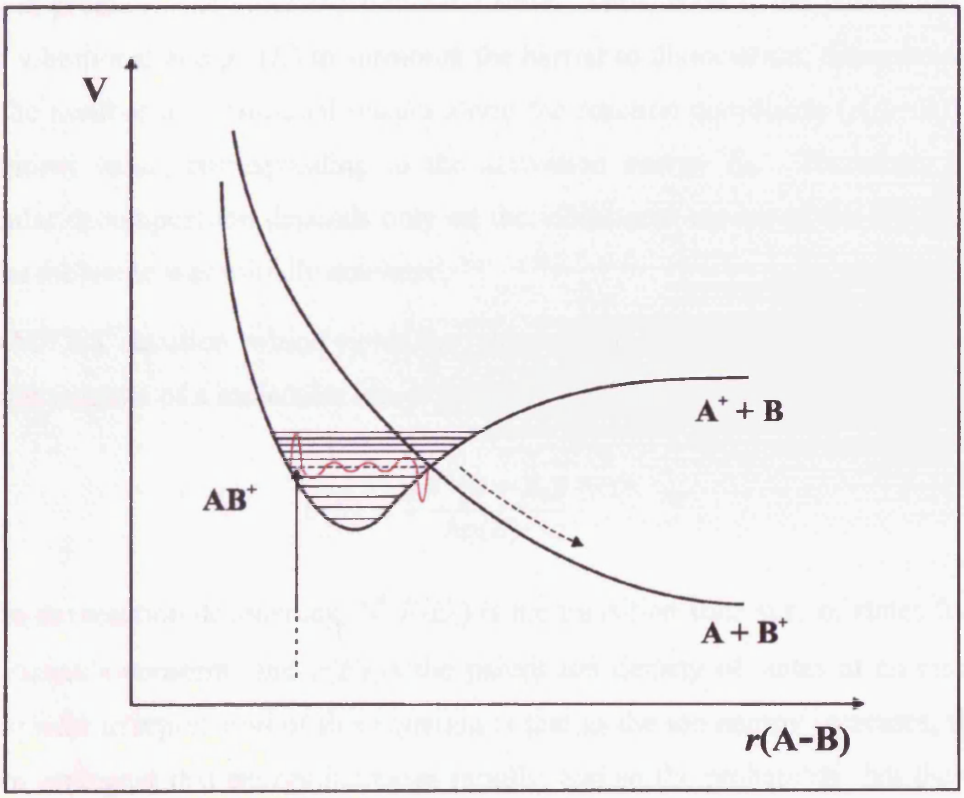

Figure 1.2 A schematic diagram showing how predissociation *via* a curve crossing from a bound potential surface to a dissociative potential surface provides a mechanism for molecular ion dissociation.

If the dissociation of a molecular ion occurs on a timescale faster than energy randomisation, then the dissociation is termed impulsive. If, however, dissociation is slower than energy randomisation, then the rate of unimolecular decomposition of the ion (1.vi) can be modelled using statistical theories:

$$AB^{*+} \rightarrow A^{+} + B \qquad \text{1.vi}$$

The two, essentially identical statistical theories used for this purpose are the quasiequilibrium theory (QET) developed by Rosenstock *et al.*[55], and the Rice-Ramsperger-Kassel-Marcus (RRKM) theory[56]. Both theories assume that molecular ions formed in excited electronic states relax rapidly by conversion of their electronic excitation energy into vibrational energy of the molecular ion in its ground state. This energy is distributed statistically among all available vibrational modes, normally within a few vibrational periods. A second assumption of QET/RRKM theory is that there exists a critical distance along the reaction coordinate which defines the barrier between the reactant (parent ion) and the dissociation products, the so-called transition state. Thus, even if the parent ion possesses sufficient vibrational energy (E) to surmount the barrier to dissociation, dissociation can only occur if the number of vibrational quanta along the reaction coordinate (r(A—B)) is greater than a critical value, corresponding to the activation energy E_0. Therefore, the rate of unimolecular decomposition depends only on the vibrational modes of the ion AB^+, and not on how the molecule was initially activated.

The RRKM/QET equation, which yields the rate constant k(E) for an individual unimolecular dissociation reaction of a molecular ion, is given by[57]:

$$k(E) = \frac{\sigma N^{\dagger}(E - E_0)}{h\rho(E)} \qquad 1.6$$

where σ is the reaction degeneracy, $N^{\dagger}(E\text{-}E_0)$ is the transition state sum of states from 0 to E-E_0, h is Planck's constant, and $\rho(E)$ is the parent ion density of states at an energy E. A simple physical interpretation of this equation is that as the ion energy increases, the number of ways of arranging this energy increases rapidly, and so the probability that the ion passes through the transition state increases accordingly. Conversely, for molecular ions possessing more vibrational modes, the density of states of the parent ion is greater, which yields a smaller value of the unimolecular dissociation rate constant k(E). The reaction degeneracy must also be considered as there may be more than one reaction coordinate (for example, more than one A—B bond) along which the dissociation may occur. For a more detailed description of the derivation of the RRKM/QET equation, and its applications, the reader is referred to the recent works of Baer and co-workers.[57,58]

In general, the relative abundance of any fragment ion is related to its rate of formation and its rate of dissociation by unimolecular decomposition. Therefore, a mass spectrum is a record in time of the position of this 'quasi-equilibrium' of those rates, and hence, the respective partial ionization cross sections of the fragment ions will depend on the time after formation of the parent ion.[4] If the initial energy deposited into the parent ion is known or assumed, then the RRKM/QET equation can be used to determine the rate constants of formation and dissociation of the fragment ions, and hence predict the relative abundances of the various fragment ions recorded in the mass spectrum. A comparison of these theoretical values to experimental mass spectra provides a means for testing whether the decay of the parent monocation is statistical or non-statistical[35] (see also Section 4.1).

1.3.2 Multiply Charged Ions: Stability and Fragmentation

At ionizing electron energies above the double ionization threshold energy, doubly charged parent ions and doubly charged fragment ions are observed in the electron ionization mass spectra of a number of small gaseous molecules, albeit in low abundance. The low abundance of such dications reflects the inherently small ionization cross sections (Section 1.4) for the formation of long-lived dications, even at ionizing electron energies well in excess of the double ionization threshold.[1,4] In fact, the majority of molecular dications formed by electron double ionization are thermodynamically unstable with respect to charge separating dissociation, and rapidly fragment on a sub-nanosecond timescale, resulting in the formation of a pair of singly charged fragment ions (1.vii).

$$\mathrm{AB}^{2+} \rightarrow \mathrm{A}^{+} + \mathrm{B}^{+} \qquad 1.\mathrm{vii}$$

In most conventional mass spectrometric experiments, singly charged fragment ions formed *via* dissociative double ionization are indistinguishable from those fragment monocations formed *via* dissociative single ionization. Thus, for many years, the widely accepted view was that double ionization represents only a minor contribution to the total ion yield following the ionization of a gaseous target molecule, for example, using photons or electrons. To distinguish between the singly charged fragment ions formed *via* single and double ionization events, respectively, an ion-coincidence technique is required.[59-62] Such a technique enables a singly charged fragment ion to be detected in coincidence with any correlated fragment monocation partner that is formed during the same double ionization event, thereby enabling the contribution to the ion yield from double ionization to be quantified. Indeed, recent measurements of the ionization cross sections of small molecules, employing an ion coincidence method, have shown that double ionization may contribute significantly to the total ion yield. For example, following electron ionization at 200 eV the contribution to the total ion yield from double ionization may exceed 25%.[13,59,63]

To understand why the majority of molecular dications undergo charge-separating dissociation prior to detection in a typical mass spectrometer, one must consider the stability of isolated diatomic dications AB^{2+} in the gas phase.[64-66] Many dication electronic states are purely dissociative, as shown in Figure 1.4 (state B), and the population of these dissociative states, either directly upon double ionization of the neutral molecule or *via* predissociation (Figure 1.3c), results in the formation of a translationally energetic pair of fragment monocations, $A^+ + B^+$. Such fragment monocations commonly share a translational kinetic energy in excess of 6 eV.[64,67] However, a thermodynamically stable dication may exist where the lowest dissociation asymptote to charge separation lies higher or very close in energy to the dissociation asymptote corresponding to $A^{2+} + B$. In this situation, the electrostatic interaction between the dication A^{2+} and the neutral B, termed the binding energy $D(A^{2+}—B)$, gives rise to a bound region on the dication potential curve that is the global minimum (Figure 1.3a).[66] Therefore, a thermodynamically stable dication is predicted to exist, provided that:

$$\mathrm{IE}(\mathrm{A}^+) + D(\mathrm{A}^{2+}—\mathrm{B}) < IE(\mathrm{B}) \qquad 1.\mathrm{vii}$$

where $IE(A^+)$ is the ionization energy of the fragment monocation A^+ and IE(B) is the ionization energy of the neutral fragment B. Indeed, thermodynamically stable diatomic dications have been observed experimentally among the rare-gas clusters ($GeNe^{2+}$, $XeNe^{2+}$, $PtHe^{2+}$) and binary metal halides (AlF^{2+}, SiF^{2+}, $FeCl^{2+}$, $CaBr^{2+}$). Stable dications are prevalent among the heavy metal fluorides, chlorides and oxides, since $IE(M^+)$ for the heavier metallic elements are often lower than IE(X) for the electronegative F, Cl or O atoms.[66]

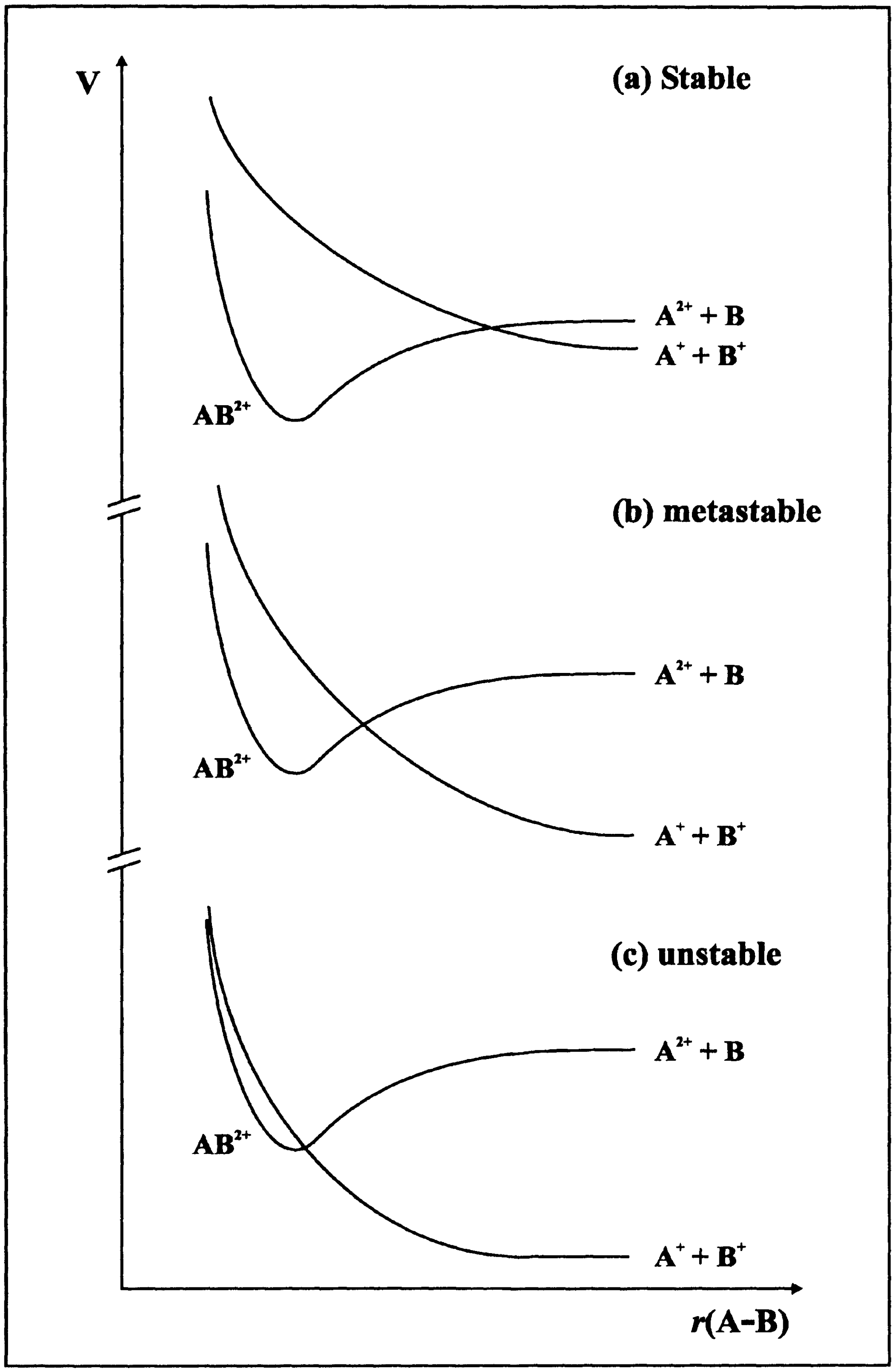

Figure 1.3 A schematic diagram of the diabatic potential energy curves for a generic diatomic dication AB^{2+}, representing: (a) thermodynamically stable dicationic states; (b) 'metastable' dicationic states; (c) thermodynamically unstable dicationic states.

For most small molecular dications AB^{2+} composed of light elements, the thermodynamic limit corresponding to $A^+ + B^+$ commonly lies below both the dissociation limit corresponding to $A^{2+} + B$ and the dicationic potential minimum. Therefore, the AB^{2+} configuration at the potential energy minimum is thermodynamically unstable with respect to charge separating dissociation. However, many small molecular dications possess "metastable" electronic states exhibiting local potential energy minima, as shown in Figure 1.4.[65] In a metastable dicationic state, kinetic stability is conferred on the AB^{2+} configuration by a potential barrier along the reaction coordinate leading to the formation of the charge separated products $A^+ + B^+$. Such a barrier arises due to the avoided crossing of the diabatic potential surfaces correlating with the $A^+ + B^+$ and $A^{2+} + B$ asymptotes. The potential surface corresponding to the dication-neutral limit is attractive at large internuclear separation, while the potential surface corresponding to the limit for forming $A^+ + B^+$ is purely repulsive. Therefore, an avoided crossing between these two potential surfaces may give rise to a local minimum in the AB^{2+} potential surface, separated from the $A^+ + B^+$ asymptote by a potential energy barrier.[65] This local potential minimum may have a depth of several electron Volts, and hence, may support a number of vibrational levels.[68-79]

Of course, the schematic representations of the diatomic dication potential energy curves in Figure 1.3 and Figure 1.4 are purely two-dimensional, whereas for polyatomic dications the corresponding potential surfaces are multidimensional. However, where such multidimensional potential surfaces have been investigated computationally, metastable dicationic states are similarly found to exist for polyatomic dications. Indeed, metastable states have been observed experimentally for a number of polyatomic dications.[65]

The lifetimes of dications in metastable states may vary considerably, and recent experiments have shown that the main decay pathway for metastable dications in low-lying vibrational states is *via* a predissociative curve crossing to a dissociative electronic state.[80-83] Therefore, the lifetime of an individual dicationic vibrational level will depend strongly on the degree of coupling between that level and the available dissociative states. For molecular dications formed by electron ionization, many will occupy metastable dicationic vibrational states which possess lifetimes on the order of several microseconds, or even on the order of seconds.[84,85] In this thesis, such metastable dications which survive for at least a few microseconds prior to fragmentation, are detected directly as single ion detections.

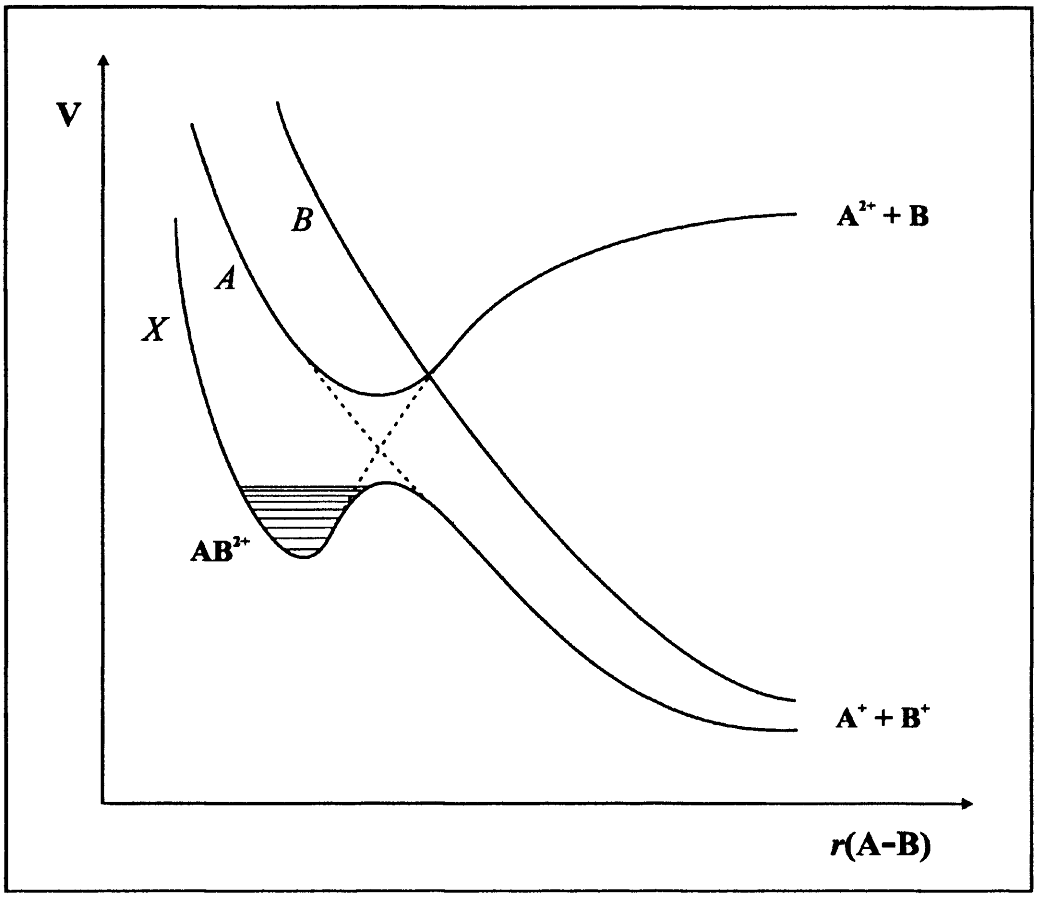

Figure 1.4 Schematic potential energy curves for a diatomic dication AB^{2+}, showing the existence of a bound metastable dicationic state with a potential barrier to charge-separating dissociation. Such potential barriers arise due to the avoided crossing of the diabatic potential surfaces correlating with the A^{2+} + B and A^{+} + B^{+} asymptotes.

In contrast to stable and metastable molecular dications, which are commonly observed in the electron ionization and photoionization mass spectra of small gaseous molecules, very few observations of long-lived triply charged molecular ions (trications) have been reported in the literature.[66,86] This is perhaps not surprising, since the stronger Coulomb repulsion between three positive charges mean that the majority of potential energy curves for molecular trications are purely repulsive. Furthermore, at ionizing energies in excess of the triple ionization threshold energy, the triple ionization cross sections for small gaseous molecules are typically several orders of magnitude smaller than the corresponding cross sections for single ionization.[87,88] Nevertheless, a small number of molecular trications with lifetimes on the order of at least several microseconds, including Cl_2^{3+}, SF^{3+}, COS^{3+} and SO_2^{3+}, have been observed in low abundance in mass spectrometric experiments.[66] The vast majority of molecular trications do however rapidly dissociate upon formation, on a sub-nanosecond timescale, to yield two or more positively charged ionic fragments. Consider, for example, the formation of a gas phase trication ABC^{3+} following electron ionization of the generic neutral molecule ABC. The trication will dissociate to form either a monocation-dication pair (1.viiib), or an ion triple composed of three singly charged ion fragments (1.viiia):

$$ABC^{3+} \rightarrow A^{+} + B^{+} + C^{+} \qquad \text{1.viiia}$$

$$ABC^{3+} \rightarrow A^{+} + BC^{2+} \qquad \text{1.viiib}$$

To distinguish between the different possible fragmentation channels of small molecular trications, an ion-ion-ion coincidence technique is required. Such a technique enables individual fragment ions to be detected in coincidence with up to two other correlated fragment ions formed during the same ionization event. In this way, the relative abundance of dication-monocation pairs and monocation triples, formed *via* dissociative triple ionization, can be measured. In general, such measurements reveal a propensity for symmetrical charge separation among the ionic fragments formed upon trication dissociation, corresponding to ion triple formation.[86,89,90]

In this thesis, time-of-flight mass spectrometry coupled with a 2-D ion coincidence technique is employed to investigate the electron ionization of a number of small gas molecules. This experimental method enables single product ions, product ion pairs and ion triples, formed following electron ionization, to be detected concomitantly, then identified and quantified. Such data allows the fragment ions formed *via* dissociative single, double and triple electron ionization to be distinguished, thereby providing detailed information on the single and multiple electron ionization processes that may occur.

1.4 Electron Ionization Cross Sections

As has been described in previous sections, the electron ionization of a molecule involves a collision between an electron and a target molecule, and the subsequent production of an ion or a number of correlated ions (and in some instances neutral fragments). A measure of the probability for such a reaction is provided in the form of an *ionization cross section* (ICS). The cross section for forming any positively charged particle in the exit channel of an electron ionization reaction, regardless of the identity of the ion formed, is termed the total electron ionization cross section (TICS).[91] The derivation and the measurement of the TICS for gaseous molecules is described in Section 1.4.1. Partial ionization cross sections (PICS) quantify the cross section for the production of a specific ion X^{m+}, and hence, provide more detailed information on the individual electron ionization processes that may take place.[4] For fragment ions formed *via* dissociative electron ionization, the cross sections for forming such ions by single, double, and triple electron ionization processes, are quantified individually in the form of precursor-specific PICS.[13] Such ionization cross-sections are described in more detail in Section 1.4.2.

The determination of partial ionization cross sections are of considerable importance to a diverse range of research fields including atmospheric and interstellar physics[2,3], plasma processing technology[1,92], and mass spectrometry. As was described in Section 1.1, the main technical difficulty in measuring accurate PICS is caused by the large kinetic energy release of ions formed *via* dissociative ionization processes. Indeed, the inefficient collection of such energetic ions in many previous PICS determinations has demanded that the PICS for a large number of small gas phase molecules are re-measured.[6] This has led to the development of a number of new experimental techniques capable of measuring reliable PICS, which allow for the complete collection of energetic fragment ions formed *via* dissociative electron ionization. In Section 1.4.4 a small selection of these newly developed techniques used in the determination of the PICS for small gas molecules, are briefly reviewed

In a typical experimental setup used to investigate the electron ionization of a gaseous molecule, a monoenergetic beam of ionizing electrons intersects a beam of target molecules, as shown schematically in Figure 1.5. Such an arrangement gives rise to a finite volume in which electrons and neutral molecules may collide. Any generalised ionization cross section σ can be expressed mathematically using a modified form of the Beer-Lambert law:

$$I = I_0 e^{-nl\sigma} \tag{1.7}$$

where I_0 is the initial electron flux, and I is the outgoing electron flux having passed a distance l through a uniform target gas of number density n. Under conditions of low target gas pressure and low electron flux ($nl\sigma \ll 1$), Eqn 1.7 can be re-written as:

$$I - I_0 = I_0 nl\sigma \tag{1.8}$$

Assuming single collision conditions, the quantity (I-I_0) corresponds to the number of ionization events N_{events} relating to the electron ionization process of interest. This gives rise to a generalised expression for the ionization cross section:

$$\sigma = \frac{N_{events}}{I_0 nl} \tag{1.9}$$

As will be shown in the sections that follow, the various types of ionization cross section are defined by the subset of electron ionization events (N_{events}) considered in the derivation of the ICS, according to Eqn 1.9.

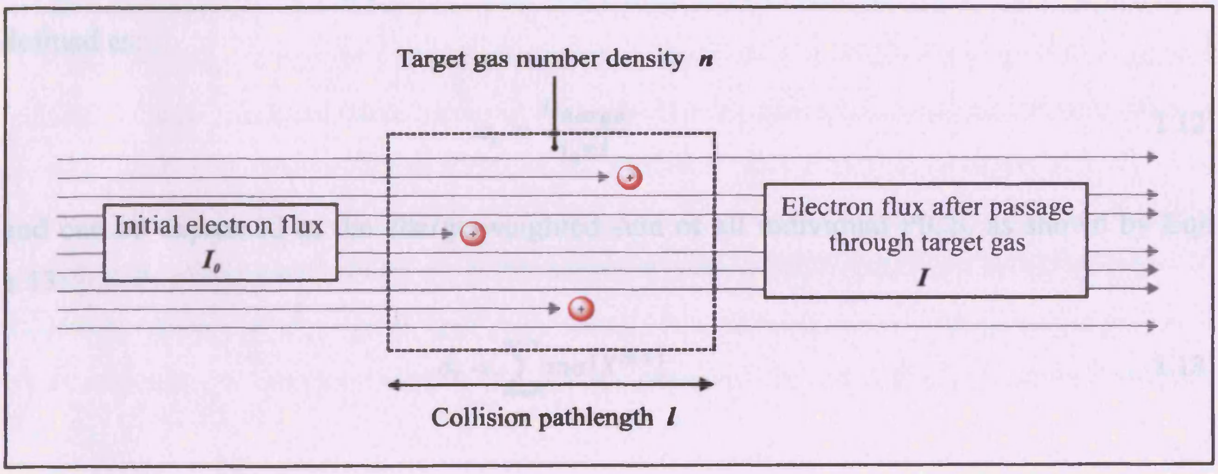

Figure 1.5 A schematic representation of a crossed-beam electron ionization experiment.

1.4.1 Total Ionization Cross-Sections

The total ionization cross section of a target molecule is, commonly, defined in one of two ways: The 'counting' TICS, or the total 'charge' ICS (gross ICS).[91] The *counting total ionization cross section* describes the cross section for forming any positively charged ion

X^{m+}, regardless of its mass or charge, following an electron-molecule collision. In this context, the term N_{events} in Eqn 1.9 is replaced by the total number of ions $\Sigma N[X^{m+}]$ formed by ionization events resulting in positive ion formation. Thus, the counting total ionization cross section σ_c is defined as:

$$\sigma_c = \frac{\sum N[X^{m+}]}{I_0 nl} \qquad 1.10$$

The counting TICS can also be expressed simply as the sum of all PICS for the target molecule of interest:

$$\sigma_c = \sum \sigma[X^{m+}] \qquad 1.11$$

An alternative definition of the TICS is the *gross ionization cross section*, also referred to as the total ionization cross section for charge production. The gross ICS describes the cross section for the production of positive ion charge following an electron-molecule collision. Therefore, N_{events} in Eqn 1.9 can be replaced by the positive charge flux I_{charge} produced by ionization events involving positive ion formation.[5] The gross ionization cross section σ_t is defined as:

$$\sigma_t = \frac{I_{charge}}{I_0 nl} \qquad 1.12$$

and can be expressed as the charge-weighted sum of all individual PICS, as shown by Eqn 1.13:

$$\sigma_t = \sum m\sigma[X^{m+}] \qquad 1.13$$

As shown by Eqn 1.12, the measurement of the gross ICS requires the determination of four quantities: The initial electron flux I_0, the electron collision pathlength l, the gas number density n, and the positive ion flux I_{charge}. A brief description of the principles involved in the measurement of these four quantities is given by the 'classic' Condenser-Plate apparatus developed by Smith and co-workers[93-95], illustrated in Figure 1.6. Indeed, such apparatus has been used in many more recent determinations of the TICS, with only slight modifications[91,96,97].

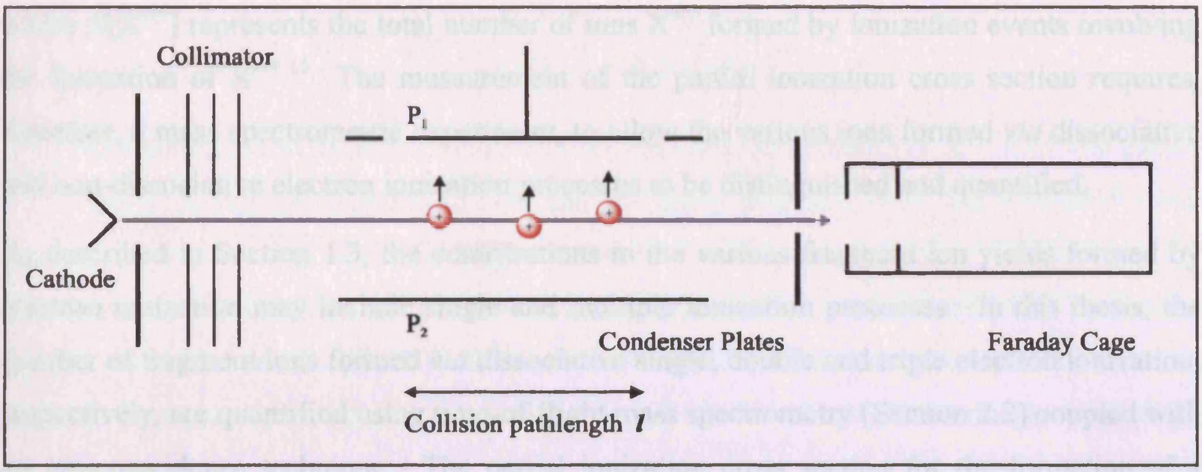

Figure 1.6 A schematic diagram of the Condenser-Plate apparatus used by Smith and co-workers[93-95], and similar to the apparatus used by Rapp, Englander-Golden[96,97] and co-workers, for the determination of the total (gross) ionization cross section.

Electrons emerge from a cathode, pass through a collimator and receive acceleration to a specified energy E, before entering a collision chamber filled with the target gas. A small electric field is applied across two condenser plates aligned parallel to the electron beam, P_1 and P_2, so that positive ions can be collected at P_1 and the total positive charge flux I_{charge} can be determined. An axial magnetic field prevents any deflection of the electron beam passing through the collision chamber and suppresses any secondary electron emission from P_1. The electron beam is then trapped in a Faraday cage, enabling the electron flux I_0 to be determined. As shown in Figure 1.6, the collision pathlength, l, is defined by the length of P_1 following in the electron beam direction. Finally, the number density of the target gas, n, is evaluated using a measurement of the gas pressure within the collision chamber (Section 1.4.4).

1.4.2 Partial Ionization Cross-Sections and Precursor-Specific PICS

The *partial ionization cross section* $\sigma[\mathrm{X}^{m+}]$ represents the cross section for the production of a specific ion X^{m+}, following an electron-molecule collision, and is defined as:

$$\sigma[\mathrm{X}^{m+}] = \frac{N[\mathrm{X}^{m+}]}{I_0 n l} \qquad \mathbf{1.14}$$

where $N[X^{m+}]$ represents the total number of ions X^{m+} formed by ionization events involving the formation of X^{m+}.[15] The measurement of the partial ionization cross section requires, therefore, a mass spectrometric experiment, to allow the various ions formed *via* dissociative and non-dissociative electron ionization processes to be distinguished and quantified.

As described in Section 1.3, the contributions to the various fragment ion yields formed by electron ionization may include single and multiple ionization processes. In this thesis, the number of fragment ions formed *via* dissociative single, double and triple electron ionization, respectively, are quantified using time-of-flight mass spectrometry (Section 2.2) coupled with an ion-coincidence technique. The partial ionization cross section for the formation of a specific fragment ion X^{m+}, involving the loss of n electrons from the neutral target molecule, is termed the *precursor-specific partial ionization cross section* $\sigma_n[X^{m+}]$:

$$\sigma_n[X^{m+}] = \frac{N_n[X^{m+}]}{I_0 n l} \qquad 1.15$$

where $N_n[X^{m+}]$ represents the number of ions X^{m+} formed by ionization events involving the loss of n electrons from the target molecule. Thus, in this context, the term 'precursor-specific' denotes the original charge state of the target molecule prior to dissociation to form a fragment ion X^{m+}. Such precursor-specific PICS $\sigma_n[X^{m+}]$ quantify the yield of each fragment ion from single (n=1), double (n=2) and triple (n=3) ionization, and hence, provide a more in-depth view of the various dissociative electron ionization processes leading to fragment ion formation.[13,62,98]

1.4.3 Relative Partial Ionization Cross Sections

As shown by equations 1.14 and 1.15, the determination of the absolute PICS and the absolute precursor-specific PICS for the formation of a particular ion, requires the accurate measurement of four experimental variables: The initial electron flux I_0, the collision pathlength l, the number density of the target gas in the collision region n, and of course, the appropriate number of ions $N_n[X^{m+}]$ formed by electron ionization events. A considerable experimental simplification is achieved by taking a ratio of the PICS for forming a selected fragment ion $\sigma[X^{m+}]$, against the PICS of another specific ion, commonly the parent ion $\sigma[\text{parent}^+]$. Such PICS are termed *relative partial ionization cross sections*[13,62,63,87,88,98-102] $\sigma_r[X^{m+}]$:

$$\sigma_r[\mathrm{X}^{m+}] = \frac{\sigma[\mathrm{X}^{m+}]}{\sigma[\mathrm{parent}^{+}]} = \frac{N[\mathrm{X}^{m+}]}{N[\mathrm{parent}^{+}]} \qquad 1.16$$

Thus, the determination of the relative PICS requires only the number of X^{m+} ions and parent ions formed during an experiment, and can be easily obtained from the measured mass spectral intensities. Where required, the relative PICS can be placed on an absolute scale by normalisation to available total ionization cross section data, or reliable absolute PICS data for the formation of the parent ion, determined under similar experimental conditions of target gas pressure and temperature.

1.4.4 Experimental Techniques for the Measurement of PICS

In this section three different experimental methods used for the determination of absolute PICS are briefly reviewed. The first method, as used by Straub and co-workers[15,103-106], involves the measurement of all four experimental variables expressed in Eqn 1.14 ($N[\mathrm{X}^{m+}]$, I_0, l, n), to directly determine the absolute PICS for each ion of interest. In the second method, as used by Tian and Vidal[16,107,108], measurements of the ion intensities are performed for a carefully prepared mixture of the target gas and a second gas, such as argon, for which the absolute PICS are well characterised. Such measurements are then placed on an absolute scale using a normalization method. Finally, the fast-neutral beam method of Becker and co-workers is briefly discussed, which can be used for the determination of the PICS of both molecules and transient species such as free radicals.[20,109]

An important feature of the apparatus used by Straub and co-workers[15], and the apparatus used by Tian and Vidal[16], is the demonstration of the complete collection of product ions formed with considerable kinetic energy. As described previously, the efficient collection of translationally energetic ions formed by dissociative ionization is essential for the determination of reliable PICS.[6]

Individual Parameter Determination

The experimental arrangement of Straub and co-workers (Figure 1.7) incorporates a short-pathlength time-of-flight mass spectrometer with position sensitive detection. A pulsed electron beam is directed through an interaction region filled with a target gas, located between two plates held at ground potential. After each electron pulse, a pulsed positive voltage is applied to the top plate to accelerate any positive ions formed towards the bottom plate. Some of these ions pass through an aperture in the bottom plate and impinge upon a position sensitive detector (PSD), allowing both the arrival time and position of each product ion to be recorded. While product ions are detected along the length of the PSD in the direction parallel to the electron beam, the transverse positional distribution of product ions arriving at the detector demonstrates the complete collection of energetic fragment ions, regardless of their initial translational kinetic energy. The ion signals from the detector are then processed to yield the number of ions $N[X^{m+}]$ produced during the experiment.

To determine absolute PICS, the electron flux I_0 is found by collecting the electron beam in a Faraday cup and measuring the current with an electrometer. The collision length l is defined by the length of the aperture in the bottom plate directly above the PSD. Finally, the target gas number density, n, is obtained from the pressure p measured by a capacitance diaphragm gauge.[110]

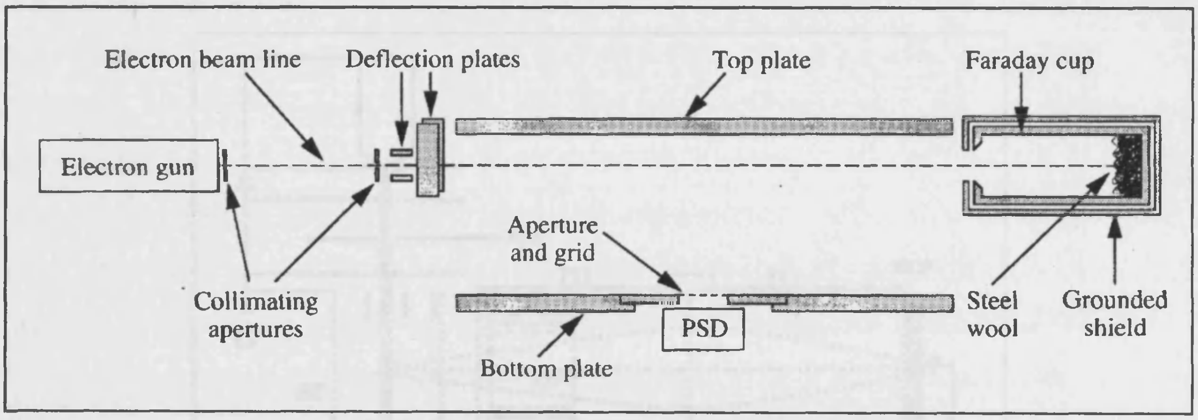

Figure 1.7 A schematic diagram of the apparatus used by Straub and co-workers.[15,103-106]

In most experiments developed for the measurement of absolute PICS, the accurate determination of the target gas number density in the interaction region, n, is the most difficult of the four variables required for the direct evaluation of $\sigma[X^{m+}]$ (Eqn 1.14). In early determinations of the PICS a McLeod gauge was most commonly used to measure the pressure, from which the target gas number density was derived. However, such pressure measurements using a McLeod gauge have been shown to be in serious error, due to problems associated with the 'mercury pumping effect'.[91] In more recent experiments, pressure measurements are often provided using a capacitance manometer or a spinning rotor gauge.

Normalisation Method

Figure 1.8 shows a schematic diagram of the focusing time-of-flight (FTOF) mass spectrometer used by Tian and Vidal for the determination of the absolute PICS for a number of small gaseous molecules.[16] The experimental arrangement bears many similarities to the two-field TOF mass spectrometer employed in this thesis, described in detail in Section 2, with some modifications. In the FTOF, the drift tube (FT) is divided into two segments, FT1 and FT2, separated by a focusing mesh (IL). By applying an appropriate negative voltage across this focusing mesh, the equipotential curves inside the apparatus behave as a symmetric spherical lens, and 'focus' the diverging ion beam from the source region onto the MCP detector plane. The complete collection of product ions is demonstrated by monitoring the dependence of the ion count rate recorded at the detector, with respect to the voltages applied to the deflector plates XD and YD.

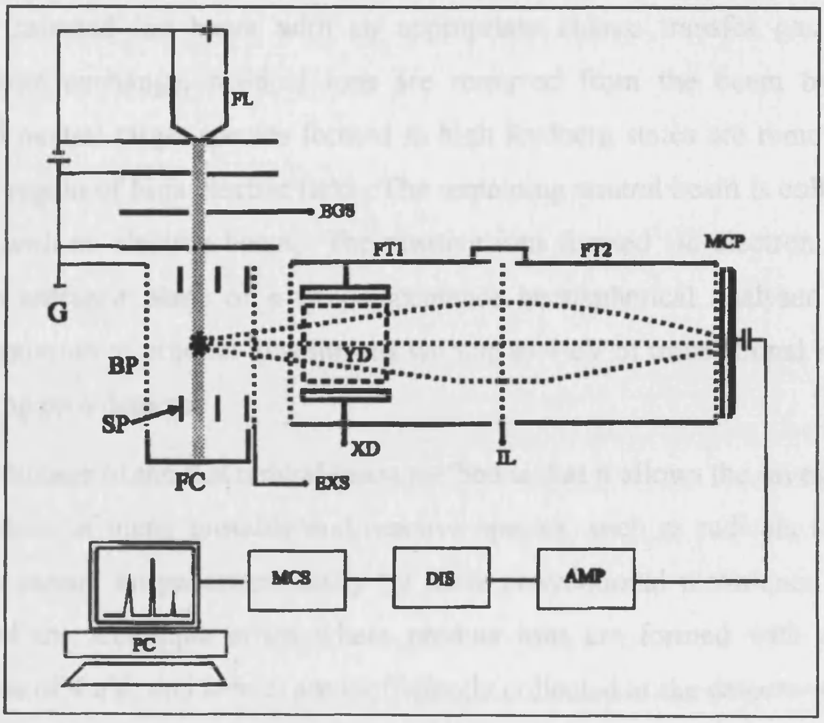

Figure 1.8 A schematic diagram of the focusing-TOF mass spectrometer used by Tian and Vidal.[16,107,108] The main components of the apparatus are labelled as follows: FL=Filament, FC=Faraday cup, BP=Backing plate, XD/YD=*x*-deflector/*y*-deflector, FT=Flight tube (1 and 2), IL=Ion lens, MCP=Microchannel plate.

The target gas of interest is premixed with a reference gas (Ar) in a suitable ratio, and the mass spectrum of the gas mixture is recorded to determine the number of product ions $N[\mathrm{X}^{m+}]$ formed *via* electron ionization of the target gas, and also the number of Ar^+ ions $N[\mathrm{Ar}^+]$ formed *via* electron ionization of the reference gas. The absolute PICS for the formation of each product ion X^{m+} is then found by normalization to the absolute PICS for forming Ar^+, $\sigma[\mathrm{Ar}^+]$, which can be obtained from the literature[15]:

$$\sigma[\mathrm{X}^{m+}] = \frac{N[\mathrm{X}^{m+}]}{N[\mathrm{Ar}^+]} \times \frac{n_{\mathrm{Ar}}}{n_{\mathrm{target}}} \times \sigma[\mathrm{Ar}^+] \qquad 1.17$$

where n_{Ar} and n_{target} are the number densities of Ar and the target gas in the mixing bottle.

Fast-Neutral Beam Method

The fast neutral beam method used by Becker, Tarnovsky and co-workers[20,109,111-115], involves the preparation of a fast neutral target beam by resonant charge exchange of a primary mass selected ion beam with an appropriate charge transfer gas (Figure 1.9). Following charge exchange, residual ions are removed from the beam by electrostatic deflection, and neutral target species formed in high Rydberg states are removed following ionization in a region of high electric field. The remaining neutral beam is collimated before being crossed with an electron beam. The positive ions formed *via* electron ionization are focused in the entrance plane of a wide-acceptance hemispherical analyser, allowing the complete transmission of product ions formed with up to 4 eV of translational kinetic energy, before impinging on a detector.

The unique advantage of the fast neutral beam method is that it allows the investigation of the electron ionization of many unstable and reactive species, such as radicals and metastable species, which cannot be generated easily by more conventional techniques. However, a disadvantage of the technique arises where product ions are formed with a translational energy in excess of 4 eV, and hence, are inefficiently collected at the detector due to the less than unit transmission efficiency of the hemispherical analyser for such energetic ions. Further complications may also arise since the internal energy content of the target species in the neutral beam is often unknown, and, therefore, the measured data may include the ionization of target species which are not in the ground electronic and/or vibrational state.

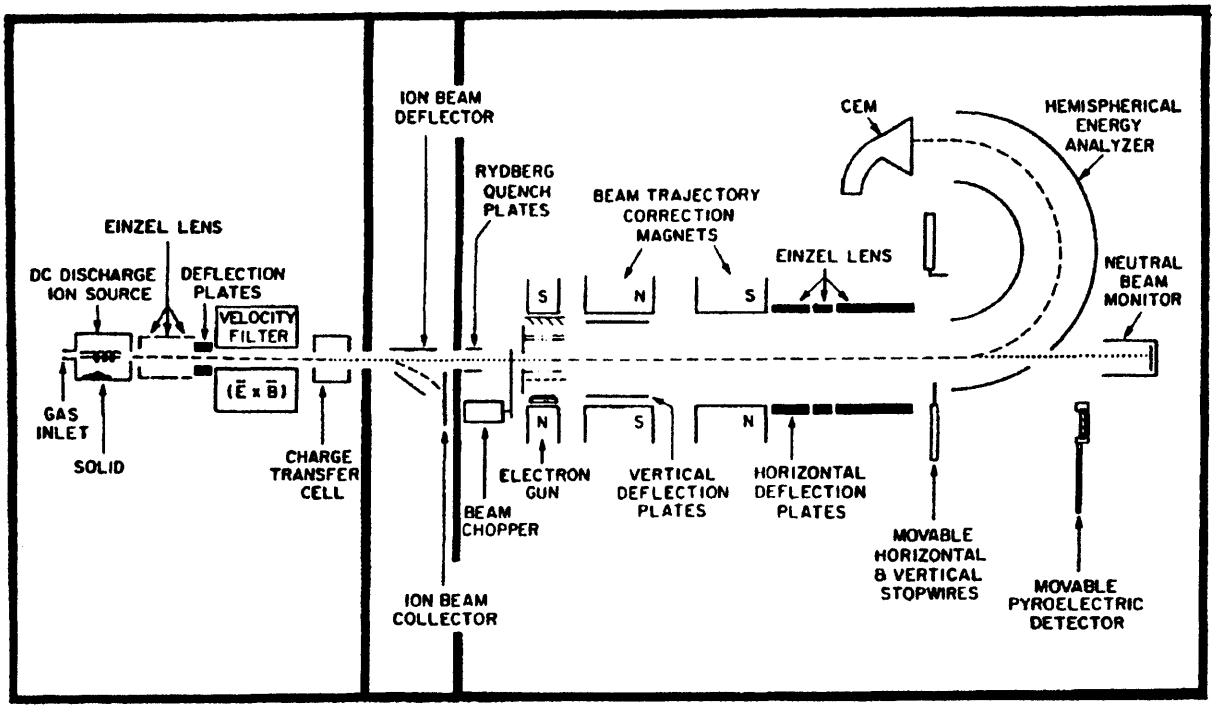

Figure 1.9 A schematic diagram of the fast neutral beam apparatus used by Becker, Tarnovsky and co-workers.[20,109]

1.5 Aims

The aim of this thesis is to provide a more detailed understanding of the dissociative ionization processes that occur following collisions between electrons and small gaseous molecules, with applications to planetary atmospheric chemistry and/or plasma processing technologies. The first major focus of this work concerned the determination of accurate and reliable relative partial ionization cross sections for electron ionization processes involving positive ion formation. A comprehensive comparison with existing ionization cross section data is presented for each molecular system investigated, and a detailed analysis of the results, and their interpretation, is provided. Relative precursor-specific PICS data and PICS for ion pair formation, following the electron ionization of C_2F_6, $SiCl_4$, C_2H_2, CO_2, and H_2O, are presented for the first time.

The second major focus of this work was to investigate the various processes involved in the charge-separating decay of small molecular dications. The dissociation dynamics of such dications is examined through the analysis of ion-coincidence data, and by the derivation of branching ratios. The results of this analysis have been interpreted to provide information on the instantaneous or sequential nature of dication fragmentation. In addition, information on the kinetic energy release involved in ion pair formation, following the charge-separating dissociations of molecular dications, has been obtained using simulations of the experimental ion coincidence data. Such data is used to derive the first estimates of the electronic state energies of the $C_2F_6^{2+}$ dication and $SiCl_4^{2+}$ dication.

1.6 References

[1] L. G. Christophorou and J. K. Olthoff, *Fundamental Electron Interactions with Plasma Processing Gases*. (Plenum, New York, 2004).

[2] E. Herbst, Annual Review of Physical Chemistry **46**, 27 (1995).

[3] M. J. McEwan, G. B. I. Scott, and V. G. Anicich, Int. J. Mass Spectrom. **172** (3), 209 (1998).

[4] T. D. Märk, in *Electron Impact Ionization*, edited by T. D. Märk and G. H. Dunn (Springer, Vienna, 1985).

[5] T. D. Mark, Plasma Physics and Controlled Fusion **34** (13), 2083 (1992).

[6] R. F. Stebbings and B. G. Lindsay, J. Chem. Phys. **114** (10), 4741 (2001).

[7] H. U. Poll, C. Winkler, D. Margreiter, V. Grill, and T. D. Mark, Int. J. Mass Spectrom. Ion Process. **112** (1), 1 (1992).

[8] O. J. Orient and S. K. Srivastava, J. Phys. B-At. Mol. Opt. Phys. **20** (15), 3923 (1987).

[9] H. U. Poll and J. Meichsner, Contributions to Plasma Physics **27** (5), 359 (1987).

[10] R. H. Vought, Phys. Rev. **71** (2), 93 (1947).

[11] E. Hille and T. D. Mark, J. Chem. Phys. **69** (10), 4600 (1978).

[12] T. D. Mark and E. Hille, J. Chem. Phys. **69** (6), 2492 (1978).

[13] N. A. Love and S. D. Price, Phys. Chem. Chem. Phys. **6** (19), 4558 (2004).

[14] C. Tian and C. R. Vidal, J. Phys. B-At. Mol. Opt. Phys. **31** (24), 5369 (1998).

[15] H. C. Straub, P. Renault, B. G. Lindsay, K. A. Smith, and R. F. Stebbings, Phys. Rev. A **52** (2), 1115 (1995).

[16] C. C. Tian and C. R. Vidal, J. Chem. Phys. **108** (3), 927 (1998).

[17] F. H. Read, in *Electron Impact Ionization*, edited by T. D. Märk and G. H. Dunn (Springer, Vienna, 1985).

[18] G. H. Wannier, Phys. Rev. **89** (1), 336 (1953).

[19] G. H. Wannier, Phys. Rev. **100** (4), 1180 (1955).

[20] K. H. Becker and V. Tarnovsky, Plasma Sources Science & Technology **4** (2), 307 (1995).

[21] J. H. D. Eland, *Photoelectron Spectroscopy*. (Butterworths, London, 1984).

[22] J. H. D. Eland, in *Vacuum Ultraviolet Photonionization and Photodissociation of Molecules and Clusters*, edited by C. Y. Ng (World Scientific, Singapore, 1991).

[23] J. M. Hollas, *Modern Spectroscopy*, Fourth ed. (Wiley, 2005).

[24] C. Bordas, F. Paulig, H. Helm, and D. L. Huestis, Review of Scientific Instruments **67** (6), 2257 (1996).

[25] A. Eppink and D. H. Parker, Review of Scientific Instruments **68** (9), 3477 (1997).

[26] D. H. Parker and A. Eppink, J. Chem. Phys. **107** (7), 2357 (1997).

[27] J. A. Davies, J. E. LeClaire, R. E. Continetti, and C. C. Hayden, J. Chem. Phys. **111** (1), 1 (1999).

[28] A. Sanov and R. Mabbs, International Reviews in Physical Chemistry **27** (1), 53 (2008).

[29] E. P. Wigner, Phys. Rev. **73** (9), 1002 (1948).

[30] S. Hsieh and J. H. D. Eland, J. Phys. B-At. Mol. Opt. Phys. **30** (20), 4515 (1997).

[31] T. Baer, Int. J. Mass Spectrom. **200** (1-3), 443 (2000).

[32] R. P. Tuckett, G. K. Jarvis, K. J. Boyle, and C. A. Mayhew, Journal of Electron Spectroscopy and Related Phenomena **103**, 93 (1999).

[33] I. G. Simm, C. J. Danby, and J. H. D. Eland, Journal of the Chemical Society-Chemical Communications (21), 832 (1973).

[34] D. M. Smith, R. P. Tuckett, K. R. Yoxall, K. Codling, P. A. Hatherly, J. F. M. Aarts, and M. Stankiewicz, J. Chem. Phys. **101** (12), 10559 (1994).

[35] G. K. Jarvis, K. J. Boyle, C. A. Mayhew, and R. P. Tuckett, J. Phys. Chem. A **102** (19), 3219 (1998).

[36] F. M. Harris, Int. J. Mass Spectrom. Ion Process. **120** (1-2), 1 (1992).

[37] J. Appell, J. Durup, F.C. Fehsenfeld, and P. Fournier, J. Phys. B-At. Mol. Opt. Phys. **6** (1), 197 (1973).

[38] C. J. Proctor, C. J. Porter, T. Ast, P. D. Bolton, and J. H. Beynon, Organic Mass Spectrometry **16** (10), 454 (1981).

[39] M. Rabrenovic, C. J. Proctor, T. Ast, C. G. Herbert, A. G. Brenton, and J. H. Beynon, J. Phys. Chem. **87** (17), 3305 (1983).

[40] W. J. Griffiths, M. L. Langford, and F. M. Harris, Rapid Communications in Mass Spectrometry **10** (9), 997 (1996).

[41] S. R. Andrews, F. M. Harris, and D. E. Parry, Chem. Phys. **166** (1-2), 69 (1992).

[42] I. W. Griffiths, D. E. Parry, and F. M. Harris, Chem. Phys. **238** (1), 21 (1998).

[43] P. G. Fournier, J. Fournier, F. Salama, P. J. Richardson, and J. H. D. Eland, J. Chem. Phys. **83** (1), 241 (1985).

[44] I. W. Griffiths, D. E. Parry, and F. M. Harris, Int. J. Mass Spectrom. **187**, 651 (1999).

[45] J. C. Severs, F. M. Harris, S. R. Andrews, and D. E. Parry, Chem. Phys. **175** (2-3), 467 (1993).

[46] R. P. Grant, F. M. Harris, S. R. Andrews, and D. E. Parry, Int. J. Mass Spectrom. Ion Process. **142** (1-2), 117 (1995).

[47] T. Ast, C. J. Porter, C. J. Proctor, and J. H. Beynon, Chem. Phys. Lett. **78** (3), 439 (1981).

[48] F. M. Penning, Naturwissenschaften **15** (40) (1927).

[49] P. E. Siska, Reviews of Modern Physics **65** (2), 337 (1993).

[50] A. Borodin, M. Yamazaki, N. Kishimoto, and K. Ohno, J. Phys. Chem. A **109** (21), 4721 (2005).

[51] B. Lescop, M. BenArfa, M. Cherid, G. LeCoz, G. Sinou, G. Fanjoux, A. LeNadan, and F. Tuffin, Journal Of Electron Spectroscopy And Related Phenomena **87** (1), 51 (1997).

[52] N. Kishimoto, T. Horio, S. Maeda, and K. Ohno, Chem. Phys. Lett. **379** (3-4), 332 (2003).

[53] N. Kishimoto, E. Matsumura, K. Ohno, and M. S. Deleuze, J. Chem. Phys. **121** (7), 3074 (2004).

[54] G. Herzberg, *Electronic Spectra and Electronic Structure of Polyatomic Molecules.* (D. Van Nostrand Company, New York, 1966).

[55] H. M. Rosenstock, M. B. Wallenstein, A. L. Wahrhaftig, and H. Eyring, Proceedings of the National Academy of Sciences of the United States of America **38** (8), 667 (1952).

[56] R. A. Marcus and O. K. Rice, Journal of Physical and Colloid Chemistry **55** (6), 894 (1951).

[57] T. Baer and P. M. Mayer, J. Am. Soc. Mass Spectrom. **8** (2), 103 (1997).

[58] T. Baer and W. L. Hase, *Unimolecular Reaction Dynamics: Theory and Experiments.* (Oxford, New York, 1996).

[59] M. R. Bruce, L. Mi, C. R. Sporleder, and R. A. Bonham, J. Phys. B-At. Mol. Opt. Phys. **27** (23), 5773 (1994).

[60] J. H. D. Eland, F. S. Wort, and R. N. Royds, Journal Of Electron Spectroscopy And Related Phenomena **41** (3-4), 297 (1986).

[61] L. J. Frasinski, K. Codling, and P. A. Hatherly, Science **246** (4933), 1029 (1989).

[62] S. Harper, P. Calandra, and S. D. Price, Phys. Chem. Chem. Phys. **3** (5), 741 (2001).

[63] P. Calandra, C. S. S. O'Connor, and S. D. Price, J. Chem. Phys. **112** (24), 10821 (2000).

[64] S. D. Price, Journal Of The Chemical Society-Faraday Transactions **93** (15), 2451 (1997).

[65] S. D. Price, Int. J. Mass Spectrom. **260** (1), 1 (2007).

[66] D. Schroder and H. Schwarz, J. Phys. Chem. A **103** (37), 7385 (1999).

[67] D. M. Curtis and J. H. D. Eland, Int. J. Mass Spectrom. Ion Process. **63** (2-3), 241 (1985).

[68] M. Lundqvist, D. Edvardsson, P. Baltzer, and B. Wannberg, J. Phys. B-At. Mol. Opt. Phys. **29** (8), 1489 (1996).

[69] A. D. J. Critchley, G. C. King, P. Kreynin, M. C. A. Lopes, I. R. McNab, and A. J. Yencha, Chem. Phys. Lett. **349** (1-2), 79 (2001).

[70] J. H. D. Eland, Chem. Phys. **294** (2), 171 (2003).

[71] J. H. D. Eland, S. S. W. Ho, and H. L. Worthington, Chem. Phys. **290** (1), 27 (2003).

[72] J. H. D. Eland, M. Hochlaf, G. C. King, P. S. Kreynin, R. J. LeRoy, I. R. McNab, and J. M. Robbe, J. Phys. B-At. Mol. Opt. Phys. **37** (15), 3197 (2004).

[73] R. I. Hall, L. Avaldi, G. Dawber, A. G. McConkey, M. A. Macdonald, and G. C. King, Chem. Phys. **187** (1-2), 125 (1994).

[74] A. J. Yencha, A. M. Juarez, S. P. Lee, and G. C. King, Chem. Phys. Lett. **381** (5-6), 609 (2003).

[75] A. J. Yencha, A. M. Juarez, S. P. Lee, G. C. King, F. R. Bennett, F. Kemp, and I. R. McNab, Chem. Phys. **303** (1-2), 179 (2004).

[76] M. Alagia, B. G. Brunetti, P. Candori, S. Falcinelli, M. M. Teixidor, F. Pirani, R. Richter, S. Stranges, and F. Vecchiocattivi, J. Chem. Phys. **120** (15), 6980 (2004).

[77] O. Furuhashi, T. Kinugawa, T. Hirayama, T. Koizumi, C. Yamada, and S. Ohtani, Chem. Phys. **295** (2), 185 (2003).

[78] O. Furuhashi, T. Kinugawa, S. Masuda, C. Yamada, and S. Ohtani, Chem. Phys. Lett. **342** (5-6), 625 (2001).

[79] O. Furuhashi, T. Kinugawa, S. Masuda, C. Yamada, and S. Ohtani, Chem. Phys. Lett. **337** (1-3), 97 (2001).

[80] S. G. Cox, A. D. J. Critchley, P. S. Kreynin, I. R. McNab, R. C. Shiell, and F. E. Smith, Phys. Chem. Chem. Phys. **5** (4), 663 (2003).

81 M. Larsson, G. Sundstrom, L. Brostrom, and S. Mannervik, J. Chem. Phys. **97** (3), 1750 (1992).

82 P. A. Martin, F. R. Bennett, and J. P. Maier, J. Chem. Phys. **100** (7), 4766 (1994).

83 D. M. Szaflarski, A. S. Mullin, K. Yokoyama, M. N. R. Ashfold, and W. C. Lineberger, J. Phys. Chem. **95** (6), 2122 (1991).

84 T. A. Field and J. H. D. Eland, Chem. Phys. Lett. **211** (4-5), 436 (1993).

85 D. Mathur, L. H. Andersen, P. Hvelplund, D. Kella, and C. P. Safvan, J. Phys. B-At. Mol. Opt. Phys. **28** (15), 3415 (1995).

86 D. Mathur, Physics Reports-Review Section of Physics Letters **391** (1-2), 1 (2004).

87 S. J. King and S. D. Price, J. Chem. Phys. **127**, 174307 (2007).

88 S. J. King and S. D. Price, Int. J. Mass Spectrom. **272** (2-3), 154 (2008).

89 J. P. Brichta, S. J. Walker, R. Helsten, and J. H. Sanderson, J. Phys. B-At. Mol. Opt. Phys. **40** (1), 117 (2007).

90 J. H. Sanderson, T. Nishide, H. Shiromaru, Y. Achiba, and N. Kobayashi, Phys. Rev. A **59** (6), 4817 (1999).

91 F. J. de Heer and M. Inokuti, in *Electron Impact Ionization*, edited by T. D. Märk and G. H. Dunn (Springer, Vienna, 1985).

92 *Database needs for modeling and simulation of plasma processing.* (National Research Council, National Academy Press, Washington, 1996).

93 P. T. Smith, Phys. Rev. **36**, 1293 (1930).

94 P. T. Smith, Phys. Rev. **37**, 808 (1931).

95 J. T. Tate and P. T. Smith, Phys. Rev. **39**, 270 (1932).

96 D. Rapp and P. Englander-Golden, J. Chem. Phys. **43** (5), 1464 (1965).

97 D. Rapp, P. Englander-Golden, and D. D. Briglia, J. Chem. Phys. **42** (12), 4081 (1965).

98 N. A. Love and S. D. Price, Int. J. Mass Spectrom. **233** (1-3), 145 (2004).

99 C. S. O'Connor and S. D. Price, Int. J. Mass Spectrom. **184** (1), 11 (1999).

100 C. S. S. Oconnor, N. C. Jones, K. Oneale, and S. D. Price, Int. J. Mass Spectrom. Ion Process. **154** (3), 203 (1996).

101 C. S. S. Oconnor, N. C. Jones, and S. D. Price, Int. J. Mass Spectrom. Ion Process. **163** (1-2), 131 (1997).

102 C. S. S. O'Connor, N. Tafadar, and S. D. Price, Journal Of The Chemical Society-Faraday Transactions **94** (13), 1797 (1998).

103 H. C. Straub, D. Lin, B. G. Lindsay, K. A. Smith, and R. F. Stebbings, J. Chem. Phys. **106** (11), 4430 (1997).

104 H. C. Straub, B. G. Lindsay, K. A. Smith, and R. F. Stebbings, J. Chem. Phys. **105** (10), 4015 (1996).

105 H. C. Straub, B. G. Lindsay, K. A. Smith, and R. F. Stebbings, J. Chem. Phys. **108** (1), 109 (1998).

106 H. C. Straub, P. Renault, B. G. Lindsay, K. A. Smith, and R. F. Stebbings, Phys. Rev. A **54** (3), 2146 (1996).

107 C. C. Tian and C. R. Vidal, J. Phys. B-At. Mol. Opt. Phys. **31** (4), 895 (1998).

108 C. C. Tian and C. R. Vidal, Phys. Rev. A **58** (5), 3783 (1998).

109 V. Tarnovsky and K. Becker, Zeitschrift Fur Physik D-Atoms Molecules and Clusters **22** (3), 603 (1992).

[110] H. C. Straub, P. Renault, B. G. Lindsay, K. A. Smith, and R. F. Stebbings, Review Of Scientific Instruments **65** (10), 3279 (1994).

[111] K. Becker, J. Mahoney, M. Gutkin, V. Tarnovsky, and R. Basner, Japanese Journal of Applied Physics Part 1-Regular Papers Brief Communications & Review Papers **45** (10B), 8188 (2006).

[112] V. Tarnovsky, R. Basner, M. Schmidt, and K. Becker, Int. J. Mass Spectrom. **208** (1-3), 1 (2001).

[113] V. Tarnovsky and K. Becker, J. Chem. Phys. **98** (10), 7868 (1993).

[114] V. Tarnovsky, H. Deutsch, and K. Becker, J. Phys. B-At. Mol. Opt. Phys. **32** (20), L573 (1999).

[115] V. Tarnovsky, P. Kurunczi, D. Rogozhnikov, and K. Becker, Int. J. Mass Spectrom. Ion Process. **128** (3), 181 (1993).

Chapter 2 Experimental Details

2.1 Introduction

In this thesis pulsed time-of-flight mass spectrometry coupled with a two-dimensional ion-coincidence technique is used to investigate the electron ionization of C_2F_6, $SiCl_4$, C_2H_2, CO_2 and H_2O. By this method positively charged single product ions, ion pairs and ion triples formed following electron collisions with target gas molecules, are detected concomitantly, then identified and quantified. Such experiments enable the determination of the relative PICS for these molecules, and also precursor-specific relative PICS, which, as described in Section 3.3, quantify the contributions to the yield of each product ion from single, double and triple ionization. The two-dimensional coincidence technique also provides information on the dynamics and energetics of the dissociations of multiply charged ions. In this chapter the key aspects of the apparatus design, experimental setup, and data sets produced by the experiment, are discussed.

2.2 Time-of-Flight Mass Spectrometry

The concept of time of flight mass spectrometry is based upon the principle that ions of varying mass, when accelerated through an electric field to the same kinetic energy, acquire different velocities and hence take different times to traverse the apparatus. Therefore, mass analysis can be performed by measuring the 'time of flight' for all ions passing through a specified distance. The relationship between the ion flight time t_{tof} and the ion mass m, for a typical TOF mass spectrometer, is derived in Appendix A as:

$$t_{tof} = k\sqrt{m} + c \qquad 2.1$$

where k and c are constants. The value of k is dependent on the geometry of the apparatus and voltage conditions used, while c is a constant that quantifies the time delay arising due to the timing electronics.

One major advantage of TOF mass spectrometry over many conventional methods is that it can be used to detect ions of all masses formed with all initial energies, continuously and simultaneously. This makes TOF mass spectrometry highly suited to the measurement of

PICS and for the study of multiply charged ions, since both require the use of a multiplex mass analysis technique.

2.2.1 Two-Field TOF Mass Spectrometry

The TOF mass spectrometer used in this thesis is based upon the standard Wiley-McLaren[1] two-field design, and is shown schematically in Figure 2.1. The spectrometer can be divided into three distinct regions: The 'source' providing the initial ion acceleration, a second 'acceleration' region, and a field-free 'drift' region. Ions are formed initially in the source region along a plane that lies perpendicular to the TOF axis. After formation these ions are accelerated through a distance *s* and out of the source, by an electric field E_s formed by a pulsed positive voltage applied to the repeller plate (RP). The ions exiting the source are then accelerated further by a second electric field E_d, formed by a grid held at a negative potential, positioned at the entrance to the ion drift region. Finally, the ions enter the field-free drift region and travel at a constant velocity before impinging on a multi-channel plate (MCP) detector. Thus, a mass spectrum is recorded by measuring the flight time for all ions between the point of formation in the source region and the detector. The geometry of the apparatus used in this thesis is indicated in Figure 2.1, while the electric field strengths can be inferred from the typical voltage conditions used, summarised in Table 2.1 (p.44).

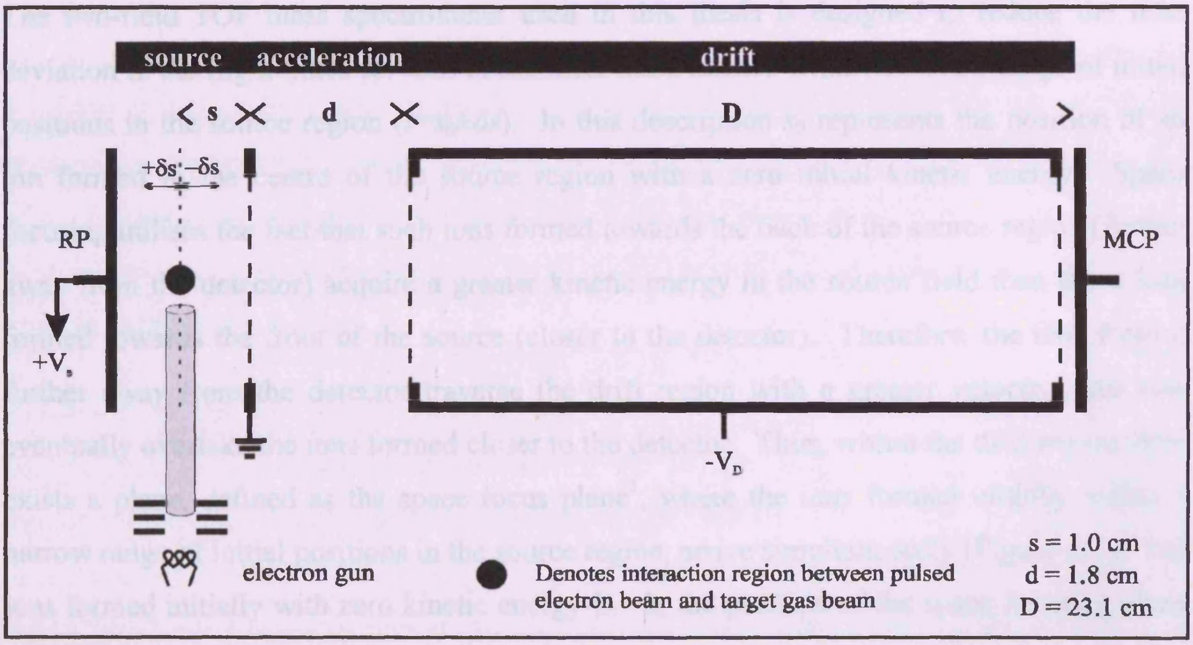

Figure 2.1 A schematic diagram of the two-field TOF mass spectrometer used in this thesis (not to scale)

A requirement of the TOF mass spectrometer used in this thesis is to combine good mass resolution with a high collection efficiency for ions formed initially with considerable kinetic energy. In a TOF mass spectrometer the mass resolution is limited by the initial spatial and kinetic energy distributions of ions formed in the source region. Methods used to reduce the time deviation for ion masses formed with an initial spatial distribution are known as space focusing, while methods used to reduce the time deviation for ion masses according to the initial kinetic energy distribution are known as energy focusing. These two aspects are now discussed in more detail.

2.2.2 Space Focusing

If all ions were formed in a single plane at the centre of the source region, perpendicular to the TOF axis, with zero initial kinetic energy, then the flight time would be the same for all ions of identical mass. In practice, however, the ions will have an initial spatial distribution in the source region. This distribution is due, in part, to the finite width of the electron beam used to ionize the target gas beam (Figure 2.1). Therefore, upon the application of an electric field to extract the ions from the source, each ion has a potential energy that is dependent on the initial position in the source region. After acceleration such ions acquire different kinetic energies and, hence, ions of identical mass will be detected with a distribution of flight times, thereby reducing the mass resolution of the TOF spectrum recorded.

The two-field TOF mass spectrometer used in this thesis is designed to reduce the time deviation in the flight times for ions of identical mass formed within a narrow range of initial positions in the source region ($s=s_0\pm\delta s$). In this description s_0 represents the position of an ion formed in the centre of the source region with a zero initial kinetic energy. Space focusing utilises the fact that such ions formed towards the back of the source region (further away from the detector) acquire a greater kinetic energy in the source field than those ions formed towards the front of the source (closer to the detector). Therefore, the ions formed further away from the detector traverse the drift region with a greater velocity, and may eventually overtake the ions formed closer to the detector. Thus, within the drift region there exists a plane, defined as the space focus plane[1], where the ions formed initially within a narrow range of initial positions in the source region, arrive simultaneously (Figure A.1). For ions formed initially with zero kinetic energy $U_0=0$, the position of the space focusing plane can be found, to first order[1], by:

$$\left(\frac{\partial t}{\partial s}\right)_{U_0=0,s} = 0 \qquad 2.2$$

and hence using Eqn A.18, an expression for the drift length defining the plane of space focus is obtained as:

$$D = 2sk_0\left(1 - \frac{d}{s\left(k_0 + {k_0}^{1/2}\right)}\right) \qquad \text{where} \qquad k_0 = \frac{sE_s + dE_d}{sE_s} \qquad 2.3$$

This relationship shows that the plane of space focus can be moved in a two-field TOF mass spectrometer, to a shorter or longer distance from the ion source, by careful manipulation of the voltages used. The aim, therefore, is to choose a set of voltage conditions such that the plane of space focus coincides with the plane of the detector. Thus, the typical operating voltages used throughout this thesis, summarised in Table 2.I, are chosen to provide a good first-order space focus for ions whilst maintaining a high collection efficiency for ions formed with considerable initial kinetic energy (Section 2.3.2).

Second-order space focusing[2] may be achieved by setting both first and second order derivatives of the flight time expression (Eqn A.18) to zero. This additional constraint means that, for a two-field TOFMS of fixed geometry, only a single solution to the second order space focusing condition may exist:

$$\frac{d}{D} = 2 + \frac{6}{(k_0 - 3)} \qquad 2.4$$

An obvious consequence of this expression is that TOF mass spectrometers obeying the condition for second order space focusing will typically incorporate a much longer acceleration region. For the current experimental geometry Eqn 2.4 yields a negative value of k_0, implying that second order space focusing conditions cannot be achieved. Suitable parameters that enable a second order focus would require a modification of the apparatus used throughout this thesis.

2.2.3 Energy Focusing

Within the TOF mass spectrometer ions are formed with an initial distribution of velocities in the source region. This is true for all ions, since each ion will possess at least a small component of thermal kinetic energy. Consider two ions (A and B) of identical mass and initial position in the source region. Ion A is formed with an initial velocity directed towards the detector ($+v_x$) while ion B is formed with the same initial velocity directed away from the detector ($-v_x$). Therefore, ion B requires an additional time to be decelerated by the source electric field E_s, such that v_x=0, then accelerated back to its original position in the source (Figure 2.2). Upon its return to this initial position, ion B will have an equal and opposite velocity ($+v_x$) to when it was formed. This additional time taken for ion B to reach the detector is termed the 'turn-around time'[3], and is discussed in more detail below. As a result of the turn-around time, the initial velocity distribution of ions gives rise to a broadening of the corresponding peaks observed in the TOF mass spectrum, thereby limiting the mass resolution.

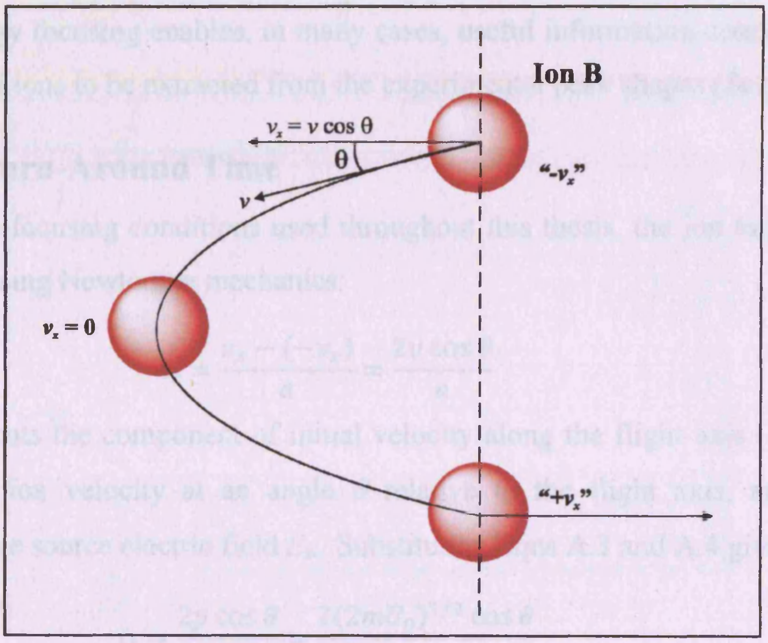

Figure 2.2 Simplified diagram showing how the 'turn-around time' arises for an ion formed in the source region with an initial velocity directed away from the detector.

One method that can be used to correct for the turn-around time in a two-field TOF mass spectrometer is known as time-lag velocity focusing[1]. In this method, a time delay is introduced between the time of ion formation and the application of the source electric field. During this time ions with an initial velocity directed away from the detector will move to a position in the source region of higher potential energy. Such ions will be accelerated to a greater kinetic energy than ions formed with an initial velocity directed towards the detector, which they may eventually overtake in the drift region. It is possible, therefore, to choose a timing delay which, for a given combination of electric fields E_s and E_d, corrects for the initial velocity distribution of ions with equal mass. This is time-lag velocity focusing.

However, this method can only be used with limited success to improve the mass resolution of TOF mass spectra. Firstly, the conditions for time-lag focusing are mass dependent and hence can only be used to achieve an energy-focus within a narrow range of ion masses. Secondly, the conditions for energy-focusing are not compatible with the conditions for space-focusing, placing a limit on the maximum mass resolution that can be obtained. Finally, increasing the time delay prior to the application of the source electric field may lead to losses of energetic low-mass ions in the source region. Therefore, in this thesis the time-lag is minimised experimentally (Appendix B) to eliminate any such ion losses. In fact, the absence of energy focusing enables, in many cases, useful information concerning the initial kinetic energy of ions to be extracted from the experimental peak shapes (Section 3.5).

2.2.4 Ion Turn-Around Time

Under the space-focusing conditions used throughout this thesis, the ion turn-around time t_t can be derived using Newtonian mechanics:

$$t_t = \frac{v_x - (-v_x)}{a} = \frac{2v\cos\theta}{a} \qquad 2.5$$

where v_x represents the component of initial velocity along the flight axis (Figure 2.2), v is the total initial ion velocity at an angle θ relative to the flight axis, and a is the ion acceleration in the source electric field E_s. Substituting Eqns A.3 and A.4 gives:

$$t_t = \frac{2p\cos\theta}{qE_s} = \frac{2(2mU_0)^{1/2}\cos\theta}{qE_s} \qquad 2.6$$

This important result shows that, under the space focusing conditions used in this thesis, the turn-around time is proportional to the component of initial ion momentum along the flight axis. It follows that:

$$t_{tof} = t_0 - \frac{p\cos\theta}{qE_s} \qquad 2.7$$

where t_0 is the flight time for an ion formed with a zero component of initial momentum along the flight axis. Therefore, the time deviation distribution in the mass spectrum is equivalent to the distribution of initial momentum components along the spectrometer axis. Ions formed with a single valued initial momentum release, isotropically distributed over all laboratory angles θ, will give rise to a flat-topped time distribution in the mass spectrum[4], centred at t_0 and with width $2p/qE_s$. Analysis of the peak widths in TOF mass spectra, under space focusing conditions, may therefore be used to extract information on the initial kinetic energy release of ions U_0.[5]

2.3 Experimental Setup

A schematic diagram of the time-of-flight mass spectrometer used in this thesis is shown in Figure 2.3. The spectrometer is housed in a single stainless steel chamber evacuated by a diffusion pump. A turbomolecular pump mounted at the detection region is used to maintain a low gas pressure in the vicinity of the ion detector during data acquisition. The glass/Teflon gas inlet system is held typically at low pressures to enable target gas molecules to enter the TOF mass spectrometer rapidly before any significant sample decomposition can occur. Gas flow into the apparatus is carefully controlled by a needle valve.

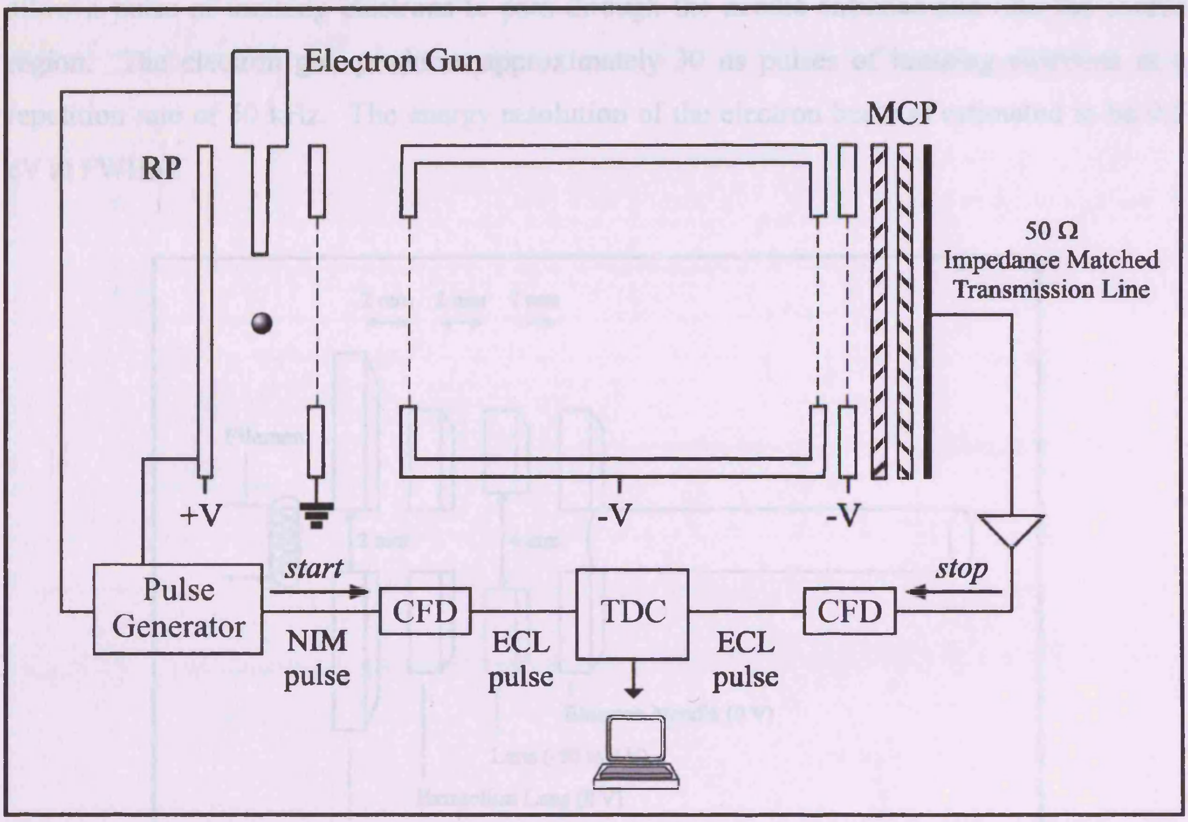

Figure 2.3 Schematic diagram of the time-of-flight mass spectrometer.

Within the apparatus, ionization of the target gas occurs following the interaction with a pulsed electron beam in the source region. Both the target gas beam and pulsed electron beam are transported to the source *via* hypodermic needles. These needles are mounted perpendicular to one another and both are aligned perpendicular to the TOF axis. Ionization of the target gas occurs at the point of intersection between the pulsed electron beam and the target gas beam at the centre of the source region.

The experiment is managed by a pulse generator operating at 50 kHz that controls the pulsing of the electron gun, repeller plate (RP), and produces start signals to begin each timing cycle of the data collection electronics. The electron gun (Figure 2.4) consists of a thoriated iridium filament, a stainless steel base plate, electron beam optics and a needle entrance to the source region. In the absence of a trigger pulse from the pulse generator, the base plate is held at a negative bias potential to prevent the passage of electrons from the filament to the needle entrance. Upon receipt of a trigger pulse, a pulse voltage is applied to the base plate to allow a pulse of ionizing electrons to pass through the needle entrance and into the source region. The electron gun produces approximately 30 ns pulses of ionizing electrons at a repetition rate of 50 kHz. The energy resolution of the electron beam is estimated to be 0.5 eV at FWHM.

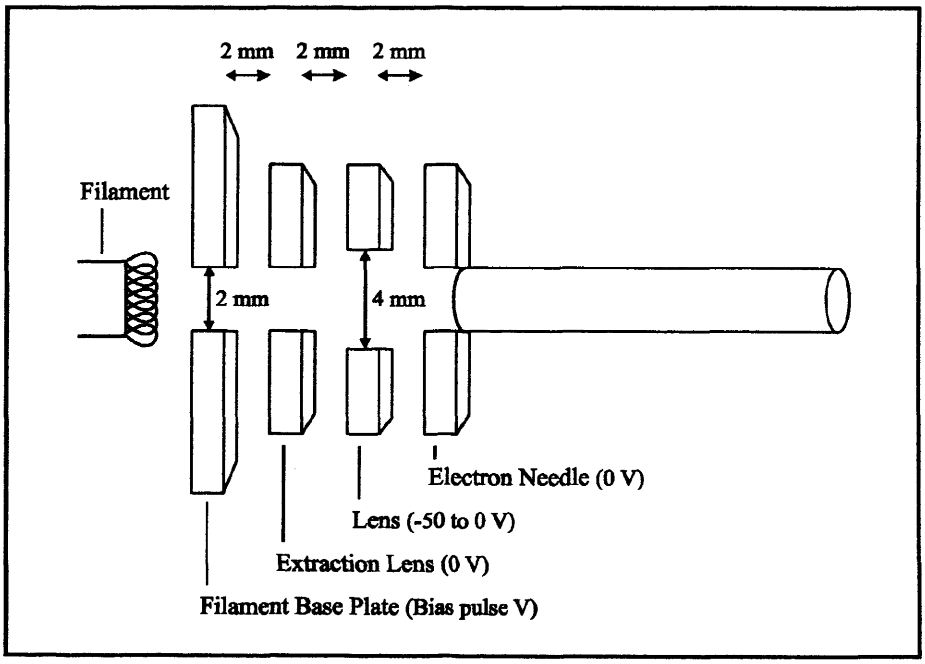

Figure 2.4 A schematic diagram of the pulsed electron gun.

Following the passage of an ionizing pulse of electrons through the source region, the repeller plate is pulsed from 0 to +400 V to extract all positive ions from the source into a second acceleration region. The electric field in the acceleration region E_d is formed by a grid held at a negative potential, positioned at the entrance to the ion drift tube. From a number of preliminary experiments performed using this apparatus (Appendix B) it was concluded that, to a small extent, the secondary electric field penetrates the source region and may partially extract ions from the source prior to the pulsing of the repeller plate. This effect results in a small deviation from the expected flight time distributions of ions of small mass such as H^+. Therefore the time delay x between the pulse of ionizing electrons and the repeller plate pulse (Figure 2.5) is minimised for most experiments described in this thesis. After acceleration ions traverse a field-free drift tube before impinging on a microchannel plate detector (MCP). 350 ns after the extraction voltage is applied to the repeller plate a 'start' signal is sent from the pulse generator to the time-to-digital convertor (TDC) *via* a constant fraction discriminator. This time delay is chosen to prevent any radio frequency noise formed by the pulsing of the repeller plate being recorded as ion signals from the detector.

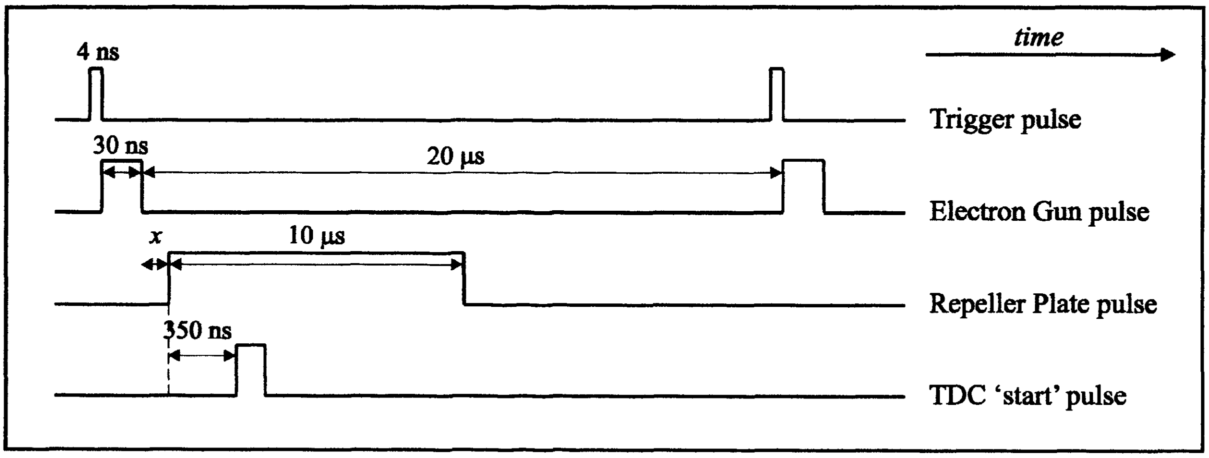

Figure 2.5 Summary of the pulse sequencing and pulse timings used for the TOF mass spectrometer.

The MCP used is a commercial design comprised of two identical parallel plates of diameter 40 mm. Each plate is composed of an array of micro-channels of approximately 15 μm diameter that function as miniature electron multipliers.[6] The channel axes are biased at a small angle to the normal of the MCP input surface and the two plates are aligned to form a chevron arrangement. Ions impinging on the MCP front surface result in an output pulse of 10^4-10^7 electrons which is collected on a copper anode. This signal is then amplified, discriminated using a CFD, and presented as a 'stop' pulse to the TDC. Following the discriminator output the CFD has a 'dead-time' of 32 ns during which time further output signals from the detector cannot be processed.

After each 'start' pulse the TDC is capable of receiving up to 32 'stop' pulses from the detector within a 5000 ns 'time window'. During this 'time window' the arrival times of ions as single ion detections, ion pairs and ion triples, are stored separately as single events in each case. The data are accumulated in a 512 kB memory module *via* a fast encoding and readout analog-to-digital conversion system interface and is transferred periodically to a personal computer. By this method, conventional TOF mass spectra and ion coincidence spectra are recorded concomitantly. The data sets that are produced by this procedure are discussed in more detail in Section 2.4.

Parameter	Typical Value	Parameter	Typical Value
RP Voltage	+400 V	CFD 'dead-time'	32 ns
Drift Tube Voltage	-2000 V	Discriminator Threshold	50 mV
MCP Front Voltage	-2450 V	Ion Count Rate	< 350 ion s^{-1}
MCP Back Voltage	-250 V	Target gas pressure	~10^{-6} Torr

Table 2.I Summary of the typical operating parameters used for experiments presented in this thesis

2.3.1 Ion Discrimination Effects

In extracting quantitative data from a pulsed electron-beam time-of-flight mass spectrometer it is important to ensure that the apparatus is able to detect all ions with equal efficiency, regardless of their mass or initial kinetic energy. Bruce and Bonham[7] have investigated a number of experimental parameters that may give rise to discrimination effects in such apparatus, through careful measurement of the Ar^{2+}/Ar^{+} ratio following the electron ionization of argon. The results of this study are summarised in Table A.1. Bruce and Bonham[7] found that the Ar^{2+}/Ar^{+} ratio was dependent on the background gas pressure, MCP bias voltage and CFD threshold setting. Specifically, this ratio was found to increase slowly as the background gas pressure is increased above 5×10^{-6} Torr, and was attributed to the greater attenuation of Ar^{+} ions than Ar^{2+} ions passing through the background gas en route to the detector. Accordingly, all experiments presented in this thesis are performed using a background gas pressure below 2×10^{-7} Torr. In accord with the recommendations of Bruce and Bonham[7], and Straub *et al.*[8], a MCP bias voltage greater than 2000 V is used in all experiments, and an experimentally optimised CFD threshold setting of 50 mV. However, both Ar^+ and Ar^{2+} ions detected in the work of Bruce and Bonham[7] are formed with only thermal kinetic energy, and hence, this previous work does not consider the effects of such experimental parameters on the collection efficiency and detection efficiency of ions formed initially with greater-than-thermal kinetic energy. Therefore, further experiments are required to ensure that under the operating parameters used in experiments documented in this thesis, energy-dependent discrimination effects do not influence the ion yields measured. These experiments are described in detail in Appendices B-C.

2.3.2 Energetic Ion Collection

As described above, when measuring PICS it is essential that the apparatus is able to collect efficiently translationally energetic ions at the detector.[9] This aspect is of particular importance when studying fragmentation processes involving multiple ionization, as such events are often characterised by large kinetic energy releases.[4,10]

The apparatus is designed to collect all ions formed with an initial translational energy of less than 10.6 eV, as shown by the calculation presented below. For the purpose of this calculation, it is assumed that ionization occurs at a point in the centre of the source region. The component of initial velocity an ion may possess perpendicular to the flight axis, v_y, and still impact on the detector (Figure 2.6), is given by:

$$\frac{r_{det}}{t_{tof}} > v_y \qquad 2.8$$

where r_{det} is the radius of the detector (20 mm) and t_{tof} is the flight time of an ion of mass m (with no component of initial velocity aligned along the flight axis). This velocity v_y can be related to the translational kinetic energy that an ion may possess, E_y, perpendicular to the flight axis, and still be detected:

$$v_y = \left(\frac{2E_y}{m}\right)^{1/2} \qquad 2.9$$

therefore:

$$E_y < \left(\frac{r_{det}}{t_{tof}}\right)^2 \frac{m}{2} \qquad 2.10$$

Of course, Equation 2.10 is independent of the mass of ion considered, since $t_{tof} \propto \sqrt{m}$. Using the flight time for the Ar^+ ion (2805 ns), the value $E_y < 10.6$ eV is obtained.

Curtis and Eland[10] determined the total kinetic energy release (KER) from the dissociation of small molecular dications to be, commonly, less than 9 eV. Thus, in the apparatus, conditions are optimised such that the majority of all ions formed by multiple ionization can be collected and quantified. In fact, losses of highly energetic ions ($E_y > 10.6$ eV) comprising ion pairs can be corrected, where necessary, from the ion coincidence data (Section 3.2.2.2).

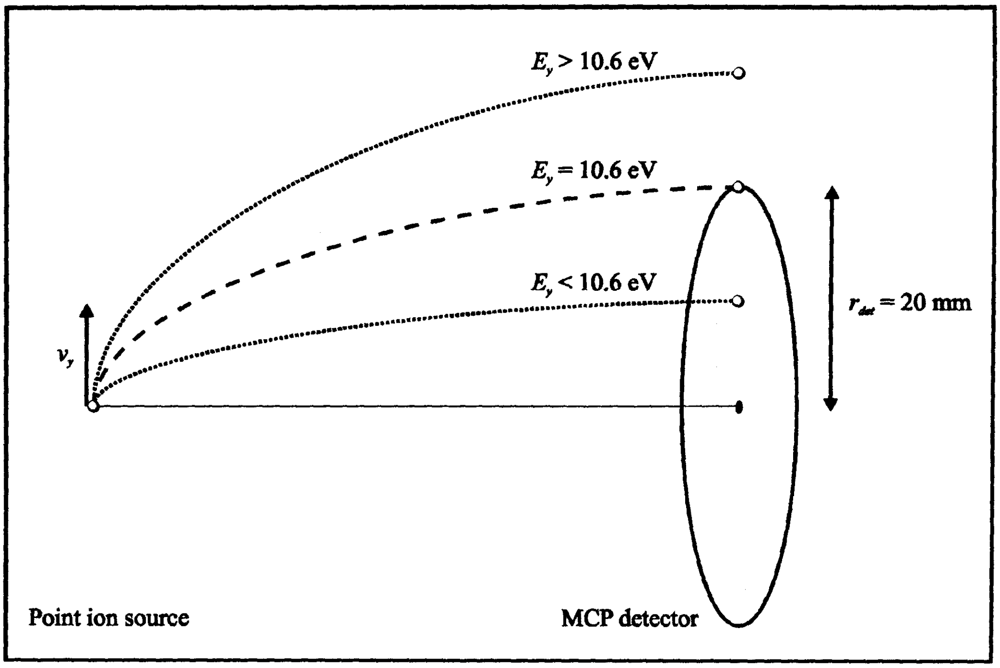

Figure 2.6 A schematic diagram showing the collection of translationally energetic ions at the detector, formed with an initial kinetic energy of up to 10.6 eV.

2.4 Data Sets

2.4.1 Singles Spectrum

The list of events resulting in the arrival of a single ion at the detector following an ionizing pulse of electrons are termed as 'singles' and are recorded as a list of individual flight times by the TDC. This data is displayed as a histogram showing the number of ion counts against time-of-flight to form a "singles mass spectrum" (Figure 2.7).

The mass scale of each mass spectrum is calibrated by measuring the respective flight times of at least two known ion peaks. These times are then used to construct a set of simultaneous equations, using the ion flight time expression $t_{tof} = k\sqrt{m} + c$ (Appendix A), and are solved to find the constants k and c.

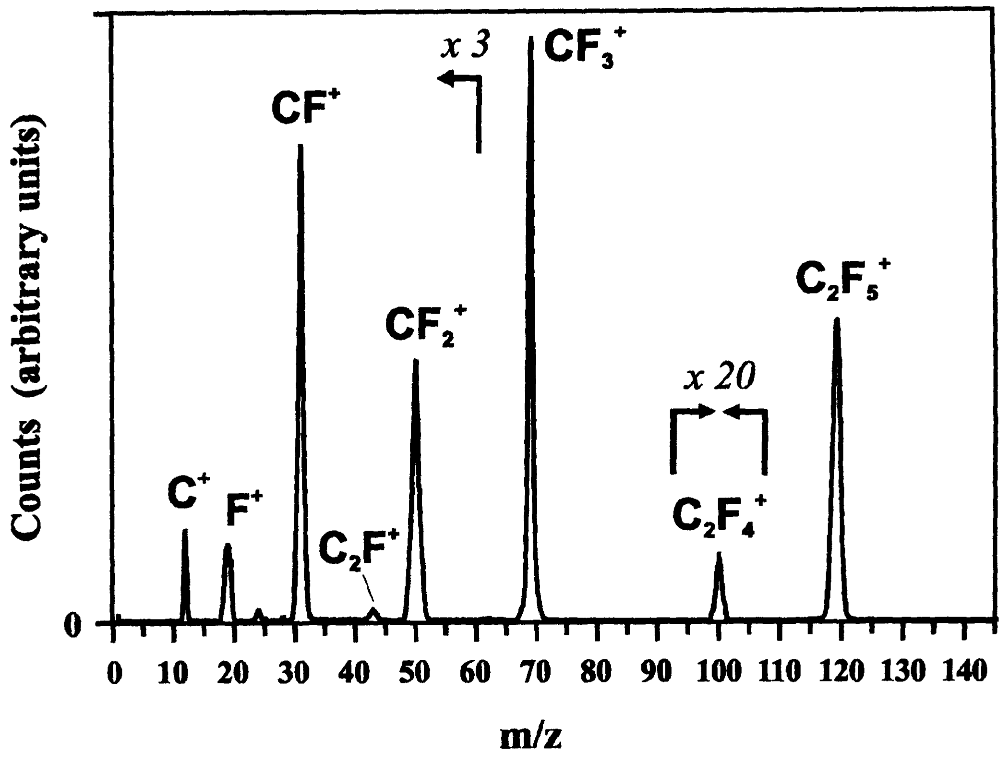

Figure 2.7 Singles mass spectrum of C_2F_6 recorded following electron ionization at 200 eV.

In the ionizing electron energy range investigated throughout this thesis (30-200 eV), single ion detections result mainly from ionization events in which only a single positively charged ion is formed. However, contributions to the singles spectrum may also arise from multiple ionization events, in which a product ion pair or ion triple are formed, due to the less than unit detection efficiency of the apparatus (f_i). Consider, for example, fragment monocations X^+ formed *via* dissociative electron ionization of the hypothetical gas phase molecule XYZ, as shown in Figure 2.8. In this figure f_i represents the probability that an ion formed is detected by the apparatus and conversely ($1-f_i$) represents that this ion is undetected by the apparatus. Ion pairs comprising X^+ are recorded as single ion detections where the X^+ ionic fragment is detected in the absence of its correlated ion partner. Similarly, ion triples comprising X^+ are also recorded as single ion detections where the X^+ ion is detected in the absence of its two correlated ion partners. Thus, the ion counts displayed in each singles spectrum may include contributions from dissociative single, double and triple ionization. In all experiments described in this thesis, contributions from quadruple and higher order ionization are neglected, due to the low intrinsic probability of removing four or more electrons from the target molecule within the energy regime under investigation.[11]

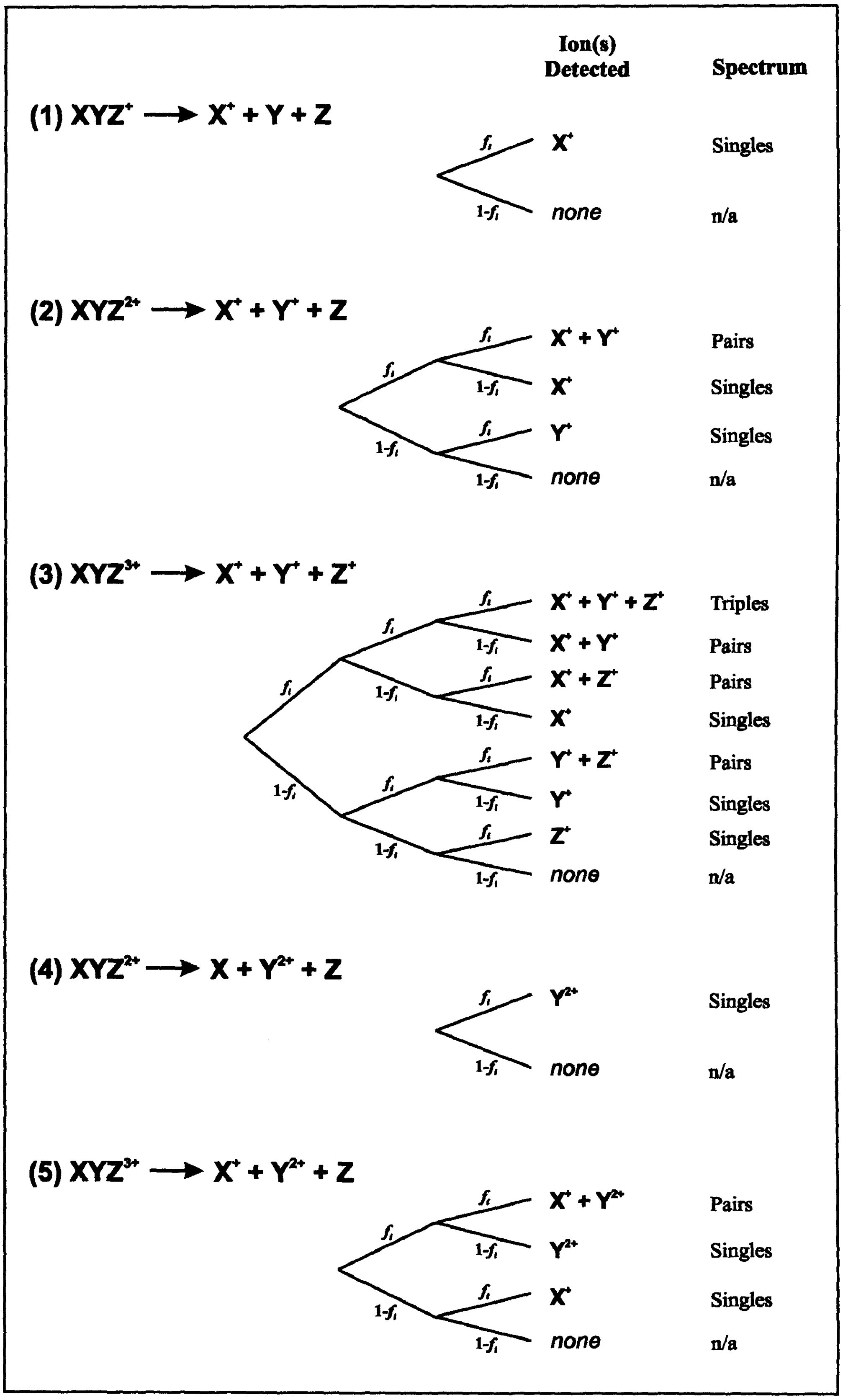

Figure 2.8 A probability tree showing the various ionization channels that contribute to the ion singles and 2-D ion coincidence spectra recorded by the experiment. The ion detection efficiency of the apparatus is denoted f_i.

To distinguish between fragment ions X^+ formed *via* dissociative single ionization and those formed *via* dissociative double and triple ionization, an ion-coincidence experiment is required.[3] In this thesis pulsed TOF mass spectrometry is coupled with a 2-D ion coincidence technique, allowing single product ions, ion pairs and ion triples formed by dissociative electron ionization, to be detected and recorded. By this method, the various contributions to the X^+ ion yield from dissociative single, double and triple ionization can be quantified. In the sections that follow, this 2-D coincidence technique is described in more detail.

2.4.2 Pairs Spectrum

Events involving the arrival of two ions at the detector following a single pulse of ionizing electrons, termed "pairs", are stored and processed offline. Ion pairs are displayed as a two-dimensional histogram of the respective flight times (t_1 versus t_2), known as a pairs spectrum (Figure 2.9). In the ionizing energy regime investigated throughout this thesis, the majority of ion pairs recorded are comprised of pairs of monocations, and are formed largely *via* dissociative double ionization. Dication-monocation pairs may also contribute to the pairs spectrum and are formed largely *via* dissociative triple ionization (Figure 2.8). As described previously, contributions to the mass spectra from quadruple ionization are assumed to be negligible at electron energies below 200 eV. The pairs data therefore enables the distinction between fragment ions X^+ formed *via* dissociative double and triple ionization and those X^+ ions formed *via* dissociative single ionization, appearing in the singles mass spectrum (Figure 2.8). By the same principle, the ion coincidence data enables the fragment dications X^{2+} formed *via* dissociative double ionization to be distinguished from those ions formed *via* dissociative triple ionization. Thus, the simultaneous acquisition of ion-coincidence data and conventional TOF mass spectra provides a more detailed understanding of the various dissociation pathways of molecular ions formed by electron ionization.

2.4.2.1 False Coincidences

To produce a 'real' ion pair, both ions must originate from the same ionization event in the source region and be detected. Of course, all pairs spectra will typically contain contributions from 'false' ion pairs, where two ions formed by separate ionization events in the source are detected in coincidence following a single ionizing electron pulse. To subtract these 'false' ion pairs from the pairs spectrum, an ion autocorrelation function[12] is used, as described in detail in Section 3.2.2.1. The ratio of 'real' ion pairs to 'false' ion pairs can be optimised experimentally by operating under conditions involving low target gas pressures (Table 2.I) and low electron flux. These conditions ensure that on average much less than one ionization event occurs in the source region per ionizing pulse of electrons, thereby reducing the number of false coincidences in the pairs spectrum.

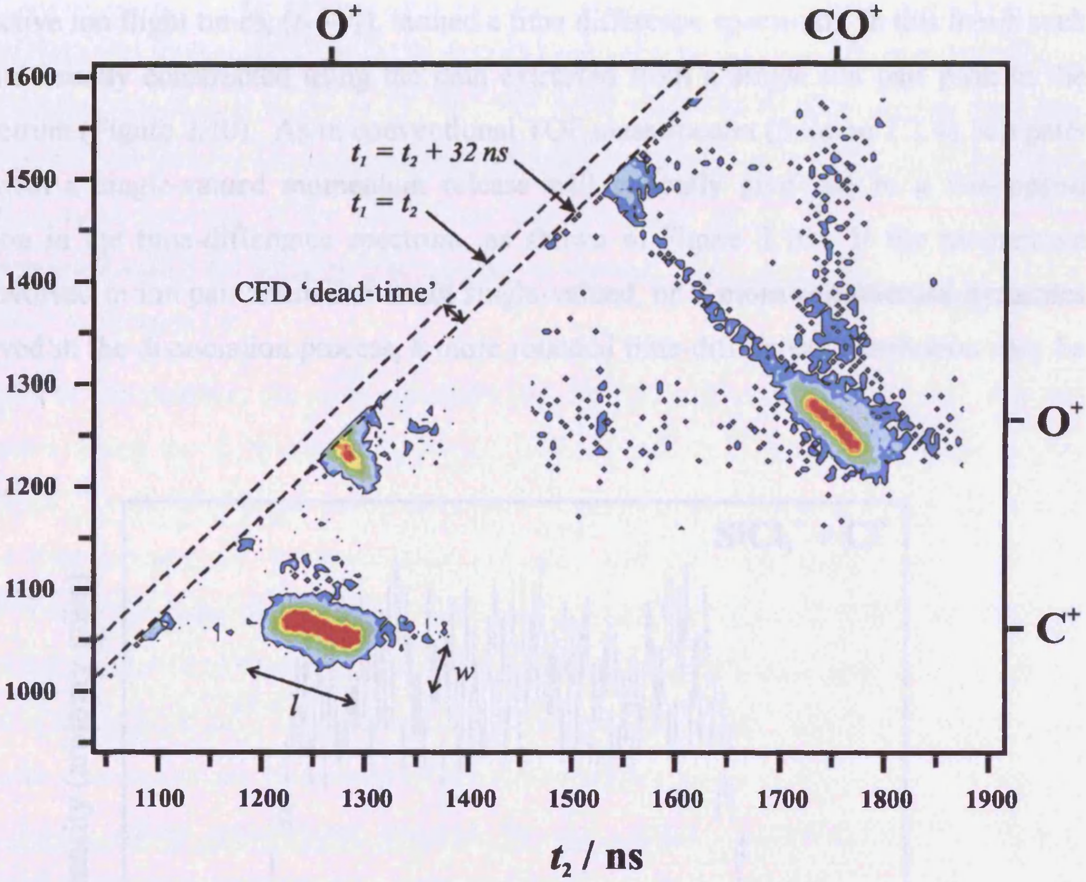

Figure 2.9 A representative pairs mass spectrum of CO_2, showing the monocation-monocation pairs formed following electron ionization at 200 eV.

2.4.2.2 Dead-time Losses

In the experiment no ion pairs are recorded if the second ion arrives within 32 ns of the first, due to the 'dead-time' of the discrimination circuitry. In this event, the flight time of the first ion to arrive at the detector is recorded but the second ion is not, and this single ion arrival time is plotted in the singles spectrum. This means that a portion of ion pairs comprising ions of identical or similar mass are 'missed' from the pairs spectrum. As shown by the $O^+ + O^+$ ion pair peak in Figure 2.9, such dead-time losses in the pairs mass spectrum occur close to the diagonal (t_1=t_2). To correct for these losses, a simple geometric procedure can be used to estimate the number of 'missed' ion pair counts, as will be described in Section 3.2.2.3.

2.4.2.3 Time Difference Spectra (t_2-t_1)

An alternative means of presenting the ion pair data is to construct a one-dimensional spectrum in which the ion pair counts are plotted as a function of the time difference between the respective ion flight times, ($t_2 - t_1$), termed a time difference spectrum. In this thesis such spectra are usually constructed using the data extracted from a single ion pair peak in the pairs spectrum (Figure 2.10). As in conventional TOF mass spectra (Section 2.2.4), ion pairs formed with a single-valued momentum release will typically give rise to a flat-topped distribution in the time-difference spectrum, as shown in Figure 2.10. If the momentum release involved in ion pair formation is not single-valued, or if more complicated dynamics are involved in the dissociation process, a more rounded time-difference distribution may be observed.

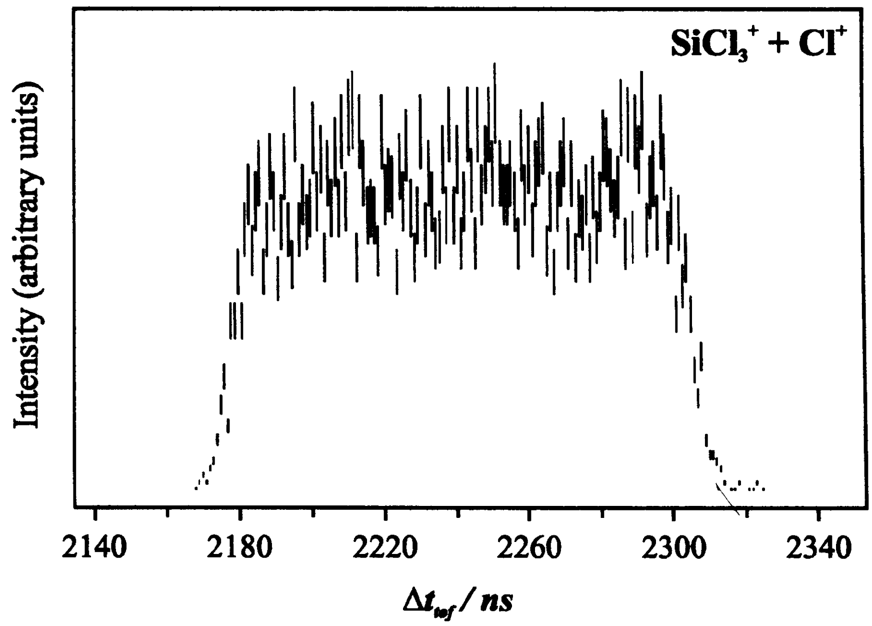

Figure 2.10 A representative time-difference spectrum for $SiCl_3^+$ + Cl^+ ion pairs formed *via* dissociative electron ionization of $SiCl_4$ at 100 eV. The flat-topped distribution is indicative of a single-valued momentum release upon ion pair formation, isotropically distributed over all laboratory angles.

2.4.2.4 The Dissociation Dynamics and Energetics of Multiply Charged Ions

The peaks appearing in the pairs mass spectrum can be interpreted to provide information on the dynamics and energetics involved in the dissociation of multiply charged ions.[3,4,13] As shown in Figure 2.9, such peaks are typically 'lozenge' shaped, of varying slope, length (l) and width (w). Previously it was shown that the time deviations of ions in the mass spectrum are proportional to the component of initial ion momentum along the spectrometer axis (Eqn 2.7). Therefore the regression of the ion pair peaks in the pairs spectrum, often referred to as the peak slope, provides a measure of the correlated momentum between the two ions comprising an ion pair.[4] In combination with the principle of conservation of linear momentum, measurements of the peak slope can, in many cases, be used to infer the dissociation mechanism for forming the ion pair of interest. This procedure is described in greater detail in Section 3.4.

The length l of the peaks in the pairs spectrum (Figure 2.9) reflect the distribution of initial ion momenta along the TOF axis, and hence, provide information on the kinetic energy release (KER) involved in ion pair formation. The peak widths w are due mainly to deviations from linearity in the dissociation process[4], and are discussed further in Section 3.4.3. Of course, the dimensions of the experimental peaks shapes are also influenced by the random initial velocities of the multiply charged ion prior to dissociation, and by the temporal resolution of the apparatus.[14] To determine the KER involved in the formation of an ion pair, Monte Carlo simulations are performed of the dissociation process in the mass spectrometer (Section 3.5). These simulations employ the full range of experimental variables, experimental conditions and reaction type which affect the simulated peak shape. The parameters of the simulated peak are then refined until a good fit to the experimental ion pair peak is obtained. Such measurements of the KER are then used in this thesis to estimate the energies of the dication or trication electronic states which dissociate to form the ion pair of interest.

2.4.3 Triples Spectrum

Events involving the arrival of three ions at the detector following a single pulse of ionizing electrons are termed "triples". The ion triples are displayed initially as a one-dimensional histogram showing the number of ion counts against time-of-flight, known as a triples mass spectrum. The triples data are then processed by specifying a time-of-flight range for a particular ion, and then extracting all ion triples containing at least one ion whose arrival time falls within this specified range. Once extracted, the respective flight times of the two remaining ions forming an ion triple are displayed as a two-dimensional histogram (t_2 versus t_3), as shown in Figure 2.11.

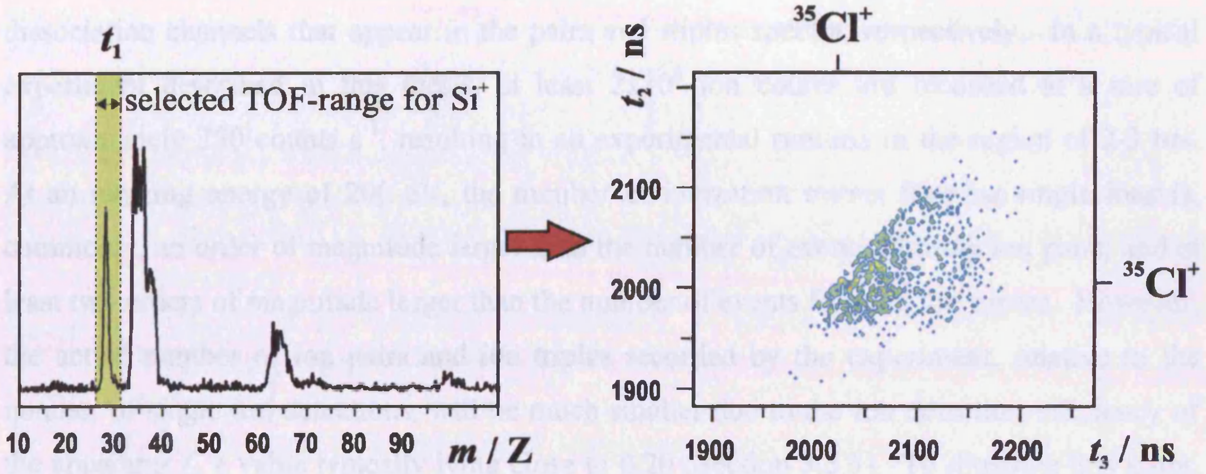

Figure 2.11 A representative one-dimensional triples mass spectrum (left) of $SiCl_4$ recorded following electron ionization at 200 eV. Ion triples are processed by selecting a TOF range for one ion comprising an ion triple t_1, for example Si$^+$ (left), and then extracting all ion triples containing at least one ion whose ion arrival time fall within this specified range. The arrival times of the two remaining ions are then plotted as a two-dimensional histogram (t_2 vs t_3) (right).

Since the probability of quadruple ionization is extremely small at ionizing electron energies ranging from 30-200 eV, the majority of ion triples recorded will consist of monocation triples formed *via* dissociative triple ionization. However, the probability of triple ionization is also typically very small within this ionizing energy regime[15,16], and so the number of ion triples recorded in most experiments represent only a small proportion of the total ion counts. This means that long experimental runtimes are required in order to collect sufficient ion triple statistics for analysis. All triples spectra will contain contributions from 'false' triples where three ions are detected following a single ionizing electron pulse, but originate from more than one separate ionization event in the source region. Under the typical operating conditions of the experiment, 'false' ion triples are composed mainly of real ion pairs formed by dissociative double ionization, detected in coincidence with a single ion from a separate ionization event. These false ion triples are subtracted from the triples mass spectrum using an extended form of the ion autocorrelation function[17], as described in Section 3.2.3.1.

2.4.4 Experimental Runtimes

When recording ion coincidence spectra it is important that sufficient data are collected to enable the various dissociation channels of multiply charged ions to be analysed. The amount of data that is required for this purpose will depend on the number of different dissociation channels that appear in the pairs and triples spectra, respectively. In a typical experiment described in this thesis, at least $2\text{x}10^6$ ion counts are recorded at a rate of approximately 250 counts s^{-1}, resulting in an experimental runtime in the region of 2-3 hrs. At an ionizing energy of 200 eV, the number of ionization events forming single ions is, commonly, an order of magnitude larger than the number of events forming ion pairs, and at least two orders of magnitude larger than the number of events forming ion triples. However, the actual number of ion pairs and ion triples recorded by the experiment, relative to the number of single ion detections, will be much smaller due to the ion detection efficiency of the apparatus f_i, a value typically lying close to 0.20 (Section 3.3.3). To illustrate this point, consider an experiment performed at 200 eV in which 10^6 events forming single ions, 10^5 events forming ion pairs, and $<10^4$ events forming ion triples, occur in the source region. Using Figure 2.8, the relative number of single ions, ion pairs and ion triples recorded by the experiment can be estimated, as shown in Table 2.II. These values should be scaled appropriately to ensure that sufficient ion-coincidence data are recorded for the target molecule under investigation.[17]

Single Ion Detections	Ion Pair Detections	Ion Triple Detections
$= (10^6 \times f_i)$ $+2 \times \left(10^5 \times f_i \times (1 - f_i)\right)$ $+3 \times (10^4 \times f_i \times (1 - f_i)^2)$	$= \left(10^5 \times f_i^2\right)$ $+3 \times \left(10^4 \times f_i^2 \times (1 - f_i)\right)$	$< \left(10^4 \times f_i^3\right)$
$= 200000 + 32000 + 3840$	$= 4000 + 960$	< 400
235840	**4960**	**400**

Table 2.II An estimate of the relative number of single ions, ion pairs and ion triples recorded in a typical experiment performed at an ionizing electron energy at 200 eV.

2.5 References

[1] W. C. Wiley and I. H. McLaren, Review Of Scientific Instruments **26** (12), 1150 (1955).

[2] J. H. D. Eland, Meas Science & Technology **4** (12), 1522 (1993).

[3] J. H. D. Eland, in *Vacuum Ultraviolet Photonionization and Photodissociation of Molecules and Clusters*, edited by C. Y. Ng (World Scientific, Singapore, 1991).

[4] J. H. D. Eland, Molecular Physics **61** (3), 725 (1987).

[5] J. L. Franklin, P. M. Hierl, and D. A. Whan, J. Chem. Phys. **47** (9), 3148 (1967).

[6] J. L. Wiza, Nuclear Instruments & Methods **162** (1-3), 587 (1979).

[7] M. R. Bruce and R. A. Bonham, Zeitschrift Fur Physik D-Atoms Molecules And Clusters **24** (2), 149 (1992).

[8] H. C. Straub, M. A. Mangan, B. G. Lindsay, K. A. Smith, and R. F. Stebbings, Review Of Scientific Instruments **70** (11), 4238 (1999).

[9] R. F. Stebbings and B. G. Lindsay, J. Chem. Phys. **114** (10), 4741 (2001).

[10] D. M. Curtis and J. H. D. Eland, Int. J. Mass Spectrom. Ion Process. **63** (2-3), 241 (1985).

[11] C. C. Tian and C. R. Vidal, Phys. Rev. A **58** (5), 3783 (1998).

[12] L. J. Frasinski, M. Stankiewicz, P. A. Hatherly, and K. Codling, Measurement Science & Technology **3** (12), 1188 (1992).

[13] J. H. D. Eland, Laser Chemistry **11** (3-4), 259 (1991).

[14] P. J. Richardson, J. H. D. Eland, P. G. Fournier, and D. L. Cooper, J. Chem. Phys. **84** (6), 3189 (1986).

[15] S. J. King and S. D. Price, Int. J. Mass Spectrom. **272** (2-3), 154 (2008).

[16] N. A. Love and S. D. Price, Phys. Chem. Chem. Phys. **6** (19), 4558 (2004).

[17] S. J. King and S. D. Price, J. Chem. Phys. **127**, 174307 (2007).

Chapter 3 Data Collection and Analysis

3.1 Introduction

This Chapter presents the various analysis procedures that are used to process the data recorded by the pulsed TOF mass spectrometer and 2-D ion coincidence technique, described in Chapter 2. Firstly, the procedures used to extract the relevant ion intensities from the recorded mass spectra are described in detail. Following this, a number of data reduction algorithms are presented, by which the measured ion intensities are processed to derive relative partial ionization cross sections (PICS) and precursor specific relative PICS. The final sections of this chapter describe the methods for analysing the ion pair peaks recorded in the 2-D coincidence spectra, used to derive information concerning the fragmentation dynamics and energetics involved in the charge-separating dissociations of molecular dications.

3.2 Spectral Intensities

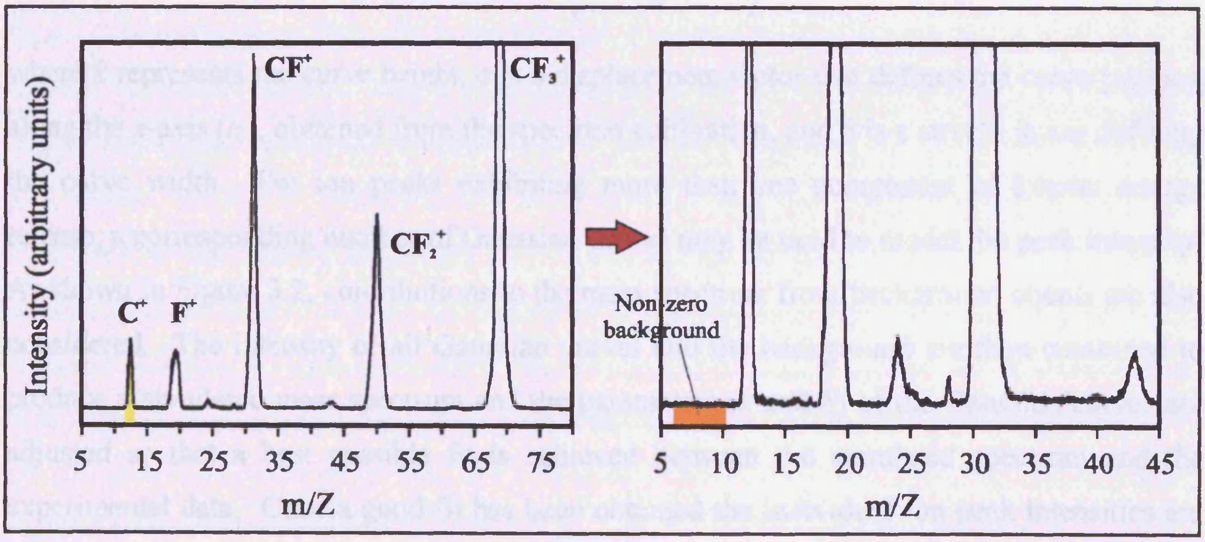

Figure 3.1 Diagram showing a typical measurement of the background count level in the singles mass spectrum of C_2F_6 recorded at 200 eV.

3.2.1 Singles Mass Spectrum

The intensities of individual ion peaks in the singles spectrum, $I_1[X^+]$ for monocations and $I_2[X^{2+}]$ for dications, are determined by summing the counts in the peak and applying a small correction to account for the nonzero baseline due to background counts. For each ion peak the level of background counts (counts per channel) is evaluated in a nearby region of the spectrum where no ion peaks are observed (Figure 3.1). This background level is then appropriately scaled to give the number of background counts that contribute to the peak of interest, and is subtracted from the raw peak intensity.

3.2.1.1 Peak Fitting

In some instances adjacent ion peaks in the singles spectrum are insufficiently resolved for the individual ion intensities to be extracted directly. Significant overlap between neighbouring peaks may arise for ions of similar mass where the respective peaks are broad due to the large translational energy release of the ions. In this event the individual ion intensities are extracted from the singles spectrum using a peak fitting procedure, as illustrated in Figure 3.2. In this procedure each ion peak is modelled using a single Gaussian curve described by the equation:

$$Intensity = k\,exp\left(\frac{-\left(t_{tof}-a\right)^2}{b^2}\right) \qquad 3.1$$

where k represents the curve height, a is a displacement factor that defines the curve position along the x-axis (t_0), obtained from the spectrum calibration, and b is a stretch factor defining the curve width. For ion peaks exhibiting more than one component of kinetic energy release, a corresponding number of Gaussian curves may be used to model the peak intensity. As shown in Figure 3.2, contributions to the mass spectrum from background counts are also considered. The intensity of all Gaussian curves and the background are then combined to produce a simulated mass spectrum and the parameters (k and b) of the Gaussian curves are adjusted so that a best possible fit is achieved between the simulated spectrum and the experimental data. Once a good fit has been obtained the individual ion peak intensities are found as the sum intensity of all appropriate Gaussian curves.

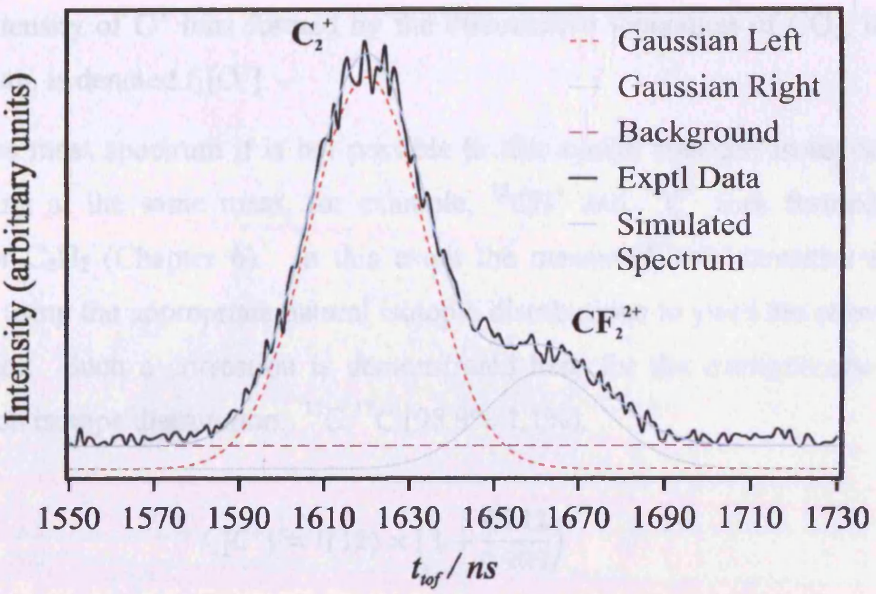

Figure 3.2 A diagram showing the peak fitting procedure used to extract the intensity of ion peaks that are unresolved in the singles mass spectrum. In this example the procedure is used to extract the intensities of overlapping C_2^+ and CF_2^{2+} fragment ion peaks in the spectrum of C_2F_6 recorded at 200 eV.

3.2.1.2 Background Gas Subtraction

In all singles mass spectra recorded there is a small but unavoidable contribution from air and H_2O present in the background gas of the vacuum chamber. Ions formed by the ionization of these background gases may add to the number of counts in the various ion peaks of interest, and are subtracted using a simple procedure illustrated by the following example. In the singles mass spectrum of CO_2 (Section 7.3), ionization of residual O_2 and H_2O contribute to the counts in the O^+ fragment ion peak at m/Z=16. To quantify these background contributions the relative intensities of O^+ with respect to O_2^+, $\sigma[O^+/O_2^+]$, and O^+ with respect to H_2O^+, $\sigma[O^+/H_2O^+]$, are measured in separate experiments on air and H_2O, as a function of ionizing electron energy. The subtraction of the ions from the residual gas can then be made by normalization to the O_2^+ and H_2O^+ peaks in each CO_2 singles spectrum:

$$I_1[\mathrm{O}^+] = I[16] - I[32] \times \sigma\left[\frac{\mathrm{O}^+}{\mathrm{O_2}^+}\right] - I[18] \times \sigma\left[\frac{\mathrm{O}^+}{\mathrm{H_2O}^+}\right] \qquad 3.2$$

In this equation, $I[16]$, $I[18]$ and $I[32]$ represent the measured peak intensities at m/Z=16, 18 and 32, respectively, after a subtraction of background counts has been applied in each case.

The final intensity of O^+ ions formed by the dissociative ionization of CO_2, in the singles mass spectrum, is denoted $I_1[O^+]$.

In the singles mass spectrum it is not possible to distinguish between isotopes of fragment ions occurring at the same mass, for example, $^{12}CH^+$ and $^{13}C^+$ ions formed by electron ionization of C_2H_2 (Chapter 6). In this event the measured ion intensities are corrected numerically using the appropriate natural isotopic distributions to yield the relevant fragment ion intensities. Such a correction is demonstrated here for the example above using the natural carbon isotope distribution: ^{12}C:^{13}C (98.9%:1.1%).

$$I_1[\mathrm{C}^+] = I(12) \times \left(1 + \frac{0.011}{0.989}\right) \tag{3.3}$$

$$I_1[\mathrm{CH}^+] = \left(I(13) - I(12) \times \frac{0.011}{0.989}\right) \times \left(1 + \frac{0.011}{0.989}\right) \tag{3.4}$$

where the final intensities of C^+ and CH^+ fragment ions are denoted $I_1[C^+]$ and $I_1[CH^+]$, respectively.

3.2.2 Pairs Mass Spectrum

As described in Section 2.4.2, ion pairs are displayed as a two-dimensional histogram of the respective ion flight times (t_1 *vs* t_2), known as a pairs spectrum. The intensity of each peak in the pairs spectrum is found simply by summing the number of counts in the peak lying within a specified region, for example, $P[X^+ + Y^+]$, as shown in Figure 3.3. The overall contribution of a fragment ion to the pairs spectrum, for example, $P[X^+]$, is then obtained as the sum of counts in all the appropriate peaks involving an X^+ ion. In this thesis a distinction is made between the ion counts in pairs which must be formed *via* triple ionization, $P_3[X^+]$, and the ion counts in the other peaks which may contain contributions from both dissociative double and triple ionization, $P_2[X^+]$. Contributions from triple ionization to the intensities of monocation pairs may arise when only two ions of an ion triple are detected, due to the less than unit ion detection efficiency of the apparatus (Figure 2.8). As described previously, ion coincidences resulting from dissociative quadruple ionization are neglected.

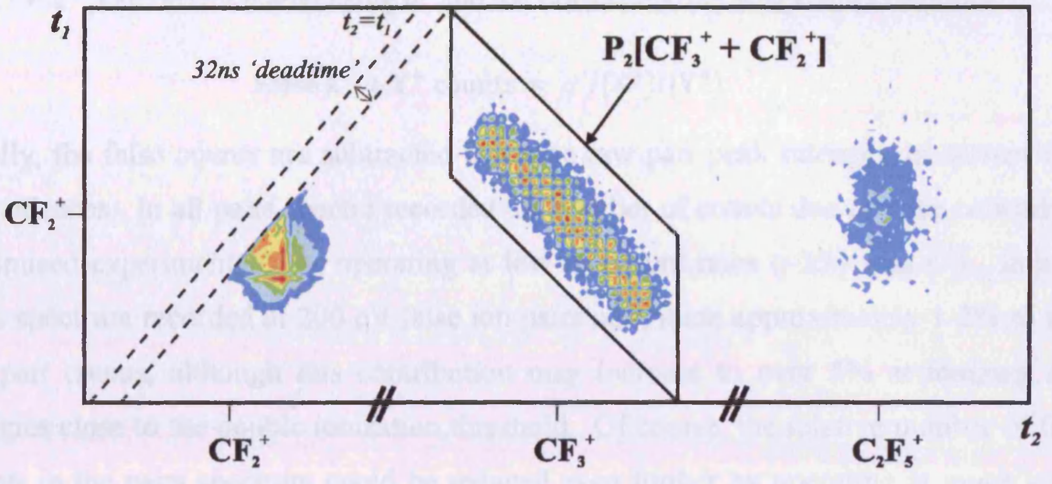

Figure 3.3 Representative ion pair peaks observed in the pairs spectrum of C_2F_6 recorded at an ionizing electron energy of 200 eV.

3.2.2.1 False Ion Coincidence Subtraction

All peaks in the pairs spectrum may contain a small contribution from 'false' ion pairs, which, as described in Section 2.4.2.1, comprise two ions that are detected in coincidence but are formed by separate ionization events. False coincidences are subtracted manually from the raw ion pair peak intensities using an ion auto-correlation function[1,2]. This subtraction procedure is now described in detail.

Firstly, a number of purely 'false' pair peaks are identified in the pairs spectrum. Such peaks have a characteristic round or ovular shape due to the absence of momentum correlation between the two ions formed by separate ionization events. These false ion pair peaks usually consist of two ion masses that cannot be formed by the same dissociative ionization event, for example, the $C_2F_5^+ + CF_2^+$ peak recorded in the pairs spectrum of C_2F_6, shown in Figure 3.3. The intensity of each false pair peak is then divided by the product of the relevant ion intensities in the corresponding singles mass spectrum to obtain a normalization factor α:

$$\alpha = \frac{P[C_2F_5^+ + CF_2^+]}{I[C_2F_5^+]I[CF_2^+]} \qquad 3.5$$

The single ion intensities in Eqn 3.5, $I[X^+]$, are the raw peak intensities measured in the corresponding singles spectrum prior to any corrections for background counts or background gases. The individual normalization factors are then used to derive an average normalization factor, α'. The number of false counts that contribute to a 'real' ion pair peak, denoted here as $X^+ + Y^+$, can be calculated using α' and the corresponding single ion intensities:

$$\text{False } X^+ + Y^+ \text{ counts} = \alpha' I[X^+] I[Y^+] \qquad 3.6$$

Finally, the false counts are subtracted from the raw pair peak intensity to correct for false coincidences. In all pairs spectra recorded the number of counts due to false coincidences is minimised experimentally by operating at low ion count rates (~250 ions s^{-1}). In a typical pairs spectrum recorded at 200 eV false ion pairs contribute approximately 1-2% to the total ion pair counts, although this contribution may increase to over 5% at ionizing electron energies close to the double ionization threshold. Of course, the relative number of false ion counts in the pairs spectrum could be reduced even further by operating at much lower ion count rates. However, this approach would require significantly longer data acquisition times that are impractical from an experimental viewpoint.

3.2.2.2 Energetic Ion Pair Loss Correction

In Section 2.3.2 it was shown that under the voltage conditions used in the apparatus, fragment ions are efficiently collected at the detector with up to 10.6 eV of translational kinetic energy. However, ions will escape detection if they are formed with a translational energy component perpendicular to the flight axis in excess of 10.6 eV. If these energetic ions comprise ion pairs, at least one of the two correlated ions will be undetected and hence a proportion of the ion pairs will be 'missed'. As shown in Figure 3.4, the ion pairs that are missed are those where the kinetic energy release between the ion fragments is aligned perpendicular to the flight axis. In the corresponding time difference spectrum (Section 2.4.2.3), such ion pairs contribute to the central region of the time difference distribution, and hence, losses of energetic ion pairs are clearly identified by a hollowing of the one-dimensional peak shape.[3] To correct for such losses, an appropriate geometric construction is used to estimate the number of counts missed, as shown in Figure 3.5, which is then added to the pairs peak intensity $P[X^+ + Y^+]$.

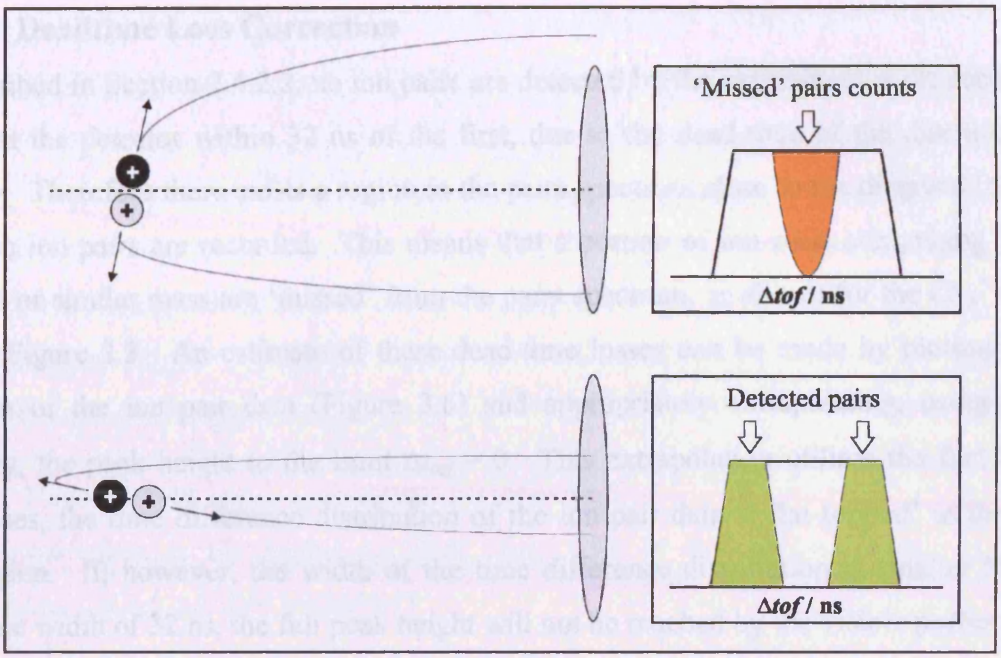

Figure 3.4 A diagram showing the collection of energetic ions comprising ion pairs at the detector. In the top example, the kinetic energy release upon the dissociation of a multiply charged molecular ion is aligned perpendicular to the flight axis, which may lead to losses of ion pair counts in the centre of the time difference distribution.

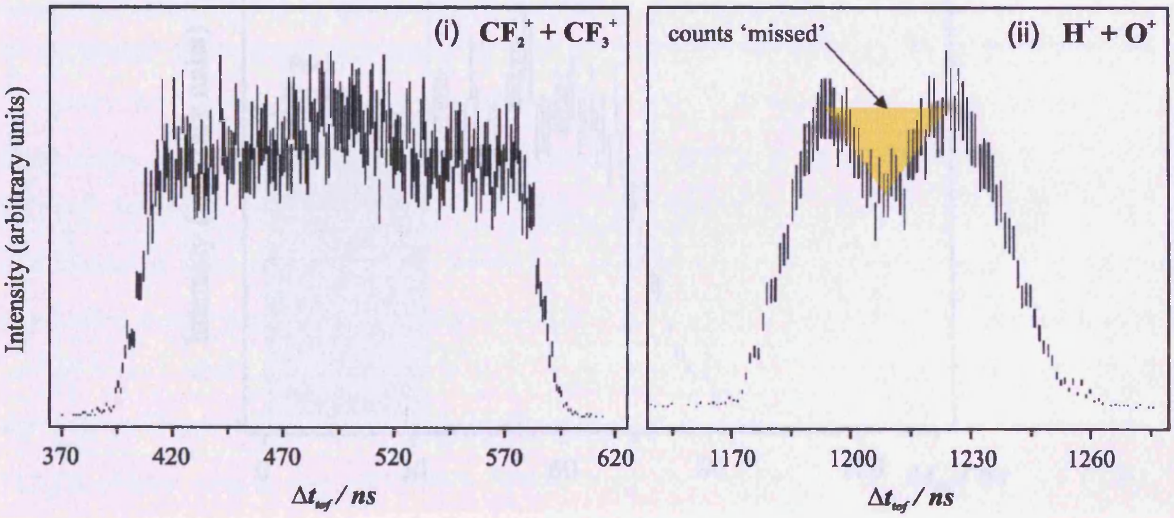

Figure 3.5 Representative time difference spectra (t_2-t_1) recorded for selected ion pairs following electron ionization of C_2F_6 (left) and H_2O (right) at 200 eV. The t_2-t_1 distribution for CF_2^+ + CF_3^+ pairs is characteristically flat-topped, indicating the complete collection of ion pairs, while for H^+ + O^+ the distribution is slightly hollow due to losses of energetic ion pairs. To correct for the lost H^+ + O^+ ion pair counts, an appropriate geometric construction is used.

3.2.2.3 Deadtime Loss Correction

As described in Section 2.4.2.2, no ion pairs are detected by the experiment if the second ion arrives at the detector within 32 ns of the first, due to the dead-time of the discrimination circuitry. Therefore there exists a region in the pairs spectrum close to the diagonal (t_1=t_2) in which no ion pairs are recorded. This means that a portion of ion pairs comprising ions of identical or similar mass are 'missed' from the pairs spectrum, as shown for the $CF_2^+ + CF_2^+$ peak in Figure 3.3. An estimate of these dead-time losses can be made by plotting a t_2-t_1 spectrum of the ion pair data (Figure 3.6) and appropriately extrapolating, using simple geometry, the peak height to the limit $\Delta t_{tof} = 0$. This extrapolation utilises the fact that, in most cases, the time difference distribution of the ion pair data is flat-topped[4] in the dead-time region. If, however, the width of the time difference distribution is smaller than the dead-time width of 32 ns, the full peak height will not be reached by the visible portion of the ion pair peak. In this event, the extrapolation procedure represents a lower limit of the true number of ion pairs lost due to the experimental dead-time. Of course, this estimated number of lost counts is added to the measured peak intensity to correct for the dead-time losses.

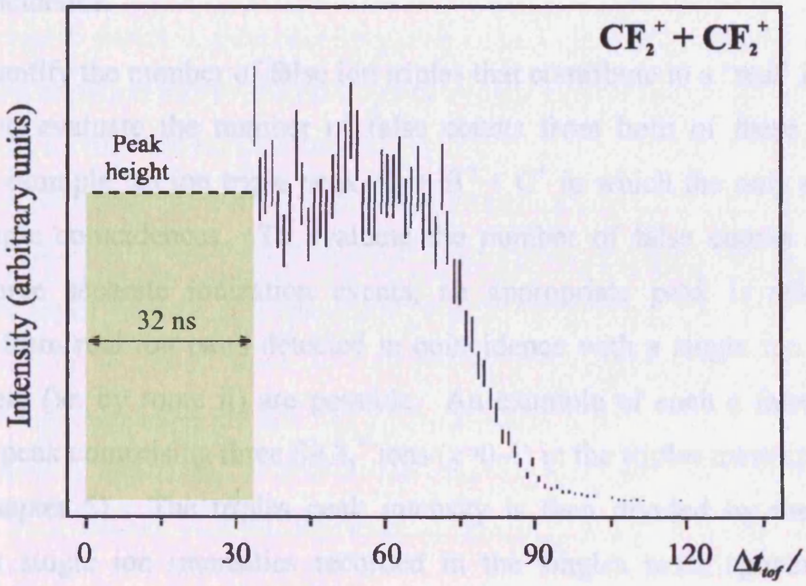

Figure 3.6 A t_2-t_1 spectrum of the $CF_2^+ + CF_2^+$ pairs coincidence data presented in Figure 3.3. The peak height is extrapolated to the limit $\Delta tof = 0$ to estimate the number of counts missed due to the experimental dead-time.

3.2.3 Triples Mass Spectrum

The ion triples data is processed by specifying a time-of-flight range for a particular ion, and then extracting all ion triples containing at least one ion whose arrival time falls within this specified range. Once extracted, the respective flight times of the two remaining ions are displayed as a two-dimensional histogram (Figure 2.11). The intensity of each ion triple peak is found by summing the number of counts in the peak, for example, $T[X^+ + Y^+ + Z^+]$. The number of ion counts for a particular fragment, for example, $T[X^+]$, in the triples spectrum is simply the sum of all the peak counts involving the formation of X^+.

3.2.3.1 False Triple Ion Coincidence Subtraction

A false ion triple in the triples spectrum may arise in one of two ways (neglecting contributions from quadruple ionization):

(i) Where three monocations formed by three separate ionization events are detected in coincidence following a single ionizing electron pulse.

(ii) Where three monocations are formed by two separate ionization events, the first forming a monocation pair and the second forming a single monocation, are detected in coincidence.

In order to quantify the number of false ion triples that contribute to a 'real' ion triple peak, it is necessary to evaluate the number of false counts from both of these possible routes. Consider, for example, an ion triple peak $A^+ + B^+ + C^+$ in which the only contributions are from false triple coincidences. To evaluate the number of false counts from ion triples formed by three separate ionization events, an appropriate peak is selected where no contributions from real ion pairs detected in coincidence with a single ion from a separate ionization event (ie. by route ii) are possible. An example of such a false triple ion peak would be any peak comprising three $SiCl_x^+$ ions (x=0-4) in the triples mass spectrum recorded for $SiCl_4$ (Chapter 5). The triples peak intensity is then divided by the product of the corresponding single ion intensities recorded in the singles mass spectrum, to obtain a normalization factor α'', relating to the number of false ion triples formed by three separate ionization events:

3 events:
$$\frac{T[A^+ + B^+ + C^+]}{I[A^+]I[B^+]I[C^+]} = \alpha'' \qquad 3.7$$

Next, a second purely false ion triple peak is selected containing counts from ion triples that may be formed by both two separate ionization events and three separate ionization events, as listed above. A normalization factor β relating to the number of false ion triples formed by two separate ionization events (involving an ion pair and a single ion) can be derived as:

$$\text{2 events:} \qquad \frac{T[\mathrm{A}^+ + \mathrm{B}^+ + \mathrm{C}^+] - \alpha'' I[\mathrm{A}^+] I[\mathrm{B}^+] I[\mathrm{C}^+]}{I[\mathrm{A}^+]P[\mathrm{B}^+ + \mathrm{C}^+] + I[\mathrm{B}^+]P[\mathrm{A}^+ + \mathrm{C}^+] + I[\mathrm{C}^+]P[\mathrm{A}^+ + \mathrm{B}^+]} = \beta \qquad 3.8$$

where, for example, $P[\mathrm{B}^+ + \mathrm{C}^+]$ represents the peak intensity of an ion pair recorded in the corresponding pairs spectrum. In Eqn 3.8, the numerator is simply the number of false ion triples due to two separate ionization events, obtained from the raw triples peak intensity minus the contribution of triples from three separate ionization events, derived using Eqn 3.7. The denominator considers all possible combinations of two separate ionization events involving real ion pair and a single ion giving rise to a false ion triple $\mathrm{A}^+ + \mathrm{B}^+ + \mathrm{C}^+$.

The number of false ion triples that contribute to a real ion triple peak $\mathrm{X}^+ + \mathrm{Y}^+ + \mathrm{Z}^+$ can now be easily found using Eqns 3.7 and 3.8, as:

$$\begin{aligned} \text{False } \mathrm{X}^+ + \mathrm{Y}^+ + \mathrm{Z}^+ = \; & \beta\left[I[\mathrm{X}^+]P[\mathrm{Y}^+ + \mathrm{Z}^+] + I[\mathrm{Y}^+]P[\mathrm{X}^+ + \mathrm{Z}^+] + I[\mathrm{Z}^+]P[\mathrm{X}^+ + \mathrm{Y}^+]\right] \\ & + \alpha'' I[\mathrm{X}^+] I[\mathrm{Y}^+] I[\mathrm{Z}^+] \end{aligned} \qquad 3.9$$

In this thesis, where possible, a number of purely false ion triple peaks are analysed for each triples spectrum to obtain more reliable estimates of the normalization factors α'' and β. The number of false ion triples that contribute to each 'real' ion peak is then calculated using Eqn 3.9, and subtracted from the raw triples peak intensity to correct for false counts. Analysis shows that in most cases, the contribution of false ion triples from two separate ionization events (ion pair and a single ion) is far greater than from three separate ionization events, and hence, the final term in this equation ($\alpha'' I[\mathrm{X}^+] I[\mathrm{Y}^+] I[\mathrm{Z}^+]$) may be neglected when calculating the number of false ion triple counts. In a typical mass spectrum recorded at 200 eV, false counts contribute a minimum of 5% to the raw triples peak intensity. Of course, the proportion of false counts may be significantly greater than this value, depending on the identity of the ion triple under investigation.

3.3 Relative Partial Ionization Cross Sections

The ion intensities recorded in the singles, pairs, and triples spectra are processed to derive relative PICS and also precursor-specific relative PICS. The relative PICS for the formation of fragment monocations X^+ are represented as $\sigma_r[\mathrm{X}^+]$, and for dications X^{2+} as $\sigma_r[\mathrm{X}^{2+}]$, and are expressed relative to the cross section for forming the parent monocation. Precursor specific relative PICS are symbolized by $\sigma_n[X^+]$ and $\sigma_n[X^{2+}]$, respectively, and represent the cross section for forming a fragment ion by single (n=1), double (n=2), or triple (n=3) ionization, relative to the cross section for forming the parent monocation. The peak intensities recorded in the ion coincidence spectra are also processed to derive relative PICS for ion pair formation by dissociation of the parent dication, represented as $\sigma_r[X^+ + Y^+]$. As described previously, contributions to the ion yield from quadruple or higher order ionization are neglected in the data analysis. In the sections that follow, the data reduction algorithms used to derive these relative PICS are presented in detail.

3.3.1 Peak Intensities in the Singles, Pairs and Triples Mass Spectra

The intensity of a fragment monocation X^+ in the singles mass spectrum can be related to the number of ions formed by ionization events during the data acquisition period:

$$I_1[X^+] = f_i N_1[X^+] + f_i(1-f_i)N_2[X^+] + f_i(1-f_i)N_{3pairs}[X^+] + f_i(1-f_i)^2 N_{3triples}[X^+] \qquad 3.10$$

In this equation, $N_n[X^+]$ represents the number of fragment ions X^+ formed by ionization events resulting in the loss of n electrons while the spectrum was being recorded. A distinction is made between dissociative triple ionization events involving the formation of a monocation-dication pair $N_{3pairs}[X^+]$ or a monocation-triple $N_{3triples}[X^+]$. The ion detection efficiency f_i must also be considered because of the transmission efficiency of the grids that define the electric fields in the apparatus, and to account for the less than unit efficiency of the detector. Thus, Eqn 3.10 contains four contributions to the intensity of X^+ in the singles spectrum, as summarised by the probability tree shown in Figure 2.8. These are ions detected from dissociative single ionization, two contributions for ion pairs formed by double or triple ionization, where X^+ is detected in the absence of its correlated ion, and a contribution from triple ionization events, where X^+ is detected in the absence of the other two correlated ions of an ion triple.

Similarly, the X^+ counts recorded in the pairs and triples spectra, $P_n[X^+]$ and $T[X^+]$, are related to the number of ions formed in Eqns 3.11-3.13. The corresponding expressions for the spectral intensities of fragment dications X^{2+} are shown in Eqn 3.14 and 3.15, and the number of parent monocations N_1[parent$^+$] formed in each experiment is related to the number of counts in the singles mass spectrum I[parent$^+$] by Eqn 3.16:

$$P_2[\mathrm{X}^+] = f_i^{\,2}N_2[\mathrm{X}^+] + 2f_i^{\,2}(1 - f_i)N_{3triples}[\mathrm{X}^+] \qquad 3.11$$

$$P_3[\mathrm{X}^+] = f_i^{\,2}N_{3pairs}[\mathrm{X}^+] \qquad 3.12$$

$$T[\mathrm{X}^+] = f_i^{\,3}N_{3triples}[\mathrm{X}^+] \qquad 3.13$$

$$I_2[\mathrm{X}^{2+}] = f_iN_{2singles}[\mathrm{X}^{2+}] + f_i(1 - f_i)N_{3pairs}[\mathrm{X}^{2+}] \qquad 3.14$$

$$P_3[\mathrm{X}^{2+}] = f_i^{\,2}N_{3pairs}[\mathrm{X}^{2+}] \qquad 3.15$$

$$I_1[\mathrm{parent}^+] = f_iN_1[\mathrm{parent}^+] \qquad 3.16$$

3.3.2 Relative PICS Determination

In this thesis relative PICS are derived for the formation of all fragment ions detected. By definition, these σ_r values are equal to the sum of the corresponding precursor specific relative PICS:

$$\sigma_r[\mathrm{X}^+] = \frac{\sigma[\mathrm{X}^+]}{\sigma[\mathrm{parent}^+]} = \sigma_1[\mathrm{X}^+] + \sigma_2[\mathrm{X}^+] + \sigma_3[\mathrm{X}^+] \qquad 3.17$$

$$\sigma_r[\mathrm{X}^{2+}] = \frac{\sigma[\mathrm{X}^{2+}]}{\sigma[\mathrm{parent}^+]} = \sigma_2[\mathrm{X}^{2+}] + \sigma_3[\mathrm{X}^{2+}] \qquad 3.18$$

Under experimental conditions of low electron flux and low ionization rate, it can be shown (Section 1.4.2) that $N_n[\mathrm{X}^+]$ is proportional to $\sigma_n[\mathrm{X}^+]$:

$$\sigma_n[\mathrm{X}^+] = kN_n[\mathrm{X}^+] \qquad 3.19$$

where k is a constant for each individual experiment, dependent on experimental variables such as the target gas pressure, electron flux, and ionization volume.[5] Thus, the relative PICS in Eqns 3.17 and 3.18 can first be expressed in terms of the number of ions formed by different ionization events N_n and then recast in terms of the measured spectral intensities using Eqns 3.10-3.16:

$$\sigma_r[\mathrm{X}^+] = \frac{N_1[\mathrm{X}^+] + N_2[\mathrm{X}^+] + N_3[\mathrm{X}^+]}{N_1[\mathrm{parent}^+]} = \frac{I_1[\mathrm{X}^+] + P_2[\mathrm{X}^+] + P_3[\mathrm{X}^+] + T[\mathrm{X}^+]}{I_1[\mathrm{parent}^+]} \qquad \mathbf{3.20}$$

$$\sigma_r[\mathrm{X}^{2+}] = \frac{N_2[\mathrm{X}^{2+}] + N_3[\mathrm{X}^{2+}]}{N_1[\mathrm{parent}^+]} = \frac{I_2[\mathrm{X}^{2+}] + P_3[\mathrm{X}^{2+}]}{I_1[\mathrm{parent}^+]} \tag{3.21}$$

Note that the σ_r values are independent of the ion detection efficiency f_i. However, if a value of f_i is available, the data reduction can be extended to derive σ_n values for all fragment ions detected. In this thesis an individual value of f_i is determined for each series of experiments involving a particular target molecule of interest (Table 3.II). The method used to determine f_i for the apparatus is now described in detail.

3.3.3 Ion Detection Efficiency Determination

To determine the ion detection efficiency f_i, experiments are performed to record the singles and pairs spectra of CF_4 at an ionizing electron energy of 100 and 200 eV. CF_4 is chosen for this purpose, since the PICS are well characterised for this molecule and can be extracted from published literature. Absolute PICS for the formation of single fragment ions σ_s, and product ion pairs σ_p, following electron ionization of CF_4, have been measured by Bruce and Bonham using pulsed TOF mass spectrometry[6], and using the covariance mapping technique[7]. The results of these separate investigations are summarised in Table 3.I, and are the culmination of a series of experimental studies on the electron ionization of CF_4[6-9], in which the various experimental parameters that may give rise to ion discrimination effects, are considered in detail.

E / eV	$\sigma[C^+]$	$\sigma[F^+]$	$\sigma[CF^+]$	$\sigma[CF_2^+]$	$\sigma[CF_3^+]$	$\sigma[CF_2^{2+}]$	$\sigma[CF_3^{2+}]$	$\sum\sigma_s$
100	0.291	0.494	0.402	0.364	3.732	0.028	0.059	5.37
200	0.296	0.583	0.38	0.341	3.472	0.033	0.062	5.167

E / eV	$\sigma[C^+ + F^+]$	$\sigma[CF^+ + F^+]$	$\sigma[CF_2^+ + F^+]$	$\sigma[CF_3^+ + F^+]$	$\sigma[F^+ + F^+]$	$\sigma[CF_2^{2+} + F^+]$	$\sum\sigma_p$
100	0.041	0.142	0.076	0.071	0.025	0	0.355
200	0.144	0.261	0.099	0.083	0.117	0.0018	0.7058

Table 3.I Absolute PICS values of Bruce and Bonham for the formation of single ions[6], and ion pairs[7], following electron ionization of CF_4. Note that the two data sets were recorded separately, and hence, the single ion cross section data contains contributions from ionization events forming both single ions and ion pairs. All values have units Å^2.

The σ_s and σ_p values of Bruce and Bonham can be related to the total number of ions recorded in the singles mass spectrum $I[X^{m+}]$, and the total number of ions recorded in the pairs spectrum $P[X^{m+}]$, as shown below by Eqns 3.22-3.23. These equations are then combined to derive an expression for f_i (Eqn 3.24). Contributions to the spectral intensities from ion triples are assumed to be small and are neglected in the analysis.

$$\sum P = 2f_i^2 k \sum \sigma_p \qquad 3.22$$

$$\sum I = f_i k \sum \sigma_s \qquad 3.23$$

$$f_i = \left(\frac{\sum P}{\sum I}\right)\left(\frac{\sum \sigma_s}{2\sum \sigma_p}\right) \qquad 3.24$$

For each determination of the ion detection efficiency, an average value of f_i is derived from at least four independent experiments, two at each ionizing electron energy. As shown in Table 3.I, typical values of f_i for the apparatus lie close to 20%, in good agreement with absolute values of f_i reported in the literature[4,10], which are the product of the transmission efficiency of the apparatus and the detector efficiency.

Molecule(s) Studied	Reference	Dates Studied	f_i value determined
Ar	Appendix C	Oct 04 → Dec 04	n/a
C_2H_2	Chapter 6	Jan 05 → Aug 05	0.19 ± 0.01
Background gases	Appendix C	Sept 05	
H_2O	Chapter 8	Oct 05 → Nov 05	0.19 ± 0.01
C_2F_6	Chapter 4	Jan 06 → May 06	0.20 ± 0.01
CO_2	Chapter 7	Aug 06 → Sept 06	0.20 ± 0.01
$SiCl_4$	Chapter 5	Nov 06 → Dec 06	0.21 ± 0.01
CHF_3	n/a	Apr 07 → May 07	0.21 ± 0.01
CH_4	n/a	Jun 07 → Jul 07	0.21 ± 0.01

Table 3.II A summary of the values of the ion detection efficiency, f_i, derived from experiments reported in this thesis.

3.3.4 Precursor Specific Relative PICS Determination

Precursor specific relative PICS σ_n can be derived for the formation of all fragment ions detected by the apparatus by consideration of the measured spectral intensities and f_i. As has described previously, these cross sections quantify the contribution to the ion yield of a particular fragment monocation X^+ or dication X^{2+}, from single, double, or triple ionization. The precursor specific relative PICS are first expressed in terms of the relevant numbers of ions formed by ionization events N_n, and are then rewritten in terms of the spectral intensities by substitution of Eqns 3.10-3.16:

$$\sigma_1[\mathrm{X}^+] = \frac{N_1[\mathrm{X}^+]}{N_1[\mathrm{parent}^+]} = \frac{I_1[\mathrm{X}^+] - \left(\frac{1-f_i}{f_i}\right)\{P_2[\mathrm{X}^+] + P_3[\mathrm{X}^+]\} + \left(\frac{1-f_i}{f_i}\right)^2 T[\mathrm{X}^+]}{I_1[\mathrm{parent}^+]} \qquad 3.25$$

$$\sigma_2[\mathrm{X}^+] = \frac{N_2[\mathrm{X}^+]}{N_1[\mathrm{parent}^+]} = \frac{\left(\frac{1}{f_i}\right)P_2[\mathrm{X}^+] - 2\left(\frac{1-f_i}{f_i^2}\right)T[\mathrm{X}^+]}{I_1[\mathrm{parent}^+]} \qquad 3.26$$

$$\sigma_3[\mathrm{X}^+] = \frac{N_3[\mathrm{X}^+]}{N_1[\mathrm{parent}^+]} = \frac{\left(\frac{1}{f_i}\right)P_3[\mathrm{X}^+] + \left(\frac{1}{f_i^2}\right)T[\mathrm{X}^+]}{I_1[\mathrm{parent}^+]} \qquad 3.27$$

$$\sigma_2[\mathrm{X}^{2+}] = \frac{N_2[\mathrm{X}^{2+}]}{N_1[\mathrm{parent}^+]} = \frac{I_2[\mathrm{X}^{2+}] - \left(\frac{1-f_i}{f_i}\right)P_3[\mathrm{X}^{2+}]}{I_1[\mathrm{parent}^+]} \qquad 3.28$$

$$\sigma_3[\mathrm{X}^{2+}] = \frac{N_3[\mathrm{X}^{2+}]}{N_1[\mathrm{parent}^+]} = \frac{\left(\frac{1}{f_i}\right)P_3[\mathrm{X}^{2+}]}{I_1[\mathrm{parent}^+]} \qquad 3.29$$

Furthermore, the overall contribution to the ion yield from single, double, and triple ionization, as a percentage of the total ion yield, can be found easily by taking an appropriate ratio of σ_n values, as shown below:

$$\mathit{single\ ionization}\ (\%) = \frac{\sum \sigma_1 + 1}{\sum_{n=1}^{n=3} \sigma_n + 1} \times 100 \qquad 3.30$$

$$\%\,double\ ionization = \frac{\sum \sigma_2}{\sum_{n=1}^{n=3} \sigma_n + 1} \times 100 \quad 3.31$$

$$triple\ ionization = \frac{\sum \sigma_3}{\sum_{n=1}^{n=3} \sigma_n + 1} \times 100 \quad 3.32$$

The Parent Monocation

The PICS derived in this thesis are, where possible, expressed relative to the cross section for forming the parent monocation. For the molecules investigated in Chapters 5-8, the parent monocation is typically formed in large abundance, making it a suitable choice as a reference ion for the derivation of relative PICS. In addition, parent monocations are formed initially with a thermal kinetic energy distribution and, hence, are least susceptible to ion discrimination effects in most mass spectrometric experiments.[11,12] This means that the existing PICS data reported in the literature are generally the most reliable for the formation of the parent monocations, thereby enabling a comparison to be made between the values of the relative PICS derived in this thesis and those derived from the existing literature data.

For some molecular systems such as CF_4 and C_2F_6, the formation of the parent monocation has not been observed in electron ionization mass spectra.[9,13] This absence is presumably due to the fact that bound parent monocation electronic states cannot be accessed for these molecules *via* a vertical transition from the ground electronic state within the Franck-Condon region. Therefore, when deriving the relative PICS for these molecules, a suitable alternative product ion must be chosen to which the cross sections for all other fragment ions are expressed relative. For example, in the study of the electron ionization of C_2F_6 (Chapter 4), all PICS are expressed relative to the formation of the $C_2F_5^+$ fragment ion. This product ion is chosen since it is formed in large abundance, with an initial kinetic energy typically below a few electron Volts.[14,15] It is noted, however, that a minor component of the $C_2F_5^+$ ion intensity is recorded in the pairs spectra of C_2F_6, as shown in Figure 4.2. Thus, the measured spectral intensities for the $C_2F_5^+$ fragment ion are given by:

$$I_1[C_2F_5^+] = f_i N_1[C_2F_5^+] + f_i(1 - f_i) P_2[C_2F_5^+] \quad 3.33$$

$$P_2[C_2F_5^+] = f_i^2 N_2[C_2F_5^+] \quad 3.34$$

This leads to a modified expression of the relative PICS, and precursor specific relative PICS, for forming fragment ions by electron ionization of C_2F_6, as shown below for the formation of fragment monocations X^+:

$$\sigma_r[X^+] = \frac{\sigma[X^+]}{\sigma[C_2F_5{}^+]} = \frac{N_1[X^+] + N_2[X^+] + N_3[X^+]}{I_1[C_2F_5{}^+] + P_2[C_2F_5{}^+]} \tag{3.35}$$

$$\sigma_n[X^+] = \frac{N_n[X^+]}{I_1[C_2F_5{}^+] + P_2[C_2F_5{}^+]} \tag{3.36}$$

Positive Ion-Negative Ion Pair Formation

Under the experimental setup described in Chapter 2 only positive ions are detected and, hence, the formation of positive ion-negative ion pairs cannot be distinguished from fragmentation to a positive ion plus a neutral:

$$XY + e^- \rightarrow X^+ + Y^- + e^- \tag{3.37}$$

Such reactions will contribute to the positive ion intensities recorded by the apparatus and therefore are included in the relative PICS values presented in this thesis. However, the cross sections for forming positive ion-negative ion pairs following electron ionization of small molecules, in the energy range 30-200 eV, are typically several orders of magnitude smaller than the corresponding total ionization cross section.[16] Therefore, the contributions of such ion pairs to the cross sections derived in this thesis are expected to be minor.

3.3.5 Relative PICS for Ion Pair Formation

By a simple extension of the data reduction procedure used to derive precursor specific relative PICS, relative cross sections for forming monocation pairs, $\sigma_r[X^+ + Y^+]$, can be derived by consideration of f_i and the spectral intensities measured in the ion coincidence spectra. Such cross sections quantify the yield of monocation pairs formed *via* dicationic dissociation. In the pairs mass spectrum, contributions to the $X^+ + Y^+$ peak counts may arise from double ionization events forming a monocation pair $N_2[X^+ + Y^+]$, or triple ionization events $N_3[X^+ + Y^+ + Z^+]$, where the ions X^+ and Y^+ are detected in the absence of the other correlated ion of an ion triple (Figure 2.8). The relevant spectral intensities measured in the ion coincidence spectra are given by:

$$P_2[\mathrm{X}^+ + Y^+] = f_i^2 N_2[\mathrm{X}^+ + Y^+] + f_i^2(1 - f_i)N_3[\mathrm{X}^+ + Y^+ + Z^+] \qquad 3.38$$

$$T[\mathrm{X}^+ + Y^+ + Z^+] = f_i^3 N_3[\mathrm{X}^+ + Y^+ + Z^+] \qquad 3.39$$

Thus, the relative PICS for monocation pair formation can be expressed in terms of the number of ion pairs formed by double ionization events $N_2[\mathrm{X}^+ + \mathrm{Y}^+]$ and then recast in terms of the measured spectral intensities using Eqns 3.38-3.39:

$$\sigma_r[\mathrm{X}^+ + Y^+] = \frac{\sigma[\mathrm{X}^+ + Y^+]}{\sigma[\mathrm{parent}^+]} = \frac{N_2[\mathrm{X}^+ + Y^+]}{N_1[\mathrm{parent}^+]} \qquad 3.40$$

$$\sigma_r[\mathrm{X}^+ + Y^+] = \left(\frac{1}{f_i}\right)\frac{P_2[\mathrm{X}^+ + Y^+] - \frac{(1 - f_i)}{f_i}T[\mathrm{X}^+ + Y^+ + Z^+]}{I_1[\mathrm{parent}^+]} \qquad \mathbf{3.41}$$

In addition to monocation pair formation, the products of dicationic dissociation may also include fragment dications X^{2+}, which are quantified by the $\sigma_2[\mathrm{X}^{2+}]$ values (Eqn 3.28). If values of $\sigma_r[\mathrm{X}^+ + \mathrm{Y}^+]$ and $\sigma_2[\mathrm{X}^{2+}]$ are derived for the formation of all monocation pairs and fragment dications detected, respectively, then dication branching ratios can easily be calculated for the molecule of interest.

3.4 The Dissociation Dynamics of Multiply Charged Molecular Ions

As described in Section 2.4.2.4, the shapes of the peaks appearing in the pairs spectrum can be interpreted to provide additional information on the dissociation dynamics of multiply charged ions.[17-20] For this purpose the most useful parameter that can be extracted from the ion pair data is the slope of the linear regression between the two ion flight times, t_1 and t_2. In this thesis the slope of a selected ion pair peak (Figure 3.3) is determined using a linear least squares fitting method[21]. Both t_1 and t_2 are given equal weightings since both ion flight times have a substantial uncertainty. When selecting ion pair data for peak slope analysis it is important to limit the number of 'stray' ion counts included in the specified peak area. In this context 'stray' counts describe any counts that do not correspond to the formation of an ion pair of interest, and include false ion coincidences. If the proportion of stray counts included in the selected peak area is too large, a biased value for the peak gradient may result. In this event, any conclusions drawn from the peak slope value concerning the dissociation mechanism may be an inaccurate description of the true reaction mechanism taking place. Therefore, for ion pairs containing contributions from a number of naturally occurring isotopes, care must also be taken to ensure that the data for only a single isotope peak are considered in the peak slope analysis (see for example Section 5.5).

3.4.1 The Interpretation of Experimental Peak Slopes

In Section 2.2.4 it was shown that under the space focusing conditions used, the flight time for an ion is proportional to the component of initial ion momentum along the TOF axis:

$$t_{tof} = t_0 - \frac{p\cos\theta}{qE_s} \qquad 3.42$$

where t_0 is the standard flight time for an ion initially at rest, q is the ion charge, E_s is the source electric field, and p is the magnitude of initial ion momentum release at an angle θ to the flight axis. Equation 3.42 shows that the deviation of the flight time δt of an ion from the standard t_0 is directly proportional to the initial momentum component along the TOF axis. Thus, for an ion pair $A^+ + B^+$ observed in the pairs spectrum, the peak slope is defined as:

$$b = \frac{\delta t_B}{\delta t_A} = \frac{p_B\cos\theta_B}{p_A\cos\theta_A}\left(\frac{q_A}{q_B}\right) \qquad 3.43$$

where ion B^+ is the first ion to arrive at the detector. The peak slope therefore provides a measure of the correlated momentum components of the two ions comprising an ion pair. The value of the peak slope obtained from the experiment can then be compared to the value predicted using a simple model of the dication (or trication) dissociation process, allowing deductions to be made on the reaction dynamics. In the sections that follow a number of model reaction mechanisms[17] are presented which describe the formation of ion pairs *via* the charge separating dissociation of small multiply charged molecular ions.

3.4.2 Two-Body Dissociation Reactions

In a two-body dissociation reaction only a single fragmentation mechanism is possible, the direct dissociation of the molecular dication to form a pair of product ions:

$$ABC^{2+} \rightarrow A^{+} + BC^{+} \qquad 3.\text{i}$$

Conservation of linear momentum requires that the two ions separate collinearly with an equal and opposite momentum:

$$-p_A = p_{BC} \qquad 3.44$$

which, by substitution into Eqn 3.43 yields a value of -1 for the peak slope. Therefore a two body dissociation reaction forming a monocation pair will appear in the pairs spectrum as a narrow bar-shaped peak with a slope of -1. An example of such a peak is displayed in Figure 2.9 for $CO^+ + O^+$ ion pairs formed following electron ionization of CO_2.

For two-body dissociations involving the formation of a dication-monocation pair, the ion charges must also be considered when predicting the value of the peak slope. Combining Eqns 3.43 and 3.44 gives rise to two possible values for the peak slope, depending on whether the dication fragment arrives at the detector before or after its correlated ion partner:

- Dication fragment detected first $\quad ABC^{3+} \rightarrow A^{2+} + BC^{+} \quad b = \frac{p_A}{p_{BC}}\left(\frac{1}{2}\right) = -0.5 \quad$ 3.45
- Dication fragment detected second $\quad ABC^{3+} \rightarrow A^{+} + BC^{2+} \quad b = \frac{p_A}{p_{BC}}\left(\frac{2}{1}\right) = -2 \quad$ 3.46

3.4.3 Three-Body Dissociation Reactions

A multiply charged ion may fragment to form an ion pair plus one or a number of neutral fragments. Such neutral fragments are undetected by the experiment and may carry away a portion of the total momentum released during the fragmentation process, making the determination of the reaction mechanism on the basis of peak slope measurements considerably more complex. In this section model reaction mechanisms[17] are presented for the charge separating decay of molecular dications (ABC^{2+}) forming an ion pair and a single neutral fragment, termed a three-body dissociation reaction. A value of the peak slope is derived for each mechanism by considering the various components of kinetic energy release during the fragmentation process and applying the simple rule of conservation of linear momentum in each distinct fragmentation step. In the following analysis it is assumed that all kinetic energy release components are single-valued and are isotropically distributed over all laboratory angles. For many of the model reaction mechanisms described, a considerable simplification is achieved in the derivation of the peak slope if linearity is conserved among the various fragments formed during the dissociation. Consider, for example, the fragmentation of a molecular dication ABC^{2+} into three fragments A^+, B^+ and C, Figure 3.7. The momentum of A^+ defines an axis and the angle of the momentum component of B^+ relative to this axis is denoted θ.

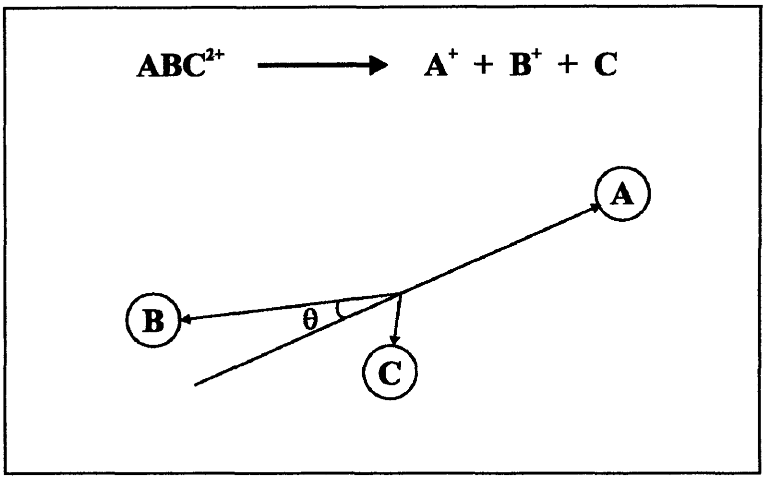

Figure 3.7 A schematic diagram showing the three-body dissociation of a molecular dication ABC^{2+}.

A simple test of linearity for the reaction can be performed by comparing the widths of the individual TOF distributions for the ionic fragments A^+ and B^+, w_A and w_B, to the width of the time-difference (t_A-t_B) distribution, w_D.[17] As described previously, assuming a single-valued momentum release, the widths w_A and w_B are proportional to the components of individual ion momentum (Section 2.2.4), while w_D is proportional to the correlated momentum between the ion fragments (Section 2.4.2.3). Thus, for a linear dissociation the width of the time-difference distribution must be equal to the sum of the widths of the two individual ion TOF distributions. If the width of the time-difference distribution is smaller than the sum of the widths of the individual ion TOF distributions, then θ can be calculated by the following expression:

$$w_D = w_A + w_B cos\theta$$

$$cos\theta = \frac{w_D - w_A}{w_B} \qquad 3.47$$

3.4.3.1 Instantaneous Explosions

An instantaneous explosion describes a reaction in which all the bonds that are broken during the fragmentation process are ruptured simultaneously upon double ionization. The various fragments separate immediately under the influence of electrostatic forces, but, as shown in Figure 3.8, the independent motion of a particular fragment may be prevented by a collision with another fragment.

In the simplest case, the neutral fragment receives no impulse from the explosion and does not impede the motion of either fragment ion. Such a reaction is termed 'unobstructed' and is shown schematically in Figure 3.8. The two fragment ions are formed with an equal and opposite momentum, and hence, give rise to a peak in the pairs spectrum with a slope of -1.

In the extreme case a fragment ion and a neutral fragment will experience a 'head-on' collision, such as shown in Figure 3.8, and do not separate until outside of the zone of Coulomb repulsion[17]. A head-on collision requires linearity, and so the fragment ion momenta can be derived as:

$$-p_A = p_{BC} \qquad \text{and} \qquad p_B = \frac{m_B}{m_{BC}} p_{BC} = -\frac{m_B}{m_{BC}} p_A \qquad 3.48$$

The peak slope predicted for a head-on collision (Eqn 3.43) is therefore equal to the mass ratio $-m_B/m_{BC}$ or $-m_{BC}/m_B$, depending on whether B^+ is the first or second ion to arrive at the detector, respectively.

The intermediate case involves a 'glancing' collision between the B^+ ion and the neutral moiety C (Figure 3.8), and results in a set of non-linear trajectories for the fragments that are formed. For such a reaction the value of the peak slope will be between the limiting values for an unobstructed explosion and a head-on collision.

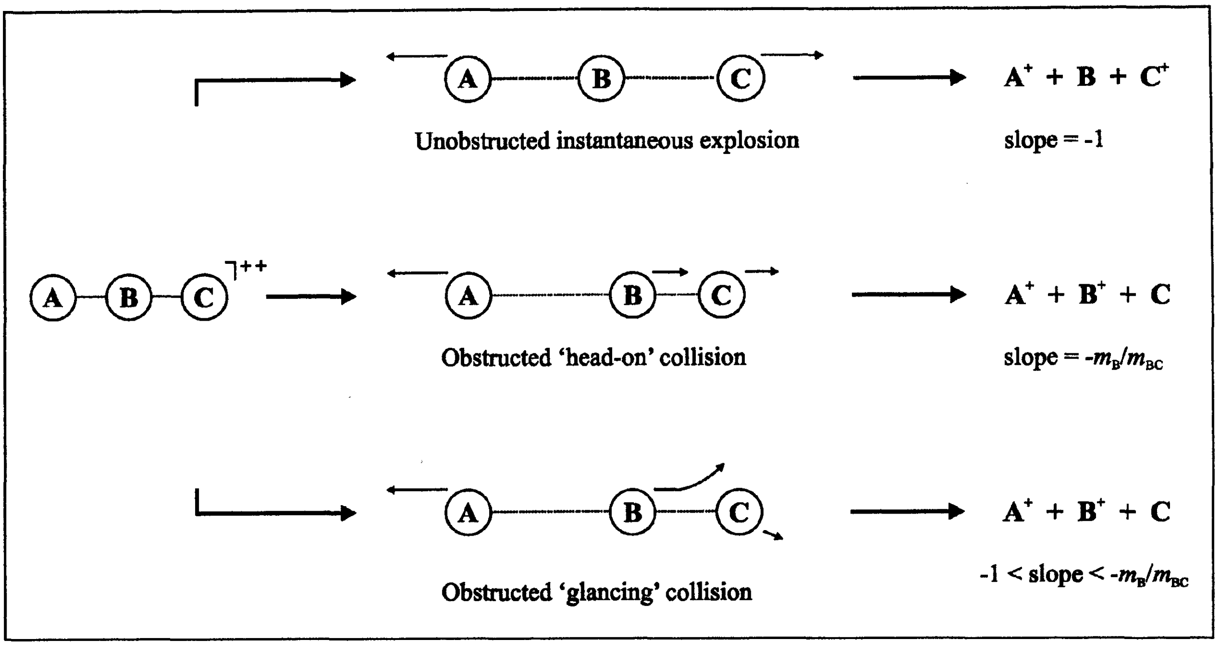

Figure 3.8 Model three-body dissociation mechanisms for forming ion pairs *via* instantaneous explosions of small molecular dications ABC^{2+}.

3.4.3.2 Sequential Decay Reactions

A sequential decay reaction involves two distinct fragmentation steps each involving a separate kinetic energy release.

- First stage $ABC \rightarrow A + BC$ U_1
- Second stage $BC \rightarrow B + C$ U_2 3.ii

Such reactions may be divided into two general classes according to whether the charge separation occurs in the initial fragmentation step or is deferred to the second step.[17] For the reaction scheme presented above, the impulse received by the fragments A and BC in the first stage, p_1, can be derived as follows. The kinetic energy release involved in the first fragmentation step, U_1, is given by:

$$U_1 = \frac{p_A{}^2}{2m_A} + \frac{p_{BC}{}^2}{2m_{BC}} \qquad 3.49$$

Noting that $p_{BC} = -p_A = p_1$ (conservation of linear momentum), U_1 can be rewritten as:

$$U_1 = \frac{p_1^2(m_A + m_{BC})}{2m_A m_{BC}}$$

And hence the first stage impulse is derived as:

$$p_1 = \left(\frac{2U_1 m_A m_{BC}}{m_{ABC}}\right)^{1/2} \qquad 3.50$$

Similarly, for the reaction scheme shown in 3.ii, the second stage impulse can be derived as:

$$p_2 = \left(\frac{2U_2 m_B m_C}{m_{BC}}\right)^{1/2} \qquad 3.51$$

For the analysis that follows, it is also useful to define the following terms:

$$k = \frac{U_2}{U_1} \quad \text{Energy release ratio} \qquad \mu = \frac{m_A m_B m_{ABC}}{m_C m_{AB}^2} \quad \text{Mass factor} \qquad 3.52$$

and the identity:

$$\frac{p_2}{p_1} = (k\mu)^{1/2}$$

Predictions of the peak slope for the different types of model three-body sequential reaction mechanisms are now presented.

3.4.3.3 Initial Charge Separation

The simplest case of initial charge separation involves the slow break-up of the fragment BC^+ outside the zone of Coulomb repulsion (Figure 3.9). Typically the kinetic energy release U_1 involved in the charge separation step will greatly exceed that of the second stage U_2. In the extreme scenario where $U_2=0$, the predicted peak slope is $-m_B/m_{BC}$ (Eqn 3.54) and hence the mechanism is experimentally indistinguishable from an instantaneous reaction involving a head-on collision. If $U_2 \neq 0$, but the fragment BC^+ undergoes free rotation prior to dissociation outside of the Coulomb zone, one may similarly predict a peak slope value lying close to $-m_B/m_{BC}$, as the additional impulse received by B^+ in the second stage is not correlated with the momentum of A^+. However, for such a reaction the corresponding peak in the pairs spectrum will appear much 'fatter' due to the non-correlated secondary KER, as shown in Figure 2.9 for the formation of C^+ + O^+ ion pairs following electron ionization of CO_2. Therefore, on the basis of this additional experimental evidence, a slow sequential dissociation mechanism involving free rotation may be distinguished from an instantaneous reaction involving a head-on collision. Of course, instantaneous reactions involving a glancing collision may also produce broad peaks in the pairs spectrum, but can be distinguished from a slow sequential mechanism by the value of the peak slope.

Next we consider the case of a linear slow sequential reaction involving an aligned secondary KER[19] (U_2) along the axis of initial charge separation (Figure 3.9). In this reaction the BC^+ fragment undergoes a secondary decay outside of the Coulomb zone in its original linear configuration. As shown in Figure 3.9, the fragment ion formed by the secondary decay of BC^+ receives a second impulse directed either towards A^+ (case I) or away from A^+ (case II). In case I the individual initial momentum components of the detected ions A^+ and B^+ are given by:

$$p_A = -p_1 \qquad \text{and} \qquad p_B = \frac{m_B}{m_{BC}} p_1 - p_2 \tag{3.53}$$

which, by use of Eqn 3.43 and Eqns 3.50-3.52, predicts a value of the peak slope:

$$b = \frac{p_B}{p_A} = -\frac{m_B}{m_{BC}} + (k\mu)^{1/2} \tag{3.54}$$

where B^+ is the first detected ion comprising an ion pair. This means that for a slow sequential decay reaction involving an aligned component of secondary KER that serves to reduce the momentum component of B^+ relative to the momentum of A^+ (Figure 3.9, case I), the value of the peak slope will be less negative than $-m_B/m_{BC}$. Such reactions can therefore be distinguished from instantaneous explosion reactions, for which the peak slope will always lie between $-m_B/m_{BC}$ and -1. In case II, where the detected ion C^+ receives an additional impulse in the secondary decay step directed away from A^+, the peak slope can be derived as:

$$b = \frac{p_C}{p_A} = -\frac{m_C}{m_{BC}} - (k\mu)^{1/2} \tag{3.55}$$

where C^+ is the first detected ion. Such a reaction will produce a peak in the pairs spectrum with a slope lying between $-m_B/m_{BC}$ and -1, and cannot be distinguished experimentally from an instantaneous reaction involving a collision. If, however, C^+ is the second detected ion of the ion pair, the peak slope becomes the reciprocal of Eqn 3.55. In this event the value of the peak slope will be more negative than $-m_{BC}/m_C$, and can now be distinguished from an instantaneous explosion mechanism for forming an ion pair $A^+ + C^+$, where C^+ is the first detected ion, for which the peak slope lies between -1 and $-m_{BC}/m_C$.

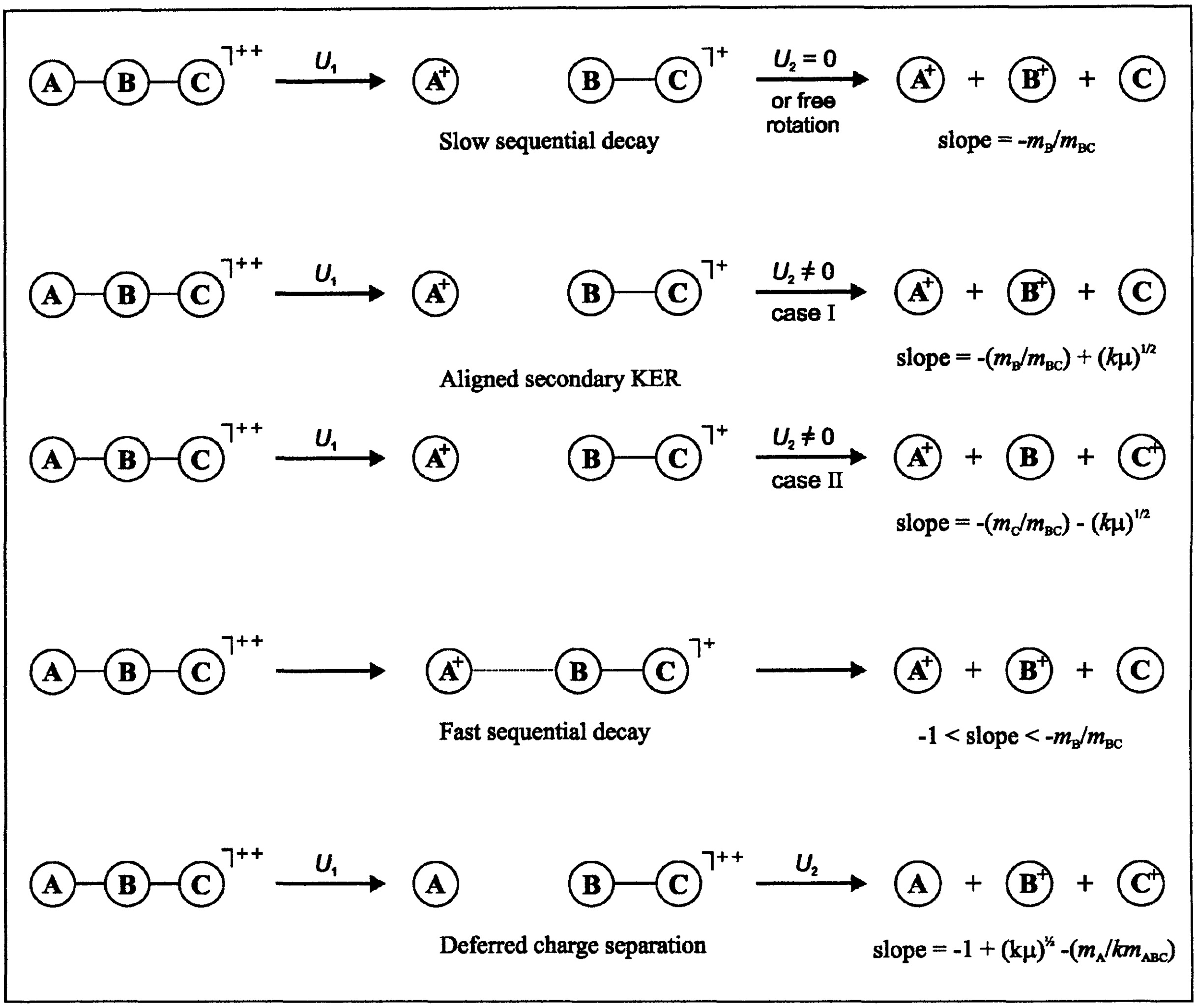

Figure 3.9 Model three-body dissociation mechanisms for forming ion pairs *via* sequential decay of small molecular dications ABC^{2+}.

3.4.3.4 Deferred Charge Separation

Deferred charge separation involves the initial loss of a neutral fragment (A), followed by charge separation of the resulting doubly charged fragment (BC^{2+}) in a second distinct step, as illustrated in Figure 3.9. For such a reaction the individual ion momenta can be derived as:

$$p_C = p_2 + \frac{m_C}{m_{BC}}p_1 \qquad \text{and} \qquad p_B = -p_2 + \frac{m_B}{m_{BC}}p_1 \qquad 3.56$$

which, by use of Eqn 3.43, predicts a value of the peak slope:

$$b = \frac{p_B}{p_C} = -1 + (k\mu)^{-1/2} - \frac{m_C}{km_{ABC}} \qquad 3.57$$

In a typical deferred charge separation reaction the dominant KER occurs in the charge separation step ($U_1 << U_2$). Therefore the corresponding value of the peak slope for a deferred charge separation reaction will generally be close to -1, and is difficult to distinguish experimentally from a mechanism involving an unobstructed instantaneous explosion. However, supporting evidence for a deferred charge separation reaction may appear in the pairs spectrum in the form of a 'metastable tail' originating from the $B^+ + C^+$ peak.[18,22] Alternatively, a deferred charge separation mechanism may be rejected if the measured appearance potential for the formation of the ion pair $B^+ + C^+$ is lower that the double ionization potential of the fragment BC obtained from the literature.[3,17]

3.4.3.5 Fast Sequential Reactions

A fast sequential reaction is considered to be a sequential reaction in which the secondary decay of the fragment BC^+ (or BC^{2+}) occurs soon after the initial fragmentation while inside the zone of Coulomb repulsion[23] (Figure 3.9). Such reactions are therefore intermediate between a slow sequential decay mechanism and an unobstructed instantaneous explosion, and correspondingly give rise to values of the peak slope that are in between the limiting values predicted for these model reaction mechanisms. Nevertheless, a fast sequential mechanism may be assigned to a particular reaction, where, for example, the experimental peak slope cannot be described in terms of a suitable glancing collision or a reasonable component of aligned KER. Further information on this class of reaction is presented in Section 4.5.1 in the analysis of the dissociations of $C_2F_6^{2+}$.

3.5 Kinetic Energy Release Determination

The shape of the peaks in the pairs spectrum can be interpreted to yield information on the kinetic energy released upon fragmentation of molecular dications.[3,19] In this thesis the KER for a reaction is extracted by constructing a time-difference (t_2-t_1) spectrum from the experimental ion pair arrival times (Section 2.4.2.3), and then performing a Monte Carlo simulation of the dissociation process in the mass spectrometer. As described in detail below, these Monte Carlo simulations employ the full range of experimental variables, experimental conditions, and reaction type which affect the simulated peak shape. The parameters of the simulated peaks are then refined until a good fit to the experimental (t_2-t_1) plot is achieved.

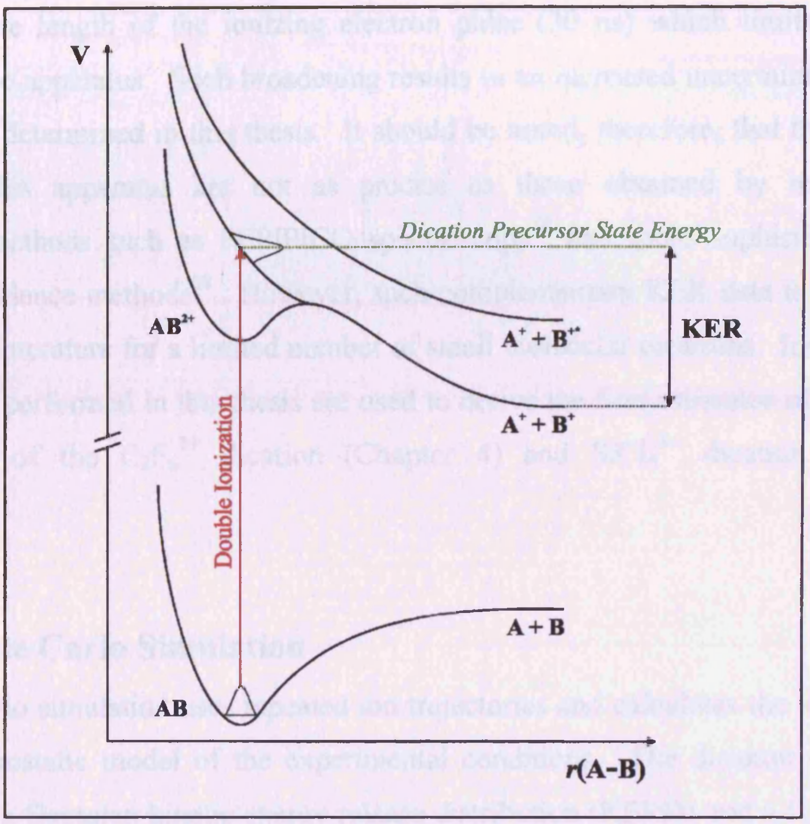

Figure 3.10 Schematic potential energy curves for a hypothetical gas phase molecule AB, showing the relationship between the asymptotic energy of the dissociation limit, the KER, and the energy of the dication precursor state giving rise to ion pair formation.

Measurement of the KER enables an estimate to be made of the energy of the dication precursor state $E(\mathrm{AB}^{2+})$ which dissociates to form the ion pair of interest (Figure 3.10). If the asymptotic energy E_{frag} of the dissociation limit is known:

$$E(AB^{2+}) = \mathrm{KER} + E_{\mathrm{frag}} \qquad 3.58$$

In this thesis the value of E_{frag} is commonly derived using data from standard thermodynamic tables[24,25] by assuming that the relevant products are formed in their ground states. Since the degree of internal excitation of the ionic fragments (and neutral fragments) is often unknown, the estimates of the precursor state energies derived using Eqn 3.58 represent a lower limit for the electronic state energies of the molecular dication AB^{2+}. Despite this, such precursor state energies have been shown to be in good accord with existing experimental and theoretical data on the electronic structure of small molecular dications.[26,27]

All ion pair peaks recorded in the pairs spectrum exhibit an additional degree of broadening due to the finite length of the ionizing electron pulse (30 ns) which limits the temporal resolution of the apparatus. Such broadening results in an increased uncertainty for the KER values that are determined in this thesis. It should be noted, therefore, that the KER values obtained by this apparatus are not as precise as those obtained by more advanced experimental methods such as PEPIPICO spectroscopy[19] and more sophisticated position sensitive coincidence methods[28]. However, such complementary KER data is only available in the reported literature for a limited number of small molecular dications. Indeed, the KER determinations performed in this thesis are used to derive the first estimates of the electronic state energies of the $C_2F_6^{2+}$ dication (Chapter 4) and $SiCl_4^{2+}$ dication (Chapter 5), respectively.

3.5.1 Monte Carlo Simulation

The Monte Carlo simulation uses repeated ion trajectories and calculates the ion flight times under an electrostatic model of the experimental conditions. The dication dissociation is modelled with a Gaussian kinetic energy release distribution (KERD) and a Gaussian spatial distribution of ionization events about the centre of the source region. The initial velocity of the neutral molecule prior to ionization is also considered and is represented by a Maxwell-Boltzmann distribution. The KERD is modelled by convoluting each individual component of KER with a Gaussian distribution, as the KERD of the detected fragments is expected to be a direct function of the reflection of the Gaussian ground state vibrational wavefunction on the respective repulsive potential energy curves of the dication states in the Franck-Condon region[10] (reflection approximation), as shown schematically in Figure 3.10.

The weighting of the initial ion velocity vectors in the simulation is also important. In the experiment, the initial direction of motion and orientation of the parent molecule before ionization is random, and so the motion of the ions formed by dicationic dissociation will be isotropic, but detection is only on a single plane. Most of the ions detected will therefore have a large component of velocity perpendicular to the TOF axis. To allow for the projection of a spherical velocity distribution onto the plane of the detector, the distribution of initial velocities must be sinusoidally weighted, thus ensuring that a higher proportion of ions have large velocity components perpendicular to the TOF axis. This procedure results in the satisfactory reproduction of a prototypical flat-topped peak[4] in the time-difference spectrum (Figure 3.11).

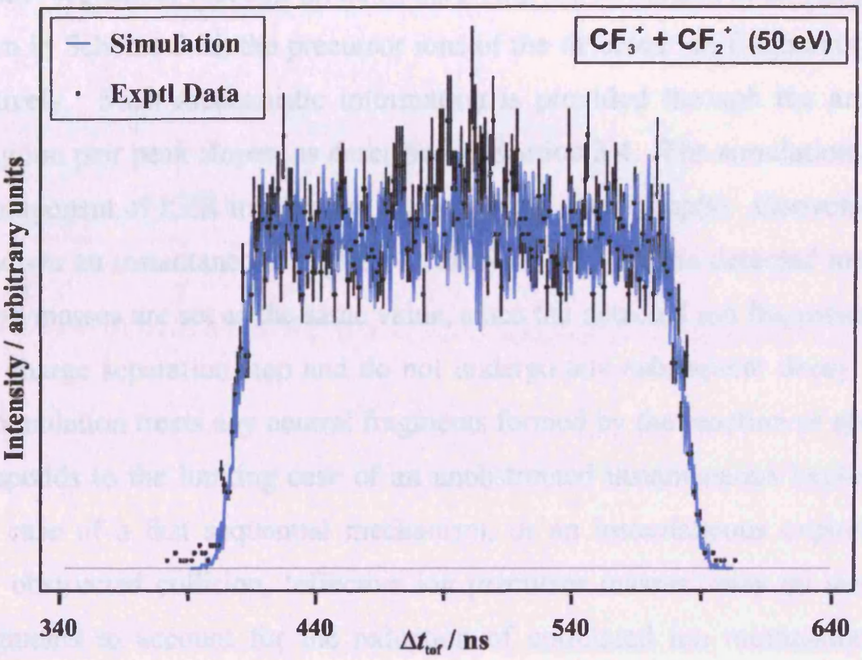

Figure 3.11 A t_2-t_1 plot of the $CF_3^+ + CF_2^+$ ion pair peak recorded in the pairs spectrum of C_2F_6 at 50 eV, compared to a Monte Carlo simulation of the reaction in the TOF mass spectrometer. The figure is representative of the good agreement that can be achieved between the simulation and experimental data, performed throughout this thesis, for the determination of the KER involved in ion pair formation.

3.5.1.1 Apparatus and Ion Parameters

To set up the simulation the following apparatus parameters are entered: Source length, acceleration length, drift length, repeller plate voltage and drift tube voltage (Table 2.I). These parameters form a description of the electrostatic model of the TOF mass spectrometer under the experimental conditions.

Subsequently, the various parameters relating to the dication dissociation reaction of interest are entered. Firstly, the masses of the detected ions and the neutral target molecule are defined. In addition, the masses of the primary ionic fragments (precursor ions) formed upon initial charge separation are entered, according to the reaction sequence:

$$ABCD^{2+} \rightarrow AB^{+} + CD^{+}$$

$$AB^{+} \rightarrow A^{+} + B \qquad \text{and} \qquad CD^{+} \rightarrow C^{+} + D \qquad 3.\text{iii}$$

Thus, for a slow sequential reaction (3.4.3.3) involving the formation of an ion pair $A^+ + C^+$, such as shown in Scheme 3.iii, the precursor ions of the detected ion fragments are AB^+ and CD^+, respectively. Such mechanistic information is provided through the analysis of the corresponding ion pair peak slopes, as described in Section 3.4. The simulation assumes that there is no component of KER involved in the secondary decay step(s). Conversely, if an ion pair is formed *via* an instantaneous explosion reaction (3.4.3.1), the detected ion masses and 'precursor' ion masses are set as the same value, since the detected ion fragments are formed in the initial charge separation step and do not undergo any subsequent decay. For such a reaction the simulation treats any neutral fragments formed by the reaction as spectators, and hence, corresponds to the limiting case of an unobstructed instantaneous explosion. In the intermediate case of a fast sequential mechanism, or an instantaneous explosion reaction involving an obstructed collision, 'effective ion precursor masses' may be derived for the detected fragments to account for the reduction of correlated ion momentum during the fragmentation process, and can be used accordingly as parameters in simulations of the KER. The derivation of these parameters is described in detail in Section 4.5.1.3.

Once a suitable description of the dication fragmentation mechanism has been constructed, the energetics of the dissociation reaction are entered. Initially an estimate of the KER associated with the reaction is entered, or a combination of weighted components of KER if the reaction KER is multi-valued. The detector radius, initial gas temperature along the jet axis and initial gas temperature perpendicular to the jet axis are also defined and entered into the simulation program.

3.5.1.2 Simulation Parameters

The simulation parameters consist of the number of ion trajectories required, the half-width of the Gaussian KERD for forming each ion pair of interest, and the half-width of the Gaussian distribution of ionization events in the source region. The time jitter distribution of the detector output is also considered in the simulation. Once all the relevant apparatus, ion and simulation parameters have been defined, the simulation is run and the data output is used to construct a simulated (t_2-t_1) spectrum, which is then compared with the experimental data (Figure 3.11). The parameters of the simulated spectrum are then refined until a good fit to the experimental (t_2-t_1) plot is achieved. In this thesis the satisfactory agreement between the simulated and experimental time-difference spectra is evaluated visually. Thus, the uncertainties in the values of the KER that are determined by this method are estimated by the deviations necessary to significantly degrade the fit between the simulated and experimental data, and are generally in the order of ± 0.4 eV.

Apparatus / Ion Parameter	Value	Simulation Parameter	Value
Detector radius	20 mm	Ion trajectories	50000
Initial gas T along jet axis	300 K	Half-width of Gaussian KERD	~1.5 eV
Initial gas T perpendicular to jet axis	300 K	Half-width of Gaussian spatial distribution in source	2 mm
		Half-width of time jitter distribution	1 ns

Table 3.III Typical values of selected parameters used in Monte Carlo simulations.

3.6 References

1. L. J. Frasinski, K. Codling, and P. A. Hatherly, Science **246** (4933), 1029 (1989).
2. L. J. Frasinski, M. Stankiewicz, P. A. Hatherly, and K. Codling, Measurement Science & Technology **3** (12), 1188 (1992).
3. J. H. D. Eland, in *Vacuum Ultraviolet Photonionization and Photodissociation of Molecules and Clusters*, edited by C. Y. Ng (World Scientific, Singapore, 1991).
4. J. H. D. Eland, F. S. Wort, and R. N. Royds, Journal Of Electron Spectroscopy And Related Phenomena **41** (3-4), 297 (1986).
5. H. C. Straub, P. Renault, B. G. Lindsay, K. A. Smith, and R. F. Stebbings, Physical Review A **52** (2), 1115 (1995).
6. M. R. Bruce and R. A. Bonham, International Journal Of Mass Spectrometry And Ion Processes **123** (2), 97 (1993).
7. M. R. Bruce, L. Mi, C. R. Sporleder, and R. A. Bonham, Journal Of Physics B-Atomic Molecular And Optical Physics **27** (23), 5773 (1994).
8. M. R. Bruce, C. Ma, and R. A. Bonham, Chemical Physics Letters **190** (3-4), 285 (1992).
9. C. Ma, M. R. Bruce, and R. A. Bonham, Physical Review A **44** (5), 2921 (1991).
10. D. M. Curtis and J. H. D. Eland, International Journal Of Mass Spectrometry And Ion Processes **63** (2-3), 241 (1985).
11. S. Feil, A. Bacher, M. Zangerl, W. Schustereder, K. Gluch, and P. Scheier, International Journal Of Mass Spectrometry **233** (1-3), 325 (2004).
12. R. F. Stebbings and B. G. Lindsay, Journal Of Chemical Physics **114** (10), 4741 (2001).

13 R. Basner, M. Schmidt, E. Denisov, P. Lopata, K. Becker, and H. Deutsch, International Journal of Mass Spectrometry **214** (3), 365 (2002).

14 G. K. Jarvis, K. J. Boyle, C. A. Mayhew, and R. P. Tuckett, Journal of Physical Chemistry A **102** (19), 3219 (1998).

15 I. G. Simm, C. J. Danby, J. H. D. Eland, and P. I. Mansell, Journal of the Chemical Society-Faraday Transactions Ii **72**, 426 (1976).

16 L. G. Christophorou and J. K. Olthoff, *Fundamental Electron Interactions with Plasma Processing Gases*. (Plenum, New York, 2004).

17 J. H. D. Eland, Molecular Physics **61** (3), 725 (1987).

18 J. H. D. Eland, Laser Chemistry **11** (3-4), 259 (1991).

19 R. Thissen, J. Delwiche, J. M. Robbe, D. Duflot, J. P. Flament, and J. H. D. Eland, Journal Of Chemical Physics **99** (9), 6590 (1993).

20 C. Maul and K. H. Gericke, International Reviews in Physical Chemistry **16** (1), 1 (1997).

21 D. York, Canadian Journal of Physics **44** (5), 1079 (1966).

22 J. H. D. Eland and B. J. Trevesbrown, International Journal of Mass Spectrometry and Ion Processes **113** (2), 167 (1992).

23 S. Hsieh and J. H. D. Eland, Journal of Chemical Physics **103** (3), 1006 (1995).

24 H. Y. Afeety, J. F. Liebman, and S. E. Stein, *"Neutral Thermochemical Data"*. (National Institute of Standards and Technology, Gaithersburg MD, 20899 (http://webbook.nist.gov), June 2005).

25 S. G. Lias, *"Ion Energetics Data"*. (National Institute of Standards and Technology, Gaithersburg MD, 20899 (http://webbook.nist.gov), June 2005).

26 S. J. King and S. D. Price, Journal of Chemical Physics **127**, 174307 (2007).

27 N. A. Love and S. D. Price, Physical Chemistry Chemical Physics **6** (19), 4558 (2004).

28 S. Hsieh and J. H. D. Eland, Journal of Physics B-Atomic Molecular and Optical Physics **30** (20), 4515 (1997).

Chapter 4 Electron Ionization of C_2F_6

4.1 Introduction

Hexafluoroethane (C_2F_6) is a man-made gas with a long environmental half-life (*ca.* 10000 y) and high global warming potential[1,2], and is widely used as a feed gas in plasma processing technologies.[1] Specifically C_2F_6 is used as an admixture gas in the reactive ion etching of Si/SiO_2 substrates in the fabrication of microelectronic devices.[2-6] When optimising such plasmas, desirable characteristics such as fast etch rates and high etch selectivity must be counterbalanced against the undesirable deposition of fluorocarbon films onto the substrate, energy consumption and exhaust content. For this purpose, and to understand the etching mechanisms taking place, a number of parameters including ion flux, ion composition and radical densities must be characterised.[1,3] Accurate models of these plasmas require, therefore, reliable measurements of the partial ionization cross-sections (PICS).[7-9] Indeed, the lack of reliable PICS data available for fluorocarbon molecules, including C_2F_6, has been highlighted in a report from the National Research Council.[10]

4.1.1 Dissociative Ionization of C_2F_6

Early measurements of the dissociative ionization of C_2F_6 were performed in 1963 by Bibby and Carter, who measured the fractional abundances of CF_3^+, $C_2F_5^+$, CF_2^+ and CF^+ ions using a Nier 60° type mass spectrometer following electron impact at 35 eV.[11] Interestingly these authors[11] also reported the formation of the $C_2F_3^+$ product ion which, despite being thermodynamically stable[12], has not been observed in all subsequent studies of the dissociative ionization of C_2F_6. In 1965 Lifshitz and Long reported the relative abundance of positive ions formed following electron ionization of C_2F_6 at 70 eV, and measured appearance potentials for the formation of CF_3^+ and $C_2F_5^+$ ions using the 'vanishing current method'.[13] The data was then compared to the results of simple RRKM calculations performed for this molecule. Such a comparison reveals that the observed relative yield of $C_2F_5^+$: CF_3^+ ions is much larger than predicted by QET theory. In both of these early studies the formation of the parent monocation, $C_2F_6^+$ was not observed.[11,13] On the basis of these results Lifshitz and Long suggested that direct decomposition from an excited electronic state of $C_2F_6^+$ may occur without transformation of excess electronic energy into vibrational energy within the molecular ion.[13] This violation of the statistical theory often used to describe the dissociation of molecular ions was subsequently confirmed by Simm *et al.* by PEPICO spectroscopy using 21.22 eV photons.[14-16] Using this technique, electrons with a single KE were selected thus enabling the dissociation products from $C_2F_6^+$ ions formed initially with a single internal energy to be studied. By comparison of this data to the PES of C_2F_6, Simm *et al.* were able to show that CF_3^+ product ions are formed exclusively by decomposition of $C_2F_6^+$ from the ground (X) state, while $C_2F_5^+$ product ions are the near-exclusive products formed by decomposition of $C_2F_6^+$ from the first excited electronic (A) state.[14,15] In addition excited electronic states of $C_2F_6^+$ lying immediately above the A band were shown to lead to CF_3^+ formation, thus providing clear evidence of an isolated electronic (A) state of $C_2F_6^+$ that decays without internal conversion.[15] Breakdown curves for the $C_2F_6^+$ ion measured in the range 14.14-18.64 eV using TPEPICO spectroscopy were reported by Inghram *et al.*[17] who reaffirmed the existence of this isolated electronic state. Using the results from pulsed field ionization mass spectrometry, Inghram *et al.* proposed that $C_2F_6^+$ ions fragment on a timescale less than 5×10^{-13} s, comparable to a vibrational time period.[17] Most recently Jarvis *et al.*[18] used TPEPICO spectroscopy to investigate the fragmentation dynamics of $C_2F_6^+$ in the photon energy range 12-25 eV. From the resulting breakdown curves Jarvis *et al.* demonstrated that the dissociation of $C_2F_6^+$ is predominantly impulsive within this energy range.[18] In addition measurements of the appearance energy and mean kinetic energy of CF_3^+, $C_2F_5^+$, CF_2^+ and CF^+ fragment ions were reported.

4.1.2 Partial Ionization Cross Sections of C_2F_6

To date there have been four measurements of the PICS of C_2F_6, induced by electron ionization, reported in the literature. Absolute PICS for the formation of $C_2F_5^+$, CF_3^+, CF_2^+ and CF^+ fragment ions have been measured, by Poll and Meichsner[19] using a quadrupole mass spectrometer, and by Jiao *et al.*[20] using Fourier Transform mass spectrometry, up to ionizing energies of 130 eV and 70 eV respectively. PICS for the formation of $C_2F_5^+$, $C_2F_4^+$, CF_x^+ (x=0-3), C_2F^+, C_2^+ and F^+ fragment ions have been measured, using time-of-flight mass spectrometry (TOFMS), by Basner *et al.*[21] from threshold to 900 eV. Iga *et al.*[22] also used TOFMS to measure PICS for the formation of $C_2F_5^+$, CF_x^+ (x=0-3) and F^+ fragment ions from threshold to 1000 eV. Of these previous works, only the most recent measurements Basner *et al.*[21] and Iga *et al.*[22] permit the efficient collection of fragment ions formed with considerable kinetic energy. Comparison of this recent data to the existing PICS data sets reveal some discrepancies concerning the formation of the smaller fragment ions CF_2^+ and CF^+, for which the PICS of Basner *et al.*[21] and Iga *et al.*[22] are considerably larger than those measured in previous studies. Interestingly, none of these previous studies report the observation of doubly charged fragment ions. Indeed, PICS for the formation of CF_2^{2+} and CF_3^{2+} dicationic fragments have only been reported following electron ionization of CF_4 above 40 eV[23-25], the smallest member of the perfluorocarbon series. Owing to the absence of such multiply charged fragments in the mass spectra of larger perfluorocarbons, CF_3^{2+} has been used as a specific product to quantify the CF_4 content in the exhaust gas of C_2F_6 – based plasmas. The total ionization cross-section (TICS) of C_2F_6 has been recorded by a number of groups[26-28], and has been calculated using the Binary-Encounter-Bethe (BEB) model[28] and the Deutsch-Märk (DM) formalism.[29]

In this study the electron ionization of C_2F_6 is investigated in the energy range 30-200 eV, using time-of-flight mass spectrometry coupled with a 2-D ion coincidence technique. Relative PICS $\sigma_r[X^{m+}]$ values are derived for the formation of all positively charged ions observed, and are expressed relative to the formation of $C_2F_5^+$, as a function of ionizing electron energy. Precursor-specific relative PICS $\sigma_n[X^{m+}]$ values are also derived for the formation of these fragment ions which, as explained in Section 3.3.4, quantify the contribution to the yield of an ion from single (n=1), double (n=2) and triple (n=3) ionization. In addition relative cross sections are derived for the formation of monocation pairs *via* the dissociation the $C_2F_6^{2+}$ dication $\sigma_r[X^+ + Y^+]$. The conclusions drawn from these values of the relative PICS are discussed in detail in Section 4.4.2.

4.1.3 The Hexafluoroethane Dication $C_2F_6^{2+}$

While the dynamics of the dissociation of $C_2F_6^+$ are now well understood, very little work has been directed towards the dissociative multiple ionization of C_2F_6. Despite a comprehensive literature search, no studies of the formation of ion pairs or multiply charged ion fragments produced by multiple ionization of C_2F_6 could be found within the reported literature. MP2 calculations place a lower limit on the double ionization energy of C_2F_6 at 35.17 eV[30], while measurements using double charge transfer (DCT) spectroscopy involving OH^+ projectiles reveal three dication electronic states at 38.7, 39.7 and 41.2 eV respectively.[31] Owing to the spin-conservation rule in these DCT experiments these three dication states are all triplet states.

In Section 4.5 the dynamics of the charge-separating dissociations of the $C_2F_6^{2+}$ dication are examined in more detail *via* the analysis of peaks appearing in the 2-D ion-coincidence spectra. From the results of this analysis dissociation mechanisms are proposed for the formation of a number of ion pairs resulting from the charge-separating decay of $C_2F_6^{2+}$. Measurements of the kinetic energy release (KER) involved in the formation of these ion pairs are then determined using Monte Carlo simulations. These KER measurements are used to provide estimates of the precursor state energy which dissociates to form the ion pair of interest.

4.2 Experimental Procedures

All experiments were performed using the time-of-flight mass spectrometer (TOFMS) described in Chapter 2. The C_2F_6 gas was a commercial sample (>98%) and was used without further purification. The operating conditions of the experiment involve low target gas pressures (< 10^{-6} Torr) and low electron flux, ensuring that on average much less than one ionization event is detected per ionizing pulse of electrons. This methodology greatly reduces the number of 'false coincidences' that contribute to the coincidence spectra recorded, as described in Section 3.2.2.1. The voltage conditions used in this study (Table 2.I) permit the efficient collection of ions formed initially with up to 11 eV of translational energy.

4.3 Data Analysis

4.3.1 Singles Mass Spectra

A representative singles mass spectrum of C_2F_6 recorded at an ionizing electron energy of 200 eV is shown in Figure 4.1. In this mass spectrum a multitude of peaks are observed corresponding to ion fragments formed by the dissociation of $C_2F_6^{n+}$. The intensities of these individual ion peaks $I_n[X^{n+}]$ appearing in the singles spectrum, are extracted using the analysis procedure described in Section 3.2.1. In agreement with previous studies of the dissociative ionization of C_2F_6, the formation of the parent monocation $C_2F_6^+$ is not observed.

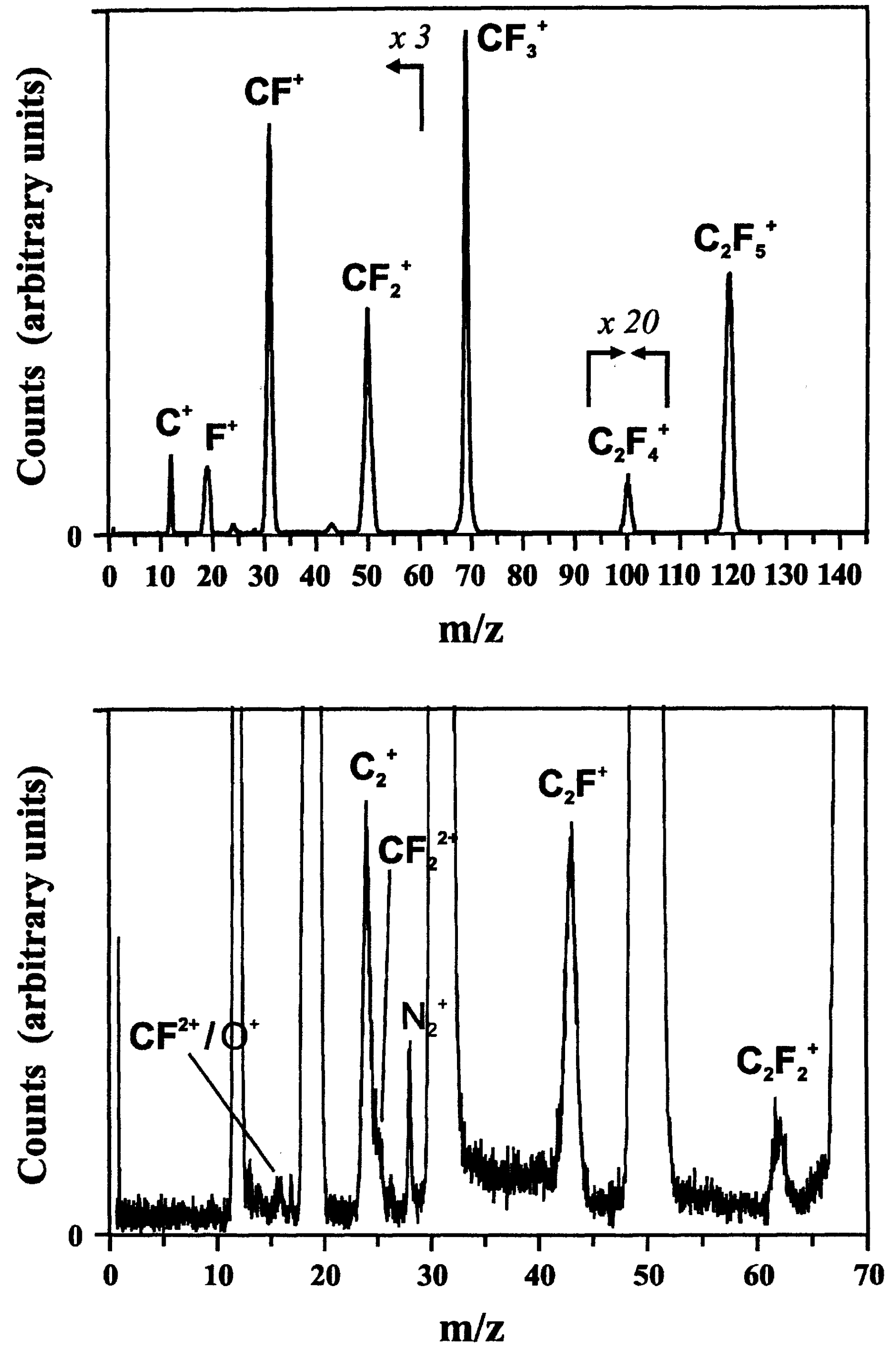

Figure 4.1: A characteristic (singles) mass spectrum of C_2F_6 following electron impact ionization at 200 eV.

Due to the low target gas pressures used, a small number of ions emanating from the ionization of residual air and water in our vacuum chamber contribute to the mass spectra, as shown in Figure 4.1. Specifically, O_2^+ ions contribute to the intensity of the CF^+ ion peak

(<<1%), while H_2O^+ ions contribute to the F^+ ion peak (<5%). These minor contributions to the mass spectra are subtracted, using the procedure outlined in Section 3.2.1.2, by normalization to the N_2^+ and OH^+ peak intensity, respectively. An analogous correction was made to the intensity of the CF^{2+} ion peak observed in the mass spectra recorded at 200 eV, to subtract contributions from O^+ ions emanating from the ionization of residual O_2 and H_2O. While the mass resolution of the apparatus is sufficient to resolve all monocation fragment peaks appearing in our mass spectra, the C_2^+ ion peak and CF_2^{2+} ion peak partially overlap at an ionizing energy above 60 eV (Figure 4.1). This overlap is caused by the large temporal widths of these peaks afforded by the large translational KE possessed by these ion fragments. To extract the intensities of C_2^+ and CF_2^{2+} ions appearing in each singles mass spectrum above 60 eV, a peak fitting procedure was used, as described in Section 3.2.1.1.

4.3.2 2-D Ion Coincidence Spectra

An illustrative pairs mass spectrum of C_2F_6 recorded at an ionizing electron energy of 200 eV is shown in Figure 4.2. At this energy 20 monocation pair peaks and a further 5 dication-monocation pair peaks are observed, as summarised in Table 4.VI. The intensities of the various ion peaks are then extracted, using the procedure described in Section 3.2.2, to yield the number of individual ion pairs $P[X^+ + Y^+]$, and also the overall contribution of each fragment ion to the pairs spectrum $P[X^+]$. In this work a distinction is made between the ion counts in pairs which must be formed *via* dissociative triple ionization of the C_2F_6 trication $P_3[X^+]$, for example $CF^+ + CF_2^{2+}$, and the ion counts in the other peaks in the pairs spectrum which may contain contributions from both dissociative double and triple ionization $P_2[X^+]$, such as $CF^+ + F^+$. The number of false coincidences is evaluated manually for each peak using an ion-autocorrelation function (Section 3.2.2.1), typically 1-2% of the raw peak intensity at higher ionizing electron energy, which is then subtracted. In the experiment no ion pairs are recorded if the second ion arrives at the detector within 32 ns of the first ion, due to the 'deadtime' of the discrimination circuitry. Such deadtime losses significantly affect the number of counts recorded in the $X^+ + X^+$ peaks in the pairs spectra ($X^+ = F^+$, CF_n^+, n=0-3). To estimate the number of ions lost, a separate one-dimensional (t_2-t_1) spectrum is constructed from the $X^+ + X^+$ coincidence data which is then appropriately extrapolated to the limit t_1=t_2, using simple geometry, to correct for the losses (Section 3.2.2.3). By inspection of the time-difference profiles for all other ion pairs observed in the pairs spectrum at 200 eV it was verified that there are no significant losses of energetic ion pairs in this work. As described in Section 3.2.2.2, losses of energetic ion pairs are characterised by a 'hollowing' of the corresponding (t_2-t_1) plot for a particular ion pair peak.

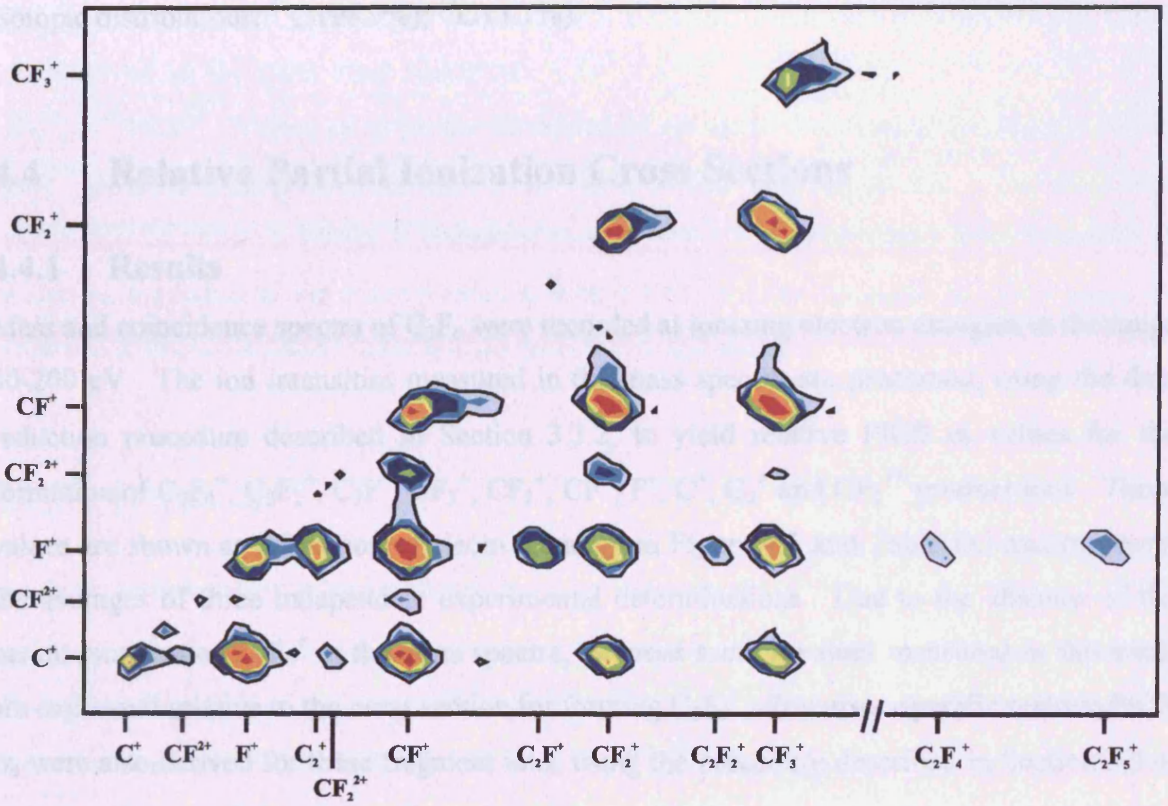

Figure 4.2 Representative 'pairs' mass spectrum of C_2F_6 recorded at 200 eV showing observed ion pairs formed *via* dissociation of $C_2F_6^{2+}$ and $C_2F_6^{3+}$.

Ion triples are processed by specifying a time-of-flight range for a particular ion, for example (CF^+), and then extracting all ion triples containing at least one ion whose arrival time t_1 lies within this specified range. Once extracted, the respective flight times of the two remaining ions, for example ($F^+ + F^+$), forming an ion triple are plotted as a 2-D histogram (t_2 *vs.* t_3). The contribution of a fragment ion $T[X^+]$ is then obtained from the number of counts in the $F^+ + F^+$ peak, after applying (where necessary) a small geometric correction to account for losses due to the experimental 'deadtime', as described above. False triple coincidences that contribute to the intensity of each triples peak are subtracted using the procedure outlined in Section 3.2.3.1. In this work it is not possible to perform measurements on $F^+ + F^+ + F^+$ ion triple formation due to the added complexity of twofold losses due to the experimental 'deadtime'. Contributions to all ion coincidence spectra from dissociative quadruple ionization are neglected, owing to the low cross sections determined for triple ionization in the energy regime of this work, as described in the sections that follow.

All ion intensities measured in this work were corrected numerically using the natural isotopic distributions: ^{12}C (98.9%); ^{13}C (1.1%).

4.4 Relative Partial Ionization Cross Sections

4.4.1 Results

Mass and coincidence spectra of C_2F_6 were recorded at ionizing electron energies in the range 30-200 eV. The ion intensities measured in the mass spectra are processed, using the data reduction procedure described in Section 3.3.2, to yield relative PICS σ_r values for the formation of $C_2F_4^+$, $C_2F_2^+$, C_2F^+, CF_3^+, CF_2^+, CF^+, F^+, C^+, C_2^+ and CF_2^{2+} product ions. These values are shown as a function of electron energy in Figure 4.3 and Table D.I and represent the averages of three independent experimental determinations. Due to the absence of the parent monocation $C_2F_6^+$ in the mass spectra, all cross section values measured in this work are expressed relative to the cross section for forming $C_2F_5^+$. Precursor-specific relative PICS σ_n were also derived for these fragment ions, using the procedure described in Section 3.3.4, and are shown in Table D.II. The values of σ_n (n=1-3) are compared in Figure 4.4. The maximum uncertainty of the σ_r values determined in this work is estimated to be ±10%, except for the formation of $C_2F_2^+$, $C_2F_4^+$ and CF_2^{2+} fragment ions, where the uncertainty may be as large as ±25%. For the σ_n values the maximum uncertainty is estimated as ±15%, except those for C_2^+, C_2F^+, $C_2F_2^+$, $C_2F_4^+$ and CF_2^{2+} formation for which the maximum uncertainty is ±30%. These estimates of the uncertainty have been derived using the average statistical error ($\pm 2\sigma$) for fragment ions whose PICS are of the same order of magnitude, using data from other cross-section determinations performed using this apparatus[7,32] (see also Chapters 6, 8). The overall contributions from single, double and triple ionization, as a percentage of the total ion yield at each ionizing electron energy, are summarized in Table D.III and Figure 4.5. In the singles and pairs mass spectra recorded at 200 eV, evidence of the formation of the CF^{2+} ion fragment is observed (Figure 4.1-4.2). From measurements of the CF^{2+} ion intensities in these spectra, the value of $\sigma_r(CF^{2+})$ is determined as 0.0007 at this ionizing energy. An upper limit of 0.0001 is assigned to the relative cross section for all possible ion fragments not observed in the mass spectra recorded in this work. Measurements of the ion detection efficiency (f_i) for these experiments, as detailed in Section 3.3.3, resulted in a value of $f_i = 0.20 \pm 0.01$.

As mentioned previously, in the pairs coincidence spectra 20 monocation pairs are observed (Table 4.VI). At ionizing energies above 75 eV, a further 5 dication-monocation pair peaks are observed in the pairs mass spectrum: $CF_2^+ + CF_2^{2+}$, $CF^+ + CF_2^{2+}$, $CF^+ + CF^{2+}$, $C^+ + CF_2^{2+}$, $C^+ + CF^{2+}$. Values of σ_r for the formation of monocation-monocation pairs formed by $C_2F_6^{2+}$ dication dissociation are shown in Table D.XVI and Figure 4.6. The maximum uncertainty of these σ_r values is estimated to be ±15%. Again an upper limit of 0.0001 is placed on the value of the relative cross section for all possible ion pairs and ion triples not observed in the coincidence mass spectra recorded in this work.

4.4.2 Discussion

4.4.2.1 Relative PICS (σ_r) Values

In Figure 4.3 a comparison is made between the $\sigma_r[X^+]$ values determined in this work and the values derived from the data of Basner *et al.*[21] Our σ_r values presented here include the first measurements of the formation of $C_2F_2^+$ and CF_2^{2+} ionic fragments following ionization of C_2F_6. In the sections that follow an additional comparison is made between the present data and the corresponding values derived from the absolute cross-section data of Iga *et al.*[22], Jiao *et al.*[20] and Poll and Meichsner[19]. It is remarked upon here that an excellent agreement is found between the data of Basner *et al.*[21] and Iga *et al.*[22] for $C_2F_5^+$ formation.

Figure 4.3 shows that CF_3^+ is the most abundant ion to be formed at all ionizing energies in the range 30-200 eV. Our σ_r values for the formation of this ion are in excellent agreement with the corresponding values of Basner *et al.*[21], Iga *et al.*[22], and Poll and Meichsner[19]. By contrast, our $\sigma_r[CF_3^+]$ values are up to 20% larger than the corresponding values of Jiao *et al.*[20], although both data sets agree within mutual error limits. The origin of this small discrepancy is most likely due to the fact that the data of Jiao *et al.*[20] overestimate $C_2F_5^+$ cross section, as has been remarked upon previously[22], resulting in a systematic reduction of their $\sigma_r[CF_3^+]$ values.

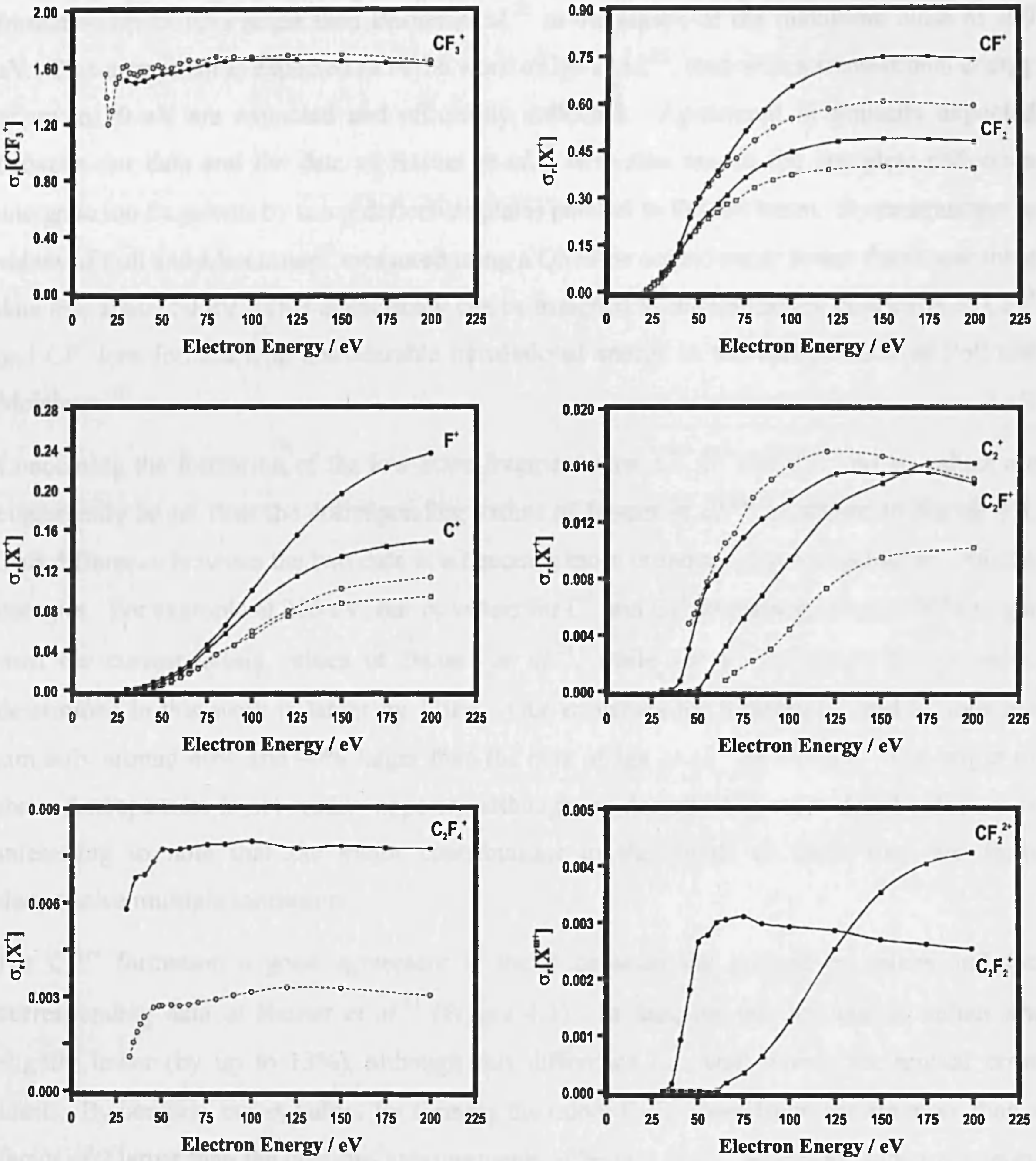

Figure 4.3 Relative PICS $\sigma_r[X^+]$ for forming ionic fragments (solid line), following electron ionization of C_2F_6. The corresponding relative PICS extracted from the data of Basner *et al.*[21] (dashed line) are also shown.

For CF_2^+ and CF^+ ion formation the present σ_r values are consistently larger than the corresponding values of Basner *et al.*[21], by around 20% near the peak maximum, although both data sets agree within experimental error limits. Our σ_r values for these ions are in excellent agreement with the data of Iga *et al.*[22], who reported PICS for CF_2^+ and CF^+

formation up to 10% larger than Basner *et al.*[21] in the region of the maximum close to 200 eV. This agreement is expected as in the work of Iga *et al.*[22], ions with a translational energy of up to 20 eV are extracted and efficiently collected. Agreement is similarly expected between our data and the data of Basner *et al.*[21] who also ensure the complete collection energetic ion fragments by using deflection plates parallel to the ion beam. By contrast the σ_r values of Poll and Meichsner[19] measured using a QMS lie considerably lower than these three data sets above 50 eV. This discrepancy can be assigned to the inefficient collection of CF_2^+ and CF^+ ions formed with considerable translational energy in the earlier study of Poll and Meichser.[19]

Concerning the formation of the low-mass fragment ions, C^+, F^+ and C_2^+, our σ_r values are consistently larger than the corresponding values of Basner *et al.*[21], as shown in Figure 4.3. This difference between the two data sets becomes more pronounced towards higher ionizing energies. For example at 200 eV, our σ_r values for C^+ and C_2^+ formation are over 50% larger than the corresponding values of Basner *et al.*[21], while for F^+ formation the σ_r value determined in this work is larger by 110%. Our σ_r values for forming C^+ and F^+ ions are similarly around 40% and 90% larger than the data of Iga *et al.*[22] at 200 eV. The origin of these discrepancies is not readily apparent although, as described in more detail below, it is interesting to note that the major contributions to the yields of these ions are from dissociative multiple ionization.

For C_2F^+ formation a good agreement is found between the present σ_r values and the corresponding data of Basner *et al.*[21] (Figure 4.3). In fact, for this ion our σ_r values are slightly lower (by up to 13%), although this difference lies well within the mutual error limits. By contrast, our σ_r values for forming the minor $C_2F_4^+$ ionic fragment are more than a factor of 2 larger than the previous measurements of Basner *et al.*[21] across the ionizing energy range. Interestingly, both PICS curves exhibit a very similar overall shape despite this difference in the magnitude of the σ_r values. Again, the origin of this discrepancy is not readily apparent. In Figure 4.3 the first measurements are reported for forming $C_2F_2^+$ and CF_2^{2+}, both minor fragment ions formed following dissociative ionization of C_2F_6. Significantly, the σ_r values determined in this work for forming $C_2F_2^+$ are similar to the σ_r values for forming $C_2F_4^+$ derived from the data of Basner *et al.*[21] On the basis of these measurements, it is perhaps surprising that $C_2F_2^+$ ions were not observed in the previous work of Basner *et al.*[21] A thorough search of the available literature data suggests that measurements on the formation of the CF_2^{2+} ionic fragment have only been reported previously following the dissociative electron ionization of CF_4.[1] These previous measurements are compared to the σ_r values measured in this work in Table 4.I. As described in the Introduction, owing to the absence of multiply charged fragments in the mass spectra of the larger perfluorocarbons, the CF_3^{2+} ion has been used as a specific product to quantify the CF_4 content in the exhaust gas of C_2F_6 – based plasmas.[2] Indeed it has previously been suggested that CF_2^{2+} and CF_3^{2+} only arise in the electron impact mass spectra of CF_4, CHF_3, and possibly the radical species CF_2 and CF_3.[2] The current measurements suggest to the contrary and, hence, CF_2^{2+} would be an unsuitable choice of 'specific product' for monitoring the CF_4 exhaust content of perfluorocarbon-based plasmas.

E / eV	[a] CF_4: $\sigma_r[CF_2^{2+}]$ / Å^2	[b] C_2F_6: $\sigma_r[CF_2^{2+}]$ / Å^2
40	0.0003	0.0000
50	0.0065	0.0000
60	0.0197	0.0000
100	0.0588	0.0028
200	0.0650	0.0090

a Data taken from Reference 1

b Current data placed onto an absolute scale by normalization to the $\sigma(C_2F_5^+)$ data of Basner *et al.*[21]

Table 4.I Comparison of $\sigma_r[CF_2^{2+}]$ values following electron ionization of CF_4 and C_2F_6, respectively, as a function of electron energy *E*.

4.4.2.2 Precursor-Specific Relative PICS

In Figure 4.4 a comparison is made between the relative precursor-specific PICS σ_n values for the formation of the various ion fragments discussed in the previous section. In respect of the relative contributions to the yield of each ion from dissociative single (n=1) and double (n=2) ionization, respectively, one may divide the product monocations into three separate groups: CF_3^+ and $C_2F_n^+$ (n=1, 2, 4, 5); CF_2^+ and CF^+; C^+, F^+ and C_2^+. The reasons for this classification are discussed in more detail below.

CF_3^+ and $C_2F_n^+$ (n=1, 2, 4, 5)

For the larger polyatomic product ions, contributions to the ion yield are dominated by dissociative single ionization across the ionizing energy range. In the case of $C_2F_5^+$

formation, the largest polyatomic product ion observed, σ_2 values do not exceed 0.0006 (not shown in Figure 4.4) and therefore contribute negligibly to the total $C_2F_5^+$ ion yield. For CF_3^+ formation, σ_2 values rise slowly to a maximum of 0.182 at 175 eV, comprising only 11.2% of the total CF_3^+ ion yield at this energy. Furthermore, while CF_3^+ is the most abundant ion to be formed by electron ionization in the energy regime of this work, it is only the third most abundant ion to be formed by dissociative double ionization above 50 eV. For the smaller C_2F^+ product ion, the σ_1 values represent the major contribution to the total ion yield although, as shown in Figure 4.4, contributions from double ionization become significant towards higher ionizing energies.

CF_2^+ and CF^+

Inspection of the σ_n values presented in Figure 4.4 reveals that CF^+ and CF_2^+ are the two most abundant ion fragments to be formed by dissociative double ionization above 50 eV. For both product ions, contributions to the ion yield from dissociative double ionization are greatest towards 200 eV, although not by a factor of three or more. For the formation of the CF^+ ion σ_1 values reach a maximum at around 85 eV before slowly decreasing towards higher ionizing energy. Above 125 eV, σ_2 values exceed σ_1 values by up to almost 50%. For the formation of CF_2^+, σ_1 values exhibit a broad maximum centred at 60 eV, while σ_2 values become over a factor of 2 larger than σ_1 values towards higher ionizing energies.

C^+, F^+ and C_2^+

For the light product ions C^+, F^+ and C_2^+, contributions to the overall yield of each ion are predominantly from dissociative double ionization towards higher ionizing energy. In Figure 4.4 it is shown that for all three product ions at 200 eV, the σ_2 values are at least a factor of 4 larger than the corresponding σ_1 values at this energy. For the formation of the atomic ions C^+ and F^+ the σ_n curves exhibit a remarkable similarity in terms of both the shape and magnitude. The σ_1 values for these ions rise slowly to a broad maximum centred at around 100 eV, before decreasing monotonically towards higher electron energy. Interestingly, dissociative single ionization contributes almost negligibly to the F^+ ion yield at ionizing energies approaching 200 eV. Indeed, a similar propensity for forming the atomic halogen ion *via* double ionization processes, is observed for Cl^+ formation following electron ionization of $SiCl_4$, studied using this apparatus (Chapter 5).

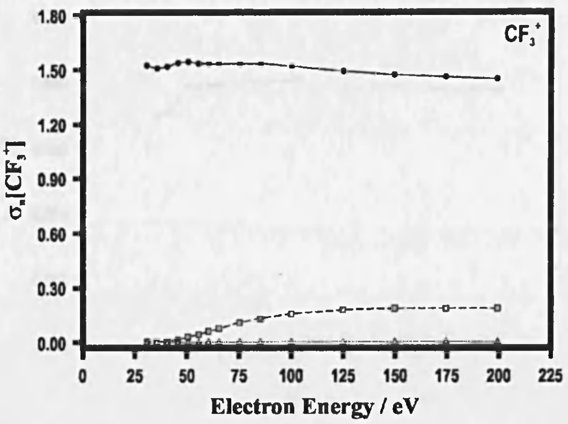
CF_3^+
$\sigma_n[CF_3^+]$
1.80
1.50
1.20
0.90
0.60
0.30
0.00
0
25
50
75
100
125
150
175
200
225
Electron Energy / eV

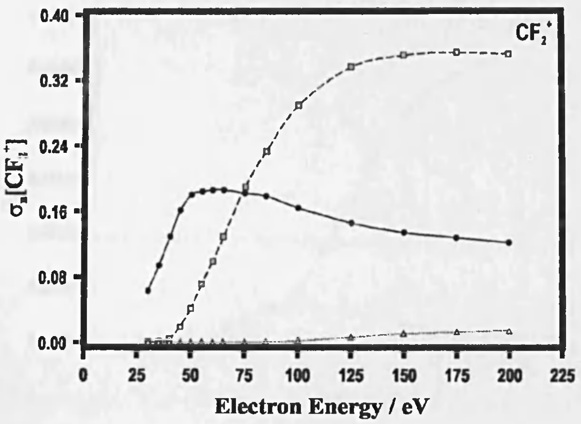
CF_2^+
$\sigma_n[CF_2^+]$
0.40
0.32
0.24
0.16
0.08
0.00
0
25
50
75
100
125
150
175
200
225
Electron Energy / eV

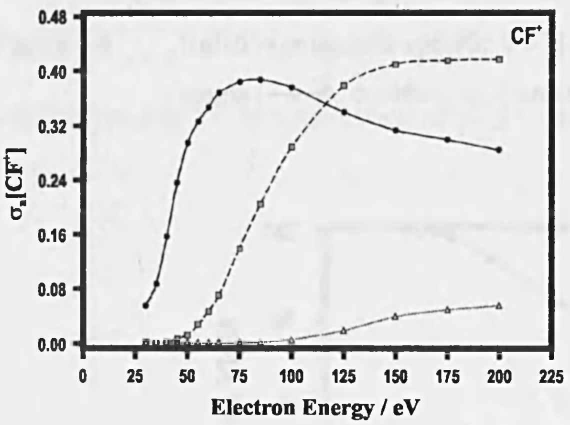
CF^+
$\sigma_n[CF^+]$
0.48
0.40
0.32
0.24
0.16
0.08
0.00
0
25
50
75
100
125
150
175
200
225
Electron Energy / eV

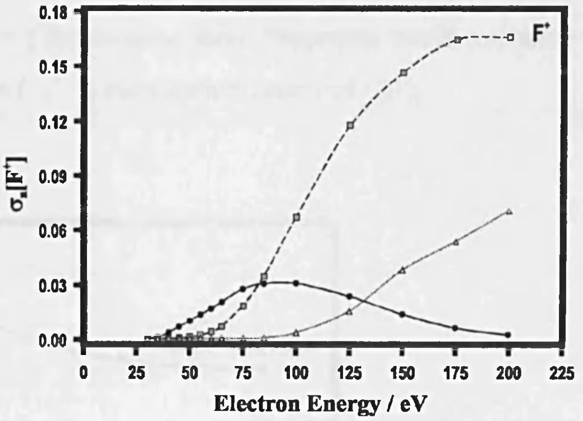
F^+
$\sigma_n[F^+]$
0.18
0.15
0.12
0.09
0.06
0.03
0.00
0
25
50
75
100
125
150
175
200
225
Electron Energy / eV

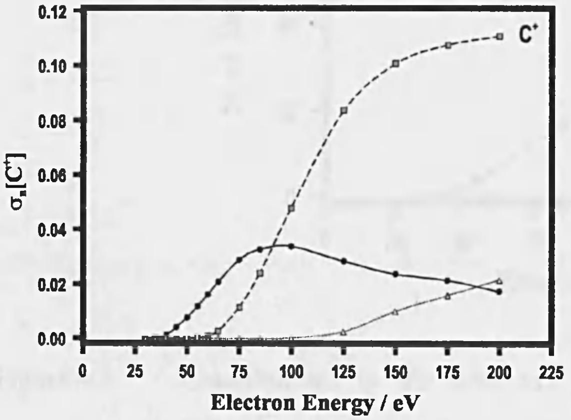
C^+
$\sigma_n[C^+]$
0.12
0.10
0.08
0.06
0.04
0.02
0.00
0
25
50
75
100
125
150
175
200
225
Electron Energy / eV

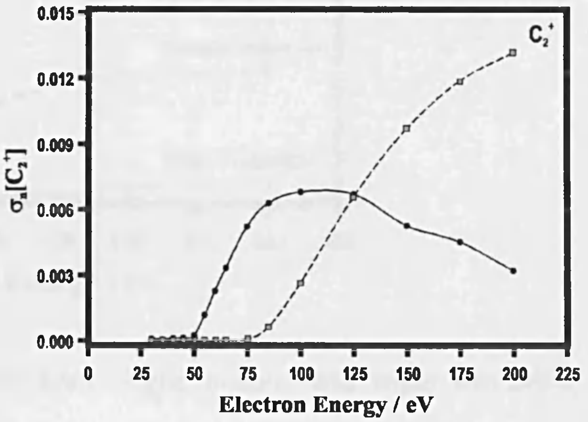
C_2^+
$\sigma_n[C_2^+]$
0.015
0.012
0.009
0.006
0.003
0.000
0
25
50
75
100
125
150
175
200
225
Electron Energy / eV

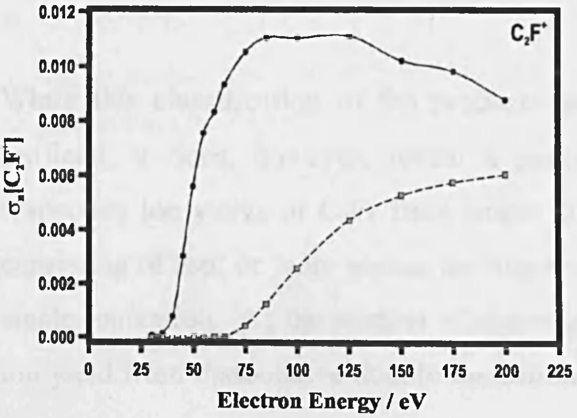
C_2F^+
$\sigma_n[C_2F^+]$
0.012
0.010
0.008
0.006
0.004
0.002
0.000
0
25
50
75
100
125
150
175
200
225
Electron Energy / eV

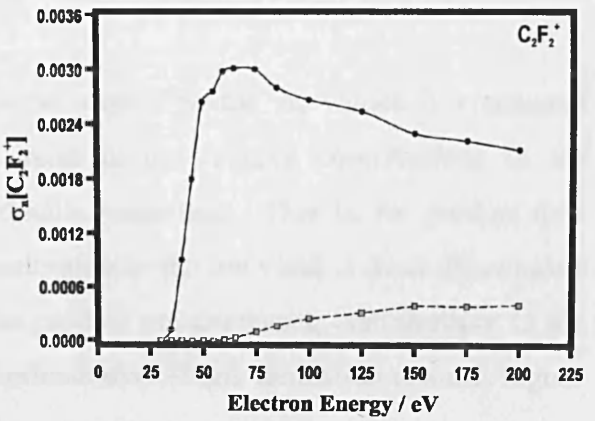
$C_2F_2^+$
$\sigma_n[C_2F_2^+]$
0.0036
0.0030
0.0024
0.0018
0.0012
0.0006
0.0000
0
25
50
75
100
125
150
175
200
225
Electron Energy / eV

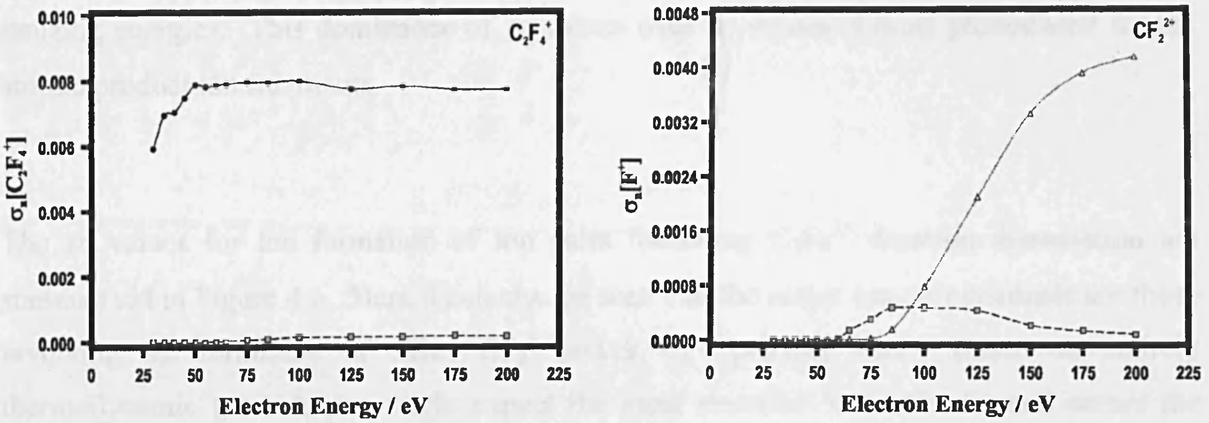

Figure 4.4 Relative precursor-specific PICS $\sigma_n[X^+]$ for forming ionic fragments *via* dissociative single (—●—), double (--■--) and triple (··△··) electron ionization of C_2F_6.

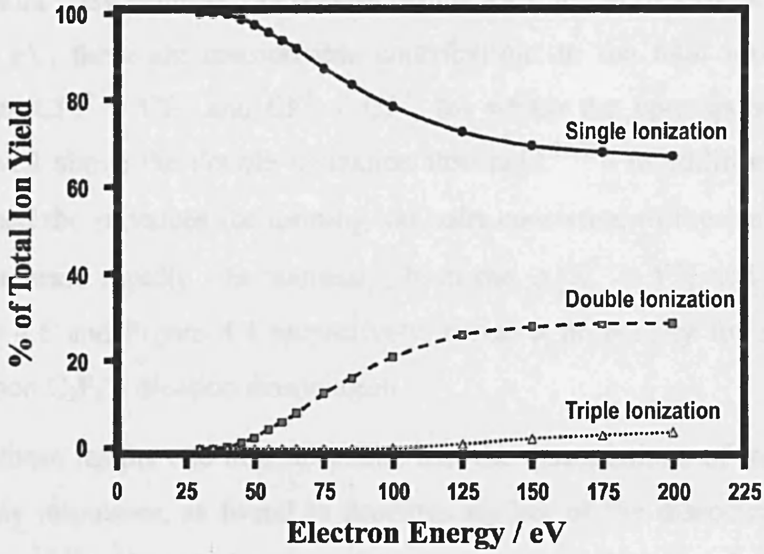

Figure 4.5 Contributions to the total ion yield from single, double, and triple ionization, following electron ionization of C_2F_6.

While this classification of the product ions with respect to the σ_n values is somewhat artificial, it does, however, reveal a general trend in the relative contributions to the respective ion yields of C_2F_6 from single and double ionization. That is, for product ions consisting of four or more atoms, the major contribution to the ion yield is from dissociative single ionization. As the number of atoms in the product ion decreases, contributions to the ion yield from dissociative double ionization dominate over single ionization towards higher ionizing energies. This dominance of σ_2 values over σ_1 values is most pronounced for the atomic product ion fragments.

The σ_r values for the formation of ion pairs following $C_2F_6^{2+}$ dication dissociation are summarised in Figure 4.6. Here it can also be seen that the major ion pair channels are those involving the formation of either CF_2^+ and/or CF^+ product ions. Based on entirely thermodynamic grounds one might expect the most abundant ion pairs formed across the ionizing energy range to comprise of $CF_3^+ + X^+$ ($X = CF_3^+, CF_2^+, CF^+$) (Table 4.VI), as the formation of such ion pairs have the lowest energy dissociation asymptotes. Indeed, in recent measurements on the acetylene dication $C_2H_2^{2+}$ it was shown that dissociation proceeds predominantly *via* the ground triplet potential energy surface ($^3\Sigma_g^-$) leading to formation of $C_2H^+ + H^+$ ion pairs.[7] By contrast, the present results for C_2F_6 show that at ionizing energies in excess of 50 eV, there are considerable contributions to the total ion pair yield from channels, such as $CF_2^+ + CF^+$ and $CF^+ + CF^+$, for which the corresponding dissociation asymptotes lie well above the double ionization threshold.[30,31] In addition, as the ionizing energy is increased the σ_r values for forming ion pairs consisting of the atomic C^+ and/or F^+ ion fragments increase rapidly. In summary, both the $\sigma_r[X^+ + Y^+]$ and $\sigma_n[X^+]$ data sets shown in Figure 4.6 and Figure 4.4 respectively, reveal a propensity for a large degree of fragmentation upon $C_2F_6^{2+}$ dication dissociation.

On the basis of these results one may speculate that the dissociations of the $C_2F_6^{2+}$ dication are predominantly impulsive, as found in previous studies of the dissociation dynamics of $C_2F_6^+$ monocation.[13-18] If such dications dissociate on a fast timescale without efficient conversion of the excess electronic energy, either *via* radiative or non-radiative transitions, then one may expect to observe considerable fragmentation of the molecule accompanying the charge-separation process. As the ionizing energy is increased, the average excess energy available to the $C_2F_6^{2+}$ dication will similarly increase, thus leading to a greater number of ion pairs consisting of smaller ionic fragments, as is observed in this study.

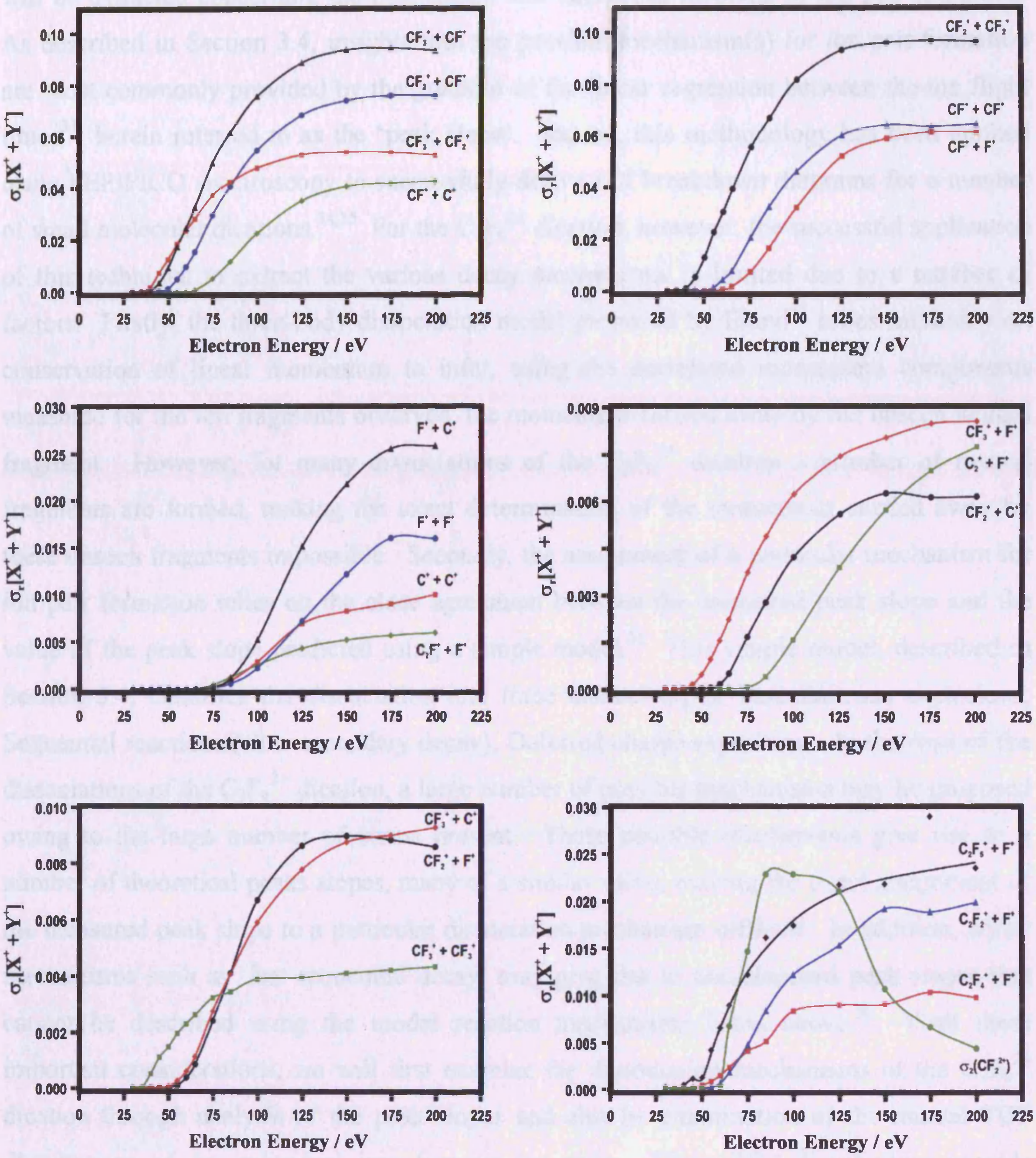

Figure 4.6 Relative PICS $\sigma_r[X^+ + Y^+]$ for forming monocation-monocation pairs following electron ionization of C_2F_6.

4.5 The Dynamics and Energetics of $C_2F_6^{2+}$ Dissociation

In this section some aspects of the charge separating dissociation of the hexafluoroethane dication $C_2F_6^{2+}$ are investigated in more detail. Specifically, through analysis of the peak shapes for ion pairs appearing in the 2-D ion coincidence spectra (Figure 4.2), information will be extracted concerning the mechanism and energetics involved in ion pair formation. As described in Section 3.4, insights into the possible mechanism(s) for ion pair formation are most commonly provided by the gradient of the linear regression between the ion flight times[33], herein referred to as the 'peak slope'. Indeed, this methodology has been applied using PEPIPICO spectroscopy to successfully derive full breakdown diagrams for a number of small molecular dications.[34,35] For the $C_2F_6^{2+}$ dication, however, the successful application of this technique to extract the various decay mechanisms is limited due to a number of factors. Firstly, the three-body dissociation model proposed by Eland[33] relies implicitly on conservation of linear momentum to infer, using the correlated momentum components measured for the ion fragments observed, the momentum carried away by the unseen neutral fragment. However, for many dissociations of the $C_2F_6^{2+}$ dication a number of neutral fragments are formed, making the exact determination of the momentum carried away by these unseen fragments impossible. Secondly, the assignment of a particular mechanism for ion pair formation relies on the close agreement between the measured peak slope and the value of the peak slope predicted using a simple model.[33] This simple model, described in Section 3.4, classifies the dissociation into three distinct types: Instantaneous explosions; Sequential reactions (slow secondary decay); Deferred charge separation. In the case of the dissociations of the $C_2F_6^{2+}$ dication, a large number of possible mechanisms may be proposed owing to the large number of atoms present. These possible mechanisms give rise to a number of theoretical peaks slopes, many of a similar value, making the exact assignment of the measured peak slope to a particular dissociation mechanism difficult. In addition, decay mechanisms such as 'fast sequential decay' may give rise to non-standard peak slopes that cannot be described using the model reaction mechanisms listed above.[36] With these important considerations, we will first examine the dissociation mechanisms of the $C_2F_6^{2+}$ dication through analysis of the peak slopes and also by examination of the mutual TOF distributions of the individual ions forming ion pairs. These TOF distributions provide information on the momentum distribution of the indivual ions, as described below, while the peak slope provides a measure of the correlated momentum components of the two ions forming an ion pair. Following this the total kinetic energy release involved in the formation of ion pairs is investigated. All KER determinations in this work are performed using Monte Carlo simulations as described in Section 3.5. The results of these KER determinations are then combined with the dissociation asymptotes derived from values in the literature, to provide estimates of the precursor-state energies for forming ion pairs.

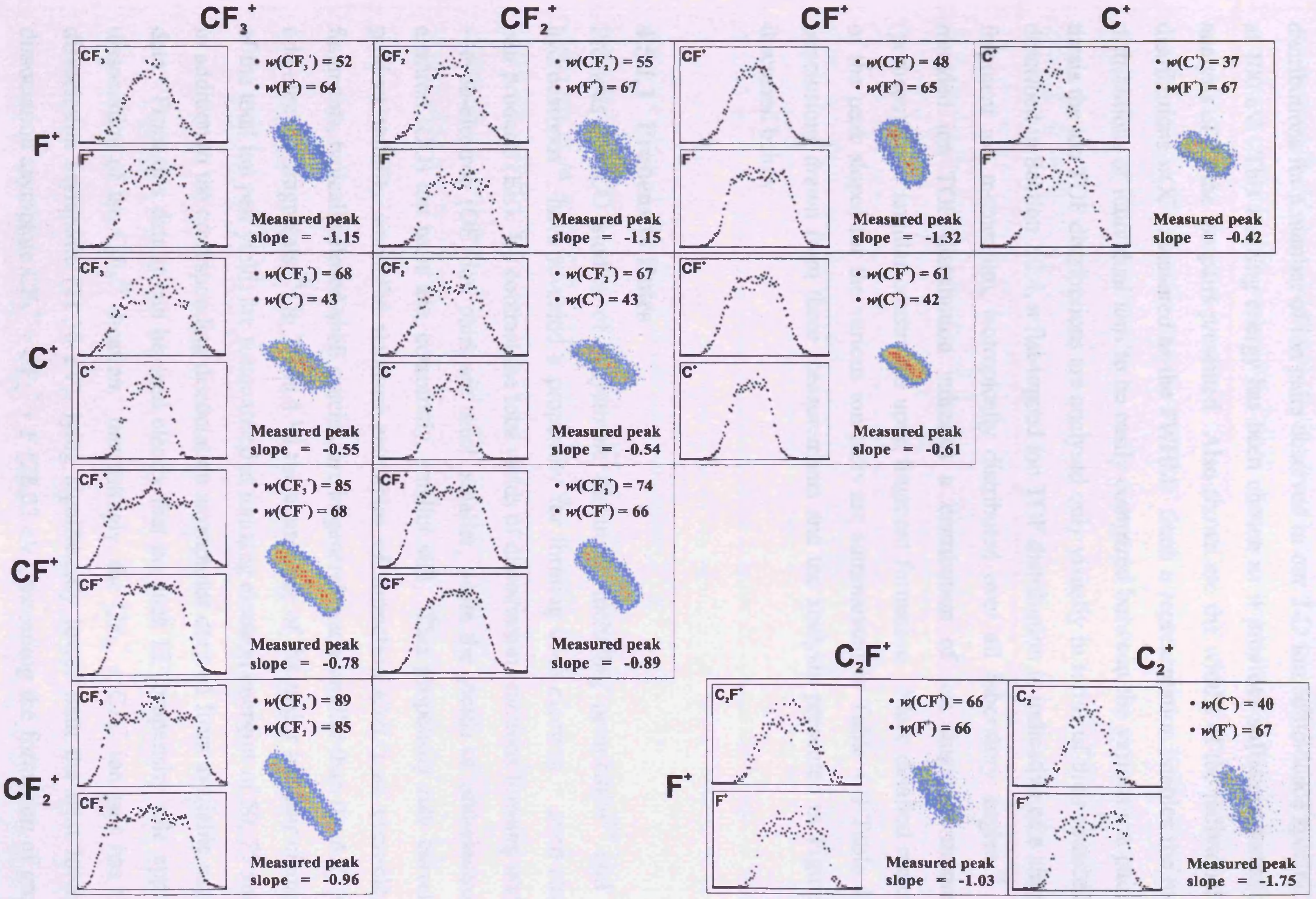

Figure 4.7 Individual ion TOF distributions, experimental peak shapes and peak slope data for ion pairs observed in the 2-D ion coincidence spectra recorded at 100 eV.

4.5.1 The Dynamics of $C_2F_6^{2+}$ Dissociation

In Figure 4.7 is shown a summary of the peak shape, peak slope and individual ion TOF distributions for a number of ion pairs observed in our 2-D ion coincidence spectra, recorded at 100 eV. This ionizing energy has been chosen as it provides sufficient statistics for the analysis of all the ion pairs presented. Also shown are the widths of the individual ion TOF distributions $w(X^+)$ measured as the FWHM. Such a representation enables the momentum distributions of individual ions to be easily compared between the various ion pairs. In this thesis the ion TOF distributions are analysed only visually in terms of their roundedness. As described in Section 2.2.4, a flat-topped ion TOF distribution is indicative of a single-valued fragment ion momentum, isotropically distributed over all laboratory angles.[33] A more rounded ion TOF distribution indicates a distribution of ion fragment momenta with (perhaps) some angular constraints upon fragment formation. More detailed measurements of the peak slopes for the various ion pairs are summarised in Table 4.II-Table 4.III. The conclusions drawn from these measurements and the analysis presented in Figure 4.7, are discussed below.

4.5.1.1 Propensity Rules

Previous PIPICO studies of polyatomic dications, including open-chain[37] and aromatic hydrocarbons[38], have revealed a propensity for forming even-electron + even-electron ion pair products (EE). By contrast the total yields of dissociation reactions forming odd-electron + even-electron (OE) ion pairs are much smaller, while the yields of odd-electron + odd-electron (OO) ion pairs are, commonly, smaller still. This propensity rule correlates with product stability since the standard enthalpies of formation (ΔH_f°) of even-electron ion fragments, typically closed-shell species, are in general much smaller than the ΔH_f° values for odd-electron fragments.[38] In Table 4.VI the abundance of the major ion pair channels (>1% of the total ion pair yield) are summarised at ionizing electron energies of 50, 75 and 100 eV, in addition to the corresponding dissociation asymptotes derived from available experimental data. From this data it can be seen clearly that no such EE propensity rule applies to the dissociation of the $C_2F_6^{2+}$ dication. Interestingly, the $CF_3^+ + CF_3^+$ ion pair has the lowest dissociation asymptote (21.38 eV), lying significantly lower than the next lowest energy dissociation asymptote $CF_3^+ + CF_2^+ + F$ (28.03 eV), assuming the formation of ground state products. Therefore, based on thermodynamic grounds one may expect $CF_3^+ + CF_3^+$ to be the most abundant ion pair formed by the dissociation of the $C_2F_6^{2+}$ dication, particularly at ionizing energies close to the double ionization threshold. However, the σ_r values shown in Figure 4.6 show this not to be the case. Indeed, the $CF_3^+ + CF_3^+$ ion pair is only the fourth most abundant ion pair channel at 40 eV. By contrast, $CF_2^+ + CF_2^+$ ion pairs are identified as a major dissociation channel of the $C_2F_6^{2+}$ dication at ionizing energies in the range 40-200 eV (Table 4.VI). Such ion pairs have a dissociation asymptote corresponding to a much higher energy (34.68 eV) and, hence, this observation would appear to contradict the propensity rule described above.

4.5.1.2 $F^+ + X^+$

For ion pairs involving the formation of an F^+ ion, the TOF distributions of the F^+ ion are all approximately 'square' indicating a single-valued momentum release for this ion fragment (Figure 4.7). In addition, the widths of the F^+ TOF distributions $w(F^+)$ are nearly identical for all such ion pairs. By contrast the TOF distributions of the coincident ion partner (X^+) in these ion pairs are significantly rounded and exhibit a shape more representative of a Gaussian-shaped function. Concerning the formation of $F^+ + CF_n^+$ ion pairs (n=1-3) all peaks appearing in our pairs coincidence spectra have a slope more negative than -1 (Table 4.II), indicating that the heavier CF_n^+ ion (plotted on the x-axis) has a smaller component of momentum parallel to the TOF axis than the lighter F^+ ion. In the case of $C^+ + F^+$ formation a smaller component of momentum is similarly observed for the C^+ ion than the F^+ ion, as reflected by a peak slope less negative than -1, since the C^+ ion is now the lighter ion observed and is plotted on the y-axis. The reduction of the momentum of the CF_n^+ ion fragment (n=0-3) in $F^+ + CF_n^+$ ion pairs and the considerable rounding of the CF_n^+ TOF distribution may be caused by one or a combination of factors, summarised below:

(i) An obstructed instantaneous explosion involving a glancing collision between CF_n^+ and the neutral fragment(s) formed[33,39]

(ii) An fast sequential decay mechanism[36] in which F^+ loss occurs on a much faster timescale than the subsequent dissociation of the remaining $C_2F_5^+$ moiety. In this event a small proportion of the momentum imparted to $C_2F_5^+$ in the charge separation 'step' is carried away by the neutral fragment(s) formed in the subsequent dissociation 'step', as shown below. It is noted however that this mechanism lies in-between the extremes of an instantaneous concerted dissociation and a sequential decay mechanism (Section 3.4.3) and, hence, the notion of distinct 'steps' occurring in the mechanism may be somewhat misleading.

(iii) A deviation from linearity in the many-body fragmentation of $C_2F_6^{2+}$. As a crude test of linearity in the formation of these ion pairs, the sum of the widths of the individual ion TOF distributions were compared to the width of the corresponding time-difference (t_2-t_1) distribution, as described by Eland[33] Such a comparison suggests that linearity is not conserved in the formation of $F^+ + C^+$ and, to a lesser extent, $F^+ + CF^+$ ion pairs.

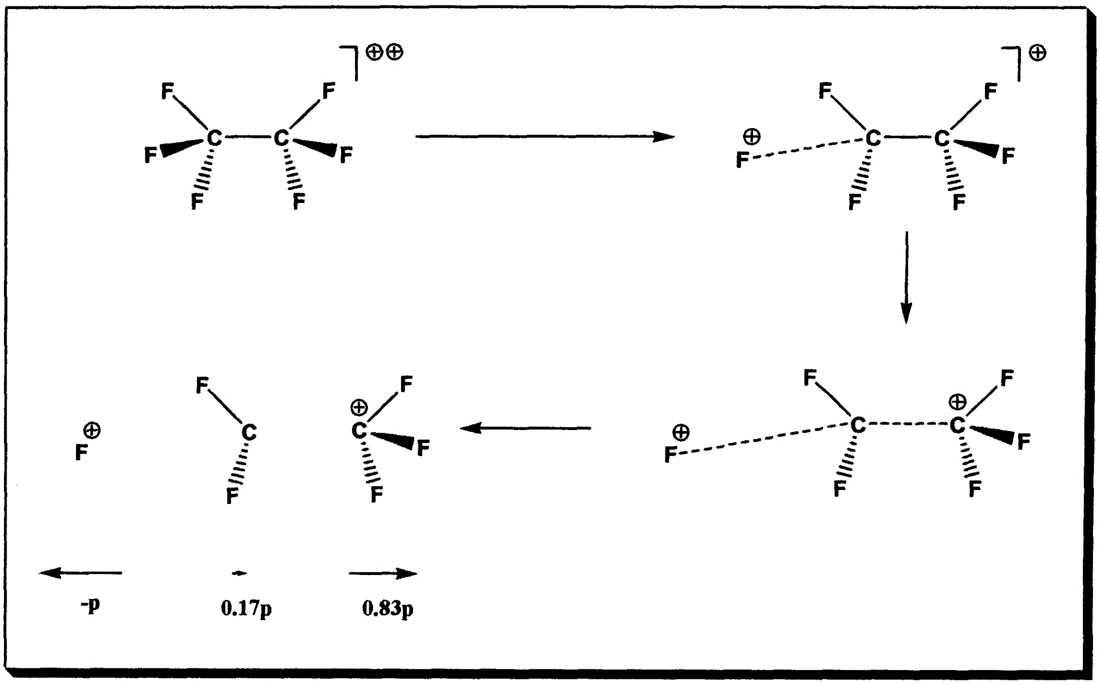

Figure 4.8 Proposed fast sequential decay mechanism for forming $F^+ + CF_3^+$ ion pairs *via* charge-separating dissociation of $C_2F_6^{2+}$.

In the light of the experimental evidence described above, a mechanism for the formation of $F^+ + CF_3^+$ ion pairs may be proposed (Figure 4.8). In this mechanism, the $C_2F_6^{2+}$ dication undergoes fast sequential decay involving initially the unobstructed loss of F^+. This fast initial 'step' is common to the formation of all $F^+ + CF_n^+$ ion pairs, thus giving rise to the single-valued momentum release observed for this ion. The transient $C_2F_5^+$ moiety then decays rapidly, albeit on a longer timescale than the loss of F^+, to form a CF_3^+ ion. The reduction in momentum of the CF_3^+ product ion relative to the momentum of F^+ is mostly likely caused by the asymmetry of the fast sequential decay process, in which a small proportion of momentum is carried away by the neutral CF_2 fragment, accounting for the peak slope measured for this ion pair (-1.20 ± 0.05). The possibility of an aligned KER[35] in the dissociation of the $C_2F_5^+$ moiety to explain the measured peak slopes is unlikely, as a reduction in the CF_3^+ momentum requires either the rotation of the $C_2F_5^+$ moiety by approximately 180°, or a rearrangement of the $C_2F_6^{2+}$ precursor ion prior to loss of F^+. However, a small component of randomly orientated KER in the decay of the $C_2F_5^+$ moiety may help to explain further the observed rounding of the CF_3^+ ion TOF distribution.

The fast sequential decay mechanism proposed in Figure 4.8 may be extended to account for the formation of the remaining F^+ + CF_n^+ ion pairs (n=0-2). For F^+ + CF_2^+ formation the measured peak slope (Table 4.II) and individual ion TOF distributions are very similar to the corresponding data for F^+ + CF_3^+ ion pairs. These similarities may be explained, using the scheme shown above, where following C-C bond cleavage the positive charge resides on the CF_2 fragment. For the formation of F^+ + CF^+ and F^+ + C^+ ion pairs, measurements of the peak slope (Table 4.II) imply a far greater reduction in the momentum of the CF^+/C^+ ion fragment relative to the momentum of F^+. These measurements can be rationalised by an 'obstructed' decay of the $C_2F_5^+$ moiety involving either a head-on or a glancing collision between the CF^+/C^+ ion and the neutral fragments formed.[33,39] Such an obstructed decay will result in a considerable component of momentum being carried away by the neutral fragment(s) formed and may help explain the lack of preservation of linearity in the formation of these ion pairs.

Ion Pair	Measured Peak Slope	Comments	Ion	Momentum Reduction Factor
$F^+ + CF_3^+$	-1.20 ± 0.05 (60 eV)	Peak slope increases very slightly with increasing E	$\mathbf{CF_3^+}$	**1.2**
$F^+ + CF_2^+$	-1.25 ± 0.06 (75 eV)	Peak slope rises to -1.15 (100 eV) and -0.97 (200 eV)	$\mathbf{CF_2^+}$	**1.25**
$F^+ + CF^+$	-1.48 ± 0.04 (75 eV)	Peak slope rises to -1.32 (100 eV) and -1.22 (200 eV)	$\mathbf{CF^+}$	**1.48**
$F^+ + C^+$	-0.42 ± 0.02 (100 eV)		$\mathbf{C^+}$	**2.38**
$F^+ + C_2^+$	-1.75 ± 0.08 (100 eV)	Peak slope decreases sharply with increasing E -2.00 (150 eV)		
$F^+ + C_2F^+$	-1.00 ± 0.04 (85 eV)	Invariant with ionizing E		

Table 4.II Summary of peak slopes for F^+ + X^+ ion pairs measured in our 2-D ion coincidence spectra.

4.5.1.3 Momentum Reduction Factors

A summary of the experimental peak slopes measured for F^+ + CF_n^+ ion pairs is shown in Table 4.II. In this table a 'momentum reduction factor' (MRF) is assigned to the various CF_n^+ ions comprising such ion pairs. The MRF factor quantifies the amount by which the momentum component of the CF_n^+ ion must be reduced, relative to the momentum of the F^+ ion, in order to reproduce the corresponding measured peak slope.

In Table 4.III is shown a summary of the experimental peak slopes measured for a number of ion pairs (not comprising an F^+ product ion), formed following the dissociation of the $C_2F_6^{2+}$ dication. For each ion pair, a value of the peak slope has been predicted by taking an appropriate ratio of the ion MRF's shown in Table 4.II above. Thus, for example, for the formation of CF_2^+ + C^+ ion pairs this ratio is given by:

$$\text{Predicted Peak Slope} = -\frac{\text{MRF(second detected ion)}}{\text{MRF(first detected ion)}} = -\frac{1.25}{2.38} = -0.53 \qquad 4.1$$

As can be seen in Table 4.III, the predicted values of the peak slope calculated in this way are in excellent agreement with the measured peak slopes for the formation of these ion pairs. Such an agreement indicates that the causes of reduction of momentum in the formation of CF_n^+ fragments are common to the mechanisms for forming both F^+ + CF_n^+ (n=0-3) and CF_n^+ + CF_m^+ ($n \leq 3$, $m \leq n$) ion pairs.

Ion Pair	*Predicted Peak Slope	Measured Peak Slope	Comments
$CF_3^+ + CF_2^+$	-0.96	-0.96 ± 0.01 (45 eV)	Invariant with ionizing *E*
$CF_3^+ + CF^+$	-0.81	-0.75 ± 0.02 (50 eV)	Peak slope decreases very slightly with increasing *E*
$CF_3^+ + C^+$	-0.50	-0.50 ± 0.03 (85 eV)	Peak slope decreases slowly with increasing *E*
$CF_2^+ + CF_2^+$	-1	-1 (manual fit)	
$CF_2^+ + CF^+$	-0.84	-0.88 ± 0.02 (55 eV)	Invariant with ionizing *E*
$CF_2^+ + C^+$	-0.53	-0.53 ± 0.03 (75 eV)	Invariant with ionizing *E*
$CF^+ + C^+$	-0.62	-0.61 ± 0.02 (85 eV)	

Table 4.III Summary of peak slopes for CF_n^+ + CF_m^+ ion pairs measured in our 2-D ion coincidence spectra.

4.5.1.4 $CF_3^+ + CF_n^+$

For CF_3^+ + CF_2^+ ion pairs the individual ion TOF distributions are both flat-topped indicating a single-valued momentum release (Figure 4.7). The narrow 'spike' in the centre of the CF_3^+ ion TOF distribution is most likely due to the small contribution from 'false' coincidences to the CF_3^+ + CF_2^+ ion pair peak. The peak slope measured for this ion pair (-0.96 ± 0.01) is suggestive of an instantaneous decay mechanism in which the neutral F fragment formed carries away only a small component of the total momentum release. By contrast, for a head-on collision between CF_2^+ and the neutral F fragment (or a sequential mechanism involving slow secondary decay of CF_3^+ to form CF_2^+) the peak slope is expected to be close to -0.72. A comparison of the sum of the widths of the individual ion TOF distributions to the width of the time difference distribution, as described above, reveals that linearity is conserved for this reaction.[33] Based on this experimental evidence a fast sequential decay mechanism is proposed for the formation of CF_3^+ + CF_2^+ ion pairs, as shown in Figure 4.9.

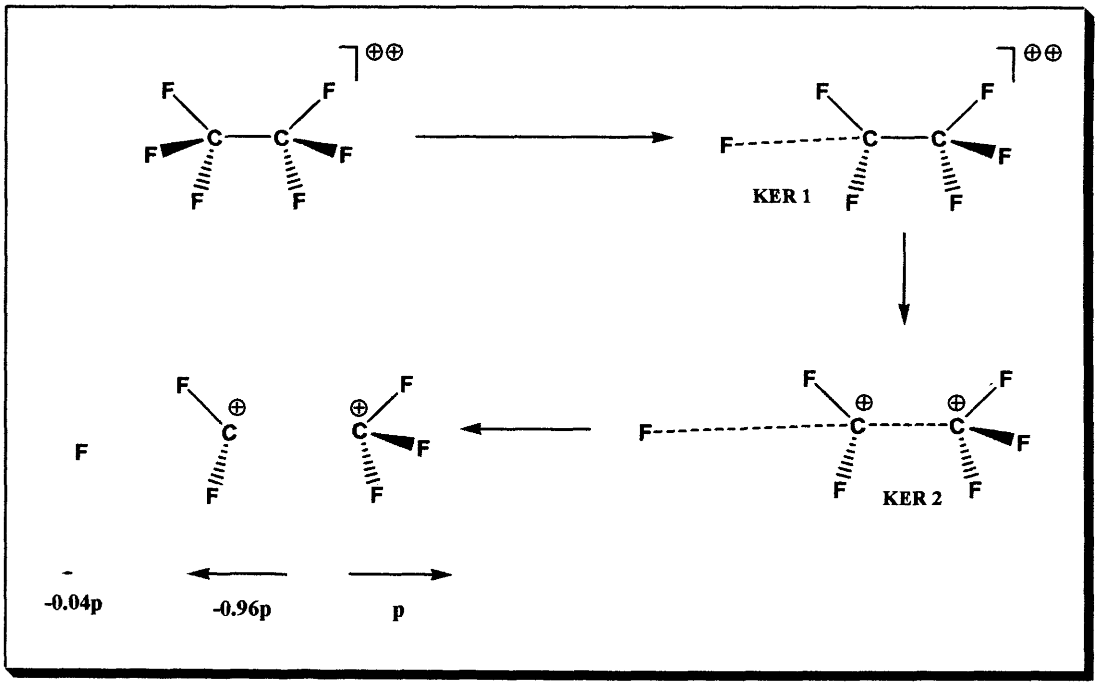

Figure 4.9 Proposed fast sequential decay mechanism for forming CF_3^++ CF_2^+ ion pairs *via* charge-separating dissociation of $C_2F_6^{2+}$.

In this mechanism, the reaction proceeds initially *via* elongation of the C-F bond resulting in the loss of a neutral F fragment. This step is again likely to be very fast, analogous to the loss of F^+ in the mechanism for forming $F^+ + X^+$ ion pairs. However, since the loss of F does not involve charge separation, the KER involved in this step (KER 1) is likely to be small, as indicated by the value of the peak slope which implies only a small component of momentum is possessed by the neutral F fragment. The main component of KER (KER 2) arises in the charge separating step resulting in the formation of the CF_3^+ + CF_2^+ ion pair. The CF_2^+ ion is formed with a single-valued momentum, close in value to the momentum of the CF_3^+ ion, and suggests that the trajectory of the CF_2^+ ion is largely unobstructed by the neutral F fragment ejected in the initial 'step'. Similarly for this reaction, assuming that the $C_2F_6^{2+}$ dication does not undergo structural rearrangement prior to dissociation, the CF_3^+ ion is also unobstructed following its formation. As described below, this mechanism may be extended to account for the formation of the remaining CF_3^+ + CF_n^+ ion pairs.

For the formation of CF_3^+ + CF^+ ion pairs the measured peak slope at 50 eV (-0.75) lies in-between the limiting values for an unobstructed instantaneous decay mechanism (-1) and a sequential mechanism involving the slow secondary decay of CF_2^+ to form CF^+ (-0.62). For this reaction a fast sequential decay mechanism is again proposed, involving the loss of neutral F prior to charge separation. In the charge separation 'step' a CF^+ ion is formed and experiences a glancing collision with a second neutral F fragment, while the CF_3^+ ion is formed without obstruction. Such a glancing collision gives rise to a small reduction in the correlated momentum of the CF^+ ion fragment and accounts for the peak slope observed. For CF_3^+ + C^+ ion pairs the individual ion TOF distributions are visibly more rounded than for the CF_3^+ + CF_n^+ ion pairs discussed above (Figure 4.7). The peak slope measured at 85 eV (-0.50) shows a considerable reduction in the momentum component of C^+ relative to CF_3^+ and is consistent with an obstructed mechanism for forming C^+ in the charge separation step. Such an obstructed collision is also likely to result in deviations from linearity for this reaction and may account for observed rounding of the C^+ ion TOF distribution.

4.5.1.5 CF_2^+ + CF_n^+ and CF^+ + C^+

For the formation of CF_2^+ + CF_n^+ ion pairs (n=0-2) the shapes of the individual ion TOF distributions exhibit a remarkable similarity to the corresponding data for CF_3^+ + CF_n^+ ion pairs. As described previously, the peak slopes for forming such ion pairs have been successfully predicted using the MRF's for the individual ions, suggesting that the dynamics involved in the formation of the individual ions comprising CF_2^+ + CF_n^+ and CF_3^+ + CF_n^+ ion pairs may be linked. Thus, for the formation of CF_2^+ + CF_n^+ ion pairs one may again propose a fast sequential decay mechanism, as outlined in Figure 4.9. For CF_2^+ + CF_2^+ only a portion of the ion pair peak is observable in the pairs spectra due to the experimental deadtime of the discrimination circuitry (Figure 4.2). Therefore measurements of the peak slope for this ion pair were performed by manually fitting a straight line to the observed portion of the peak (Table 4.III). Indeed, a crude estimate of the peak slope obtained by this method (-1.0) suggests an instantaneous mechanism for forming these ion pairs. One should note however that this value of the peak slope cannot distinguish between a concerted instantaneous explosion forming CF_2^+ + CF_2^+, and a fast sequential decay mechanism involving initial loss of F followed by the formation of two unobstructed CF_2^+ ions in the charge-separation step. For the formation of CF_2^+ + CF^+ the measured peak slope at 55 eV (-0.88) indicates a small reduction in the momentum of CF^+ relative to CF_2^+. As in the formation of CF_3^+ + CF^+ ion pairs, this reduction of momentum can be rationalised by a glancing collision involving CF^+ in the charge-separation step. Similarly, for the formation of CF_2^+ + C^+ ion pairs, the measured peak slope at 75 eV (-0.53) reveals a considerable reduction in the correlated momentum of the C^+ ion fragment. This reduction of momentum is again rationalised by an obstructed collision upon formation of the C^+ ion fragment in the charge-separation step.

For the formation of CF^+ + C^+ ion pairs the peak slope at 85 eV (-0.61) once more reveals a considerable reduction in the correlated momentum of C^+. The observed peak slope has an equal value to the value predicted using the appropriate MRF's for these ions, suggesting that both CF^+ and C^+ are involved in obstructed collisions upon formation in the charge-separation step, in the same manner as described above.

4.5.1.6 $C_2^+ + F^+$

The peak slopes measured for the formation of C_2^+ + F^+ ion pairs decrease rapidly with increasing ionizing energy: -1.75 ± 0.08 (100 eV); -2.00 ± 0.05 (150 eV); -2.12 ± 0.05 (200 eV). Indeed, a similar trend in the peak slope data has been observed for the formation of C_2^+ + H^+ ion pairs *via* the dissociation of the acetylene dication[7,35] $C_2H_2^{2+}$ (see also Chapter 6). In this earlier work[7,35] the decreasing peak slope is attributed to the slow secondary decay of C_2H^+ to form C_2^+, involving an aligned KER in this secondary decay step. The similarity between these two sets of peak slope data suggests an aligned component of secondary KER in the formation of C_2^+ + F^+ ion pairs. Based upon the fast sequential decay mechanism proposed for the formation of F^+ + CF_n^+ ion pairs (Figure 4.8), as described above, a reduction in the correlated momentum of C_2^+ would be expected due to the asymmetry of the 'steps' involving loss of F^+ (charge separation) and the secondary decay of the $C_2F_5^+$ moiety. The correlated momentum of C_2^+ may also be reduced further *via* an obstructed collision in this secondary dissociation step, thus explaining the value of the peak slope. However, in the decay of the $C_2F_5^+$ moiety to form C_2^+ it is difficult to rationalise why a second component of

KER should be aligned parallel to the axis of charge separation. Thus, a more likely explanation for the trend in values of the peak slope is a sequential mechanism for forming this ion pair involving the formation of C_2F^+ in the initial charge separation 'step' (Figure 4.10). The expected value of the peak slope for a sequential mechanism involving the secondary decay of C_2F^+ to C_2^+ is -1.79, in close agreement with the observed peak slope at 100 eV. An increasing component of aligned KER in the secondary decay of C_2F^+ in its original configuration would explain the sharp decrease in peak slope values towards 200 eV.

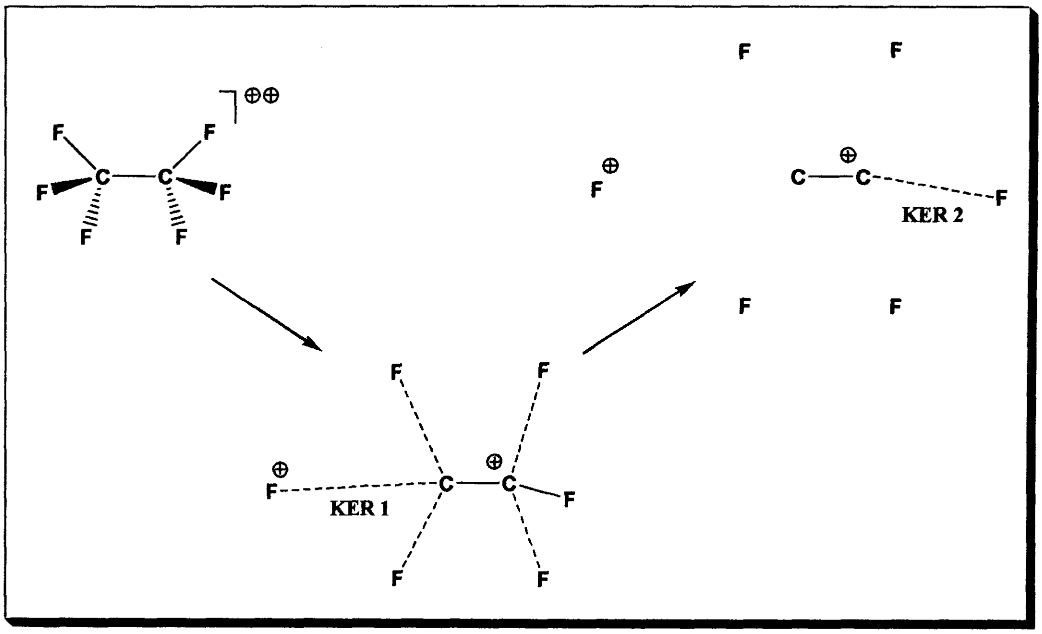

Figure 4.10 Proposed sequential decay mechanism for forming C_2^+ + F^+ ion pairs *via* charge separating dissociation of $C_2F_6^{2+}$. In the secondary decay of C_2F^+, a small component of KER (KER 2) is aligned parallel to the direction of the original charge separation.

4.5.1.7 Summary

By analysis of the peak slope data and individual ion TOF distributions, mechanisms have been proposed for the formation of ion pairs resulting from the dissociation of the $C_2F_6^{2+}$ dication. Fast sequential decay mechanisms are proposed for the formation of almost all such ion pairs, thus suggesting that the dissociations of the $C_2F_6^{2+}$ dication are predominantly impulsive, as has been observed in previous studies of the dissociations of the $C_2F_6^+$ monocation.[14-18] A common feature of these fast sequential decay mechanisms is the initial cleavage of a C-F bond, forming an F^+ ion or a neutral F fragment, prior to any other dissociation step(s). This asymmetry may explain the relatively low yield of CF_3^+ + CF_3^+ ion pairs (Figure 4.6) requiring cleavage of the C-C bond only. Furthermore, the impulsive nature of the dissociations of the $C_2F_6^{2+}$ dication may help explain both the apparent violation of the EE propensity rule described in Section 4.5.1.1.

4.5.2 The Energetics of $C_2F_6^{2+}$ Dissociation

The kinetic energy of the ion pairs formed by dissociation of the $C_2F_6^{2+}$ dication have been determined using Monte Carlo simulations of the peaks observed in the pairs mass spectra, as described in Section 3.5. The parameters used in these simulations must be carefully chosen to accommodate the various dissociation mechanisms described above. These proposed fast sequential decay mechanisms, often involving obstructed collisions of the ionic fragments formed, result in a reduction of the correlated momentum of the fragment ion(s) observed and, hence, a significant component of the total KER may be carried away by the unseen neutral fragment(s). In the limiting case of a slow sequential reaction, the component of KER possessed by the neutral fragment(s) is considered implicitly in the simulations by specifying the mass of the ionic precursors for each ion observed. Such precursor ion masses are inferred directly from measurements of the corresponding peak slope. In the case of fast sequential reactions, 'effective' ion precursor masses may be derived for the various ions comprising ion pairs using the momentum reduction factors (MRF's) shown in Table 4.II. The use of these effective ion precursor masses (Table 4.IV) as variables in the KER simulations account for the partitioning of the total KER among the observed ions and neutral fragments formed in the dissociations of the $C_2F_6^{2+}$ dication.

Ion	m/Z	MRF $F^+ + CF_n^+$	Effective Precursor Mass	MRF $CF_n^+ + CF_m^+$ (n=3,2, m=2-0), (n=1, m=0)	Effective Precursor Mass
CF_3^+	69	1.2	82.8	1	69
CF_2^+	50	1.25	62.5	1.04	52*
CF^+	31	1.48	45.9	1.23	38.2
C^+	12	2.38	28.6	1.98	23.8
F^+	19	1	19	-	-

Table 4.IV 'Effective' ion precursor masses for ion fragments comprising ion pairs, used in simulations of the KER involved in $C_2F_6^{2+}$ dication dissociation.

A summary of the results of the KER determinations performed is shown in Table 4.V, which, in combination with the dissociation asymptotes derived from values in the literature[40,41], provide estimates of the precursor-state energies for forming ion pairs (Table 4.VI). Since the degree of internal excitation of the ionic fragments is often unknown, these estimates represent a lower limit for the electronic state energies of $C_2F_6^{2+}$. Interestingly, the KER for formation of $CF_3^+ + CF_2^+$ ion pairs suggests a precursor state of $C_2F_6^{2+}$ lying at 32.4 eV, significantly lower than the value of the adiabatic double ionization potential (35.17 eV) calculated previously at the MP2 level of theory.[30] However, the lack of available experimental data concerning the electronic states of the $C_2F_6^{2+}$ dication[31] makes the assignment of each fragmentation reaction to a particular electronic state difficult.

Ion Pair	KER / eV	†Ionizing E / eV	Comments
$CF_3^+ + C^+$	6.2 ± 0.3	85	
$CF_3^+ + F^+$	4.1 ± 0.3	60	
$CF_3^+ + CF^+$	4.8 ± 0.2	50	
$CF_3^+ + CF_2^+$	4.4 ± 0.2	45	Steady increase in KER to 5.0 eV (IE>75eV)
$CF_2^+ + C^+$	5.8 ± 0.3	75	
$CF_2^+ + F^+$	4.7 ± 0.3	75	
$CF_2^+ + CF^+$	4.2 ± 0.2	50	2nd component of KER visible above 65 eV
$CF_2^+ + CF_2^+$	2.4 ± 0.2	45	
$CF^+ + CF^+$	3.2 ± 0.3	75	Second component of KER observed at all IE's above 75eV, determined as 4.0 ± 0.4 eV
$CF^+ + C^+$	6.6 ± 0.5	75	2nd component of KER visible above 85 eV

† Denotes the lowest ionizing energy at which KER determinations were performed.

Table 4.V Summary of the KER determinations performed in this work for ion pairs formed by charge-separating dissociation of the $C_2F_6^{2+}$ dication. Note that contributions to the ion pair peaks from dissociative triple ionization are negligible at the lowest ionizing electron energies for which simulations are performed (Figure 4.4).

Ion Pair	Neutral Fragment(s)		Dissoc. Limit / eV	Ion Pair Propensity / % 50 eV	75 eV	100 eV	KER	PSE
$C_2F_5^+ + F^+$	none	EE					-	-
$C_2F_4^+ + F^+$	F	OE	36.31				-	-
$CF_3^+ + C^+$	3F	EO	38.81		1.2	1.4	6.2	45.01
	F_2 + F		37.17					43.37
$CF_3^+ + F^+$	CF_2	EE	34.01	1.9	2.7	2.5	4.1	**38.11**
	CF + F		39.37					43.47
	C + 2F		44.97					49.07
$CF_3^+ + CF^+$	2F	EE	31.06	***24.1***	***22.2***	***18.4***	4.8	**35.86**
	F_2		29.41					34.21
$CF_3^+ + CF_2^+$	F	EO	28.03	***32.7***	***16.6***	***11.7***	4.4	**32.43**
$CF_3^+ + CF_3^+$	none	EE	21.38	3.8	1.4	0.9	-	
$C_2F_2^+ + F^+$	3F	OE					-	
	F_2 + F							
$CF_2^+ + C^+$	4F	OO	45.46		1.2	1.7	5.8	51.26
	F_2 + 2F		43.82					49.62
	$2F_2$		42.17					47.97
$CF_2^+ + F^+$	F + CF_2	OE	40.66		1.1	1.6	4.7	**45.36**
	2F + CF		46.02					50.72
	3F + C		51.62					56.32
	F + F_2 + C		49.98					54.68
$CF_2^+ + CF^+$	3F	OE	37.71	3.3	13.2	13.3	4.2	41.91
	F_2 + F		36.06					40.26
$CF_2^+ + CF_2^+$	2F	OO	34.68	***33.6***	***24.8***	***19.9***	2.4	**37.08**
	F_2		33.04					35.44
$C_2F^+ + F^+$	4F	EE						
	2F + F_2							
	$2F_2$							
$CF^+ + C^+$	5F	EO	48.49		2.3	5.5	6.6	55.09
	F_2 + 3F		46.84					53.44
	$2F_2$ + F		45.19					51.79
$CF^+ + F^+$	CF_3 + F	EE	39.88		3.3	7.8		
	CF_2 + 2F		43.69					
	CF_2 + F_2		42.04					
	CF + 3F		49.04					
	CF + F_2 + F		47.39					
	C + 4F		54.65					
	C + 2F + F_2		53.00					
	C + $2F_2$		51.35					
$CF^+ + CF^+$	4F	EE	40.73		9.2	11.2	3.2	43.93
	F_2 + 2F		39.08					42.28
	$2F_2$		37.44					
$C_2^+ + F^+$	5F	OE	56.37					
	F_2 + 3F		54.72					
	$2F_2$ + F		53.08					
$F^+ + C^+$		EO				1.3		
$C^+ + C^+$		OO						

Table 4.VI Summary of the precursor-state energies for ion pair formation following charge-separating decay of $C_2F_6^{2+}$. In this table KER denotes the kinetic energy release involved in ion pair formation, derived from experiments described in this thesis. These values of the KER are combined with the corresponding dissociation limit, derived from standard thermodynamic tables, to estimate the energy of the dication precursor state (PSE) which dissociates to form the ion pair of interest.

4.6 Conclusions

Relative PICS for the formation of fragment ions, following dissociative electron ionization of C_2F_6 in the energy range 30-200 eV, have been measured using time-of-flight mass spectrometry coupled with a 2-D ion coincidence technique. A comparison of this data with the recently reported absolute PICS of C_2F_6 measured by Basner *et al.*[21], and Iga *et al.*[22], has been made. Such a comparison reveals a good agreement for the formation of the heavier ion fragments, CF_n^+ (n=1-3) and C_2F^+, but a poorer agreement for the formation of the low-mass ions C^+, F^+ and C_2^+, for which the present measurements are significantly larger than reported previously. Precursor specific relative PICS have also been derived for the formation of the various fragment ions observed, which quantify the contribution to the yield of each ion from single, double, and triple ionization. These values show that for the larger fragment ions comprised of four atoms or more, contributions to the ion yields are predominantly from dissociative single ionization across the ionizing energy range. For the major fragment ions comprised of three atoms or less, the dominant contribution to the ion yield is from dissociative double ionization at electron energies above 100 eV. Relative cross sections for the formation of ion pairs *via* dissociative double ionization have been derived and reveal a propensity for a large degree of fragmentation upon $C_2F_6^{2+}$ dication dissociation. Analysis shows that the major dissociation channels of $C_2F_6^{2+}$ above 50 eV do not correlate with thermodynamic stability, and suggests that the dissociations of the $C_2F_6^{2+}$ dication are predominantly impulsive. The relative PICS data presented in this work also include the first measurements for the formation of $C_2F_2^+$ and CF_2^{2+} fragment ions following electron ionization.

Through the analysis of the peaks observed in the 2-D ion coincidence spectra, additional information has been extracted concerning the fragmentation dynamics and energetics of the

$C_2F_6^{2+}$ dication. Fast sequential decay mechanisms are proposed for the formation of monocation pairs *via* dissociation of the $C_2F_6^{2+}$ dication. A common feature of these mechanisms is the initial cleavage of the C-F bond, leading to the formation of an F^+ ion or a neutral F fragment, prior to any other dissociation steps. This characteristic of $C_2F_6^{2+}$ fragmentation explains the low propensity for forming $CF_3^+ + CF_3^+$ ion pairs, which has the lowest energy dissociation asymptote, and is further evidence of the impulsive nature of $C_2F_6^{2+}$ dissociation. By simulations of the peaks in the ion coincidence spectra, the KER involved in ion pair formation has been determined, thus providing estimates of the dication precursor state energies for forming ion pairs. These present measurements further highlight the lack of available data in the literature concerning the electronic states of the $C_2F_6^{2+}$ dication.

4.7 References

[1] L. G. Christophorou and J. K. Olthoff, *Fundamental Electron Interactions with Plasma Processing Gases*. (Plenum, New York, 2004).

[2] K. Furuya and Y. Hatano, Japanese Journal of Applied Physics Part 1-Regular Papers Short Notes & Review Papers **43** (1), 342 (2004).

[3] F. Gaboriau, G. Cartry, M. C. Peignon, and C. Cardinaud, Journal of Physics D-Applied Physics **39** (9), 1830 (2006).

[4] R. Jayaraman, R. T. McGrath, and G. A. Hebner, Journal of Vacuum Science & Technology a-Vacuum Surfaces and Films **17** (4), 1545 (1999).

[5] H. H. Park, K. H. Kwon, J. L. Lee, K. S. Suh, O. J. Kwon, K. I. Cho, and S. C. Park, Journal of Applied Physics **76** (8), 4596 (1994).

[6] P. Ho, J. E. Johannes, R. J. Buss, and E. Meeks, Journal of Vacuum Science & Technology a-an International Journal Devoted to Vacuum Surfaces and Films **19** (5), 2344 (2001).

[7] S. J. King and S. D. Price, J. Chem. Phys. **127**, 174307 (2007).

[8] S. J. King and S. D. Price, Int. J. Mass Spectrom. **272** (2-3), 154 (2008).

[9] *Electron Impact Ionization*, edited by T. D. Märk and G. H. Dunn (Springer, Vienna, 1985).

[10] *Database needs for modeling and simulation of plasma processing*. (National Research Council, National Academy Press, Washington, 1996).

[11] M. M. Bibby and G. Carter, Transactions of the Faraday Society **59**, 2455 (1963).

[12] R. A. Morris, A. A. Viggiano, and J. F. Paulson, J. Phys. Chem. **97** (23), 6208 (1993).

[13] C. Lifshitz and F. A. Long, J. Phys. Chem. **69** (11), 3746 (1965).

[14] I. G. Simm, C. J. Danby, and J. H. D. Eland, Journal of the Chemical Society-Chemical Communications (21), 832 (1973).

[15] I. G. Simm, C. J. Danby, and J. H. D. Eland, Int. J. Mass Spectrom. Ion Phys. **14** (3), 285 (1974).

Chapter 5 Electron Ionization of $SiCl_4$

5.1 Introduction

Silicon tetrachloride ($SiCl_4$) is widely used as a feed gas for the plasma etching of GaN[1], GaAs[2,3] and ZnO[4] substrates. In such plasmas the formation of both neutral $SiCl_x$ and ionic $SiCl_x^+$ fragments has been shown to play a significant role in the fast and smooth etching of the substrate layers. $SiCl_4$ is also employed as a precursor gas in the formation of nanocrystalline-Si[5,6], and Si-containing films[7], *via* plasma enhanced chemical vapour deposition (PECVD). The optimization and modelling of these plasma environments requires accurate and reliable data on the partial ionization cross-sections (PICS) for forming both the parent ion and the various ionic fragments resulting from single and multiple ionization.[8-11]

5.1.1 Dissociative Ionization of $SiCl_4$

In comparison with many other molecules of importance to plasma processing technologies[12], relatively few studies have been conducted to investigate the dissociative ionization of $SiCl_4$. The dissociation dynamics of the valence electronic states of $SiCl_4^+$ has been investigated by Tuckett and co-workers using photoelectron-photoion coincidence spectroscopy (PEPICO)[13], threshold-PEPICO spectroscopy[14,15], and *via* photoion-fluorescence and photoelectron-fluorescence coincidence techniques.[15] A summary of the results of these studies is shown in Table 4.I. Interestingly, the formation of $SiCl_2^+$ ions and $SiCl^+$ ions are observed only *via* the dissociation of excited electronic states lying ~2 eV and ~3 eV, respectively, above the corresponding thermodynamic thresholds for forming these ions. In addition, the non-radiative decay observed for the excited *D* electronic state may be characteristic of an isolated state, as has been observed in the valence electronic state manifold of $C_2F_6^+$ (Chapter 4).[15] Such observations are further evidence of nonstatistical dissociation processes occurring in the molecular ions of halogenated compounds.[16] Appearance energies (AE's) for the formation of singly-charged and doubly-charged ionic fragments of $SiCl_4$ have been measured following electron-impact ionization using a Nier type 60° mass spectrometer[17], and by photoionization mass spectrometry.[18]

Electronic State	Energy Range / eV	Dissociation Dynamics	Ionic Product(s)
X	11.5-12.5	Bound electronic state	$SiCl_4^+$
A ***B***	12.7-14.5	Decays leading exclusively to $SiCl_3^+$ + Cl formation. Repulsive states (not fully resolved in the TPEPICO spectra).	$SiCl_3^+$
C	~15.0-15.8	Decays radiatively. PIFCO measurements show fluorescence to the ground *X* state, yielding $SiCl_4^+$, or to the *A* state, forming $SiCl_3^+$.	$SiCl_4^+$: $SiCl_3^+$ (1:4)
D	~18.1-18.2	Vibrational structure observed in TPES spectra. Decays non-radiatively to form mainly $SiCl_2^+$. Perhaps an isolated state.	$SiCl_3^+$: $SiCl_2^+$ (1:4)
E	>20.1	Decays to form $SiCl^+$ product ions almost exclusively.	$SiCl^+$ (major)

Table 4.I Dissociation dynamics of the valence electronic states of $SiCl_4^+$ determined in previous studies.[13-15]

5.1.2 Partial Ionization Cross Sections of $SiCl_4$

The only previous determination of the PICS of $SiCl_4$ was reported by Basner *et al.*[19], who measured absolute PICS for the formation of positively charged fragments up to an ionizing energy of 900 eV, using electron-impact time-of-flight mass spectrometry. It is this lack of available data concerning the PICS of $SiCl_4$, in addition to the limited information relating to the dissociative multiple ionization of $SiCl_4$, which, in part, motivates this study.

In this study the electron ionization of $SiCl_4$ is investigated in the energy range 30-200 eV, using time-of-flight mass spectrometry coupled with a 2-D ion-coincidence technique. Relative PICS $\sigma_r[X^{m+}]$ are derived for the formation of fragment ions $SiCl_x^+$ (x=1-3), Si^+, Cl^+, Cl_2^+, $SiCl_x^{2+}$ (x=1-2), Si^{2+}, and Cl^{2+}, expressed relative to the formation of $SiCl_4^+$, as a function of ionizing electron energy. A comparison of this data with the recent PICS of Basner *et al.*[19] reveals a good overall agreement. Precursor-specific relative PICS values are also derived for the formation of these fragment ions $\sigma_n[X^{m+}]$, which, as explained in Section 3.3.4, quantify the contribution to the yield of an ion from single (n=1), double (n=2) and triple (n=3) ionization. The respective contributions of these precursor-specific relative PICS provide insight into the origin of a double-maximum structure observed recently in the PICS curves for the formation of $SiCl_3^+$ and $SiCl_2^+$ fragment ions.[19,20] The relative PICS data also includes the first quantitative measurements for the formation of Cl_2^+ following dissociative electron ionization of $SiCl_4$. The shape of precursor specific relative PICS curves for forming Cl_2^+ show a remarkable similarity to those for Cl^+, and reveal that the major pathways for forming such ions in this energy regime are *via* dissociative double ionization. In addition relative cross sections are derived for the formation of product ion pairs formed *via* the dissociation of the $SiCl_4^{2+}$ dication $\sigma_r[X^+ + Y^+]$.

5.1.3 The Silicon Tetrachloride Dication $SiCl_4^{2+}$

To date there have been very few studies to investigate the charge separating dissociations of the $SiCl_4^{2+}$ dication. Photoion-photion efficiency curves and ion pair branching ratios have been measured by Boo *et al.*[21], using photoion-photoion coincidence (PIPICO) spectroscopy in the photon energy range 38-133 eV. The photoion-photoion efficiency curves measured in this earlier work exhibit a broad structureless feature below 100 eV, assigned to non-resonant double ionization processes, while a series of prominent peaks above 100 eV are attributed to core electron Si(2p) excitations leading to dissociative double ionization. However, to date the energetics of the electronic states of the $SiCl_4^{2+}$ dication remain unknown. In this work the peaks observed in the 2-D ion coincidence spectra are interpreted to yield information on the dissociation dynamics and energetics of the $SiCl_4^{2+}$ dication. By simulations of the kinetic energy release (KER) involved in ion pair formation, estimates are derived of the precursor state energy of the $SiCl_4^{2+}$ dication which dissociates to form the ion pair of interest. These measurements represent the first estimates of the electronic state energies of $SiCl_4^{2+}$.

5.2 Experimental Procedures

All experiments in this study were performed using a time-of-flight mass spectrometer (TOFMS) of Wiley-McLaren design[22] as described in detail in Section 2.3. $SiCl_4$ used in this work was a commercial sample (>99%) which was thoroughly degassed prior to use *via* a sequence of freezing, pumping and thawing cycles. The sample was then held at a temperature of 273 K using a water-ice bath, and the vapour above the sample allowed to pass through the apparatus for a period of 20 min prior to each experiment. Firstly, this procedure was found to greatly reduce to the number of ions emanating from background gases, such as N_2, O_2 and H_2O, appearing in our mass spectra. Secondly, by preconditioning the gas inlet system in this way any potential problems that may be caused by the hydrolysis of $SiCl_4$ were eliminated, as evidenced by the extremely minor contributions of HCl^+ ions, $SiCl_{4-x}(OH)_x^+$ ions (x=1-4), and $H^+ + Cl^+$ ion pairs, to the mass spectra. The corrosive nature of $SiCl_4$ and its various dissociation products could give rise to a gradual decrease of the MCP performance, as has been observed in a recent study of BCl_3.[23] However, measurements of the pulse height distribution from the MCP detector were found to remain approximately constant throughout each experimental run, showing that MCP degradation was not a problem in this study.

The operating conditions of the experiment involve low electron flux and low target gas pressures, typically $< 10^{-6}$ Torr, ensuring that on average much less than one ionization event occurs per pulse of ionizing electrons. This methodology greatly reduces the number of 'false coincidences' that contribute to the ion-coincidence mass spectra, as has been discussed previously. The voltage conditions used in this study (Table 2.I) permit the efficient collection of ions formed with up to 11 eV of translational kinetic energy.

5.3 Data Analysis

5.3.1 Singles Mass Spectra

A representative singles mass spectrum of $SiCl_4$ recorded at an ionizing electron energy of 200 eV is shown in Figure 4.1. This figure shows the various ion peaks observed in the singles mass spectra, including the parent monocation $SiCl_4^+$ and a number of ionic fragments formed by the dissociation of $SiCl_4^{m+}$. The intensities of individual ion peaks, $I_1[X^+]$ for monocations and $I_2[X^+]$ for dications, appearing in the singles spectrum, are extracted using the analysis procedure described in Section 3.2.1. When extracting these intensities, a small correction was made to the intensity of Si^{2+}, Si^+ and $SiCl^{2+}$ ions measured in each mass spectrum, to account for minor contributions to these ion peaks from the ionization of residual air in our vacuum chamber. Specifically, O_2^+ ions contribute to the intensity of the $SiCl^{2+}$ ion peak, while N_2^+ and N^+ ions contribute to the Si^+ and Si^{2+} ion peaks, respectively. These minor contributions to the mass spectra are subtracted, using the procedure outlined in Section 3.2.1.2, by normalization to the O^+ peak intensity. Owing to the poorer mass resolution of the apparatus at higher ion mass, some overlap is observed between the isotope peaks of the various ions. For these ions the ion counts are summed over a mass range to include the respective isotopes of Si and Cl: ^{28}Si (92.3%), ^{29}Si (4.7%) and ^{30}Si (3.0%); ^{35}Cl (75.8%), ^{37}Cl (24.2%). In the case of $SiCl^+$ and $SiCl_3^{2+}$ fragments, the singles spectrum is not sufficiently resolved to extract the individual contributions of these ions. This overlap is caused mainly by the large intensity of the $SiCl^+$ ion peak relative to the low intensity of

$SiCl_3^{2+}$ ions. Specifically, the minor contributions to the $SiCl^+$ peak intensity from $^{29}Si^{37}Cl^+$ (*m/Z*=66) (1.1%) and $^{30}Si^{37}Cl$ (*m/Z*=67) (0.7%), cannot be distinguished from the major isotopes of $SiCl_3^{2+}$ (*m/Z*=66.5,67.5,68.5,69.5). Therefore, in this work combined cross-sections for forming these ions are reported. In addition, some overlap is observed between the Cl^{2+} (*m/Z*=17.5,18.5) and H_2O^+ (*m/Z*=18) peaks, and also the Cl_2^+ (*m/Z*=70,72,74) and $SiCl^+/SiCl_3^{2+}$ peaks. To more accurately extract the intensities of Cl^{2+} and Cl_2^+ ions appearing in each singles mass spectrum, a peak fitting procedure was used, as described in Section 3.2.1.1.

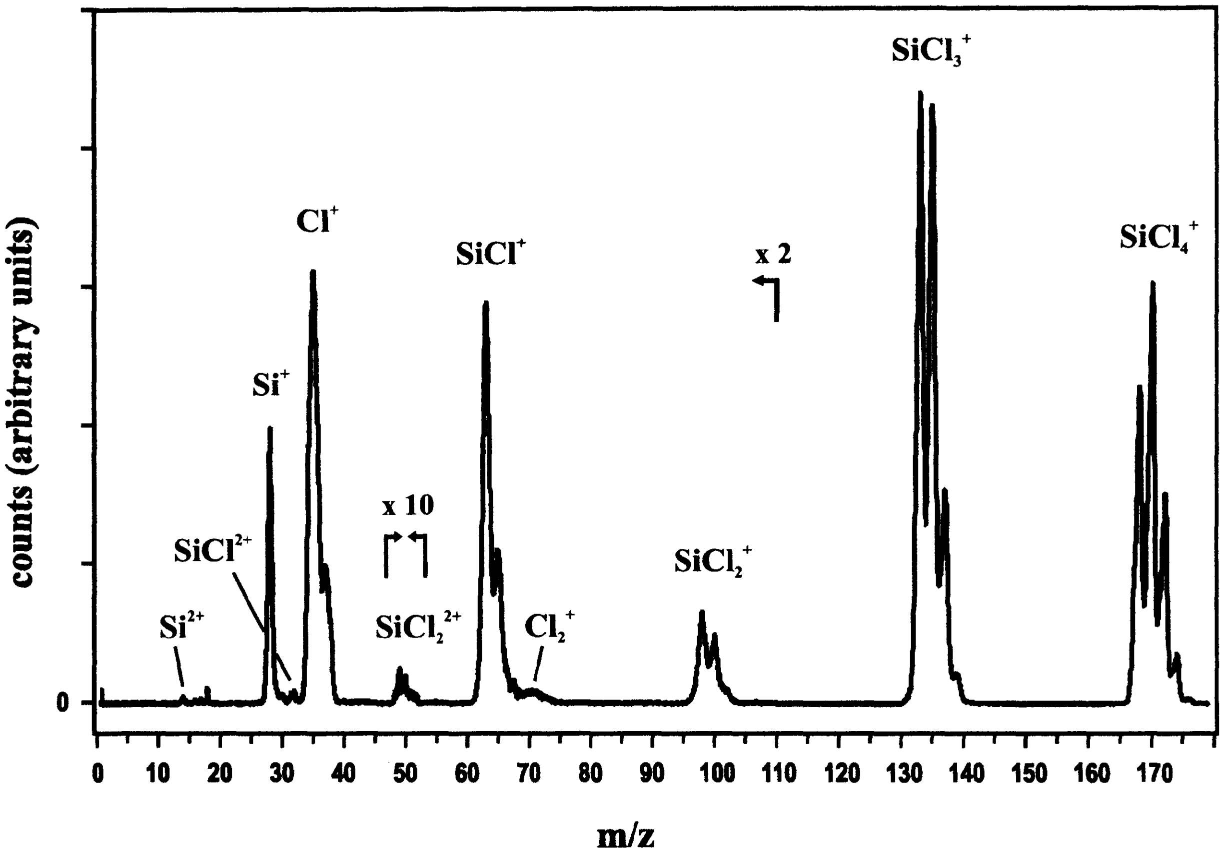

Figure 4.1 A characteristic (singles) mass spectrum of $SiCl_4$ following electron impact ionization at 200 eV.

5.3.2 2-D Ion Coincidence Spectra

A representative pairs mass spectrum of $SiCl_4$ recorded at an ionizing electron energy of 200 eV is shown in Figure 4.2. At this energy 7 monocation pair peaks and a further 3 dication-monocation pair peaks are observed. The intensities of the various ion pair peaks are then extracted, using the procedure described in Section 3.2.2, to yield the number of individual ion pairs $P[X^+ + Y^+]$, and also the overall contribution of a fragment ion to the pairs spectrum $P_n[X^+]$. In this work a distinction is made between the ion counts in pairs which must be formed *via* dissociative triple ionization of the $SiCl_4^{3+}$ trication $P_3[X^+]$, for example Cl^+ + $SiCl_2^{2+}$, and the ion counts in the other peaks in the pairs spectrum which may contain contributions from both dissociative double and triple ionization $P_2[X^+]$, such as $SiCl^+$ + Cl^+. The number of false coincidences is evaluated manually for each peak using an ion-autocorrelation function (Section 3.2.2.1), typically 1-2% of the raw peak intensity at higher ionizing electron energy, which is then subtracted. In the experiment no ion pairs are recorded if the second ion arrives at the detector within 32 ns of the first ion, due to the 'deadtime' of the discrimination circuitry. Such deadtime losses significantly affect the number of counts recorded in the Cl^+ + Cl^+ peak in the pairs spectra. To estimate the number of ions lost, a separate one-dimensional (t_2-t_1) spectrum is constructed from the Cl^+ + Cl^+ coincidence data which is then appropriately extrapolated to the limit t_1=t_2, using simple geometry, to correct for the losses (Section 3.2.2.3).

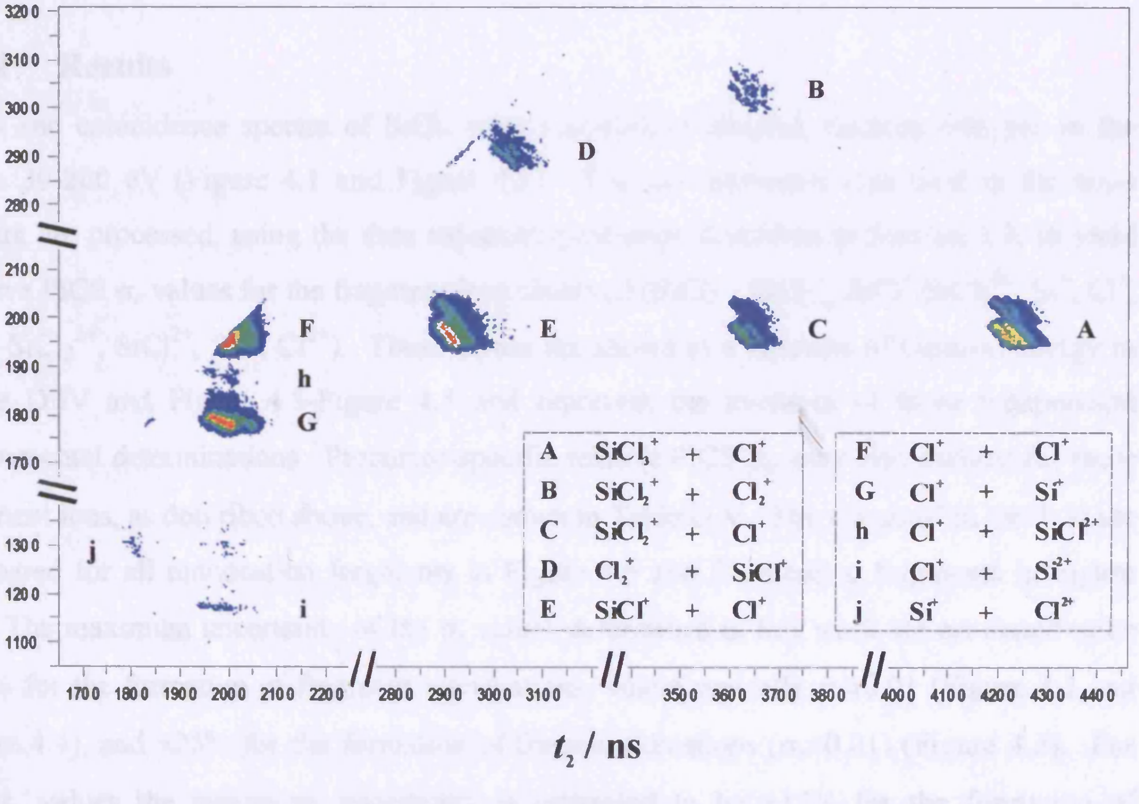

Figure 4.2 Representative 'pairs' mass spectrum of $SiCl_4$ recorded at 200 eV showing observed ion pairs formed *via* charge-separating dissociation of $SiCl_4^{2+}$ and $SiCl_4^{3+}$.

Ion triples are processed by specifying a time-of-flight range for a particular ion, for example (Si^+), and then extracting all ion triples containing at least one ion whose arrival time t_1 lies within this specified range. Once extracted, the respective flight times of the two remaining ions, for example ($Cl^+ + Cl^+$), forming an ion triple are plotted as a 2-D histogram (t_2 *vs.* t_3). The contribution of a fragment ion $T[X^+]$ is then obtained from the number of counts in the $Cl^+ + Cl^+$ peak, after applying (where necessary) a small geometric correction to account for losses due to the 'deadtime', as described above. False triple coincidences that contribute to the intensity of each triples peak are subtracted using the procedure outlined in Section 3.2.3.1. In this work it has not been possible to perform measurements on $Cl^+ + Cl^+ + Cl^+$ ion triple formation due to the added complexity of twofold losses due to the experimental 'deadtime'. Contributions to the ion coincidence spectra from dissociative quadruple ionization are neglected, owing to the low cross sections determined for triple ionization in the energy regime of this work, as described below.

5.4 Relative Partial Ionization Cross Sections

5.4.1 Results

Mass and coincidence spectra of $SiCl_4$ were recorded at ionizing electron energies in the range 30-200 eV (Figure 4.1 and Figure 4.2). The ion intensities measured in the mass spectra are processed, using the data reduction procedure described in Section 3.3, to yield relative PICS σ_r values for the fragment ions observed ($SiCl_3^+$, $SiCl_2^+$, $SiCl^+/SiCl_3^{2+}$, Si^+, Cl^+, Cl_2^+, $SiCl_2^{2+}$, $SiCl^{2+}$, Si^{2+}, Cl^{2+}). These values are shown as a function of electron energy in Table D.IV and Figure 4.3-Figure 4.5 and represent the averages of three independent experimental determinations. Precursor-specific relative PICS σ_n were also derived for these fragment ions, as described above, and are shown in Table D.V. The values of σ_n (n=1-3) are compared for all monocation fragments in Figure 4.6 and for dication fragments in Figure 4.7. The maximum uncertainty of the σ_r values determined in this work are estimated to be ±10% for the formation of fragment monocations, where typically σ_r>0.01 (Figure 4.3 and Figure 4.4), and ±25% for the formation of fragment dications (σ_r<0.01) (Figure 4.5). For the σ_n values the maximum uncertainty is estimated to be ±15% for the formation of monocation fragments, where typically σ_n>0.01 (Figure 4.6), and ±30% for the formation of fragment dications (σ_n<0.01) (Figure 4.7). These estimates of the uncertainty have been derived using the average statistical error (±2σ) of previous cross-section determinations performed using this apparatus[10,11] (see also Chapters 6, 8). The overall contributions from single, double and triple ionization, as a percentage of the total ion yield at each ionizing electron energy, are summarized in Table D.VI and Figure 4.8. In the singles mass spectra no evidence is observed for the formation of metastable $SiCl_4^{2+}$ ions and an upper limit of 0.0002 is assigned to the $\sigma_r[SiCl_4^{2+}]$ values. Measurements of the ion detection efficiency (f_i) for the experiments, as detailed in Section 3.3.3, resulted in a value of $f_i = 0.20 \pm 0.01$.

In the pairs coincidence spectra 7 monocation pairs are observed: $SiCl_x^+ + Cl^+$ (x=1-3), $Si^+ + Cl^+$, $Cl^+ + Cl^+$ and $SiCl_x^+ + Cl_2^+$ (x=1,2). In addition, at ionizing energies above 65 eV a further 3 ion pairs and 4 ion triples from the dissociation of $SiCl_4^{3+}$ are observed in the ion coincidence mass spectra: $Cl^+ + SiCl^{2+}$, $Cl^+ + Si^{2+}$, $Si^+ + Cl^{2+}$, $SiCl_x^+ + Cl^+ + Cl^+$ (x=1,2), $Si^+ + Cl^+ + Cl^+$, $SiCl^+ + Cl_2^+ + Cl^+$. Again an upper limit of 0.0002 is placed on the relative cross section for all possible ion pairs and ion triples not observed in the coincidence mass spectra recorded in this work. Values of σ_r for the formation of monocation pairs formed by $SiCl_4^{2+}$ dication dissociation are shown in Table D.XVII and Figure 4.9.

5.4.2 Discussion

5.4.2.1 Relative PICS (σ_r) Values

The values of σ_r determined for the formation of monocation fragments ($SiCl_3^+$, $SiCl_2^+$, $SiCl^+$, Si^+, Cl^+) are shown in Figure 4.3 and Figure 4.4 respectively. In these Figures a comparison is made between these σ_r values and the values derived from the data of Basner *et al.*[19] Across the entire energy range a good agreement is found between the two data sets for the formation of these monocation fragments. Only for the formation of Si^+ is there a small disagreement between the σ_r values of Basner *et al.*[19] and the present σ_r values, which are up to 25% lower, although both data sets agree within experimental error limits. In Figure 4.4 are shown, for the first time, measurements for the formation of Cl_2^+, a minor ionic fragment following dissociative electron ionization of $SiCl_4$. It is interesting to note here that both the shape and the magnitude of the $\sigma_r[Cl_2^+]$ cross section curve closely matches that for $SiCl_3^{2+}$ formation derived from the data of Basner *et al.*[19] (not shown in Figure 4.4 for clarity). While this observation may be purely coincidental, one potential explanation for this

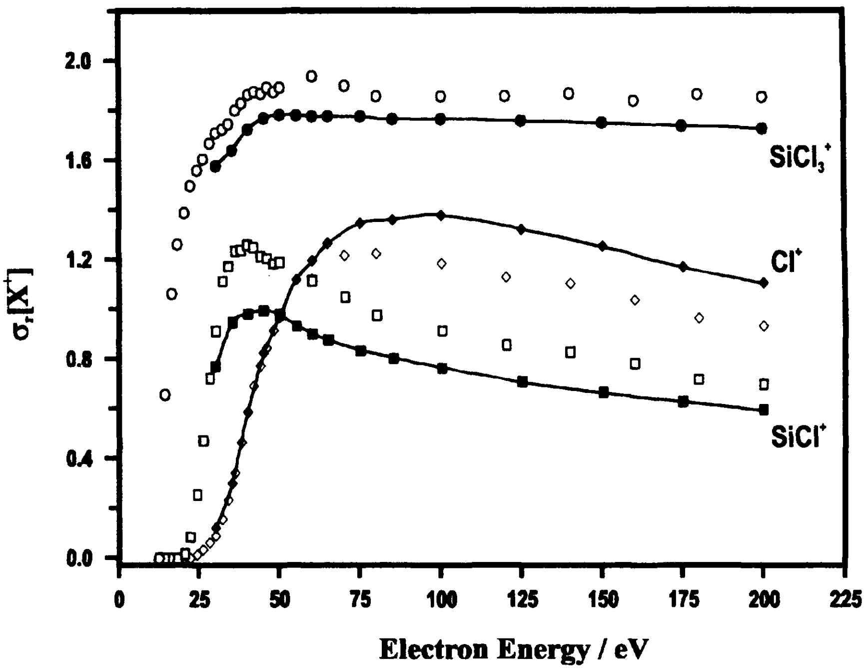

Figure 4.3 Relative PICS $\sigma_r[X^+]$ for forming monocation fragments, $SiCl_3^+$ (●), Cl^+ (♦), $SiCl^+$ (■), following electron ionization of $SiCl_4$. The corresponding relative PICS extracted from the data of Basner *et al.*[19] (open symbols) are also shown.

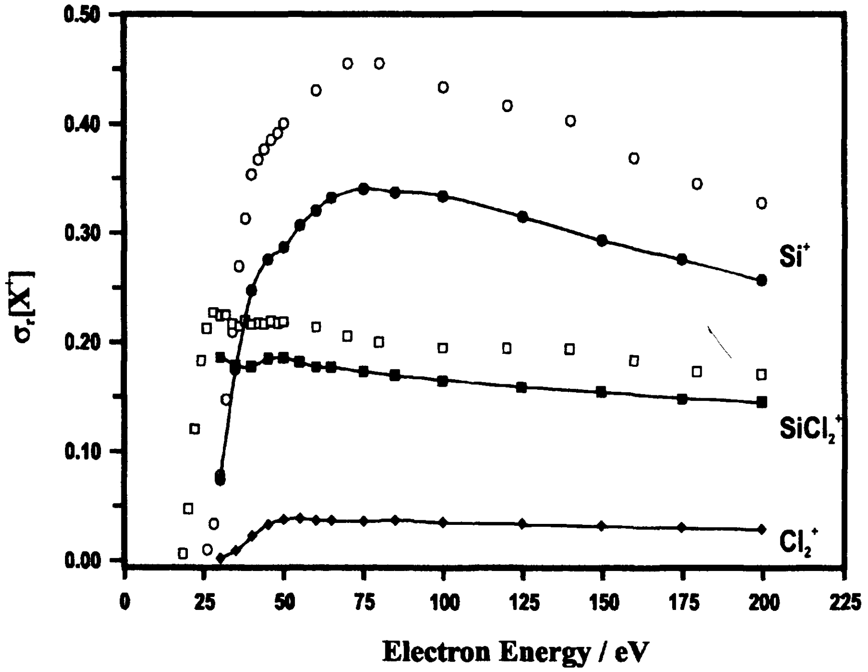

Figure 4.4 Relative PICS $\sigma_r[X^+]$ for forming monocation fragments, Si^+ (●), $SiCl_2^+$ (■), Cl_2^+ (♦),following electron ionization of $SiCl_4$. The corresponding relative PICS extracted from the data of Basner *et al.*[19] (open symbols) are also shown.

similarity may be due to problems in assigning the contributions of Cl_2^+ ions and $SiCl_3^{2+}$ ions in this earlier study. As described below, a dominant proportion of the Cl_2^+ ions detected are formed as ion pairs *via* dissociative double ionization. Thus, in the pairs mass spectra (Figure 4.2) Cl_2^+ + $SiCl_x^+$ (x=1,2) ion pairs are assigned unambiguously, as for ion pairs comprising $SiCl_3^{2+}$ ions, the only possible (real) correlated ion partner is Cl^+.

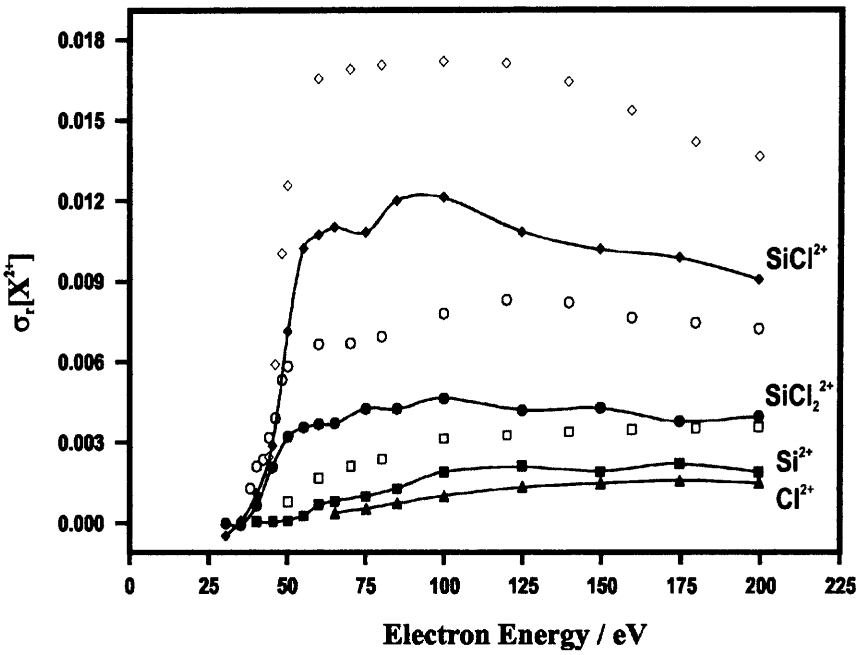

Figure 4.5 Relative PICS $\sigma_r[X^{2+}]$ for forming dication fragments, $SiCl^{2+}$ (♦), $SiCl_2^{2+}$ (●), Si^{2+} (■), Cl^{2+} (▲), following electron ionization of $SiCl_4$. The corresponding relative PICS extracted from the data of Basner *et al.*[19] (open symbols) are also shown.

In Figure 4.5 the values of σ_r for the formation of dication fragments ($SiCl_2^{2+}$, $SiCl^{2+}$, Si^{2+}) are compared to the corresponding values derived from the data of Basner *et al.*[19] Such a comparison reveals that the present σ_r values for dication fragment formation are systematically lower, but, do agree within combined error limits. In addition relative cross sections for the formation of Cl^{2+} ions have been determined, which, as the $\sigma_r[Cl^{2+}]$ values show, is a very minor ionic fragment to be formed within the energy regime of this work. Despite this, the data suggest that the threshold for Cl^{2+} formation lies below 65 eV, significantly lower than previous photoionization measurements of the appearance energy reported by Cooper *et al.*[18] (190±20 eV) As described above, no evidence is observed for the formation of metastable $SiCl_4^{2+}$ ions and an upper limit of 0.0002 is placed on the values of

$\sigma_r[SiCl_4^{2+}]$. This upper limit is an order of magnitude lower than the corresponding value of $\sigma_r[SiCl_4^{2+}]$ derived from the data of Basner *et al.*[19] at 200 eV. The origin of this discrepancy is not readily apparent.

5.4.2.2 Precursor-Specific Relative PICS

In Figure 4.6 a comparison is made between the relative precursor-specific PICS σ_n values for the formation of monocation fragments. In respect of the relative contributions to the yield of each ion from dissociative single (n=1) and double (n=2) ionization, respectively, one may place these monocation fragments into three distinct groups: $SiCl_3^+$ and $SiCl^+$, where contributions from σ_1 are greater than from σ_2 across the ionizing energy range; $SiCl_2^+$ and Si^+, where values of σ_1 and σ_2 are almost identical at an ionizing energy above 75 eV; Cl^+ and Cl_2^+, where contributions to the ion yield are dominated by dissociative double ionization above 40-45 eV. By contrast, a comparison of the σ_1 cross section curves for these ion fragments reveals a different trend. For $SiCl_3^+$ formation the σ_1 curve exhibits a small low-energy maximum close to 35 eV, above which $\sigma_1[SiCl_3^+]$ remains almost constant. For the formation of $SiCl_2^+$ and $SiCl^+$ ionic fragments σ_1 values exhibit a pronounced narrow low-energy maximum at 30 eV and 35 eV respectively, before decreasing sharply towards higher ionizing electron energy. The values of σ_1 for Si^+, Cl^+ and Cl_2^+ ionic fragments also show a pronounced maximum, this time close to 45 eV, before decaying rapidly towards higher ionizing energy. The shapes of the relative cross section curves for σ_2 values are similar for all the monocation fragments shown in Figure 4.6. As described below, these observations help to explain many of the features of the absolute cross section curves reported in the recent electron ionization studies of $SiCl_4$ and $TiCl_4$ by Basner *et al.*[19,20]

In the recent $SiCl_4$ absolute PICS measurements of Basner *et al.*[19], a 'double maximum' structure was observed for the cross section curves of $SiCl_4^+$, $SiCl_3^+$ and $SiCl_2^+$ ions. For these ions, the cross section curves are characterised by a narrow low-energy maximum close to 30 eV, followed by a slight decline and then a second broad maximum at higher ionizing energy. It is noted here that such a double maximum structure is not as readily apparent in the present σ_r values, where the relative shapes of the fragment ion and $SiCl_4^+$ ion curves are, to an extent, self-cancelling. Basner *et al.*[19,20] proposed that the narrow low energy maxima of the cross section curves for these ions are due mainly to indirect ionization channels, while the second broad maxima at higher energies are due to direct ionization processes. The σ_1

values for these ions provide additional evidence in support of this explanation of the low-energy maxima. Specifically, for the formation of $SiCl_2^+$ ions, the shape of the σ_1 curve is characteristic of that predicted for a resonant-type ionization channel centred at around 30 eV, with a much smaller contribution from direct ionization processes at higher energy.[24] As is shown by the σ_2 values, the origin of the second broad maximum in the $SiCl_2^+$ cross section data of Basner *et al.*[19] is due mainly to contributions to the $SiCl_2^+$ ion yield from dissociative double ionization.

For $SiCl^+$ formation, the absolute PICS values of Basner *et al.*[19] similarly reveal a pronounced low energy maximum at around 35 eV. Again, the shape of the σ_1 curve measured in this work for this ion (Figure 4.6) is indicative of a dominant indirect ionization process that is resonant close to an energy of 35 eV.[24] The absence of a second maximum at a higher ionizing energy in the data of Basner *et al.*[19], can be explained by the dominant contribution from dissociative single ionization over double ionization within this energy regime, as described above. That is, the rapid decrease in σ_1 values at higher ionizing energy outweighs the increasing contribution from σ_2 and σ_3 values, thus giving rise to the monotonic decay in the PICS values of Basner *et al.*[19] for $SiCl^+$ formation.

Concerning the formation of Si^+ ionic fragments, both the present $\sigma_r[Si^+]$ values (Figure 4.4) and the absolute PICS data of Basner *et al.*[19] exhibit a single broad maximum at approximately 75 eV. However, a closer inspection of both data sets reveal a small 'shoulder' in the respective cross section curves at around 45 eV, coinciding with the narrow maximum that is observed in the σ_1 values centred at 45 eV (Figure 4.6). Thus one may conclude that indirect ionization processes also contribute significantly to the Si^+ ion yield from single ionization, albeit at a slightly higher ionizing energy than for $SiCl_x^+$ formation (x=1-3). This displacement of the peak in σ_1 values, coupled with a rapidly increasing contribution from dissociative double ionization (σ_2) above 45 eV, provides an alternative description of the observed structure of the Si^+ cross section curve than has been reported previously.[19,20] For Cl^+ and Cl_2^+ formation, contributions to the yield of these ions are dominated by dissociative double ionization (Figure 4.6), giving rise to a single broad maximum in the corresponding σ_r cross section curves (Figure 4.3 and Figure 4.4). In Figure 4.7 it is shown that contributions to the yields of the fragment dications $SiCl^{2+}$, Si^{2+} and Cl^{2+} are from both double and triple ionization.

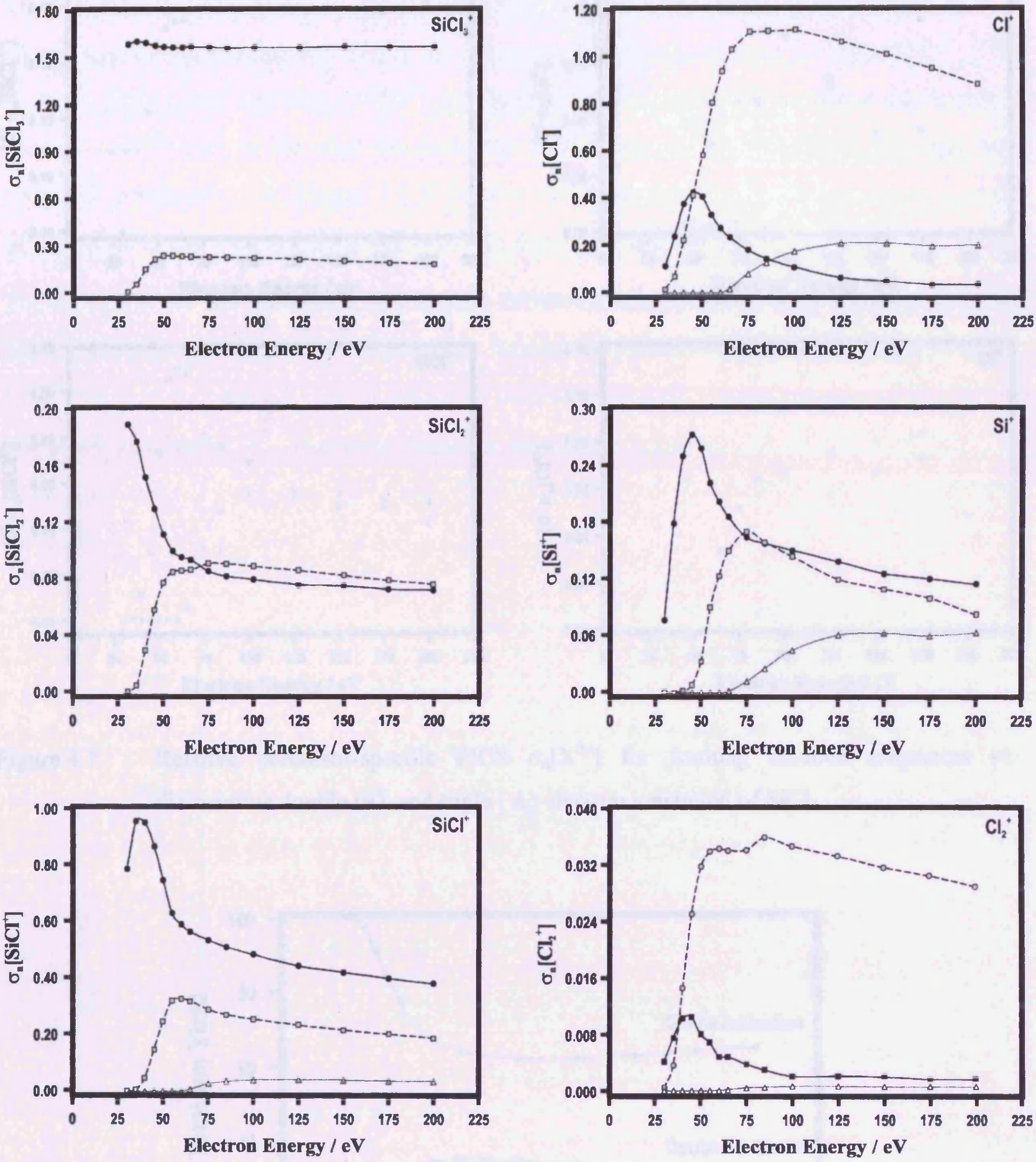

Figure 4.6 Relative precursor-specific PICS $\sigma_n[X^+]$ for forming monocation fragments *via* dissociative single (—●—), double (--■--) and triple (··▲··) electron ionization of $SiCl_4$.

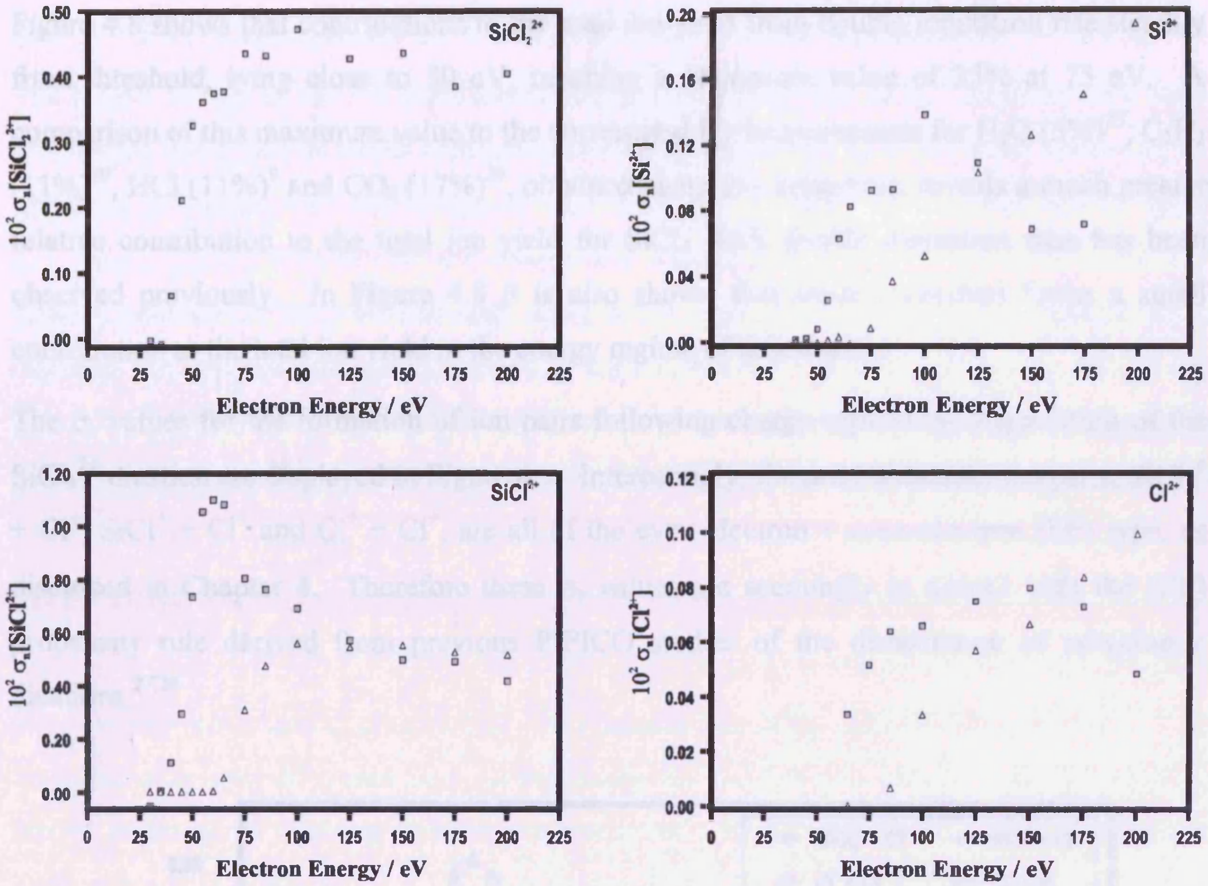

Figure 4.7 Relative precursor-specific PICS $\sigma_n[X^{2+}]$ for forming dication fragments *via* dissociative double (■), and triple (▲) electron ionization of $SiCl_4$.

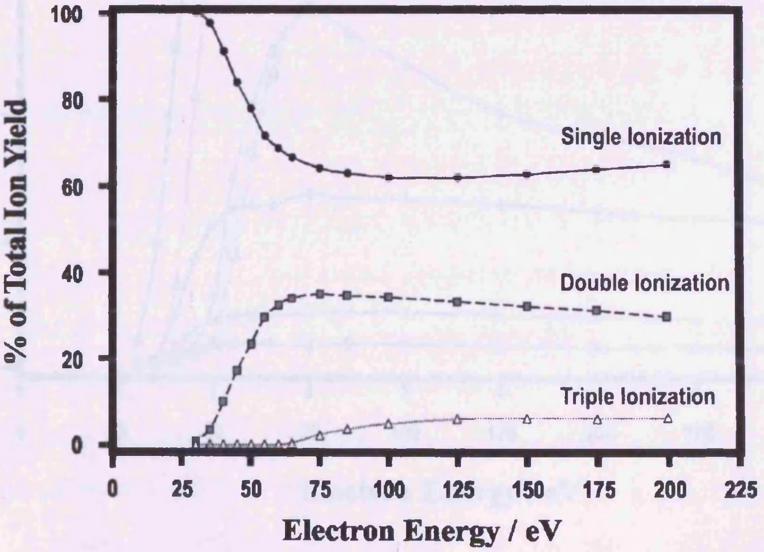

Figure 4.8 Contributions to the total ion yield from single, double, and triple ionization, following electron ionization of $SiCl_4$.

Figure 4.8 shows that contributions to the total ion yield from double ionization rise steadily from threshold, lying close to 30 eV, reaching a maximum value of 35% at 75 eV. A comparison of this maximum value to the corresponding measurements for H_2O (5%)[25], C_2H_2 (11%)[10], HCl (11%)[9] and CO_2 (17%)[26], obtained using this apparatus, reveals a much greater relative contribution to the total ion yield for $SiCl_4$ from double ionization than has been observed previously. In Figure 4.8 it is also shown that triple ionization forms a small contribution to the total ion yield in the energy regime of this work.

The σ_r values for the formation of ion pairs following charge-separating dissociation of the $SiCl_4^{2+}$ dication are displayed in Figure 4.9. Interestingly, the most abundant ion pairs, $SiCl_3^+ + Cl^+$, $SiCl^+ + Cl^+$ and $Cl^+ + Cl^+$, are all of the even-electron + even-electron (EE) type, as discussed in Chapter 4. Therefore these σ_r values are seemingly in accord with the (EE) propensity rule derived from previous PIPICO studies of the dissociation of polyatomic dications.[27,28]

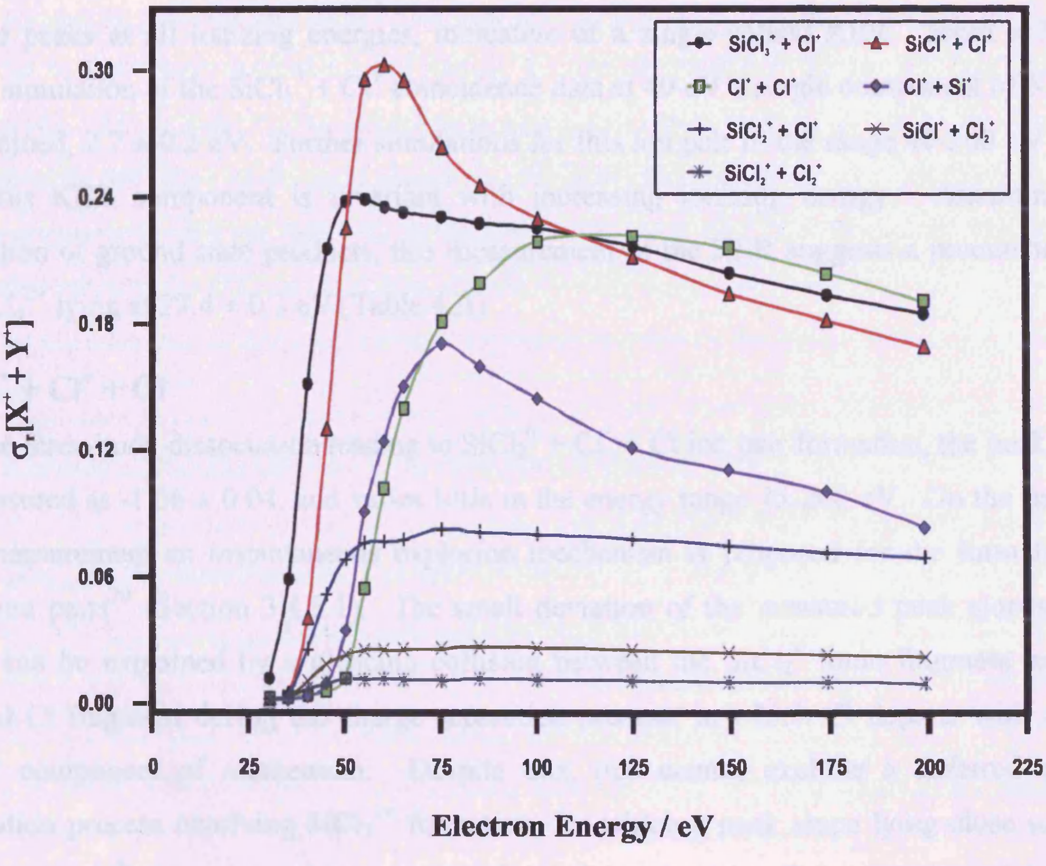

Figure 4.9 Relative PICS $\sigma_r[X^+ + Y^+]$ for forming monocation-monocation pairs following electron ionization of $SiCl_4$.

5.5 The Energetics of Dissociative Double Ionization of $SiCl_4$

The kinetic energy of the ion pairs formed by dissociation of the $SiCl_4^{2+}$ dication have been determined using Monte Carlo simulations of the peaks observed in the pairs spectrum, as described in Section 3.5. The results of these KER determinations are summarised in Table 4.II, which, in combination with the dissociation limits derived from values in the literature, provide estimates of the precursor-state energies for forming ion pairs. These measurements represent the first estimates of the electronic state energies of the $SiCl_4^{2+}$ dication. For all ion pairs simulations were performed on a single isotope peak (of lowest combined mass) and all KER components were modelled using a Gaussian distribution with a width of 1.2 eV at FWHM.

$SiCl_3^+ + Cl^+$

For the formation of $SiCl_3^+ + Cl^+$ ion pairs, the slope of peaks in the pairs spectra are all equal to -1, within error limits, as expected for a simple two-body dissociation process.[29] The corresponding time-difference (t_2-t_1) distributions for this ion pair exhibit well-defined flat-topped peaks at all ionizing energies, indicative of a single-valued KER. From a Monte Carlo simulation of the $SiCl_3^+ + Cl^+$ coincidence data at 40 eV a single component of KER is determined, 2.7 ± 0.2 eV. Further simulations for this ion pair in the range 40-200 eV show that this KER component is invariant with increasing ionizing energy. Assuming the formation of ground state products, this measurement of the KER suggests a precursor state of $SiCl_4^{2+}$ lying at 27.4 ± 0.3 eV (Table 4.II).

$SiCl_2^+ + Cl^+ + Cl$

For the three-body dissociation leading to $SiCl_2^+ + Cl^+ + Cl$ ion pair formation, the peak slope is measured as -1.06 ± 0.04, and varies little in the energy range 45-200 eV. On the basis of this measurement an instantaneous explosion mechanism is proposed for the formation of such ion pairs[29] (Section 3.4.3.1). The small deviation of the measured peak slopes from unity can be explained by a glancing collision between the $SiCl_2^+$ ionic fragment and the neutral Cl fragment during the charge separation process, in which Cl departs with only a minor component of momentum. Despite this, one cannot exclude a deferred charge separation process involving $SiCl_3^{2+}$ formation, for which a peak slope lying close to -1 is also expected.[29] It is noted, however, that for both mechanisms the proportion of the total KER partitioned to the neutral Cl fragment is small and, hence, can be ignored. From Monte Carlo simulations of the $SiCl_2^+ + Cl^+$ coincidence data, a single component of KER is determined, 2.6 ± 0.2 eV, that is invariant within the ionizing energy range 45-200 eV. Assuming the formation of ground state products, this measurement of the KER suggests a precursor state of $SiCl_4^{2+}$ lying at 33.6 ± 0.3 eV. (Table 4.II)

$SiCl^+ + Cl^+ + (2Cl)$

For $SiCl^+ + Cl^+$ ions pairs formed *via* dissociative double ionization the slope of the linear regression is -1.11 ± 0.04. This value lies between the limiting values for an unobstructed instantaneous Coulomb explosion (-1) and for a sequential process forming $SiCl^+$ *via* the secondary decay of $SiCl_2^+$ or $SiCl_3^+$ ions (-1.56 and -2.11) respectively[29] (Section 3.4.3). The peak slope data are consistent with an instantaneous explosion mechanism for forming $SiCl^+ + Cl^+$ ion pairs, involving a glancing collision between $SiCl^+$ and the neutral fragment(s) formed. One notes that the apparatus is unable to detect neutral fragments and therefore the products of this dissociation reaction could include either Cl_2 or 2Cl (Table 4.II). Analysis of the individual TOF distributions for these ions comprising such ion pairs shows that Cl^+ is formed with a single-valued momentum distributed isotropically over all angles, as characterised by a flat-topped peak[29] (Section 2.2.4). The corresponding TOF distribution for $SiCl^+$ is visibly more rounded, and serves as further evidence of a glancing collision mechanism. To account for the reduction in correlated momentum of the $SiCl^+$ fragment, as quantified by the value of the peak slope, an 'effective' ion precursor with m/Z=70 is used in the simulations for this ion pair. As described in Section 4.5.1.3, the use of an effective ion precursor mass in the KER simulations account for the partitioning of the total KER among the detected ions and undetected neutral fragments formed in the dissociation of the $SiCl_4^{2+}$ dication.

From a Monte Carlo simulation of the coincidence data for this ion pair at 40 eV a single component of KER is determined, 2.6 ± 0.2 eV. The value of this KER component increases very slowly in the ionizing energy range 50-200 eV, to a maximum of 3.2 ± 0.2 eV. This gradual increase in values of the KER is most likely due to an increasing contribution from $SiCl^+ + Cl^+$ ion pairs from dissociative triple ionization with increasing electron energy. In Table 4.II the two possible dissociation limits for this reaction are shown, $SiCl^+ + Cl^+ + Cl_2$ and $SiCl^+ + Cl^+ + 2Cl$, which, in combination with the KER determined at 40 eV, suggest a $SiCl_4^{2+}$ precursor state lying at 33.1 ± 0.4 eV and 35.6 ± 0.4 eV, respectively.

$Si^+ + Cl^+ + (3Cl)$

In the reaction producing $Si^+ + Cl^+$ ion pairs the peak slope is measured as -0.54 ± 0.05 at 50 eV, decreasing slowly with increasing ionizing energy, -0.42 ± 0.04 (100 eV) and -0.40 ± 0.04 (200 eV). These values are consistent with the limiting value for a sequential dissociation mechanism (Section 3.4.3.2) involving the secondary decay of $SiCl^+$ to form Si^+ (-0.44).[29] Alternatively, on the basis of the measurements of the peak slope listed above, an instantaneous dissociation mechanism may be proposed involving a head-on collision between the Si^+ product ion and a neutral Cl fragment. Once again, the identities of the neutral fragments formed in this reaction are unknown and may consist of either Cl_2 + Cl or 3Cl fragments (Table 4.II). Interestingly, the TOF distribution for Si^+ ions comprising $Si^+ + Cl^+$ ion pairs is Gaussian-shaped, whereas that for Cl^+ is essentially square. In addition, the width of the time difference (t_2-t_1) distribution for this ion pair is narrower than the combined widths of the individual ion TOF distributions, suggesting a small but measureable deviation from linearity for this reaction.[29]

From a Monte Carlo simulation of the coincidence data for this ion pair at 50 eV a single component of KER is determined, 4.3 ± 0.3 eV. This value represents a lower limit of the total KER involved in $Si^+ + Cl^+$ ion pair formation. Assuming the formation of ground state products, the two possible dissociation limits for this reaction, $Si^+ + Cl^+ + Cl_2 + Cl$ and $Si^+ + Cl^+ + 3Cl$, in combination with the KER measurement, suggest a precursor state of $SiCl_4^{2+}$ lying at 39.5 ± 0.4 eV and 42.0 ± 0.4 eV, respectively (Table 4.II).

$SiCl_2^+ + Cl_2^+$

All coincidence peaks for the formation of $SiCl_2^+ + Cl_2^+$ ion pairs have a slope of -1, as predicted for a simple two-body dissociation process.[29] From simulations of the coincidence data for this ion pair a single KER component is determined that is invariant with ionizing electron energy, 2.7 ± 0.3 eV. Assuming the formation of ground state products, this KER measurement suggests a precursor state energy of $SiCl_4^{2+}$ lying at 29.7 ± 0.4 eV (Table 4.II).

$SiCl^+ + Cl_2^+ + Cl$

In the reaction producing $SiCl^+ + Cl_2^+$ ion pairs the slope of the linear regression is -1.01 ± 0.04. This value of the peak slope suggests that such ion pairs may be formed by either an unobstructed instantaneous explosion, or a deferred charge separation involving $SiCl_3^{2+}$ formation[29] (Section 3.4.3). From the coincidence data for $SiCl^+ + Cl_2^+$ ion pairs a single KER component is determined, 3.0 ± 0.3 eV, that is almost constant in the ionizing energy range 45-200 eV. This kinetic energy release, assuming the formation of ground state products, suggests a dissociative precursor state lying at 31.0 ± 0.4 eV (Table 4.II). This precursor state energy lies at the lower limit of the appearance potential (AP) for $SiCl_3^{2+}$ formation measured by Cooper *et al.*[18], 31.9 ± 0.5 eV, and hence an instantaneous mechanism would appear the most likely mechanism for the formation of this ion pair.

$Cl^+ + Cl^+$ + ***neutrals***

In the present experimental setup measurements of the peak slope and KER determinations are difficult to perform for monocation pairs of identical mass, due to the deadtime of the discrimination circuitry (Section 2.4.2.2). Because of this restriction it has not been possible to identify the mechanism for $Cl^+ + Cl^+$ formation in this work.

Ion Pair	Neutral Products	KER / eV	Dissociation Limit[a] / eV	Precursor-State Energy / eV
$SiCl_3^+ + Cl^+$	none	2.7	24.70[b]	27.4 ± 0.3
$SiCl_2^+ + Cl^+$	Cl	2.6	30.95	33.6 ± 0.3
$SiCl^+ + Cl^+$	2Cl	2.6	32.99[c]	35.6 ± 0.4
	Cl_2		30.48[c]	33.1 ± 0.4
$Si^+ + Cl^+$	3Cl	4.3	37.68	42.0 ± 0.4
	$Cl_2 + Cl$		35.17	39.5 ± 0.4
$SiCl_2^+ + Cl_2^+$	none	2.7	26.95	29.7 ± 0.4
$SiCl^+ + Cl_2^+$	Cl	3.0	28.99	31.0 ± 0.4

a Unless stated otherwise, the various dissociation limits are derived from values of heat of formation and fragment ionization energy taken from the NIST Chemistry Webbook[30,31]

b Calculated using the experimental ionization energy (7.65±0.15eV) of $SiCl_3$ measured by Fisher and Armentrout[32]

c Calculated using the experimental ionization energy (7.33eV) of SiCl measured by Marijnissen and ter Meulen[33]

Table 4.II Summary of the precursor-state energies for ion pair formation following charge-separating decay of $SiCl_4^{2+}$, determined in this work.

The estimates of the $SiCl_4^{2+}$ electronic state energies derived in this work (Table 4.II), coupled with the absence of metastable $SiCl_4^{2+}$ ions from the mass spectra recorded, suggest a double ionization threshold for $SiCl_4$ lying in the region of 27.4 eV. Tsai and Eland[34] have derived an empirical formula for estimating the double ionization energy for closed shell molecules, which, for $SiCl_4$ predicts a double ionization energy of 33.0 ± 1.2 eV, in poor agreement with the present data. Of course, the estimates presented in Table 4.II represent a lower limit for the electronic state energies of $SiCl_4^{2+}$ since the degree of internal excitation of the ionic fragments is unknown. With this important proviso, the present measurements imply that the ground electronic state of the $SiCl_4^{2+}$ dication dissociates to form exclusively $SiCl_3^+$ + Cl^+ pairs, while the formation of the other ion pairs observed arise from the dissociation of excited states lying higher in the electronic state manifold of $SiCl_4^{2+}$. Clearly, theoretical calculations are required to enable the assignment of the various ion pairs to particular electronic states of the $SiCl_4^{2+}$ dication.

5.6 Conclusions

Relative PICS for the formation of fragment ions, following dissociative electron ionization of $SiCl_4$ in the energy range 30-200 eV, have been measured using time-of-flight mass spectrometry coupled with a 2-D ion coincidence technique. A comparison of this data with the recent absolute cross-sections of $SiCl_4$ measured by Basner *et al.*[19], reveals a good agreement for the formation of monocation fragments, although a small disagreement exists for the formation of the minor dication fragments. Precursor-specific relative PICS have also been derived for the formation of the various fragment ions observed, which quantify the contribution to the yield of each ion from single (n=1), double (n=2) and triple (n=3) ionization. These values have been interpreted to explain the double-maximum structure observed in the absolute PICS curves for a number of ionic fragments, measured in recent studies on $SiCl_4$ and $TiCl_4$.[19,20] The overall conclusions drawn from the current measurements are that the low-energy maxima are due to contributions from single ionization involving predominantly indirect ionization processes, while the higher-energy maxima are due to dissociative double ionization. The relative PICS values derived in this work also include the first quantitative measurements of the formation of Cl_2^+, a minor fragment ion following electron ionization of $SiCl_4$. In addition measurements of the relative PICS for forming ion pairs following the charge separating dissociation of the $SiCl_4^{2+}$ dication have been presented. All of the relative PICS measurements described in this work can be placed on an absolute scale by normalization to the $SiCl_4^+$ cross section data of Basner *et al.*[19]

Through analysis of the peaks observed in the 2-D ion coincidence spectra additional information has been extracted concerning the dynamics and energetics involved in the charge separating dissociations of the $SiCl_4^{2+}$ dication. Such analysis suggests that the majority of ion pairs observed are formed by concerted instantaneous mechanisms, many involving a glancing collision between the silicon-containing ion fragment and neutral Cl fragment(s) formed. By simulations of the peaks appearing in the ion coincidence spectra, the KER involved in ion pair formation has been determined, thus providing estimates of the precursor state energies for forming ion pairs. These measurements represent the first estimates of the electronic state energies of the $SiCl_4^{2+}$ dication.

5.7 References

[1] E. Zhirnov, S. Stepanov, W. N. Wang, Y. G. Shreter, D. V. Takhin, and N. I. Bochkareva, Journal of Vacuum Science & Technology A **22** (6), 2336 (2004).

[2] A. S. Agarwal, V. Berry, R. Alapati, and K. J. Nordheden, Journal of the Electrochemical Society **152** (3), G210 (2005).

[3] S. Golka, S. Schartner, W. Schrenk, and G. Strasser, Journal of Vacuum Science & Technology B **25** (3), 839 (2007).

[4] E. Mastropaolo, A. M. Gundlach, C. Fragkiadakis, P. B. Kirby, and R. Cheung, Electronics Letters **43**, 1467 (2007).

[5] A. Benami, G. Santana, A. Ortiz, A. Ponce, D. Romeu, J. Aguilar-Hernandez, G. Contreras-Puente, and J. C. Alonso, Nanotechnology **18** (15) (2007).

[6] X. Y. Lin, K. X. Lin, C. J. Huang, Y. P. Yu, Y. L. Luo, C. Y. Yu, and H. A. Rui, Journal of Applied Physics **98** (3) (2005).

[7] O. Sanchez, J. M. Martinez-Duart, R. J. Gomez-Sanroman, R. Perez-Casero, M. A. Aguilar, C. Falcony, F. Fernandez-Gutierrez, and M. Hernandez-Velez, Journal of Materials Science **34** (12), 3007 (1999).

[8] *Database needs for modeling and simulation of plasma processing.* (National Research Council, National Academy Press, Washington, 1996).

[9] S. Harper, P. Calandra, and S. D. Price, Phys. Chem. Chem. Phys. **3** (5), 741 (2001).

[10] S. J. King and S. D. Price, J. Chem. Phys. **127**, 174307 (2007).

[11] N. A. Love and S. D. Price, Phys. Chem. Chem. Phys. **6** (19), 4558 (2004).

[12] L. G. Christophorou and J. K. Olthoff, *Fundamental Electron Interactions with Plasma Processing Gases.* (Plenum, New York, 2004).

[13] J. C. Creasey, I. R. Lambert, R. P. Tuckett, K. Codling, L. J. Frasinski, P. A. Hatherly, M. Stankiewicz, and D. M. P. Holland, J. Chem. Phys. **93** (5), 3295 (1990).

[14] D. M. Smith, R. P. Tuckett, K. R. Yoxall, K. Codling, and P. A. Hatherly, Chem. Phys. Lett. **216** (3-6), 493 (1993).

[15] D. M. Smith, R. P. Tuckett, K. R. Yoxall, K. Codling, P. A. Hatherly, J. F. M. Aarts, and M. Stankiewicz, J. Chem. Phys. **101** (12), 10559 (1994).

16 G. K. Jarvis, K. J. Boyle, C. A. Mayhew, and R. P. Tuckett, J. Phys. Chem. A **102** (19), 3219 (1998).

17 R. H. Vought, Phys. Rev. **71** (2), 93 (1947).

18 L. Cooper, E. E. Rennie, L. G. Shpinkova, D. M. P. Holland, and D. A. Shaw, Int. J. Mass Spectrom. **220** (3), 359 (2002).

19 R. Basner, M. Gutkin, J. Mahoney, V. Tarnovsky, H. Deutsch, and K. Becker, J. Chem. Phys. **123** (5) (2005).

20 K. Becker, J. Mahoney, M. Gutkin, V. Tarnovsky, and R. Basner, Japanese Journal of Applied Physics Part 1-Regular Papers Brief Communications & Review Papers **45** (10B), 8188 (2006).

21 B. H. Boo, S. M. Park, and I. Koyano, J. Phys. Chem. **99** (36), 13362 (1995).

22 W. C. Wiley and I. H. McLaren, Review Of Scientific Instruments **26** (12), 1150 (1955).

23 N. A. Love and S. D. Price, Int. J. Mass Spectrom. **233** (1-3), 145 (2004).

24 *Electron Impact Ionization*, edited by T. D. Märk and G. H. Dunn (Springer, Vienna, 1985).

25 S. J. King and S. D. Price, Int. J. Mass Spectrom., In Press.

26 S. J. King and S. D. Price, Int. J. Mass Spectrom. **272** (2-3), 154 (2008).

27 S. Leach, J. H. D. Eland, and S. D. Price, J. Phys. Chem. **93** (22), 7583 (1989).

28 E. Ruhl, S. D. Price, S. Leach, and J. H. D. Eland, Int. J. Mass Spectrom. Ion Process. **97** (2), 175 (1990).

29 J. H. D. Eland, Molecular Physics **61** (3), 725 (1987).

30 H. Y. Afeety, J. F. Liebman, and S. E. Stein, *"Neutral Thermochemical Data"*. (National Institute of Standards and Technology, Gaithersburg MD, 20899 (http://webbook.nist.gov), June 2005).

31 S. G. Lias, *"Ion Energetics Data"*. (National Institute of Standards and Technology, Gaithersburg MD, 20899 (http://webbook.nist.gov), June 2005).

32 E. R. Fisher and P. B. Armentrout, J. Phys. Chem. **95** (12), 4765 (1991).

33 A. Marijnissen and J. J. terMeulen, Chem. Phys. Lett. **263** (6), 803 (1996).

34 B. P. Tsai and J. H. D. Eland, Int. J. Mass Spectrom. Ion Process. **36** (2), 143 (1980).

Chapter 6 Electron Ionization of Acetylene

6.1 Introduction

The ionization of acetylene is a process of relevance to planetary atmospheric chemistry, plasma devices and flames. Infrared emission spectra measurements, including those obtained during the *Voyager* and *Cassini* space missions, have identified acetylene, as a component of planetary atmospheres such as Jupiter[1,2], Uranus[3], Saturn[4], Titan[5], and in the interstellar medium[6]. In these environments, where dissociative ionization can occur, both the parent ion and fragment ions of acetylene play an important role in the ion-molecule reaction chemistry[7-9]. For example, such reactions have recently been implicated in the formation of diacetylene, responsible, in part, for the stratospheric haze of Jupiter[7,10]. The formation of ions in acetylene-air flames may also serve as precursors to polycyclic species and soot particles[11]. The accurate modelling of such environments requires, therefore, reliable information on the formation efficiency of the parent ion and the various ionic fragments. To provide this information a mass spectrometric experiment is required to measure the yield of the different ionic products from ionizing events; such yields are conveniently expressed in the form of partial ionization cross sections (PICS).

The dissociative ionization of C_2H_2 has been studied by a number of techniques, including photoionization mass spectrometry[12-14], electron ionization mass spectrometry[15-20], charge inversion translational energy loss mass spectrometry[21] and by more complex coincidence techniques[22-26]. Measurements of the appearance potential for forming fragment ions *via* photoionization have been performed using a quadrupole mass spectrometer[13] (QMS), a time-of-flight (TOF) mass spectrometer[12], and using the PEPICO technique[23,24,26]. Photoionization efficiency curves[13,14] and photoion yield curves[12] have been reported, while photon emission following fragment photoion formation has been investigated using FIPCO spectroscopy[22]. With respect to previous studies of the electron ionization of C_2H_2, appearance potentials and translational energy distributions for a number of different fragment ions have been measured by Davister and Locht using a QMS coupled with retarding potential analysis[15-18,20]. Appearance potentials and electron ionization efficiency curves for these fragment ions have also been measured, using a QMS, by Plessis and co-workers[19]. The total electron ionization cross section of C_2H_2 has been recorded[27], and has been calculated using the Binary-Encounter-Bethe model[28,29] and the Deutsch-Märk formalism[30].

6.1.1 Partial Ionization Cross Sections of C_2H_2

Early measurements of the partial ionization efficiency curves following electron ionization of C_2H_2 were made by Tate and Smith[31] and in 1967 Gaudin and Hagemann[32] determined the first partial electron ionization cross sections of acetylene for electron energies between 100 and 2000 eV. More recently Zheng and Srivastava[33] determined absolute PICS of C_2H_2 between threshold and 800 eV using a segmented QMS and time-of-flight mass spectrometer. In 1998 Tian and Vidal[34] reported absolute PICS following dissociative ionization of C_2H_2 for electron energies from threshold to 600 eV. Most recently, Feil *et al.*[35] used a double focusing two sector field mass spectrometer to determine absolute partial electron ionization cross sections up to 1000 eV, including a determination of kinetic energy distributions for some fragment ions. Despite this wealth of data there exists some significant discrepancies between the individual sets of data, particularly concerning the cross sections for producing light ion fragments such as H^+ and C^+, which may be formed with considerable kinetic energy.[15,17] It is the lack of agreement between these recent experimental determinations of absolute PICS of C_2H_2 which has partially motivated the present study. Of these recent measurements, only the work of Tian and Vidal[34] demonstrates the efficient collection of energetic fragment ions, although Feil *et al.*[35] carefully considered the losses of energetic ions in their experiments. To date, the recommended value of the total ionization cross section of acetylene[36] is derived from the data of Tian and Vidal[34].

In this study the electron ionization of C_2H_2 is investigated in the energy range 30-200 eV, using time-of-flight mass spectrometry coupled with a 2-D ion coincidence technique. Relative partial ionization cross sections $\sigma_r[X^+]$ are derived for the formation of H^+, H_2^+, C^{2+}, C^+/C_2^{2+}, $CH^+/C_2H_2^{2+}$, CH_2^+, C_2^+ and C_2H^+ ions, expressed relative to the formation of $C_2H_2^+$, as a function of ionizing electron energy. These values are then compared extensively to the existing PICS data for acetylene listed above. As expected, the σ_r values derived in this work are shown to be in excellent agreement with the recommended PICS data of Tian and Vidal, where the efficient collection of energetic ion fragments was also permitted. Precursor-specific relative PICS are then derived for the formation of these fragment ions $\sigma_n[X^{m+}]$, which, as explained in Section 3.3.4, quantify the contribution to the yield of a fragment ion X^{m+} from single (n=1), double (n=2) and triple (n=3) ionization. These σ_n values show that dissociative double ionization contributes significantly to the total yield of H^+ and C^+ fragment ions at higher ionizing energies. Such fragment ions are typically formed with a large kinetic energy release due to the mutual electrostatic repulsion of the ions[37], thus explaining the smaller yields measured for these ionic fragments in some previous determinations of the PICS[33,35]. Relative cross sections $\sigma_r[X^+ + Y^+]$ for the formation of product ion pairs are also derived, formed *via* the dissociation of the $C_2H_2^{2+}$ dication.

6.1.2 The Acetylene Dication $C_2H_2^{2+}$

The 2-D ion coincidence technique used in this work also provides information on the energetics and dissociation dynamics of the acetylene dication. $C_2H_2^{2+}$ has attracted considerable experimental and theoretical attention as it is one of the smallest known metastable hydrocarbon dications. The energies of the electronic states of $C_2H_2^{2+}$ have been studied using photoion-photoion coincidence (PIPICO) spectroscopy[25,38], threshold photoelectron coincidence spectroscopy (TPEsCO)[39,40], double charge transfer (DCT) spectroscopy[41,42], and theoretical methods[25,40,41,43-48]. In 1993 Thissen *et al.*[25] derived a full breakdown scheme of the acetylene dication using data from a PEPIPICO study. Using this template, branching ratios are derived for the charge separating dissociations of $C_2H_2^{2+}$ observed in our ion-coincidence spectra. These results are then compared to high-level *ab initio*/RRKM calculations involving the lowest energy electronic states of $C_2H_2^{2+}$.[48]

6.2 Experimental Procedures

All the experiments in this study were performed on a time-of-flight mass spectrometer of Wiley-McLaren design[49] as described in detail in Section 2.3. The acetylene gas used was a commercial sample and was liberated from propanone contamination using a solid CO_2/propanone ice bath held at -78°C. The flow of acetylene into the apparatus was carefully controlled by a needle valve.

The operating conditions of the experiment involve low target gas pressures ($< 10^{-6}$ Torr) and low electron fluxes, ensuring that on average much less than one ionization event is detected per ionizing pulse of electrons. This methodology significantly reduces the contribution of 'false coincidences' to the coincidence spectra recorded, as described in previous chapters.

6.2.1 Ion Discrimination Effects

In extracting quantitative data from the experiment one must ensure that the apparatus is detecting all ions, regardless of their mass or initial kinetic energy, with equal efficiency. Previously a number of preliminary experiments have been described (Section 2.3.1), in which a range of voltage conditions were established where mass and energy dependent discrimination effects do not influence the measured ion yields. However, any energy dependent discrimination effects in the mass spectrometer are particularly pertinent when studying fragmentation processes which generate H^+.[50] This is because if a dissociation event forms a proton, these light ions carry away much of the kinetic energy and will possess considerable velocities. To further investigate energy dependent discrimination effects in the experiment, the intensities of all singly charged fragment ions were measured following electron impact ionization of acetylene at 100 eV, relative to the intensity of $C_2H_2^+$ signals, whilst systematically changing a number of experimental parameters (Appendix B). By carefully optimizing the yields of the fragment ions with respect to the yield of $C_2H_2^+$, it was verified that under the standard voltage conditions used the above discrimination effects do not influence the measured ion yields. However, even under these standard voltage conditions asymmetric peaks are observed in the 2-D coincidence spectra for ion pairs containing an H^+ ion (Figure 6.2). These asymmetric peaks may be due to two factors. Firstly, the constant voltage applied to the drift tube may penetrate the source region and partially extract light H^+ ions from the source before the repeller plate is pulsed from 0 to +400 V. Secondly, the asymmetry in the coincidence peaks may indicate the loss of energetic H^+ ions formed with an initial velocity component aligned parallel to the flight axis and away from the detector. Such fast ions will traverse the source region following their formation and may collide with the repeller plate before it is pulsed. Therefore, it may be possible that a proportion of energetic H^+ ions are less efficiently detected through collisions with the repeller plate in the source region. One should note that such collisions involving heavier fragment ions are considerably less probable, as ions with larger mass typically acquire a much smaller initial velocity upon formation. By varying the delay time between the electron pulse and repeller plate pulse at an ionizing energy of 100 eV, it was found that the asymmetry in the H^+ pair peaks could be reduced by decreasing the delay time between the electron pulse and the ions extraction (Figure B.3). However, such a decrease in the extraction delay did not significantly change the H^+ ion yield (Figure B.2). Thus it is concluded that the asymmetry in the coincidence peaks involving H^+ ions is due largely to the influence of a penetrating electric field from the drift tube into the source region, and not to the loss of energetic H^+ ions at the repeller plate. In the source region, calculations suggest conservatively, that H^+ ions must be formed with an initial kinetic energy markedly in excess of 7 eV to escape detection through collisions with the repeller plate. By measurement of the kinetic energy release distribution of H^+ ions, Davister and Locht have shown that only a minor proportion of H^+ ions are formed with a kinetic energy in excess of 7 eV following electron ionization of C_2H_2 at 99 eV.[15] Again this indicates that H^+ losses due to collisions with the repeller plate should be small. Indeed, as is shown below, the PICS determined in this work for formation of H^+ ions are in excellent agreement with the recommended values in the literature of Tian and Vidal[34], indicating that losses of energetic H^+ ions are not a problem in this study.

6.3 Data Analysis

6.3.1 Singles Mass Spectra

A representative singles mass spectrum of C_2H_2 recorded at an ionizing electron energy of 200 eV is shown in Figure 6.1. The intensities of individual ion peaks in the singles spectrum, $I_1[X^+]$ for monocations and $I_2[X^{2+}]$ for dications, are extracted using the analysis procedure described in Section 3.2.1. Due to the low target gas pressures employed, a small number of ions from the residual gas contribute to all mass spectra recorded. Specifically ionization of N_2 results in the formation of N^+ ions which are indistinguishable from the small CH_2^+ peak from C_2H_2, at $m/Z = 14$. To a much lesser extent, ionization of H_2O yields H^+ ions which, as well as protons from the ionization of C_2H_2, contribute to the H^+ peak in the mass spectrum. These minor contributions to the mass spectra are subtracted, using the procedure outlined in Section 3.2.1.2, by normalization to the N_2^+ and H_2O^+ peaks in each acetylene mass spectrum. In all singles mass spectra the intensity of the $m/Z = 14$ peak could not could not be evaluated directly owing to significant overlap with the intense neighbouring peak (CH^+) at $m/Z = 13$. The CH^+ peak is broad due to the significant translational energy of these fragment ions. Thus, the intensities of the $m/Z = 13$ and 14 peaks were extracted using a peak fitting procedure, as described in Section 3.2.1.1. At electron energies below 50 eV a similar fitting procedure was used to extract the C_2^+ intensities, $I_1[C_2^+]$.

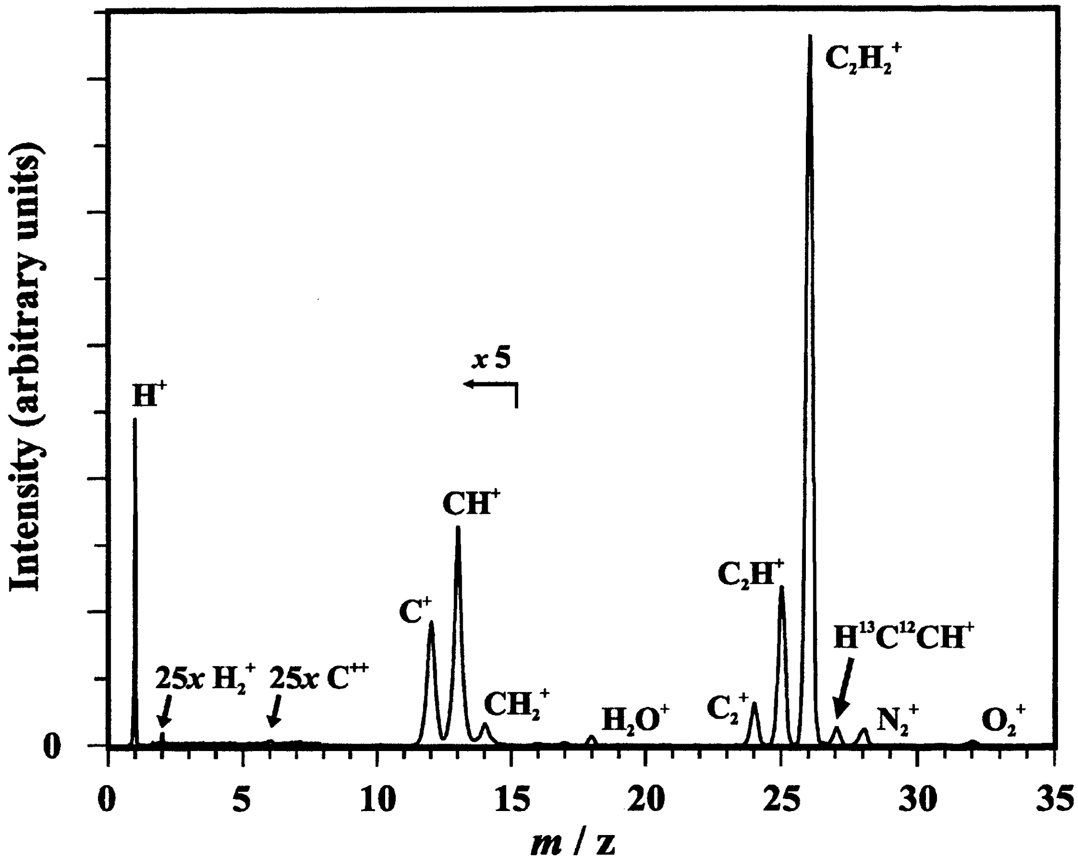

Figure 6.1 A characteristic (singles) mass spectrum of C_2H_2 following electron impact ionization at 200 eV.

6.3.2 2-D Ion Coincidence Spectra

A representative pairs mass spectrum of C_2H_2 recorded at an ionizing electron energy of 200 eV is shown in Figure 6.2. The intensities of the various ion peaks are then extracted, using the procedure described in Section 3.2.2, to yield the number of individual ion pairs $P[X^+ + Y^+]$, and also the overall contribution of each individual fragment ion to the pairs spectrum $P[X^+]$. In this work a distinction is made between the ion counts in pairs which must be formed *via* dissociative triple ionization of the acetylene trication $P_3[X^+]$, for example $C^{2+} + H^+$, and the ion counts in the other peaks in the pair spectrum which may contain contributions from both dissociative double and triple ionization $P_2[X^+]$, such as $CH^+ + H^+$. False coincidence contributions are subtracted from each 'pairs' spectrum using an ion-autocorrelation function, as described in Section 3.2.2.1. Typically false counts contribute between 1 and 5 % to the pair peak intensity in the pairs spectra, depending on the ion pair under investigation. The size of false count correction increases to above 5% of the raw pairs peak intensity at ionizing electron energies closer to the double ionization threshold of C_2H_2 where the dissociative double ionization cross section is low. In the experiment no ion pairs are recorded if the second ion reaches the detector within 32 ns of the first, due to the 'deadtime' of the discrimination circuitry. Such losses significantly affect the number of counts observed in ion pairs of identical mass, specifically $H^+ + H^+$, $C^+ + C^+$, $CH^+ + CH^+$, and to a lesser extent the $C^+ + CH^+$ channel. An estimate of these losses is made by plotting a one-dimensional (t_1–t_2) spectrum for a given peak which exhibits these discrimination loses, and appropriately extrapolating, using simple geometry, the number of ion counts to include the deadtime (Section 3.2.2.3).

Ion triples are processed by specifying a time-of-flight range for a particular ion, for example CH^+, and then extracting all ion triples containing at least one ion whose arrival time falls within this specified range. Once extracted, the respective flight times of the two remaining ions forming an ion triple with CH^+ are displayed as a two-dimensional histogram (t_2 *vs.* t_3). The contribution of a fragment ion, for example $T[CH^+]$, in this triples spectrum is the sum of all the peak counts involving the formation of CH^+, after applying (where necessary) a small geometric correction to account for losses due to the 'deadtime', as described above. False triple coincidences that contribute to the intensity of each triples peak are subtracted using the procedure outlined in Section 3.2.3.1. Owing to the low cross sections observed in this work for dissociative triple ionization of C_2H_2, contributions to the ion yields from ion triples are negligible and neglected below 100 eV. For this reason, contributions to the coincidence spectra from dissociative quadruple ionization are also neglected.

Under the voltage conditions used in the experiment ions may reach the detector provided they have a translational energy component of less than 11 eV perpendicular to the TOF axis. Curtis and Eland determined the total kinetic energy release (KER) from dicationic dissociation to, commonly, be less than 9 eV.[51] Thus, in the apparatus conditions are optimised such that the majority of all ions formed by multiple ionization can be collected. In fact the loss of energetic ions from multiple ionization can be easily evaluated and corrected, if necessary, from the shape of the coincidence signals (Section 3.2.2.2). One notes however that it is not possible to correct for the losses of energetic fragment ions from single ionization, if such fragment ions are formed with a kinetic energy of greater than 11 eV. However, the good agreement of the data produced by this experiment with other studies where complete collection of fragment ions is demonstrated[52], clearly indicates such losses of energetic fragment ions from single ionization is, in most cases, very small.

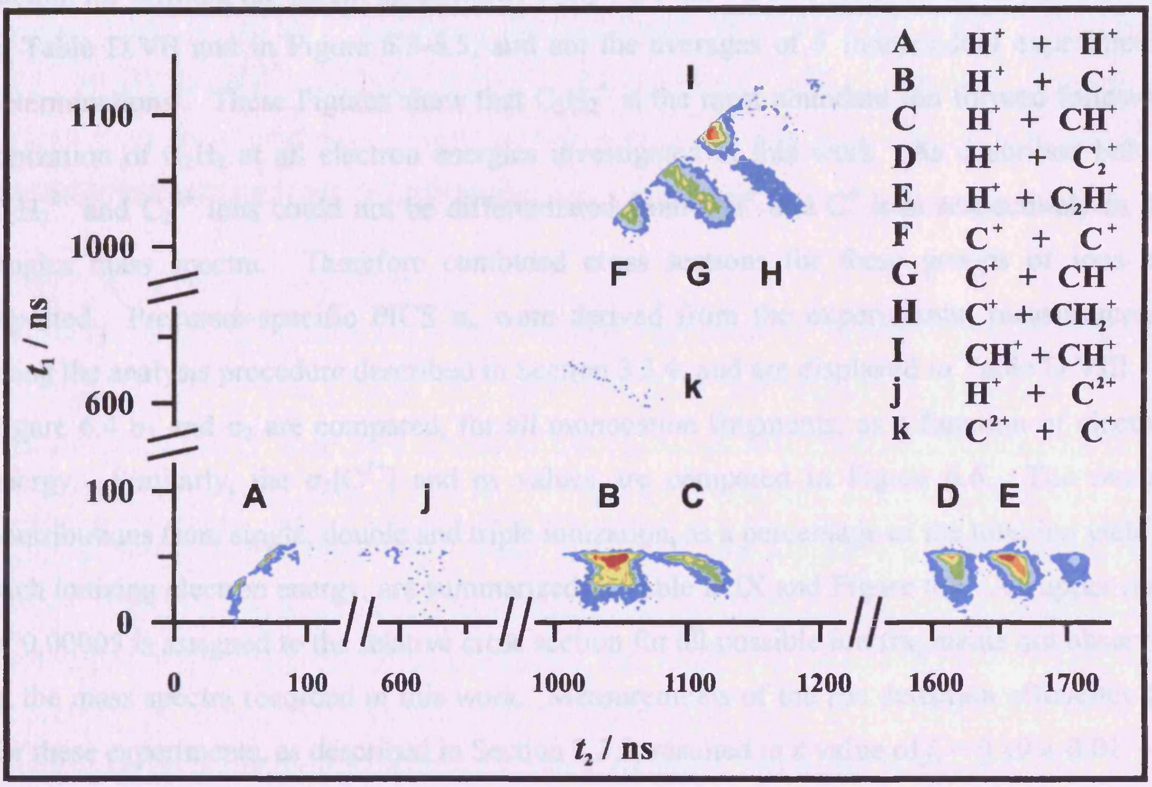

Figure 6.2 Observed ion pairs in the dissociation of $C_2H_2^{2+}$ and $C_2H_2^{3+}$ formed by electron-impact ionization at 200 eV.

In the singles mass spectra of acetylene the isotopes of several carbon-containing ions occurring at the same mass, for example, $^{12}CH^+$ and $^{13}C^+$, could not be distinguished. Thus the measured ion intensities were corrected numerically using the natural isotopic distribution ^{12}C:^{13}C (98.9% : 1.1%). Similar corrections were made to the intensities of carbon-containing ion pairs recorded in the 2-D coincidence spectra.

6.4 Relative Partial Ionization Cross Sections

6.4.1 Results

Mass and coincidence spectra of C_2H_2 were recorded at ionizing electron energies between 30-200 eV (Figure 6.1 and Figure 6.2). All spectra were processed, as described in Section 3.3.2, to yield σ_r values for the formation of all the fragment ions observed: H^+, H_2^+, C^{2+}, C^+/C_2^{2+}, $CH^+/C_2H_2^{2+}$, CH_2^+, C_2^+ and C_2H^+. These values, expressed relative to the cross section for forming the parent monocation $C_2H_2^+$, are shown as a function of electron energy in Table D.VII and in Figure 6.3-6.5, and are the averages of 5 independent experimental determinations. These Figures show that $C_2H_2^+$ is the most abundant ion formed following ionization of C_2H_2 at all electron energies investigated in this work. As described below, $C_2H_2^{2+}$ and C_2^{2+} ions could not be differentiated from CH^+ and C^+ ions respectively in the singles mass spectra. Therefore combined cross sections for these groups of ions are reported. Precursor-specific PICS σ_n were derived from the experimental measurements, using the analysis procedure described in Section 3.3.4, and are displayed in Table D.VIII. In Figure 6.4 σ_1 and σ_2 are compared, for all monocation fragments, as a function of electron energy. Similarly, the $\sigma_2[C^{2+}]$ and σ_3 values are compared in Figure 6.6. The overall contributions from single, double and triple ionization, as a percentage of the total ion yield at each ionizing electron energy, are summarized in Table D.IX and Figure 6.7. An upper limit of 0.00005 is assigned to the relative cross section for all possible ion fragments not observed in the mass spectra recorded in this work. Measurements of the ion detection efficiency (f_i) for these experiments, as described in Section 3.3.3, resulted in a value of $f_i = 0.19 \pm 0.01$.

In the pairs spectra 9 dissociation channels of the acetylene dication were observed: $H^+ + H^+$, $H^+ + C^+$, $H^+ + CH^+$, $H^+ + C_2^+$, $H^+ + C_2H^+$, $C^+ + C^+$, $C^+ + CH^+$, $C^+ + CH_2^+$ and $CH^+ + CH^+$. In addition, at electron energies above 100 eV two ions pairs and three ion triples resulting from dissociation of the acetylene trication are observed: $C^{2+} + H^+$, $C^{2+} + C^+$, $CH^+ + C^+ + H^+$, $C^+ + C^+ + H^+$, $C^+ + H^+ + H^+$. Values of σ_r for the formation of monocation-monocation pairs formed by $C_2H_2^{2+}$ dication dissociation are shown in Table D.XVIII and Figure 6.8.

6.4.2 Discussion

In this section the significant aspects of the cross sections derived in this work are discussed. Where appropriate, comparisons are made between the present relative PICS (King and

Price) and values derived from the absolute PICS presented by Tian and Vidal[34], and Zheng and Srivastava[33]. A further comparison is also made with the recent absolute measurements of Feil *et al.*[35]

Single Ionization

Single ionization of C_2H_2 dominates over double ionization at all electron energies investigated in this study (Figure 6.7), accounting for 98% of the total ion yield at 50 eV, 92% at 75 eV, decreasing to around 89% above 125 eV. The appearance thresholds for forming $C_2H_2^+$ (11.40 eV)[19] and singly charged fragments C_2H^+ (17.35 eV)[20,26], C_2^+ (18.44 eV)[17], H^+ (18.83 eV)[15], CH_2^+ (19.74 eV)[17], CH^+ (20.83 eV)[16], C^+ (21.16 eV)[17], from single ionization are all at energies below the lowest energy that can be reached with the electron gun and were not investigated in this study.

Double and Triple Ionization

Double ionization contributes 2% to the ionization yield at 50 eV, and this value rises steadily to a maximum of 11% at 175 eV. It is noted that these percentages do not account for any losses of energetic H^+ ions from single ionization, nor do they consider contributions to the double ionization cross section from $C_2H_2^{2+}$ and C_2^{2+} ions. As is described below, these dications could not be distinguished from CH^+ and C^+ ions respectively in the singles mass spectra. However, these factors are to an extent self correcting and, as will be demonstrated, have only a small effect on the measured total ion yields from single and double ionization respectively. The cross sections measured for triple ionization in this work are very low. For example, at 200 eV triple ionization contributes less than 0.2 % to the total ion yield.

C_2H^+ formation

The values of $\sigma_r[C_2H^+]$ determined in this work show that C_2H^+ is the second most abundant ion formed following ionization of C_2H_2 at all electron energies investigated (Figure 6.3). Over the entire energy range there is excellent agreement between our $\sigma_r[C_2H^+]$ values and the values derived from the data of Tian and Vidal[34], and also Feil *et al.*[35] Our data and the $\sigma_r[C_2H^+]$ values of Zheng and Srivastava[33] also agree within their mutual error limits. However, between 60 eV and 100 eV our $\sigma_r[C_2H^+]$ values are 15-19 % larger than those of Zheng and Srivastava which, in fact, lie close to our values of $\sigma_1[C_2H^+]$ in this energy range. It has been reported previously[34] that in their experiments Zheng and Srivastava do not demonstrate the complete collection of highly translationally energetic fragment ions. One possible explanation therefore of our larger $\sigma_r[C_2H^+]$ values is that Zheng and Srivastava lose a small proportion of energetic C_2H^+ ions.

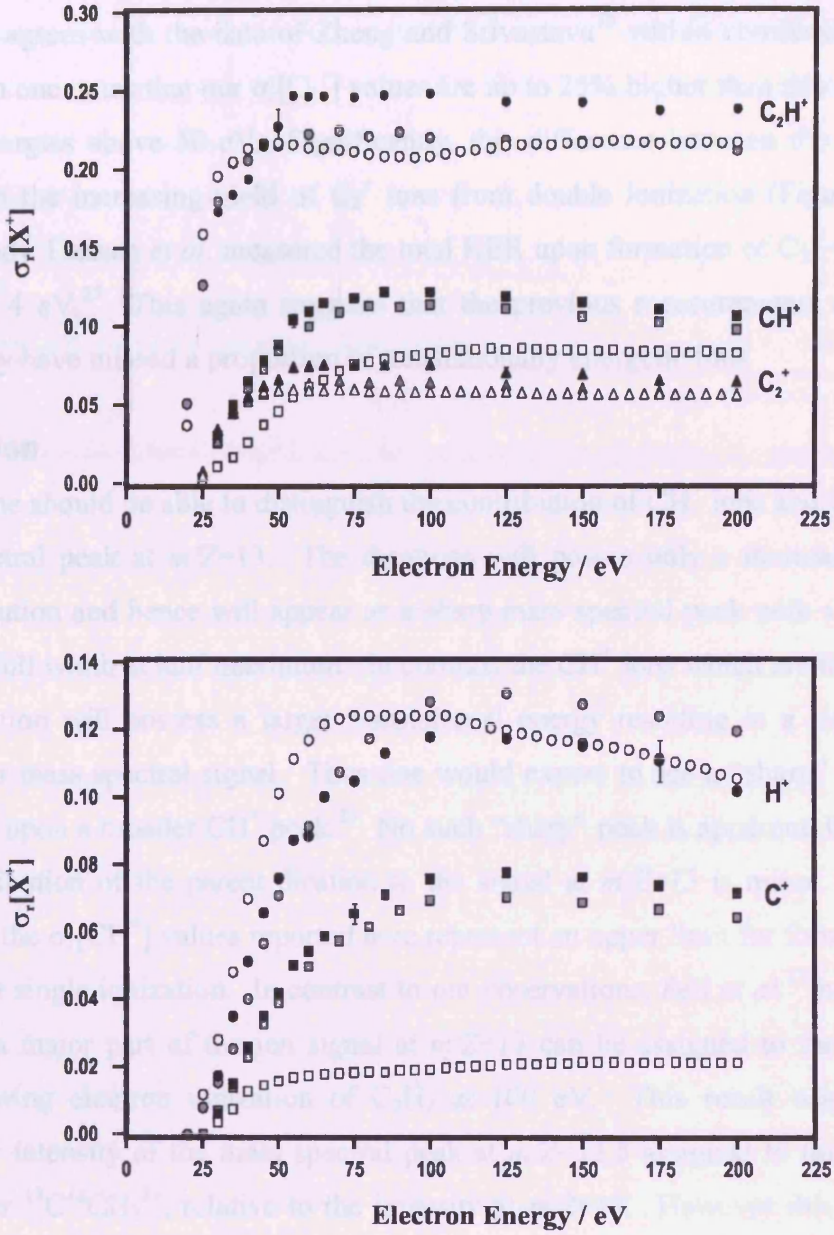

Figure 6.3 Relative PICS for forming the most abundant ionic fragments following electron ionization of C_2H_2. The error bars expressed in this figure represent two standard deviations of five separate determinations. The corresponding relative PICS extracted from the data of Tian and Vidal[34] (grey) and Zheng and Srivastava[33] (white) are also shown.

C_2^+ formation

The values of $\sigma_r[C_2^+]$ measured in this work (Figure 6.3) are again in excellent agreement with the values of Tian and Vidal[34], and Feil *et al.*[35] across the entire ionizing energy range. Our data also agrees with the data of Zheng and Srivastava[33] within combined error limits, although again one notes that our $\sigma_r[C_2^+]$ values are up to 25% higher than this determination at ionizing energies above 50 eV. Significantly, this difference between the two data sets coincides with the increasing yield of C_2^+ ions from double ionization (Figure 6.4). In a PEPIPICO study Thissen *et al.* measured the total KER upon formation of $C_2^+ + H^+$ ion pairs to be at least 4 eV.[25] This again suggests that the previous measurements of Zheng and Srivastava may have missed a proportion of translationally energetic ions.

CH^+ formation

In principle one should be able to distinguish the contribution of CH^+ ions and $C_2H_2^{2+}$ ions to the mass spectral peak at *m/Z*=13. The dications will posses only a thermal translational energy distribution and hence will appear as a sharp mass spectral peak with a width of less than 10 ns at full width at half maximum. In contrast the CH^+ ions which are the products of ionic dissociation will possess a larger translational energy resulting in a larger temporal width for their mass spectral signal. Thus one would expect to see a "sharp" dication peak superimposed upon a broader CH^+ peak.[25] No such "sharp" peak is apparent, thus it appears that the contribution of the parent dication to the signal at *m/Z*=13 is minor. This means, however, that the $\sigma_1[CH^+]$ values reported here represent an upper limit for forming CH^+ ions from C_2H_2 *via* single ionization. In contrast to our observations, Feil *et al.*[35] have suggested recently that a major part of the ion signal at *m/Z*=13 can be assigned to the formation of $C_2H_2^{2+}$, following electron ionization of C_2H_2 at 100 eV. This result was obtained by measuring the intensity of the mass spectral peak at *m/Z*=13.5 assigned to the formation of the isotopomer $^{13}C^{12}CH_2^{2+}$, relative to the intensity at *m/Z*=13. However this measurement was made prior to correction for discrimination effects giving rise to losses of energetic ions. Therefore the peak intensity of ions formed with thermal energy are enhanced strongly compared to fragments formed with greater kinetic energy such as CH^+.

Over the range of ionizing electron energy investigated in this study, there is an excellent agreement between our data and the $\sigma_r[CH^+ + C_2H_2^{2+}]$ values derived from the data of Tian and Vidal[34] (Figure 6.3). There is a reasonable agreement between our data and $\sigma_r[CH^+ + C_2H_2^{2+}]$ values derived from the data of Feil *et al.*[35], with both data sets agreeing within the combined error limits at most ionizing electron energies. Figure 6.3 shows that there is a significant discrepancy between the values of $\sigma_r[CH^+ + C_2H_2^{2+}]$ determined in this work and the corresponding values of Zheng and Srivastava[33], with our cross sections being considerably larger at all ionizing energies. Previous experiments[16,35] have shown that CH^+ ions from electron ionization of C_2H_2 are formed with a kinetic energy in excess of a few eV even below the double ionization threshold. Thus, again one may conclude that the values of Zheng and Srivastava do not include the contribution of energetic fragment ions.

C^+ formation

For C^+ our data are again in excellent agreement with the $\sigma_r[C^+]$ values derived from the measurements of Tian and Vidal[34] (Figure 6.3), who demonstrate the complete collection of C^+ ions. There is a discrepancy between our cross sections and $\sigma_r[C^+]$ values derived from the data of Feil *et al.*[35] and of Zheng and Srivastava[33]. Davister and Locht have shown that C^+ ions are formed by dissociative electron ionization of C_2H_2 with considerable translational kinetic energy.[17] Feil *et al.* have attempted to correct for losses of energetic C^+ ions in the source region of their mass spectrometer through analysis of the C^+ ion *z*-profiles.[35] Despite this, the cross sections they derive for forming C^+ ions are up to a factor of 2 smaller than the cross sections measured in this work. Therefore one may rationalise our larger cross sections for C^+ formation as resulting from losses of translationally energetic ions in the study of Feil *et al.*[35] and of Zheng and Srivastava.[33]

H^+ formation

Figure 6.3 shows that the $\sigma_r[H^+]$ values derived in this work are again in very good agreement with the data of Tian and Vidal[34]. Our $\sigma_r[H^+]$ values also agree well with the data of Zheng and Srivastava[33]. As was described by Tian and Vidal[34], in the work of Zheng and Srivastava H^+ ions were detected using a TOF mass spectrometer whereas all heavier ions were detected using a QMS. Thus Zheng and Srivastava were able to more efficiently detect energetic H^+ ions, explaining the good agreement between their $\sigma_r[H^+]$ values and the present data despite the discrepancies for heavier fragment ions. When H^+ ions are formed by the dissociative ionization of C_2H_2, a major proportion of the kinetic energy released is partitioned into translational energy of the light H^+ ion fragment. Previous experiments[15,25] have shown that H^+ ions from the ionization of $C_2H_2^+$ possess significant kinetic energies. The good agreement between the $\sigma_r[H^+]$ values derived in this work and the data of Tian and Vidal[34] suggest that any such losses of energetic H^+ ions in this apparatus are small.

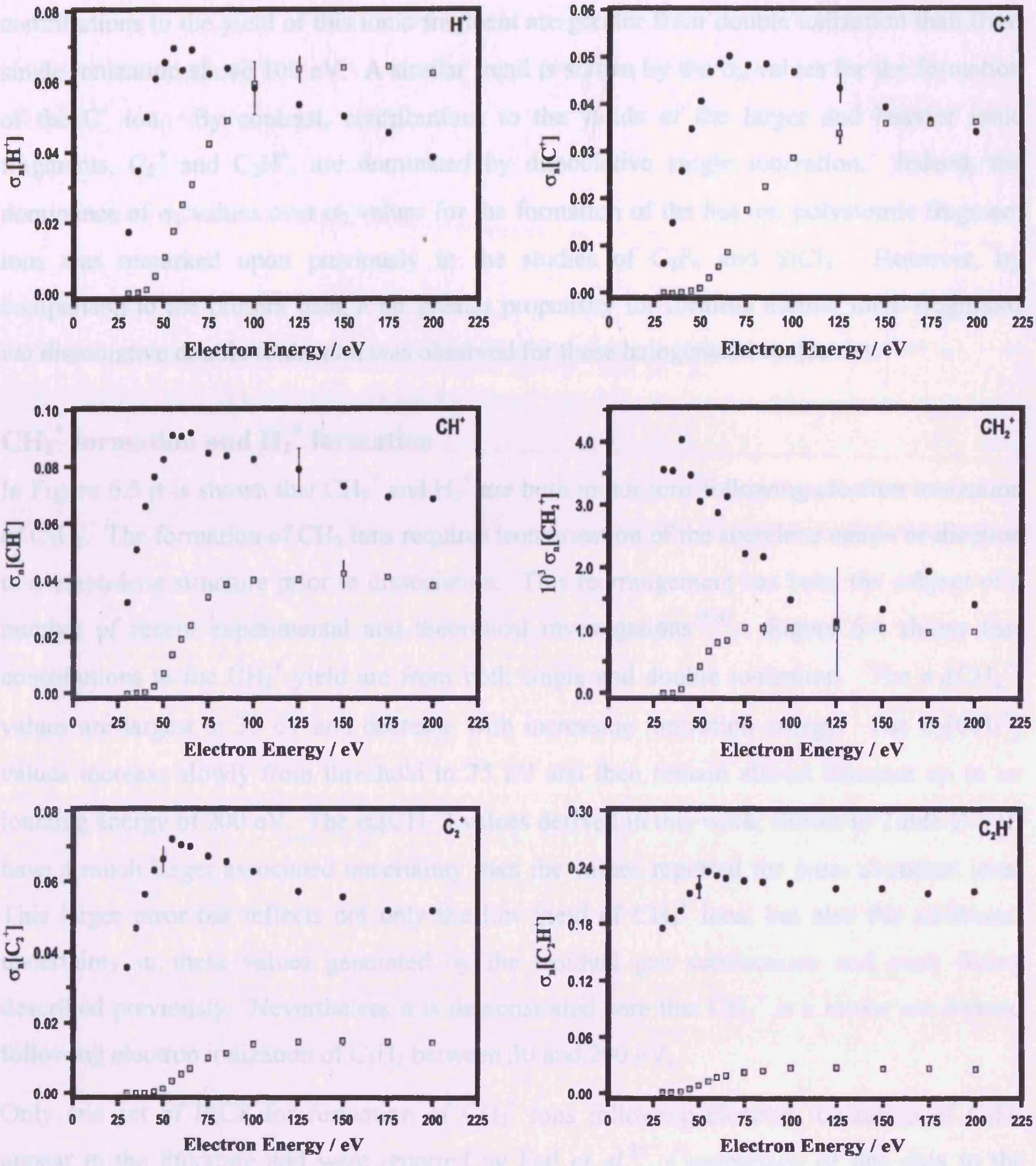

Figure 6.4 Relative precursor specific PICS for forming monocation fragments *via* dissociative single (—●—), double (--■--) and triple (··△··) electron ionization of C_2H_2. The representative error bars show two standard deviations of five separate determinations.

Precursor-Specific Relative PICS of the Major Ionic Fragments

Figure 6.4 shows that H^+ is the most abundant ion to be formed by dissociative double ionization in the energy range 30-200 eV. The σ_n values for H^+ formation reveal that contributions to the yield of this ionic fragment are greater from double ionization than from single ionization above 100 eV. A similar trend is shown by the σ_n values for the formation of the C^+ ion. By contrast, contributions to the yields of the larger and heavier ionic fragments, C_2^+ and C_2H^+, are dominated by dissociative single ionization. Indeed, the dominance of σ_1 values over σ_2 values for the formation of the heavier polyatomic fragment ions was remarked upon previously in the studies of C_2F_6 and $SiCl_4$. However, by comparison to the present data, a far greater propensity for forming atomic ionic fragments *via* dissociative double ionization was observed for these halogenated molecules.

CH_2^+ formation and H_2^+ formation

In Figure 6.5 it is shown that CH_2^+ and H_2^+ are both minor ions following electron ionization of C_2H_2. The formation of CH_2 ions requires isomerisation of the acetylene cation or dication to a vinylidene structure prior to dissociation. This rearrangement has been the subject of a number of recent experimental and theoretical investigations[53-57]. Figure 6.4 shows that contributions to the CH_2^+ yield are from both single and double ionization. The $\sigma_1[CH_2^+]$ values are largest at 30 eV and decrease with increasing ionization energy. The $\sigma_2[CH_2^+]$ values increase slowly from threshold to 75 eV and then remain almost constant up to an ionizing energy of 200 eV. The $\sigma_r[CH_2^+]$ values derived in this work, shown in Table D.VII, have a much larger associated uncertainty than the values reported for more abundant ions. This larger error bar reflects not only the low yield of CH_2^+ ions, but also the additional uncertainty in these values generated by the residual gas subtractions and peak fitting described previously. Nevertheless it is demonstrated here that CH_2^+ is a minor ion formed following electron ionization of C_2H_2 between 30 and 200 eV.

Only one set of PICS for formation of CH_2^+ ions following electron ionization of C_2H_2 appear in the literature and were reported by Feil *et al.*[35] Comparison of this data to the current measurements reveal that the $\sigma_r[CH_2^+]$ values derived in this work are considerably smaller than those of Feil *et al.* between 30 and 200 eV. This difference in $\sigma_r[CH_2^+]$ values is almost certainly due to the different methods used to correct for $^{13}CH^+$ contributions to the peak intensity at $m/Z=14$. In the measurements in this study, contributions of $^{13}CH^+$ ions are subtracted from the CH_2^+ peak intensity using the natural isotopic distribution of ^{12}C and ^{13}C as described above. In the data of Feil *et al.*[35], $^{13}CH^+$ ions that contribute to the peak at $m/Z=14$ were identified as the ions with low kinetic energy.

H_2^+ was observed only in low abundance in the singles spectra and is a minor ion formed by electron ionization of C_2H_2. Tian and Vidal put forward an upper limit of 0.0017 for $\sigma_r[H_2^+]$[34], a value considerably larger than the present data indicates (Table D.VII). As shown in Figure 6.5, $\sigma_r[H_2^+]$ values rise from a threshold lying below 30 eV, then remain approximately constant above 45 eV.

C^{2+} formation

As shown in Figure 6.5, C^{2+} is a minor ion fragment formed following electron ionization of C_2H_2. The $\sigma_r[C^{2+}]$ values rise gradually from threshold to 200 eV and remain over three orders of magnitude smaller than the corresponding cross-sections for formation of the most abundant fragment ion C_2H^+, at all ionizing energies. This data suggests that the threshold for forming C^{2+} ions lies below an ionizing energy of 75 eV. Figure 6.6 shows that C^{2+} is formed predominantly *via* double ionization within the energy regime of this work. Formation of C^{2+} *via* triple ionization $\sigma_3[C^{2+}]$ comprises approximately one third of the total C^{2+} ion yield above 175 eV.

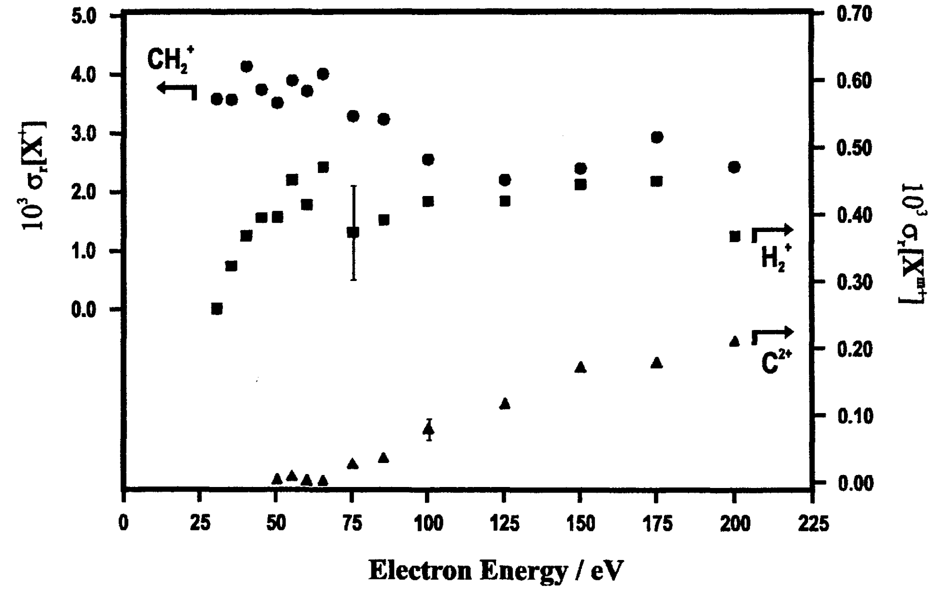

Figure 6.5 Relative PICS for forming minor ionic fragments following electron ionization of C_2H_2. The error bars expressed in this figure represent two standard deviations of five separate determinations.

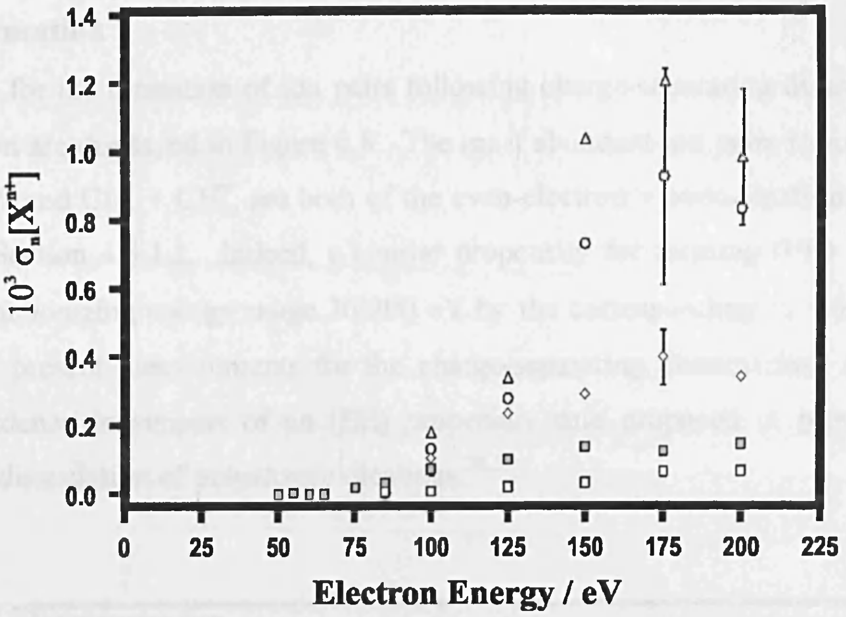

Figure 6.6 Relative precursor specific PICS for forming C^{2+} *via* double ionization (■), and triple ionization (□), following ionization of C_2H_2 by electron impact. Also shown are relative precursor specific PICS for forming H^+ (○), C^+ (Δ), and CH^+ (◊) *via* dissociative triple ionization.

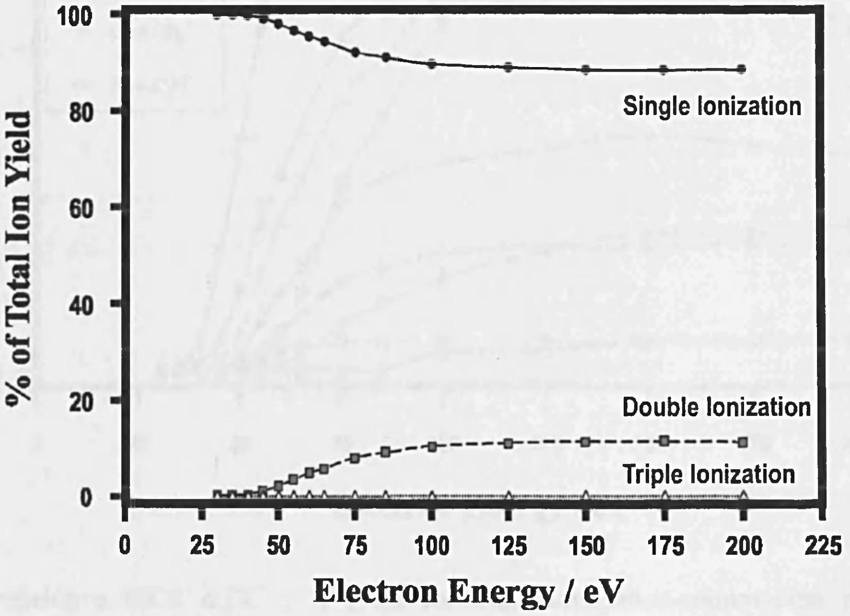

Figure 6.7 Contributions to the total ion yield from single, double, and triple ionization, following electron ionization of C_2H_2.

Ion Pair Formation

The σ_r values for the formation of ion pairs following charge-separating dissociation of the $C_2H_2^{2+}$ dication are displayed in Figure 6.8. The most abundant ion pairs formed below 100 eV, $C_2H^+ + H^+$ and $CH^+ + CH^+$, are both of the even-electron + even-electron (EE) type, as discussed in Section 4.5.1.1. Indeed, a similar propensity for forming (EE) ion pairs was observed in the ionizing energy range 30-200 eV by the corresponding σ_r values for $SiCl_4$. Therefore the present measurements for the charge-separating dissociations of $C_2H_2^{2+}$ are additional evidence in support of an (EE) propensity rule proposed in previous PIPICO studies of the dissociation of polyatomic dications.[58,59]

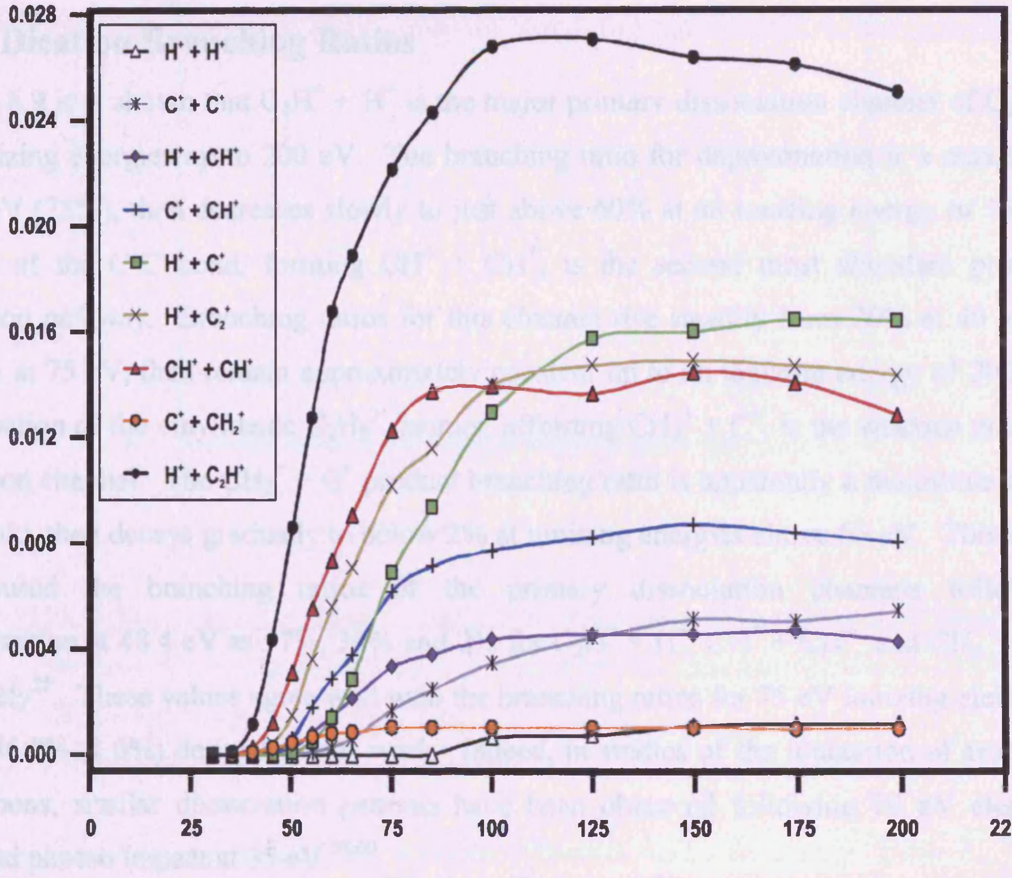

Figure 6.8 Relative PICS $\sigma_r[X^+ + Y^+]$ for forming monocation-monocation pairs following electron ionization of C_2H_2.

6.5 Dissociation of $C_2H_2^{2+}$

In this section some aspects of the charge-separating dissociations of the acetylene dication are discussed. The ion pairs observed in the coincidence spectra can be grouped into two general classes. Firstly, primary dissociations of $C_2H_2^{2+}$ into pairs of monocations and, secondly, ion pairs involving the secondary decay of a primary product ion. In an earlier photoion coincidence study Thissen *et al.* derived an overall breakdown scheme for the acetylene dication.[25] Using this template the relative yields (branching ratios) of the primary two body dissociations (Figure 6.9), and for forming all possible monocation pairs (Table 6.I), have been derived, as a function of ionizing electron energy.

6.5.1 Dication Branching Ratios

In Figure 6.9 it is shown that $C_2H^+ + H^+$ is the major primary dissociation channel of $C_2H_2^{2+}$ at all ionizing energies up to 200 eV. The branching ratio for deprotonation is a maximum near 40 eV (75%), then decreases slowly to just above 60% at an ionizing energy of 75 eV. Cleavage of the C-C bond, forming $CH^+ + CH^+$, is the second most abundant primary dissociation pathway. Branching ratios for this channel rise steadily from 20% at 40 eV to over 35% at 75 eV, then remain approximately constant up to an ionizing energy of 200 eV. Decarbonation of the vinylidenic $C_2H_2^{2+}$ isomer, affording $CH_2^+ + C^+$, is the weakest primary dissociation channel. The $CH_2^+ + C^+$ product branching ratio is apparently a maximum close to threshold, then decays gradually to below 2% at ionizing energies above 65 eV. Thissen *et al.* measured the branching ratios of the primary dissociation channels following photoionization at 48.4 eV as 57%, 38% and 2% for $C_2H^+ + H^+$, $CH^+ + CH^+$, and $CH_2^+ + C^+$, respectively[25]. These values agree well with the branching ratios for 75 eV ionizing electrons (61.6%, 36.8%, 1.6%) derived in this work. Indeed, in studies of the ionization of aromatic hydrocarbons, similar dissociation patterns have been observed following 70 eV electron impact and photon impact at 35 eV.[58,60]

In a recent theoretical study, Zyubina *et al.* employed an *ab initio*/RRKM approach to calculate branching ratios for primary dissociations on both the ground triplet ($^3\Sigma_g^-$) and lowest singlet ($^1\Delta_g$) potential energy surfaces of $C_2H_2^{2+}$.[48] These calculations were performed as a function of available dication internal energy E_{int}. If fragmentation were to occur solely on the $^3\Sigma_g^-$ potential energy surface, theory predicts that the branching ratio for deprotonation should decrease steadily from 100% to 62%, as E_{int} increases from 3.7 eV to 20 eV. By contrast, the branching ratio of the $CH^+ + CH^+$ channel should increase from 0.2% to 37%, while the branching ratio for forming $CH_2^+ + C^+$ is predicted to remain below 2%. On the $^1\Delta_g$ surface, calculations predict that the branching ratio for $CH_2^+ + C^+$ formation is largest at $E_{int} = 4.2$ eV (50%), then decays sharply to below 3% as the available dication internal energy is increased. From the $^1\Delta_g$ state, calculations indicate the branching ratio for deprotonation rises rapidly from 30% to above 65% as E_{int} increases from 4.2 eV to 8 eV, while the $CH^+ + CH^+$ branching ratio remains almost constant (~26%) when $E_{int}>5$ eV.

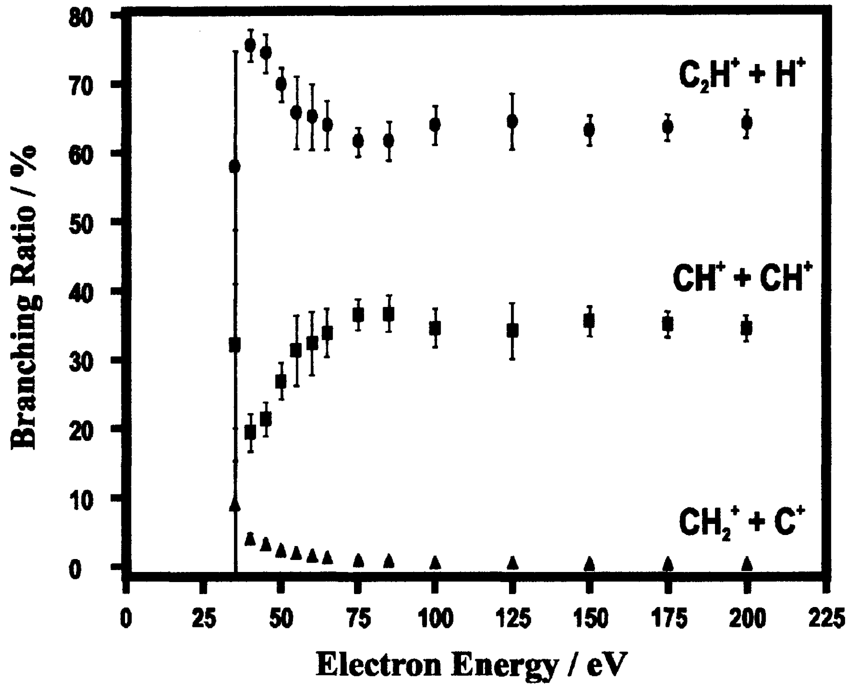

Figure 6.9 Branching ratios for primary charge-separating dissociation of $C_2H_2^{2+}$, shown as a function of ionizing electron energy. The error bars represent two standard deviations of five experimental determinations.

If one assumes that increasing the available dication internal energy from 3-20 eV corresponds approximately to increasing the ionizing electron energy from 40-75 eV[58,60] the branching ratios derived in this work are in good accord with the theoretical study of Zyubina *et al.*[48] Such a comparison suggests that dissociation of $C_2H_2^{2+}$ occurs predominantly on the ground triplet PES. Specifically, the decrease in the branching ratio for forming $C_2H^+ + H^+$ concurrent with a steady increase in the branching ratio for forming $CH^+ + CH^+$, between 40 eV and 75 eV, agrees well with the calculations of Zyubina *et al.* for the $^3\Sigma_g^-$ surface.

However, calculations on $C_2H_2^{2+}$ fragmentation purely on the ground triplet PES fail to account for the formation of CH_2^+ + C^+ observed below 65 eV (>2%), implicating the population of the $^1\Delta_g$ surface. In addition, the branching ratios observed for the C_2H^+ + H^+ channel at lower ionizing electron energy (40-50 eV), are smaller than predicted for population of only the $^3\Sigma_g^-$ state. Similarly the observed branching ratio for the CH^+ + CH^+ channel is larger than predicted for population of only the $^3\Sigma_g^-$ state. These discrepancies between theory and experiment can be explained by the involvement of the $^1\Delta_g$ state in the fragmentation of $C_2H_2^{2+}$. Of course, there may be some minor contribution from excited potential energy surfaces in this energy regime.

E / eV	$H^+ + C_2H^+$	$CH^+ + CH^+$	$C^+ + CH_2^+$	$H^+ + C_2^+$	$C^+ + CH^+$	$C^+ + C^+$	$H^+ + CH^+$	$H^+ + C^+$	$H^+ + H^+$
200	27.7(10)	14.2(10)	1.10(14)	15.9(10)	9.2(11)	6.3(7)	5.1(2)	19.1(7)	1.4(4)
175	27.9(9)	15.0(13)	1.04(11)	15.7(7)	9.3(7)	5.7(13)	5.4(4)	18.7(7)	1.3(4)
150	28.1(15)	15.4(16)	1.11(9)	15.9(7)	9.5(5)	5.8(9)	5.1(3)	18.0(9)	1.2(3)
125	29.8(18)	15(3)	1.15(3)	16.2(18)	9.3(11)	4.9(9)	5.2(5)	17.6(11)	0.8(3)
100	31.4(19)	16.3(14)	1.23(11)	16.4(4)	9.2(9)	4.1(7)	5.2(2)	15.4(10)	0.8(3)
85	33.1(17)	19(2)	1.41(11)	15.8(8)	9.7(5)	3.4(6)	5.2(5)	12.8(9)	
75	34.8(15)	19 (2)	1.64(7)	16.0(6)	9.7(7)	2.6(7)	5.2(3)	10.8(4)	
65	42(3)	20(3)	1.87(18)	15.7(6)	8.3(9)	1.3(5)	4.7(5)	6.3(10)	
60	46(4)	20(4)	2.2(3)	15.3(11)	7.9(11)	0.8(3)	4.0(2)	3.8(4)	
55	50(5)	21(4)	2.6(2)	14.1(12)	6.9(12)	0.35(9)	3.2(2)	2.0(5)	
50	59(2)	21(3)	3.0(3)	10.2(5)	4.1(6)	0.05(3)	1.7(5)	0.5(3)	
45	68(3)	19(3)	3.9(4)	6.6(8)	1.9(6)	0.15(16)	0.7(3)	0.2(40	
40	72(3)	16(4)	4.7(8)	3.7(8)	2.6(17)	0.25(23)	0.6(14)	-0.2(5)	
35	53(24)	12(15)	9.6(11)	4.7(20)	12(7)	1(3)	7(9)	1(2)	

Table 6.I Branching ratios for charge-separating dissociation of the acetylene dication, $C_2H_2^{2+}$, expressed relative to the cross section for forming $C_2H_2^+$, as a function of electron energy *E*. The value in parenthesis indicates the standard deviation in the last figure.

6.5.2 The Energetics of Dissociative Double Ionization

The kinetic energy of the ion pairs formed by dissociation of the acetylene dication have been determined using Monte Carlo simulations of the peaks observed in the pairs spectrum, as described in Section 3.5. All KER determinations were made from data recorded at electron energies between 55 and 65 eV, as these ionizing energies are the lowest which provide sufficient coincidence signals to produce a statistically significant result. Table 6.II summarises the results of these KER determinations, which, in combination with the dissociation limits derived from values in the literature, provide estimates of the precursor-state energies for forming ion pairs. In the sections that follow here the present KER measurements are compared with available experimental and theoretical data.

Ion Pair	Neutral Products	KER / eV		Dissociation Limit[a] / eV	Precursor-State Energy / eV	
		This work	Thissen *et al.*[b]		This work	Theory
$C_2H^+ + H^+$	none	3.5 ± 0.5	$3.3 \pm 1.0^{(1)}$ $3.7 \pm 0.5^{(2)}$ $5.0 \pm 0.4^{(3)}$ $5.5 \pm 0.4^{(4)}$	30.06	33.6 ± 0.5	$^3\Sigma_g^-$: 34.25^c, 33.90^d, 34.50^e $^1\Delta_g$: 35.38^c
$C^+ + CH_2^+$	none	3.5 ± 0.5	$4.2 \pm 0.7^{(2)}$ $4.5 \pm 0.4^{(3)}$	30.74	34.2 ± 0.5	$^1\Delta_g$: 34.55^c, 34.19^d $^3\Sigma_g^-$: 35.03^c, 34.39^d
$CH^+ + CH^+$	none	-	$4.4 \pm 1.0^{(2)}$ $5.0 \pm 0.3^{(3)}$ $5.4 \pm 0.2^{(4)}$	31.25		$^3\Sigma_g^-$: 36.08^c, 37.3^d $^1\Delta_g$: 35.12^c ^1A_g: 34.56^d
$H^+ + C_2^+$	H	4.0 ± 0.5	$4.0^{(3)}$ $6.0^{(4)}$	35.85	39.9 ± 0.5	
$C^+ + CH^+$	H	4.2 ± 0.5	$4.4 \pm 0.7^{(3)}$ $5.7^{(4)}$	35.40	39.6 ± 0.5	
$H^+ + CH^+$	C	-	~5	37.73		
$H^+ + C^+$	CH	-	~5	38.35		
$C^+ + C^+$	2H	-	-	39.54		
$H^+ + H^+$	C_2	-	6 ± 1	38.05		

a The dissociation limits are derived from values of heat of formation and fragment ionization energy taken from the NIST Chemistry Webbook[61,62]

b Data taken from Ref[25]. KER determinations performed at a photon energy: (1) 34.8 eV, (2) 38.0 eV, (3) 40.8 eV, (4) 48.4 eV.

c *Ab initio* calculations on the $^3\Sigma_g^-$ and $^1\Delta_g$ potential energy surfaces by Zyubina *et al.*[48]

d *Ab initio* calculations on the $^3\Sigma_g^-$ (^1A_g), and $^1\Delta_g$ potential energy surfaces by Duflot *et al.*[46]

e *Ab initio* calculations on the $^3\Sigma_g^-$ potential energy surface of Li and Schlegel.[44]

Table 6.II A comparison of the KER and precursor-state energies for ion pair formation following charge-separating decay of $C_2H_2^{2+}$ determined in this study, to recent experimental and theoretical work.

$C_2H^+ + H^+$

Deprotonation of $C_2H_2^{2+}$ is the dominant dication dissociation channel at all ionizing energies above the double ionization threshold, as is shown by the product branching ratios (Table 6.I) and σ_r values for monocation-pair formation (Figure 6.8). From a Monte Carlo simulation of this ion pair at 55 eV, a single kinetic energy release of 3.5 ± 0.5 eV is determined, in good agreement with corresponding data from earlier PIPICO measurements of Thissen *et al.*[25] at photon ionizing energies of 34.8 eV and 38 eV respectively (Table 6.II). When comparing energy transfer in electron ionization with photon ionization only a proportion of the energy of the incident electron is transferred to the target molecule, and the similarity of electron ionization spectra recorded at 70 eV to PI mass spectra recorded at 35 eV was remarked upon above. Previous investigations have shown that the $C_2H^+ + H^+$ dissociation channel stems from population of the X $^3\Sigma_g^-$ state of $C_2H_2^{2+}$ [25,46-48] and involves the formation of ground state products, C_2H^+ ($^3\Pi$) + H^+. The kinetic energy release value determined in this work gives a barrier to deprotonation on the $^3\Sigma_g^-$ ground triplet surface lying at 33.6 ± 0.5 eV in good agreement with previous values.[25,44,46,48]

In all of the coincidence spectra recorded above 35 eV a weak metastable tail emerging from the $C_2H^+ + H^+$ ion peak is observed. This metastable dissociation has been studied in detail previously and show that such metastable $C_2H_2^{2+}$ ions have a lifetime of 80 ns.[25,35]

$C^+ + CH_2^+$

For decarbonation a single KER of 3.5 ± 0.5 eV is determined following ionization by 65 eV electrons. In combination with the thermodynamic threshold this KER measurement suggests a precursor state of the vinylidene dication complex at 34.2 ± 0.5 eV (Table 6.II). The kinetic energy release determined in this work is slightly smaller, but in reasonable agreement with the measurements of Thissen *et al.* at photon ionizing energies of 38 eV and 40.8 eV.[25] As discussed above, theoretical studies predict decarbonation of the vinylidene dication to occur (mainly) on the ground singlet potential energy surface[48], and the branching ratios derived in this work (Figure 6.9) are in accord with this prediction.

$CH^+ + CH^+$

In the current experimental setup kinetic energy release determinations cannot easily be performed on monocation pairs with identical mass. Due to the 'deadtime' of the discrimination circuitry a proportion of $CH^+ + CH^+$ ions are missed in the pairs spectra. An estimate of the number of these missing counts is made using a simple geometric correction

(Section 3.2.2.3). It is noted however that this correction procedure increases the uncertainty in the dication branching ratios derived for forming ion pairs of identical mass (Table 6.I, Figure 6.9). As described above, the branching ratios derived for CH^+ + CH^+ formation appear consistent with those calculated by Zyubina *et al.*[48] involving a dominant contribution of the ground triplet surface. As shown in Figure 6.9, there is a significant increase in CH^+ + CH^+ production between 40 eV and 75 eV, consistent with an increasing number of acetylene dications with sufficient energy available to surmount the barrier to C-C bond cleavage on the $^3\Sigma_g^-$ surface.[25,48]

Recent calculations suggest that the lowest energy barrier to C-C bond cleavage of the acetylene dication occurs on the first excited singlet surface ($^1\Sigma_g^+$).[25,46,48] Furthermore, the first excited triplet surface ($^3\Pi$) is likely to dissociate, *via* a conical intersection, on to the $^1\Sigma_g^+$ surface.[48] Thus population of these excited electronic states should lead to an increase in the formation of CH^+ + CH^+ as the ionizing electron energy increases, as observed in the present data.

$C_2^+ + H^+$

In a previous photoionization study, Thissen *et al.* described the formation of C_2^+ + H^+ ion pairs from $C_2H_2^{2+}$ as a secondary decay of C_2H^+ to C_2^+, on the basis of peak shapes, peak slopes and intramolecular isotope effects by comparison with $HCCD^{2+}$.[25] From the dication product branching ratios derived in this work (Table 6.I) it is seen that C_2H^+ + H^+ decays preferentially to C_2^+ + H^+ following electron ionization below 100 eV, whereas above 100 eV the secondary dissociation of C_2H^+ favours the formation of C^+, forming a C^+ + H^+ ion pair.

The peak slopes measured for this ion pair are close to -1 below 65 eV, then rapidly become more negative with increasing electron energy (-1.9 at 100 eV, -2.6 at 200 eV). These values are consistent with observed trend in similar peak slopes measured using the PEPIPICO technique[25], with the caveat that the peak slopes measured in this study are the reciprocal of those of Thissen *et al.*, where the arrival times of the first and second ions of each ion pair in the coincidence spectra are plotted on opposite axes. For secondary decay of C_2H^+ to C_2^+ with no kinetic energy release in the secondary step the peak slope is expected to be -1.04, as is observed within experimental error below 65 eV (Section 3.4.3.3). The sharp rise in peak slope values above 65 eV was accounted for by Thissen *et al.* by the dissociation pathway involving an aligned KER in the secondary decay step ($C_2H^+ \rightarrow C_2^+ + H$) rising faster than the KER in the primary charge separation ($C_2H_2^{2+} \rightarrow C_2H^+ + H^+$).[25]

A Monte Carlo simulation of the coincidence data for this ion pair at 55 eV determines a kinetic energy release of 4.0 ± 0.5 eV, identical to the KER determination of Thissen *et al.* using 40.8 eV photons.[25] The asymptote for the formation of ground state products C_2^+ ($^4\Sigma_g^-$) + H (^2S) lies at 35.9 eV, suggesting a barrier to C_2^+ + H^+ formation of 39.9 ± 0.5 eV, in good agreement with the linearly extrapolated appearance potential (AP) of Thissen *et al.* (39.5 eV).[25]

$CH^+ + C^+$

The CH^+ + C^+ ion pair accounts for less than 10% of all charge separating dissociations of $C_2H_2^{2+}$ at ionizing energies below 200 eV, and has previously been described as a secondary decay of the CH^+ + CH^+ ion pair.[25] The peak slopes measured for this reaction do not vary with electron energy (-0.86 ± 0.04) and are in excellent agreement with the slopes measured by Thissen *et al.* following photoionization at 47 eV and 48.4 eV.[25] For a slow secondary decay of CH^+ to C^+ with no secondary KER, the expected peak slope for forming the CH^+ + C^+ ion pair is -0.92 (Section 3.4.3.3). The slightly lower peak slopes observed experimentally has been previously explained by a small component of KER in the secondary decay step, aligned along the direction of initial charge separation.[25]

From a Monte Carlo simulation at an ionizing electron energy of 55 eV a kinetic energy release of 4.2 ± 0.5 eV is determined, in good agreement with the KER measured by Thissen *et al.* at a photon energy of 40.8 eV (4.4 ± 0.7 eV).[25] Assuming the formation of ground state products CH^+ ($^1\Sigma^+$) + C^+ (^2P), which thermodynamic tables indicate lie at 35.4 eV[61,62], this suggests a barrier to CH^+ + C^+ formation of 39.6 ± 0.5 eV. This threshold agrees excellently with the linearly extrapolated AP of Thissen *et al.* (40.0 ± 0.5 eV) within experimental error limits.[25]

$H^+ + CH^+$

H^+ + CH^+ comprises a small proportion of ion pairs resulting from charge separating dissociation of $C_2H_2^{2+}$. As shown in Table 6.I, the branching ratio for this channel increases steadily from threshold and remains fairly constant above 65 eV at around 5%.

The peak slopes for this ion pair are close to -0.4 at an ionizing energy below 75 eV, and increase only slightly to around -0.5 at an electron energy above 150 eV. These peak slope values are in reasonable agreement with the corresponding measurements of Thissen *et al.* following photoionization of C_2H_2.[25] These authors have suggested that the H^+ + CH^+ ion pair is formed *via* a fast secondary dissociation (20 fs) of the CH^+ + CH^+ ion pair, where one CH^+ ion decays within the zone of Coulombic repulsion of the other CH^+ ion.

$H^+ + C^+$

Experimental peak shapes for C^+ + H^+ ion pairs exhibit a 'butterfly' peak shape (Figure 6.2) and has been described previously as resulting from secondary decay of C_2H^+ to C^+ + CH, with a small aligned KER.[25] Table 6.I shows that the dication branching ratio for this ion pair increases steadily from threshold to 200 eV, and becomes larger than the C_2^+ + H^+ branching ratio above 100 eV. Thus primary C_2H^+ ions decay preferentially to C^+ + CH as the ionizing electron energy exceeds 100 eV.

$C^+ + C^+$, $H^+ + H^+$

In the present experimental setup, measurements of peak slopes and KERs are difficult to perform for ion pairs of identical mass. As described above for the formation of CH^+ + CH^+, the dication branching ratios for forming C^+ + C^+ and H^+ + H^+ possess a greater uncertainty due to the geometric correction applied to these ion pair peaks. As shown in Table 6.I, the dication branching ratio for formation of C^+ + C^+ rises steadily from threshold to a maximum of over 6% at an ionizing energy of 200 eV.

6.6 Dissociations of the Acetylene Trication $C_2H_2^{3+}$

As described previously, in the coincidence mass spectra recorded at 200 eV two ion pairs and three ion triples are observed arising from the dissociation of the acetylene trication. Of these dissociation channels of $C_2H_2^{3+}$, the formation of the ion triples CH^+ + C^+ + H^+ and C^+ + C^+ + H^+ are the most abundant up to an ionizing electron energy of 200 eV. The precursor-specific relative PICS derived for ions formed by triple ionization (Figure 6.6) are very low, although these values represent a lower limit due to possible losses of translationally energetic ions as described previously. Typically the $\sigma_3[X^+]$ values measured in this work are around two orders of magnitude smaller than the corresponding $\sigma_2[X^+]$ values.

6.7 Conclusions

Time-of-flight mass spectrometry coupled with a 2-D ion coincidence technique has been used to measure relative partial ionization cross sections for the formation of positively charged ions following electron ionization of acetylene in the energy range 30-200 eV. Using this methodology relative precursor-specific PICS have been derived, which, for the first time for acetylene, quantify the contribution to the yield of each fragment ion from single, double and triple ionization. These measurements can be placed on an absolute scale by comparison with the recommended[36] PICS of Tian and Vidal[34].

Although a good agreement is found between the present data and several recent determinations of the PICS of acetylene[33-35] for the heavier ion fragments (C_2H^+ and C_2^+), some discrepancies exist between the available data for the lighter ion fragments such as CH^+, C^+ and H^+. For these lighter ions the cross sections measured in this work are, in many instances, significantly larger than some recent determinations.[33,35] These differences are attributed to losses of some translationally energetic fragment ions in these previous determinations. Overall the cross sections measured in this study are in excellent agreement with the data of Tian and Vidal[34] who demonstrated the efficient collection of energetic fragment ions.

The relative precursor specific PICS values reveal that contributions to the C_2H^+ and C_2^+ ion yields are dominated by dissociative single ionization across the ionizing energy range. By contrast, contributions to the yields of the lighter ion fragments H^+, C^+, CH_2^+, and to a lesser extent CH^+, from dissociative double ionization, are comparable to contributions from dissociative single ionization above 100 eV. Analysis shows that dissociative double ionization contributes 2% of the total ion yield at 50 eV, rising to over 10% at 200 eV. Contributions from dissociative triple ionization to the total ion yield remain very low within the energy range investigated in this work.

The analysis of the 2-D coincidence spectra provides information on the dynamics and energetics of charge separating dissociation of the acetylene dication ($C_2H_2^{2+}$). Simulations of peaks in the coincidence spectra provide estimates of the precursor state energies for forming product ion pairs and are in good agreement with data from a recent photoionization study by Thissen *et al.*[25] and theory[25,44,46,48]. A breakdown scheme for $C_2H_2^{2+}$ is derived[25] which yields branching ratios for primary (two body) charge separating dissociation of $C_2H_2^{2+}$. Comparison of this scheme with recent *ab initio*/RRKM calculations[48] suggests that below 75 eV, $C_2H_2^{2+}$ dissociates predominantly on the ground triplet potential energy surface ($^3\Sigma_g^-$) with a much smaller contribution from dissociation *via* the lowest singlet potential energy surface ($^1\Delta_g$).

6.8 References

1 V. G. Kunde, F. M. Flasar, D. E. Jennings, B. Bezard, D. F. Strobel, B. J. Conrath, C. A. Nixon, G. L. Bjoraker, P. N. Romani, R. K. Achterberg, A. A. Simon-Miller, P. Irwin, J. C. Brasunas, J. C. Pearl, M. D. Smith, G. S. Orton, P. J. Gierasch, L. J. Spilker, R. C. Carlson, A. A. Mamoutkine, S. B. Calcutt, P. L. Read, F. W. Taylor, T. Fouchet, P. Parrish, A. Barucci, R. Courtin, A. Coustenis, D. Gautier, E. Lellouch, A. Marten, R. Prange, Y. Biraud, C. Ferrari, T. C. Owen, M. M. Abbas, R. E. Samuelson, F. Raulin, P. Ade, C. J. Cesarsky, K. U. Grossman, and A. Coradini, Science **305** (5690), 1582 (2004).

2 P. V. Sada, G. L. Bjoraker, D. E. Jennings, G. H. McCabe, and P. N. Romani, Icarus **136** (2), 192 (1998).

3 T. Encrenaz, H. Feuchtgruber, S. K. Atreya, B. Bezard, E. Lellouch, J. Bishop, S. Edgington, T. de Graauw, M. Griffin, and M. F. Kessler, Astronomy And Astrophysics **333** (2), L43 (1998).

4 R. Courtin, D. Gautier, A. Marten, and B. Bezard, Astrophys. J. **287** (2), 899 (1984).

5 A. Coustenis, R. K. Achterberg, B. J. Conrath, D. E. Jennings, A. Marten, D. Gautier, C. A. Nixon, F. M. Flasar, N. A. Teanby, B. Bezard, R. E. Samuelson, R. C. Carlson, E. Lellouch, G. L. Bjoraker, P. N. Romani, F. W. Taylor, P. G. J. Irwin, T. Fouchet, A. Hubert, G. S. Orton, V. G. Kunde, S. Vinatier, J. Mondellini, M. M. Abbas, and R. Courtin, Icarus **189** (1), 35 (2007).

6 E. Herbst, Annual Review of Physical Chemistry **46**, 27 (1995).

7 V. G. Anicich and M. J. McEwan, Planet Space Sci. **45** (8), 897 (1997).

8 M. J. McEwan and V. G. Anicich, Mass Spectrometry Reviews **26** (2), 281 (2007).

9 P. Redondo, M. J. Ruiz, R. Boronat, C. Barrientos, and A. Largo, Theoretical Chemistry Accounts **104** (3-4), 199 (2000).

10 J. Evans, in *Chemistry World* (2004), Vol. 1(10).

11 I. A. Larionova, B. S. Fialkov, K. Y. Kalinich, A. B. Fialkov, and B. S. Ospanov, Combustion Explosion And Shock Waves **29** (3), 341 (1993).

12 G. Cooper, T. Ibuki, Y. Iida, and C. E. Brion, Chem. Phys. **125** (2-3), 307 (1988).

13 T. Hayaishi, S. Iwata, M. Sasanuma, E. Ishiguro, Y. Morioka, Y. Iida, and M. Nakamura, J. Phys. B-At. Mol. Opt. Phys. **15** (1), 79 (1982).

14 Y. Ono and C. Y. Ng, J. Chem. Phys. **74** (12), 6985 (1981).

15 M. Davister and R. Locht, Chem. Phys. **189** (3), 805 (1994).

16 M. Davister and R. Locht, Chem. Phys. **191** (1-3), 333 (1995).

17 R. Locht and M. Davister, Chem. Phys. **195** (1-3), 443 (1995).

18 R. Locht and C. Servais, Zeitschrift Fur Physikalische Chemie-International Journal Of Research In Physical Chemistry & Chemical Physics **195**, 153 (1996).

19 P. Plessis and P. Marmet, Int. J. Mass Spectrom. Ion Process. **70** (1), 23 (1986).

20 C. Servais and R. Locht, Chem. Phys. Lett. **236** (1-2), 96 (1995).

21 C. J. Reid, J. A. Ballantine, S. R. Andrews, and F. M. Harris, Chem. Phys. **190** (1), 113 (1995).

22 K. Furuya, K. Maruyama, E. Koto, A. Matsuo, and T. Ogawa, J. Phys. B-At. Mol. Opt. Phys. **33** (8), 1475 (2000).

23 G. K. Jarvis, K. M. Weitzel, M. Malow, T. Baer, Y. Song, and C. Y. Ng, Phys. Chem. Chem. Phys. **1** (22), 5259 (1999).

24 K. Norwood and C. Y. Ng, J. Chem. Phys. **91** (5), 2898 (1989).

25 R. Thissen, J. Delwiche, J. M. Robbe, D. Duflot, J. P. Flament, and J. H. D. Eland, J. Chem. Phys. **99** (9), 6590 (1993).

26 K. M. Weitzel, J. Mahnert, and M. Penno, Chem. Phys. Lett. **224** (3-4), 371 (1994).

27 G. Josifov, D. Lukic, N. Duric, and M. Kurepa, Journal Of The Serbian Chemical Society **65** (7), 517 (2000).

28 K. K. Irikura, Y. K. Kim, and M. A. Ali, Journal Of Research Of The National Institute Of Standards And Technology **107** (1), 63 (2002).

29 Y. K. Kim, M. A. Ali, and M. E. Rudd, Journal Of Research Of The National Institute Of Standards And Technology **102** (6), 693 (1997).

30 H. Deutsch, K. Becker, S. Matt, and T. D. Mark, Int. J. Mass Spectrom. **197**, 37 (2000).

31 J. T. Tate, P. T. Smith, and A. L. Vaughan, Physics Review **39**, 270 (1935).

32 A. Gaudin and R. Hagemann, J. Chim. Phys.-Chim. Biol. **64** (7-8), 1209 (1967).

33 S. H. Zheng and S. K. Srivastava, J. Phys. B-At. Mol. Opt. Phys. **29** (14), 3235 (1996).

34 C. C. Tian and C. R. Vidal, J. Phys. B-At. Mol. Opt. Phys. **31** (4), 895 (1998).

35 S. Feil, K. Gluch, A. Bacher, S. Matt-Leubner, D. K. Bohme, P. Scheier, and T. D. Mark, J. Chem. Phys. **124** (21), 4307 (2006).

36 T. Shirai, T. Tabata, H. Tawara, and Y. Itikawa, Atomic Data And Nuclear Data Tables **80** (2), 147 (2002).

37 B. P. Tsai and J. H. D. Eland, Int. J. Mass Spectrom. Ion Process. **36** (2), 143 (1980).

38 J. H. D. Eland, F. S. Wort, P. Lablanquie, and I. Nenner, Zeitschrift Fur Physik D-Atoms Molecules And Clusters **4** (1), 31 (1986).

39 R. I. Hall, L. Avaldi, G. Dawber, A. G. McConkey, M. A. Macdonald, and G. C. King, Chem. Phys. **187** (1-2), 125 (1994).

40 T. Kinugawa, P. Lablanquie, F. Penent, J. Palaudoux, and J. H. D. Eland, Journal Of Electron Spectroscopy And Related Phenomena **141** (2-3), 143 (2004).

41 S. R. Andrews, F. M. Harris, and D. E. Parry, Chem. Phys. **166** (1-2), 69 (1992).

42 O. Furuhashi, T. Kinugawa, S. Masuda, C. Yamada, and S. Ohtani, Chem. Phys. Lett. **342** (5-6), 625 (2001).

43 N. Jeffreys, S. R. Andrews, D. E. Parry, and F. M. Harris, Rapid Communications In Mass Spectrometry **10** (13), 1693 (1996).

44 X. S. Li and H. B. Schlegel, J. Phys. Chem. A **108** (3), 468 (2004).

45 J. Palaudoux and M. Hochlaf, J. Chem. Phys. **126** (04), 4302 (2007).

46 D. Duflot, J. M. Robbe, and J. P. Flament, J. Chem. Phys. **102** (1), 355 (1995).

47 J. A. Pople, M. J. Frisch, K. Raghavachari, and P. V. Schleyer, Journal Of Computational Chemistry **3** (4), 468 (1982).

48 T. S. Zyubina, Y. A. Dyakov, S. H. Lin, A. D. Bandrauk, and A. M. Mebel, J. Chem. Phys. **123** (13), 4320 (2005).

49 W. C. Wiley and I. H. McLaren, Review Of Scientific Instruments **26** (12), 1150 (1955).

50 S. Feil, A. Bacher, M. Zangerl, W. Schustereder, K. Gluch, and P. Scheier, Int. J. Mass Spectrom. **233** (1-3), 325 (2004).

51 D. M. Curtis and J. H. D. Eland, Int. J. Mass Spectrom. Ion Process. **63** (2-3), 241 (1985).

52 N. A. Love and S. D. Price, Phys. Chem. Chem. Phys. **6** (19), 4558 (2004).

53 A. S. Alnaser, I. Litvinyuk, T. Osipov, B. Ulrich, A. Landers, E. Wells, C. M. Maharjan, P. Ranitovic, I. Bochareva, D. Ray, and C. L. Cocke, J. Phys. B-At. Mol. Opt. Phys. **39** (13), S485 (2006).

54 S. Boye-Peronne, D. Gauyacq, and J. Lievin, J. Chem. Phys. **124** (21), 4305 (2006).

55 S. Hayakawa, M. Takahashi, K. Arakawa, and N. Morishita, J. Chem. Phys. **110** (6), 2745 (1999).

56 S. Hayakawa, K. Tomozawa, T. Takeuchi, K. Arakawa, and N. Morishita, Phys. Chem. Chem. Phys. **5** (11), 2386 (2003).

57 T. Osipov, C. L. Cocke, M. H. Prior, A. Landers, T. Weber, O. Jagutzki, L. Schmidt, H. Schmidt-Bocking, and R. Dorner, Phys. Rev. Lett. **90** (23), 3002 (2003).

58 S. Leach, J. H. D. Eland, and S. D. Price, J. Phys. Chem. **93** (22), 7583 (1989).

59 E. Ruhl, S. D. Price, S. Leach, and J. H. D. Eland, Int. J. Mass Spectrom. Ion Process. **97** (2), 175 (1990).

60 S. Leach, J. H. D. Eland, and S. D. Price, J. Phys. Chem. **93** (22), 7575 (1989).

61 H. Y. Afeety, J. F. Liebman, and S. E. Stein, *"Neutral Thermochemical Data"*. (National Institute of Standards and Technology, Gaithersburg MD, 20899 (http://webbook.nist.gov), June 2005).

62 S. G. Lias, *"Ion Energetics Data"*. (National Institute of Standards and Technology, Gaithersburg MD, 20899 (http://webbook.nist.gov), June 2005).

Chapter 7 Electron Ionization of CO_2

7.1 Introduction

Ionization of CO_2 is a process of importance in a number of planetary atmospheres[1-3] and plasma environments. Recent astrophysical models of the Martian atmosphere, where CO_2 is subject to magnetotail electron-ionization, predict an extensive ion-molecule chemistry involving the products of both dissociative and non-dissociative ionization[1]. Furthermore the existence of a CO_2^{2+} layer in the atmosphere of Mars has recently been predicted[3]. Such models require accurate and reliable data on the formation efficiency of both the parent ion and the various ionic fragments resulting from both single and multiple ionization. This information is often most conveniently expressed in the form of partial ionization cross sections (PICS).

7.1.1 Partial Ionization Cross Sections of CO_2

The dissociative ionization of CO_2 has been the subject of a number of investigations employing a variety of techniques: electron-ionization mass spectrometry[4-17], photoionization mass spectrometry[18-29], collisions with positrons[30], collisions with high translational energy ions[31], ultrafast laser pulses[32] and coincidence techniques[18,19,21-24,31-35]. Concentrating on the previous cross section determinations for electron ionization of CO_2, the total ionization cross section has been measured from threshold to 100 eV by Asundi *et al.*[4] and from threshold to 1000 eV by Rapp and Englander-Golden[11]. The total dissociative ionization cross section has been derived by Rapp *et al.*[12] *via* measurements of the number of ions formed with greater than 0.25 eV of translational kinetic energy. Cross sections for the formation of CO_2^+ and CO_2^{2+} ions were reported by Märk and Hille[9] at an ionizing energy between threshold and 180 eV and absolute cross sections for the formation of CO_2^+ ions were obtained by Freund *et al.*[7] for energies up to 200 eV. PICS for the formation of singly charged fragment ions CO^+, O^+ and C^+ have been measured, using a quadrupole mass spectrometer (QMS), by Crowe and McConkey[6] up to an ionizing energy of 300 eV and by Orient and Srivastava[10] in the energy range 10-510 eV. Straub *et al.*[13] measured PICS for the formation of singly and doubly charged ions from threshold to 1000 eV using a time-of-flight mass spectrometer coupled with position sensitive ion detection. In this way Straub *et al.*[13] were able to demonstrate the complete collection of all ionic fragments, including those formed with considerable translational kinetic energy. Tian and Vidal[15] used a focusing time-of-flight mass spectrometer (TOFMS) to measure PICS up to an electron energy of 300 eV and cross sections for the formation of ion pairs up to 600 eV using a covariance mapping technique[14]. Comparison of these more recent determinations to the existing PICS data sets revealed some considerable discrepancies, particularly concerning the formation of the fragment ions C^+ and O^+, for which the PICS values of Straub *et al.*[13] and Tian and Vidal[15] are considerably larger than those measured in previous studies. Such discrepancies were attributed to the inefficient collection of energetic ion fragments in the earlier determinations of these PICS.

In this study the electron ionization of CO_2 is investigated in the energy range 30-200 eV, using time-of-flight mass spectrometry coupled with a 2-D ion coincidence technique. Relative PICS $\sigma_r[X^{m+}]$ are derived for the formation of C^+, O^+, CO^+, C^{2+}, O^{2+} and CO_2^{2+} ions, expressed relative to the formation of the parent monocation CO_2^+. The data are shown to be in excellent agreement with the existing PICS data for forming these ions reported by Straub *et al.*[13] and Tian and Vidal[15]. Relative precursor-specific relative PICS $\sigma_n[X^{m+}]$ are then derived, which quantify the contribution to the yield of the various fragment ions from single (n=1), double (n=2) and triple (n=3) ionization. These precursor-specific relative PICS include, for the first time, measurements on the formation of ion triples following electron-ionization of CO_2. In addition, relative PICS for the formation of product ion pairs formed *via* the dissociation of the CO_2^{2+} dication are reported.

7.1.2 The Carbon Dioxide Dication CO_2^{2+}

The 2-D ion coincidence technique used in this work also provides information on the energetics and dissociation dynamics of the CO_2 dication and trication. The energies of the electronic states of CO_2^{2+} have been extensively studied using photoion-photion coincidence (PIPICO) spectroscopy[18,19,22-24], photoelectron-photoelectron coincidence (PEPECO) spectroscopy[33,36], threshold photoelectrons coincidence spectroscopy[33,37] (TPEsCO), double charge transfer (DCT) spectroscopy[38], position sensitive ion coincidence spectroscopy[5] and theoretical methods[24,39,40]. In this study simulations are performed to determine the kinetic energy release involved in ion pair formation following dissociative double ionization of CO_2. These measurements show that indirect processes play a significant role in ion pair formation close to the double ionization threshold.

7.2 Experimental Procedures

All experiments in this study were performed using a TOF mass spectrometer of Wiley-McLaren design, as has been described in detail in Section 2.3. The CO_2 gas used was a commercial sample of good purity (>99.8%). The operating conditions of the experiment again involve low target gas pressures ($< 10^{-6}$ Torr) and low electron flux, ensuring that on average much less than one ionization event is detected per ionizing pulse of electrons. As has been described previously, this methodology greatly reduces the number of 'false coincidences' that contribute to the coincidence spectra recorded. The voltage conditions used in this study are those described in Section 2.3 and permit the efficient collection of ions formed initially with up to 11 eV of translational energy.

7.3 Data Analysis

7.3.1 Singles Mass Spectra

A representative singles mass spectrum of CO_2 recorded at an ionizing electron energy of 200 eV is shown in Figure 7.1. The intensities of individual ion peaks, $I_1[X^+]$ for monocations and $I_2[X^{2+}]$ for dications, appearing in the singles mass spectrum, are extracted using the analysis procedure described in Section 3.2.1. Due to the low target gas pressures employed in this study, a small number of ions emanating from traces of residual gases in the vacuum chamber contribute to each singles mass spectrum recorded. Specifically, ionization of residual O_2 and H_2O results in the formation of ions which contribute to the counts in the O^+ and O^{2+} peaks, while ionization of residual N_2 yields N_2^+ and N^+ ions which contribute to the counts in the CO^+ and CO^{2+} peaks respectively. These minor contributions to the mass spectrum are subtracted, using the procedure outlined in Section 3.2.1.2, by normalization to the H_2O^+ and O_2^+ peak intensities, respectively. This normalization procedure can only be performed by assuming that the formation of O_2^+ following ionization of CO_2 is negligible. To test this assumption the yield of O_2^+ ions with respect to Ar^+ ions were measured in the mass spectra of air recorded in preliminary experiments (Appendix C). These ratios are in very good agreement with the ratio of O_2^+ to Ar^+ ions measured in all the CO_2 spectra, confirming that the formation of O_2^+ following ionization of CO_2 is negligible.

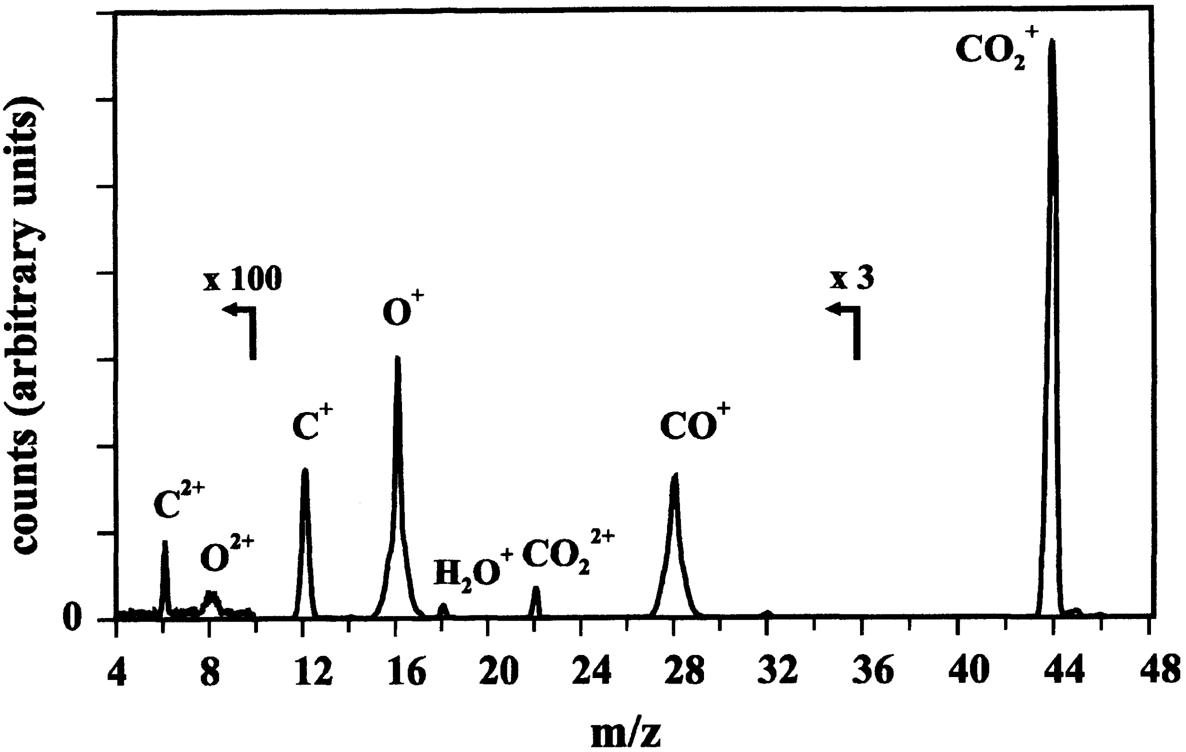

Figure 7.1 A characteristic (singles) mass spectrum of CO_2 following electron impact ionization at 200 eV.

7.3.2 Ion Coincidence Spectra

A representative pairs mass spectrum of CO_2 recorded at an ionizing electron energy of 200 eV is shown in Figure 7.2. The intensities of the various ion peaks are then extracted, using the procedure described in Section 3.2.2, to yield the number of individual ion pairs $P[X^+ + Y^+]$, and also the overall contribution of each individual fragment ion to the pairs spectrum $P[X^+]$. In this work a distinction is made between the ion counts in pairs which must be formed *via* dissociative triple ionization of the CO_2 trication $P_3[X^+]$, for example $CO^+ + O^{2+}$, and the ion counts in the other peaks in the pairs spectrum which may contain contributions from both dissociative double and triple ionization $P_2[X^+]$, such as $C^+ + O^+$. The number of false coincidences is evaluated manually for each peak using an ion-autocorrelation function (Section 3.2.2.1), typically less than 2% of the raw peak intensity for monocation pairs formed at higher ionizing energy, which is then subtracted. A further correction is made to the intensity of the $O^+ + O^+$ and $O^{2+} + O^+$ peaks to account for the small contributions from ionization of residual O_2 in the vacuum chamber described above. In the experiment no ion pairs are recorded if the second ion arrives at the detector within 32 ns of the first ion, due to the 'deadtime' of the discrimination circuitry. Such deadtime losses significantly affect the number of counts recorded in the $O^+ + O^+$ peak in the pairs spectra. To estimate the number of ions lost, a separate one-dimensional (t_2-t_1) spectrum is constructed from the $O^+ + O^+$ coincidence data which is then appropriately extrapolated to the limit $t_1=t_2$, using simple geometry, to correct for the losses (Section 3.2.2.3).

Metastable CO_2^{2+} Ions

In the CO_2 pairs spectra a 'tail' is observed originating from the $CO^+ + O^+$ ion pair peaks, extending to the limit $t_1=t_2\approx1545$ ns, arising from the slow dissociation of CO_2^{2+} ions in metastable states[14,33,41] (Figure 7.2). These counts are included in the yields measured for the formation of CO^+ and O^+ ions *via* dissociative double ionization. Metastable CO_2^{2+} ions which survive for at least 1500 ns will be recorded as single ion detections. Thus the cross sections measured for the formation of CO_2^{2+} ions in this work are for CO_2^{2+} ions which have a lifetime longer than about 1500 ns.

In all the coincidence spectra recorded any contributions from dissociative quadruple ionization are neglected, due to the low cross sections measured for triple ionization of CO_2 in the energy regime of this work, as described in the sections that follow. Therefore, there is only one possible 'real' triple ion coincidence, $C^+ + O^+ + O^+$. Ion triples are processed by specifying a time-of-flight range for the C^+ ion and then extracting all ion triples containing at least one ion whose arrival time t_1 lies within this specified range. Once extracted, the respective flight times of the two remaining ions ($O^+ + O^+$) forming an ion triple are displayed as a two-dimensional histogram (t_2 *vs.* t_3). The contribution of a fragment ion $T[X^+]$ is then obtained from the number of counts in the $O^+ + O^+$ peak, after applying a small geometric correction to account for losses due to the 'deadtime', as described above. False triple coincidences that contribute to the intensity of each triples peak are subtracted using the procedure outlined in Section 3.2.3.1.

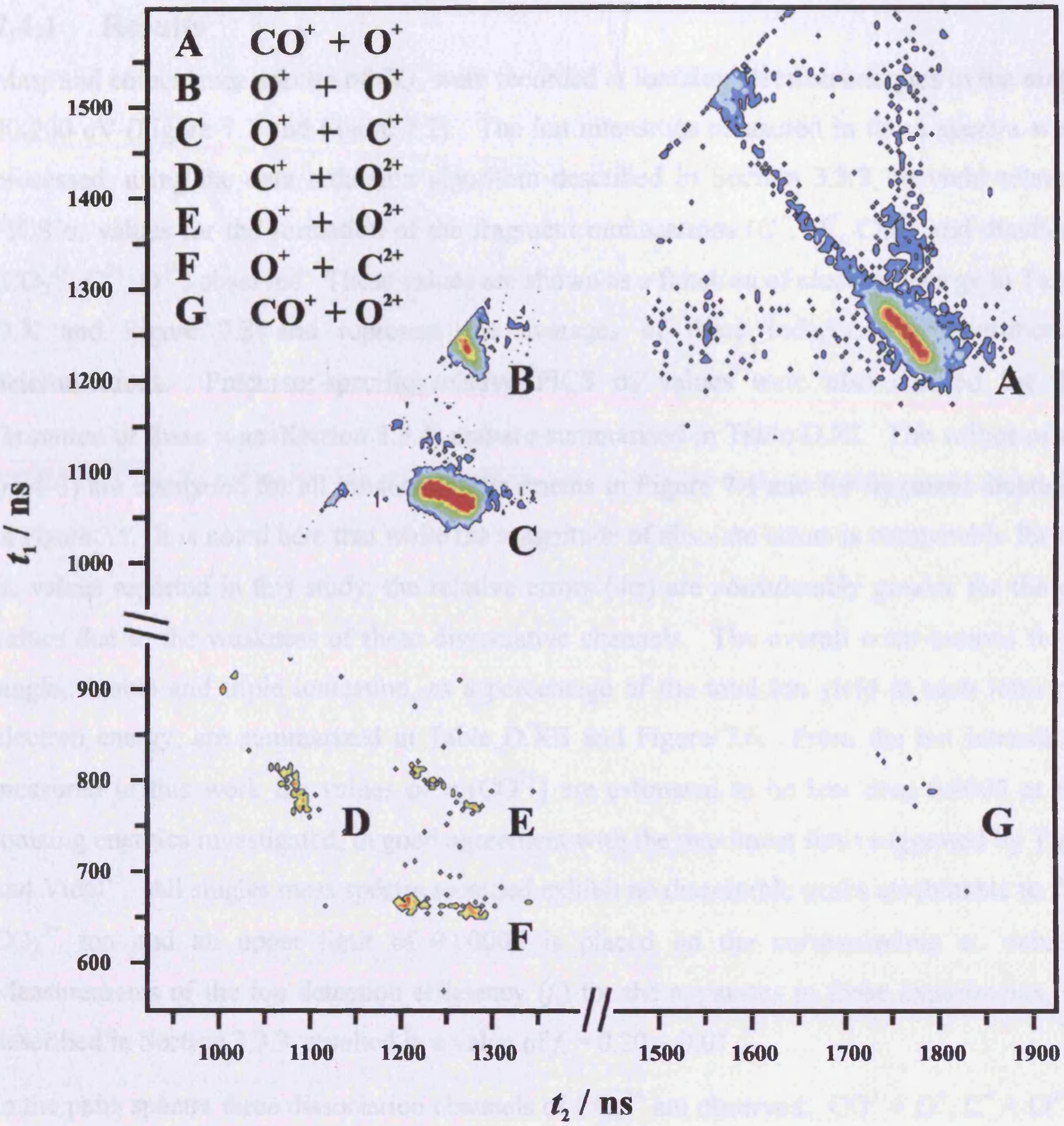

Figure 7.2 Representative 'pairs' mass spectrum of CO_2 recorded at 200 eV showing observed ion pairs formed *via* charge-separating dissociation of CO_2^{2+} and CO_2^{3+}. Notice also a 'tail' emanating from the $CO^+ + O^+$ ion pair peak arising from the slow dissociation of metastable CO_2^{2+} ions.

All ion intensities measured in this work were corrected numerically using the natural isotopic distributions: ^{12}C:^{13}C (98.93% : 1.07%), ^{16}O:^{17}O:^{18}O (99.76% :0.04%:0.20%).

7.4 Relative Partial Ionization Cross Sections

7.4.1 Results

Mass and coincidence spectra of CO_2 were recorded at ionizing electron energies in the range 30-200 eV (Figure 7.1 and Figure 7.2). The ion intensities measured in these spectra were processed, using the data reduction algorithm described in Section 3.3.2, to yield relative PICS σ_r values for the formation of the fragment monocations (C^+, O^+, CO^+) and dications (CO_2^{2+}, C^{2+}, O^{2+}) observed. These values are shown as a function of electron energy in Table D.X and Figure 7.3 and represent the averages of three independent experimental determinations. Precursor-specific relative PICS σ_n values were also derived for the formation of these ions (Section 3.3.4) and are summarised in Table D.XI. The values of σ_n (n=1-3) are compared for all monocation fragments in Figure 7.4 and for fragment dications in Figure 7.5. It is noted here that while the magnitude of absolute errors is comparable for all σ_n values reported in this study, the relative errors (4σ) are considerably greater for the σ_3 values due to the weakness of these dissociative channels. The overall contributions from single, double and triple ionization, as a percentage of the total ion yield at each ionizing electron energy, are summarized in Table D.XII and Figure 7.6. From the ion intensities measured in this work the values of $\sigma_r[CO^{2+}]$ are estimated to be less than 0.0005 at all ionizing energies investigated, in good agreement with the maximum limit suggested by Tian and Vidal[15]. All singles mass spectra recorded exhibit no discernible peaks attributable to the CO_2^{3+} ion and an upper limit of 0.00002 is placed on the corresponding σ_r values. Measurements of the ion detection efficiency (f_i) for the apparatus in these experiments, as described in Section 3.3.3, resulted in a value of $f_i = 0.20 \pm 0.01$.

In the pairs spectra three dissociation channels of CO_2^{2+} are observed: $CO^+ + O^+$, $C^+ + O^+ + O$ and $O^+ + O^+ + C$. At electron energies above 75 eV, an additional four ion pairs and one ion triple resulting from dissociation of CO_2^{3+} are observed: $C^+ + O^{2+} + O$, $O^+ + O^{2+} + C$, $CO^+ + O^{2+}$, $O^+ + C^{2+} + O$ and $C^+ + O^+ + O^+$. Values of σ_r for the formation of monocation-monocation pairs formed by CO_2^{2+} dication dissociation are shown in Table D.XIX and Figure 7.7. The conclusions drawn from the coincidence signals concerning the energetics of dissociative double ionization of CO_2^{2+} and the dynamics of dissociative triple ionization of CO_2 are discussed below.

7.4.2 Discussion

7.4.2.1 Relative PICS (σ_r) Values

The values of $\sigma_r[X^+]$ determined in this work for the formation of monocation fragments ($X^+ = CO^+, O^+, C^+$), are shown in Figure 7.3. Over the entire ionizing energy range there is excellent agreement between these $\sigma_r[X^+]$ values and the values derived from the data of Straub *et al.*[13] and Tian and Vidal[15]. Both of these previous studies efficiently collected ion fragments with considerable translational kinetic energy, and hence, the close agreement between these data sets and the present $\sigma_r[X^+]$ values demonstrate the expected efficient collection of such energetic ion fragments in this apparatus. By contrast, the $\sigma_r[X^+]$ values for the formation of these monocation fragments derived from the data of Orient and Srivastava[10] lie considerably lower than these data sets. The lower PICS measurements for the formation of CO^+, O^+ and C^+ by Orient and Srivastava[10], and in previous studies[6], can be explained[15] by the inefficient collection of ionic fragments formed with a translational energy in excess of a few electron volts.

Comparing (Figure 7.3) the values of $\sigma_r[C^{2+}]$ for the formation of dication fragments to the corresponding values derived from the data of Straub *et al.*[13] and Tian and Vidal[15] shows excellent agreement. A similar comparison of $\sigma_r[O^{2+}]$ values reveals a good agreement between the current measurements and the data of Straub *et al.*[13] The $\sigma_r[O^{2+}]$ values derived in this work are on average around 30 % smaller than the values derived from the data of Tian and Vidal[15], but both data sets agree within their mutual error limits.

7.4.2.2 Precursor-Specific Relative PICS

Unless noted below, the values for σ_1 and σ_2 derived in this work for the different fragment ions are in good agreement with values extracted from the existing covariance mapping data of Tian and Vidal[14]. One notes that no values of σ_3 for the different fragement ions involving the detection of ion triples have been determined before.

Comparison of the $\sigma_1[CO^+]$ and $\sigma_2[CO^+]$ values (Figure 7.4) to the data of Tian and Vidal[14] reveals that at ionizing energies above 100 eV, the contribution of CO^+ ions from double ionization is significantly larger than reported previously, whereas contributions to the CO^+ ion yield from single ionization are lower. The origin of this discrepancy is not readily apparent. One possible explanation for these differences is that Tian and Vidal extracted the

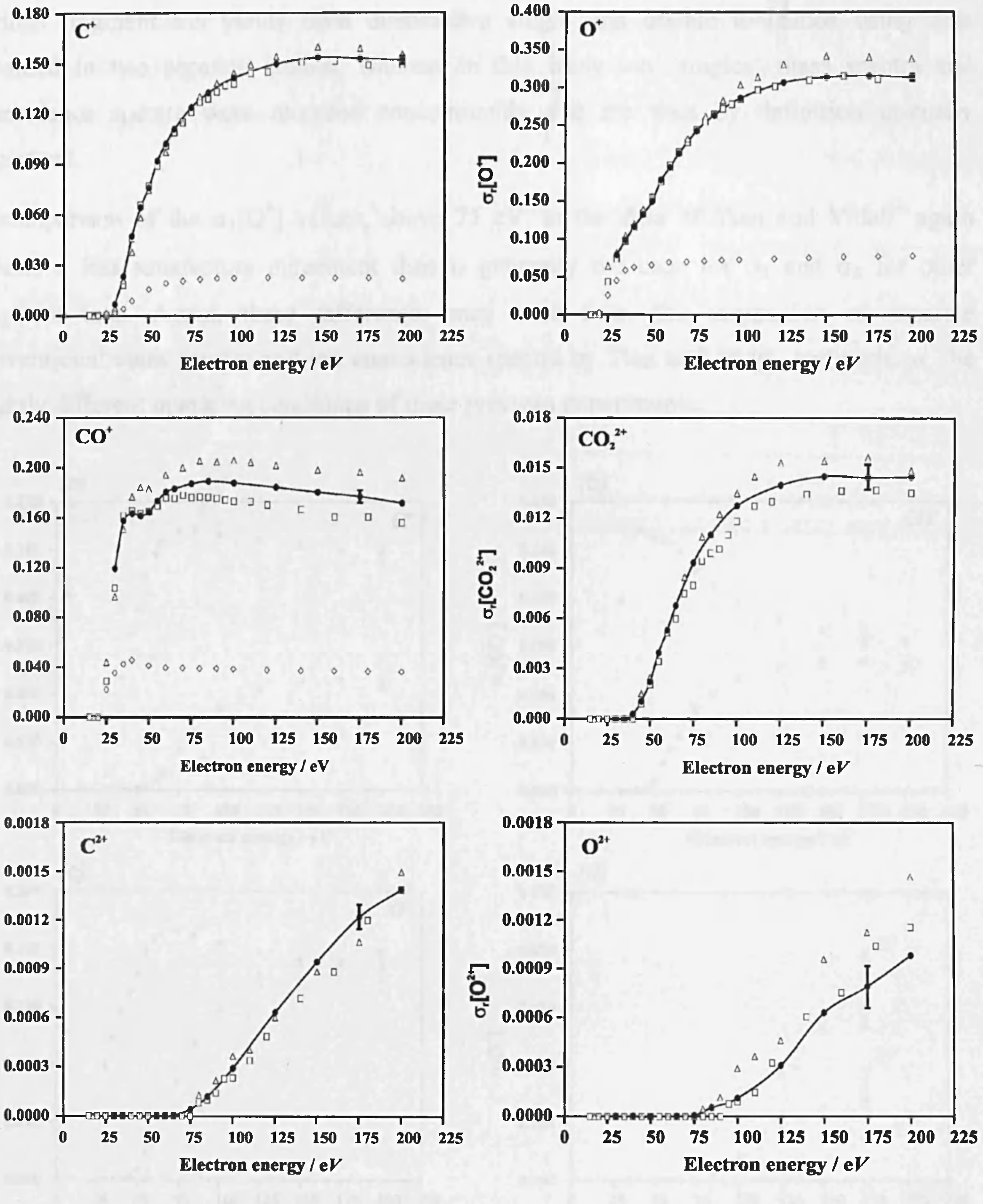

Figure 7.3 Relative PICS $\sigma_r[X^{n+}]$ for forming fragment ions (●) following electron ionization of CO_2. The error bars expressed in this figure represent four standard deviations of three separate determinations. The corresponding relative PICS extracted from the data of Tian and Vidal[15] (△), Straub *et al.*[13] (□) and Zheng and Srivastava[10] (◊) are also shown.

various fragment ion yields from dissociative single and double ionization using data recorded in two separate studies, whereas in this study ion 'singles' mass spectra and coincidence spectra were recorded concomitantly and are thus by definition mutually consistent.

A comparison of the $\sigma_1[O^+]$ values, above 75 eV, to the data of Tian and Vidal[14] again reveals a less satisfactory agreement than is generally the case for σ_1 and σ_2 for other fragment ions. Again, these differences may arise from the acquisition of separate conventional mass spectra and ion coincidence spectra by Tian and Vidal, and perhaps, the slightly different operating conditions of these previous experiments.

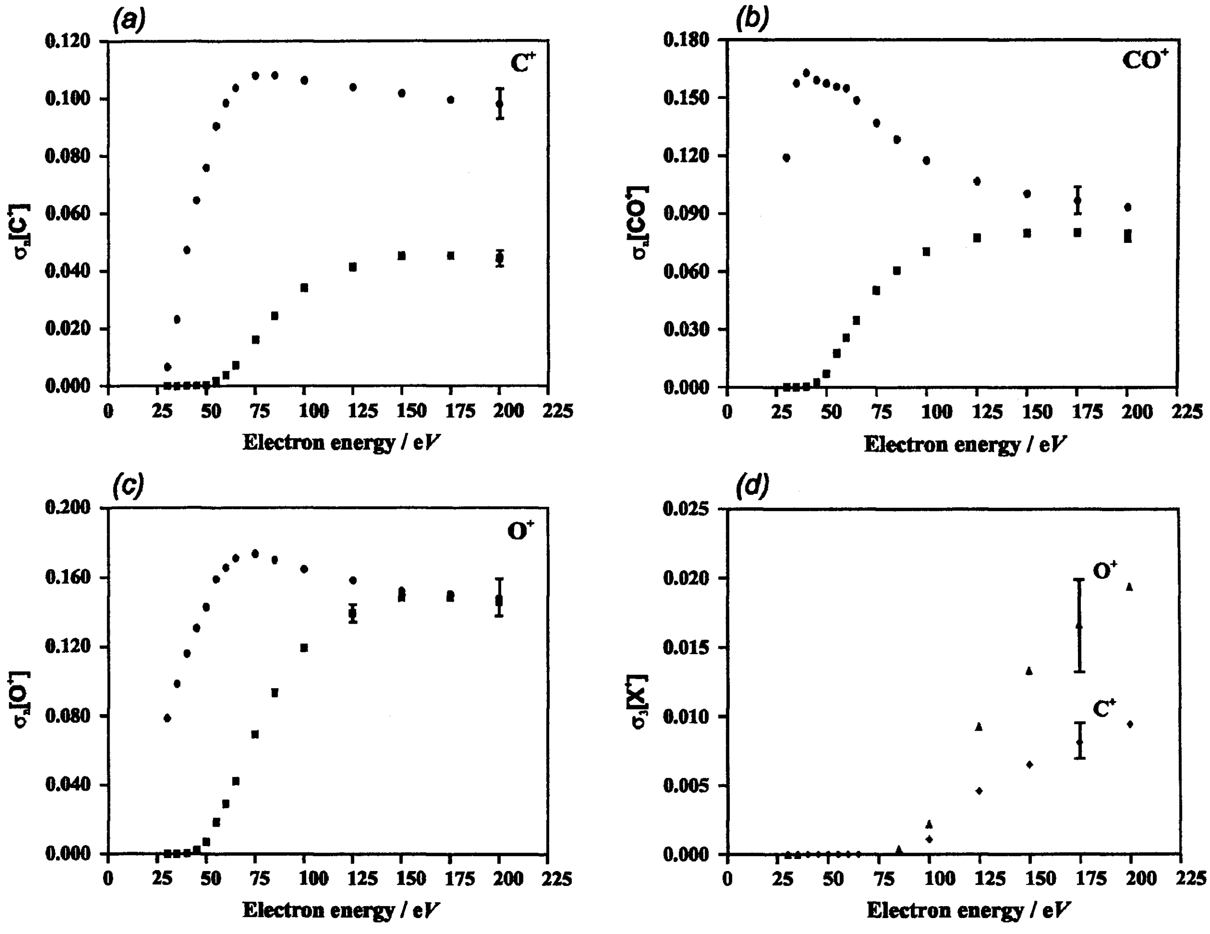

Figure 7.4 Precursor specific relative PICS for forming monocation fragments *via* single ionization (●), and *via* double ionization (■), following electron ionization of CO_2 (graphs a-c). Relative precursor specific PICS for forming monocation fragments C^+ (♦) and O^+ (▲) *via* triple ionization, are shown in graph (d). The representative error bars show four standard deviations of three separate determinations.

In Figure 7.5 it is shown that contributions to the C^{2+} ion yield are from both double and triple ionization. From the $\sigma_2[C^{2+}]$ values a threshold for C^{2+} formation is determined at 72±3 eV, in good agreement with previous determinations.[15,16] Recently, Straub *et al.*[13] showed that at 200 eV C^{2+} ions are formed with a near-thermal kinetic energy distribution. On this basis it was proposed that the most likely mechanism for forming C^{2+} ions at this ionizing energy was *via* dissociative double ionization. However, the present measurements show that at 200 eV contributions to the C^{2+} ion yield are from both double and triple ionization in almost equal proportions. Thus, C^{2+} ions are formed with very low translational kinetic energy from both double and triple ionization.

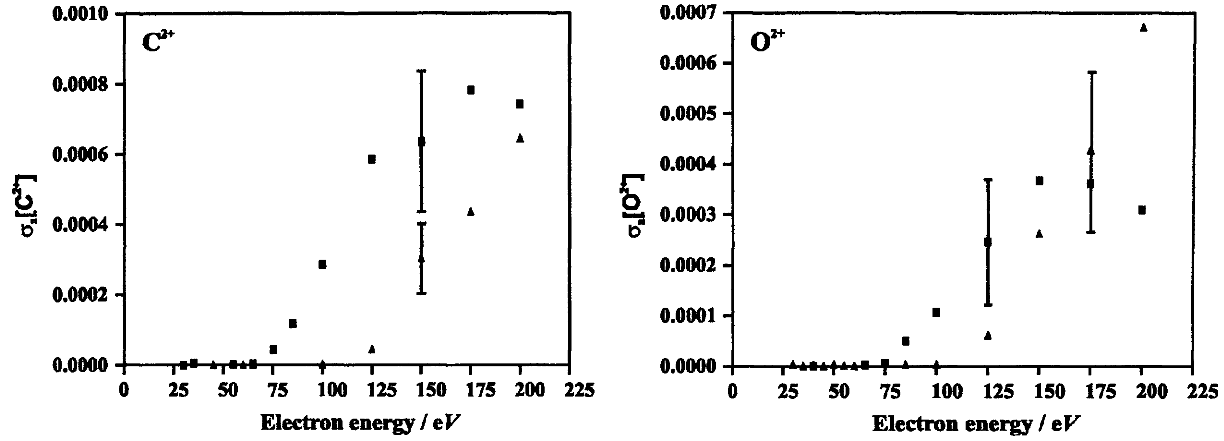

Figure 7.5 Relative precursor specific PICS for forming dication fragments *via* double ionization (■), and *via* triple ionization (▲), following electron ionization of CO_2. The representative error bars show four standard deviations of three separate determinations.

In Figure 7.5 it is seen that contributions to the O^{2+} ion yield are also from both double and triple ionization. From the $\sigma_2[O^{2+}]$ values a threshold for O^{2+} formation is determined at 74±3 eV, again in good agreement with a previous determination.[15] At 200 eV contributions to the O^{2+} ion yield from triple ionization are far greater than from double ionization. Comparison of this data to values derived from the data of Tian and Vidal[14] shows that the $\sigma_2[O^{2+}]$ values and $\sigma_3[O^{2+}]$ values derived in this work are slightly lower than reported previously.

Figure 7.6 shows that contributions to the total ion yield from double ionization rise steadily from threshold, lying close to 35 eV, reaching a maximum value of 17% at 150 eV. Within the electron energy range investigated, contributions to the total ion yield from triple ionization do not exceed 2%, therefore justifying the neglect of quadruple ionization in this study. It is noted, however, that the total contributions from triple ionization measured in this work (Table D.XI) are almost an order of magnitude greater than the corresponding values derived from the data of Tian and Vidal[14], whose measurements did not include the formation of product ion triples. The σ_r values for the formation of ion pairs following charge-separating dissociation of the CO_2^{2+} dication are displayed in Figure 7.7. All three ion pairs shown are of the odd-electron + odd-electron (OO) type (Section 4.5.1.1) and provide no additional evidence to support or contradict the propensity rule for dication dissociation discussed in previous chapters.

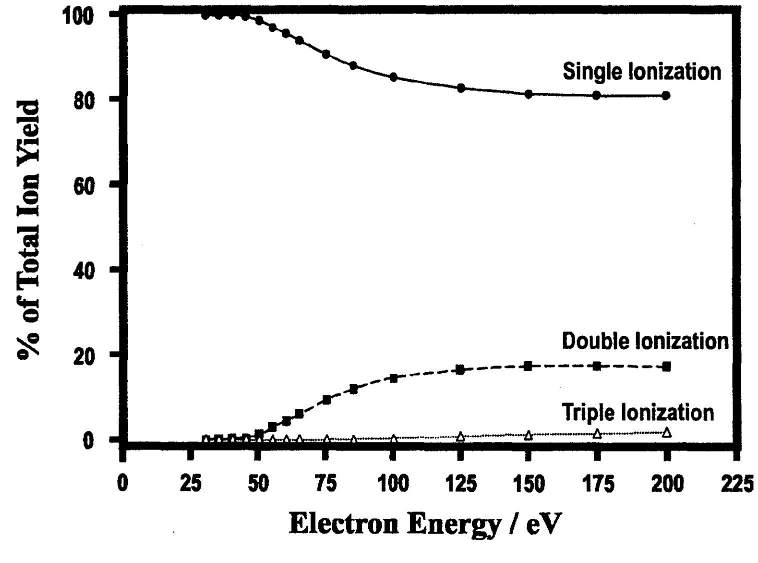

Figure 7.6 Contributions to the total ion yield from single, double, and triple ionization, following electron ionization of CO_2.

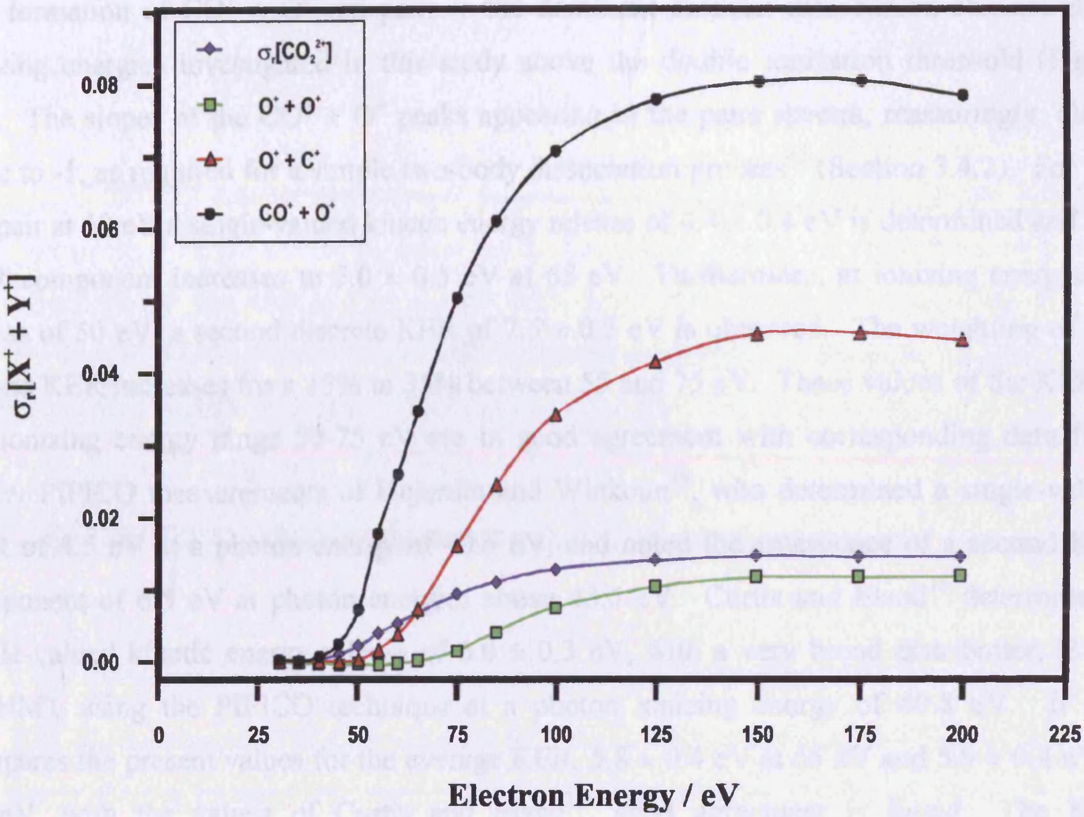

Figure 7.7 Relative cross sections σ_r for forming monocation-monocation pairs following electron ionization of CO_2. Also shown for comparison are the σ_r values for formation of the parent dication CO_2^{2+}.

7.5 The Energetics of Dissociative Double Ionization

The kinetic energy of the ion pairs formed by dissociation of the CO_2^{2+} dication have been determined using Monte Carlo simulations of the peaks observed in the pairs spectrum, as described in Section 3.5. All KER determinations were made from data recorded at electron energies above 50 eV, as the coincidence spectra recorded at electron energies lower than 50 eV contained insufficient coincidence signals to produce statistically significant results. In these simulations all KER components were modelled using a Gaussian distribution with a width of 1.2 eV at FWHM.[23] In the sections that follow here these KER measurements are compared with available experimental and theoretical data.

$CO^+ + O^+$

The formation of $CO^+ + O^+$ ion pairs is the dominant dication dissociation channel at all ionizing energies investigated in this study above the double ionization threshold (Figure 7.7). The slopes of the $CO^+ + O^+$ peaks appearing in the pairs spectra, reassuringly, all lie close to -1, as required for a simple two-body dissociation process[42] (Section 3.4.2). For this ion pair at 50 eV a single-valued kinetic energy release of 4.4 ± 0.4 eV is determined and this KER component increases to 5.0 ± 0.5 eV at 65 eV. Furthermore, at ionizing energies in excess of 50 eV, a second discrete KER of 7.5 ± 0.5 eV is observed. The weighting of this second KER increases from 15% to 35% between 55 and 75 eV. These values of the KER in the ionizing energy range 50-75 eV are in good agreement with corresponding data from earlier PIPICO measurements of Dujardin and Winkoun[19], who determined a single-valued KER of 4.5 eV at a photon energy of 40.5 eV, and noted the emergence of a second KER component of 6.5 eV at photon energies above 43.5 eV. Curtis and Eland[18] determined a single-valued kinetic energy release of 6.0 ± 0.3 eV, with a very broad distribution (3 eV FWHM), using the PIPICO technique at a photon ionizing energy of 40.8 eV. If one compares the present values for the average KER, 5.8 ± 0.4 eV at 65 eV and 5.9 ± 0.4 eV at 75 eV, with the values of Curtis and Eland[18], good agreement is found The KER measurements in this work do not agree quite as well with a more recent PIPICO investigation by Masuoka[23], who used a curve fitting procedure to extract the kinetic energy release distribution of $CO^+ + O^+$ ion pairs formed by photoionization in the energy range 40-100 eV.

The kinetic energy release obtained in this work at 50 eV, assuming the formation of ground state products CO^+ ($^2\Sigma^+$) + O^+ (^4S_u), a dissociation limit which lies at 33.15 eV[43,44] with respect to CO_2 in its ground state (X $^1\Sigma_g^+$), suggests a dissociative precursor state lying at 37.55 ± 0.4 eV. Previous measurements of the appearance potential for $CO^+ + O^+$ formation have been reported by Masuoka[22] (39.2 ± 0.3 eV) and by Millie *et al.*[24] (39.7 ± 0.5 eV), using the PIPICO method, and by Slattery *et al.*[33] (38.65-38.80 eV) using TPEsCO spectroscopy coupled with an ion-coincidence technique. Of these previous experimental studies, only the TPEsCO-ion-ion coincidence technique of Slattery *et al.*[33] selectively probes $CO^+ + O^+$ ion pairs formed exclusively *via* direct dissociative double ionization. Theory similarly predicts a barrier to $CO^+ + O^+$ formation on the ground $^3\Sigma_g^-$ surface of the CO_2^{2+} dication at 38.7 eV.[39] The lower precursor state energy observed in this study suggests that indirect processes are being sampled contributing significantly to the $CO^+ + O^+$ ion yield from states lying below the threshold for direct ion pair formation. Indeed, recent TOF-PEPECO measurements[33] have observed CO^+ + O^+ formation below the double ionization threshold, involving autoionization of oxygen atoms:

$$CO_2 + e^- \rightarrow CO_2^{*+} + 2e^- \rightarrow CO^+ + O^* + 2e^- \rightarrow CO^+ + O^+ + 3e^- \qquad 7.\mathrm{i}$$

Using this PEPECO data, Slattery *et al.*[33] proposed a threshold for indirect formation of CO^+ + O^+ ion pairs of 35.56 ± 0.10 eV, below even the precursor state energy determined in this work with 50 eV electrons. The second KER component observed at ionizing electron energies above 55 eV, measured as 7.5 ± 0.5 eV, implies a precursor state energy lying higher in the electronic state manifold of CO_2^{2+} at 40.65 ± 0.5 eV.

$C^+ + O^+ + O$

Tian and Vidal[14] described the formation of $C^+ + O^+ + O$ ion pairs from CO_2^{2+} as a secondary decay process:

$$CO_2^{2+} \rightarrow CO^+ + O^+ \rightarrow O + C^+ + O^+ \qquad 7.\mathrm{ii}$$

The peak slopes measured in this work for forming this ion pair lie close to -0.43 below 65 eV, then gradually become less negative with increasing electron energy (-0.34 at 100 eV, -0.26 at 200 eV). In addition, a broadening of the C^+ + O^+ ion pair peak is observed in the pairs spectrum, with increasing ionizing energy. Tian and Vidal[14] attributed this broadening of the ion pair signals to an increasing contribution from concerted processes involving higher electronic states of CO_2^{2+}. For a slow secondary decay of CO^+ to C^+ + O, with no kinetic energy release in the secondary step (Section 3.4.3.3), the peak slope is expected[42] to be -0.43, as observed in the present work within experimental error below 65 eV. For a concerted process forming C^+ + O^+ ion pairs, the peak slope should lie between -0.43 and -1, depending on whether the dissociation process involves a head-on-collision between C^+ and the neutral O fragment formed, or an unobstructed instantaneous Coulomb explosion.[42] Thus, if concerted processes contribute significantly to the C^+ + O^+ ion yield with increasing ionization energy, as proposed by Tian and Vidal[14], one would expect values of the peak slope to increase from -0.43 towards -1. The fact that the peak slope values become less negative than -0.43 above 65 eV, can be explained slow by a secondary decay mechanism (Scheme 7.ii) involving the growth of a small component of aligned energy release[42] in the secondary decay of the CO^+ ion. This aligned secondary KER, coupled with small deviations from linearity in this three-body dissociation process, may also give rise to the observed broadening of C^+ + O^+ ion pair peaks in the pairs spectra.

From a Monte Carlo simulation of the coincidence data that are measured for this ion pair at 60 eV two components of kinetic energy release are determined, 6.0 ± 0.5 eV and 9.5 ± 0.5 eV, with weightings of 7:3. The asymptote for the formation of ground state products C^+ (^2P_u) + O^+ (^4S_u) + O (^3P_g) lies at 41.55 eV[43,44], suggesting precursor states for C^+ + O^+ formation at 47.55 ± 0.5 eV and 51.05 ± 0.5 eV, respectively. The lower of these values is in good agreement with previous measurements of the appearance potential for forming C^+ + O^+ *via* photoionization.[22,24]

$O^+ + O^+ + C$

In the present experimental setup kinetic energy release determinations cannot be easily performed for monocation pairs with identical mass, due to the deadtime of the discrimination circuitry. Despite this, by manually fitting a straight line to the visible portion of O^+ + O^+ ion pair peaks, observed in the pairs mass spectrum at higher ionizing energies (Figure 7.2), peak slopes all lying close to -1 are determined. These measurements are consistent with a concerted mechanism for forming O^+ + O^+ ion pairs.[42]

7.6 Dissociation of CO_2^{3+}

In the coincidence mass spectra recorded at 200 eV four ion pairs and one ion triple are observed, arising from the dissociation of the carbon dioxide trication CO_2^{3+}. Analysis shows that dissociation of CO_2^{3+} to form an ion triple, C^+ + O^+ + O^+, is the most abundant trication dissociation channel at all ionizing energies investigated in this study. Indeed, the propensity of symmetric charge separation among the ion fragments formed upon dissociative multiple ionization of CO_2 has been observed previously, in studies using intense laser pulses[32] and involving collisions with high energy ions.[31,45]

Values of the peak slope measured for O^{2+} + O^+ ion pairs above 125 eV all lie close to -0.50. Assuming that this dissociation reaction is approximately linear, these values suggest the formation of O^{2+} + O^+ + C is *via* a concerted process[46], in which the central C atom remains almost stationary. For the formation of O^{2+} + CO^+ ion pairs the values of the peak slope similarly all lie close to -0.50, as predicted for a two-body trication dissociation process (Section 3.4.2). For C^{2+} + O^+ formation a peak slope close to -0.10 is measured at ionizing energies above 125 eV. If this reaction were to proceed *via* an instantaneous Coulomb explosion, where the central C^+ ion is obstructed by the neutral O atom, one predicts a minimum peak slope of -0.21.[42] The more negative peak slopes that measured in this work show that the C^{2+} ion carries a much smaller component of correlated momentum than predicted for an instantaneous explosion reaction.[14] For dissociation of CO_2^{3+} into O^{2+} + C^+ ion pairs, values of the peak slope are measured at around -1.40. If this reaction were to proceed *via* an instantaneous explosion, in which the departing C^+ ion is obstructed by the neutral O atom, a maximum peak slope of -1.17 is predicted. This again suggests that the correlated momentum partitioned to the central carbon ion is much lower than is predicted for a concerted process. This feature of the fragmentation of CO_2^{3+} has been explained previously[14] by using the charge exchange model of Eland *et al.*[47] In this model, the charge is shared equally among the various fragments (neutral and ionic) during dissociation by a process of rapid exchange, until the distance between the fragments becomes too large. This zone of continuous charge exchange is defined by an interfragment distance of approximately 2-7 Å, and represents the typical distances at which potential curve crossings may occur, as predicted by Landau-Zener based theories[48,49]. Therefore in the charge exchange model, every fragment formed within the charge exchange zone will experience the effect of Coulomb repulsion and will gain momentum from the release of any unbalanced repulsion. For the central C^+ or C^{2+} ions comprising monocation-dication pairs, the process of rapid charge exchange in the CO_2^{3+} trication serves to partially balance the Coulomb repulsion forces experienced by these ionic fragments, resulting in a smaller component of correlated momentum for these ions than is predicted using a localised charge model[42].

7.7 Conclusions

TOF mass spectrometry coupled with a 2-D ion coincidence technique has been used to measure relative partial ionization cross sections for the formation of positively charged ions following electron ionization of CO_2 in the energy range 30-200 eV. Precursor-specific relative PICS have also been derived for these ions, which quantify the contribution to the yield of each ion from single, double and triple ionization. These measurements include, for the first time, contributions from ion triples formed by dissociative electron ionization.

Excellent agreement is found between the present data and two recent determinations of the PICS of CO_2[13,15] that similarly permit the efficient collection of ions formed initially with considerable kinetic energy. The relative precursor-specific PICS reveal that contributions to the C^+ ion yield are dominated by dissociative single ionization across the ionizing energy range. By contrast, contributions to the yield of O^+ and CO^+ fragments ions from dissociative double ionization, are comparable to contributions from dissociative single ionization above 100 eV. It was also shown that contributions to the yield of fragment dications, C^{2+} and O^{2+}, are from both double and triple ionization. Fragment ions formed *via* dissociative triple ionization are shown to comprise 1.8 % of the total ion yield at 200 eV, much greater than reported previously[14].

The analysis of the 2-D coincidence spectra provides information on the dynamics and energetics of charge separating dissociation of the CO_2^{2+} dication. The KER involved in ion pair formation has been determined by simulations of the peaks appearing in the coincidence spectra, thus providing estimates of the precursor state energies of CO_2^{2+} for forming ion pairs. From these KER measurements it is concluded that indirect double ionization contributes significantly to the yield of $CO^+ + O^+$ pairs at electron energies below 55 eV.

7.8 References

[1] S. A. Haider, J. Geophys. Res-Space Phys. **102** (A1), 407 (1997).
[2] S. A. Haider, Indian Journal Of Radio & Space Physics **17** (5), 183 (1988).
[3] O. Witasse, O. Dutuit, J. Lilensten, R. Thissen, J. Zabka, C. Alcaraz, P. L. Blelly, S. W. Bougher, S. Engel, L. H. Andersen, and K. Seiersen, Geophys. Res. Lett. **29** (8) (2002).
[4] R. K. Asundi, M. V. Kurepa, and J. D. Craggs, Proceedings Of The Physical Society Of London **82** (530), 967 (1963).
[5] B. Bapat and V. Sharma, J. Phys. B-At. Mol. Opt. Phys. **40** (1), 13 (2007).
[6] A. Crowe and J. W. McConkey, J. Phys. B-At. Mol. Opt. Phys. **7** (3), 349 (1974).
[7] R. S. Freund, R. C. Wetzel, and R. J. Shul, Phys. Rev. A **41** (11), 5861 (1990).
[8] R. Locht and M. Davister, Int. J. Mass Spectrom. Ion Process. **144** (1-2), 105 (1995).
[9] T. D. Mark and E. Hille, J. Chem. Phys. **69** (6), 2492 (1978).
[10] O. J. Orient and S. K. Srivastava, J. Phys. B-At. Mol. Opt. Phys. **20** (15), 3923 (1987).
[11] D. Rapp and Englande.P, J. Chem. Phys. **43** (5), 1464 (1965).
[12] D. Rapp, Englande.P, and D. D. Briglia, J. Chem. Phys. **42** (12), 4081 (1965).
[13] H. C. Straub, B. G. Lindsay, K. A. Smith, and R. F. Stebbings, J. Chem. Phys. **105** (10), 4015 (1996).
[14] C. C. Tian and C. R. Vidal, Phys. Rev. A **58** (5), 3783 (1998).
[15] C. C. Tian and C. R. Vidal, J. Chem. Phys. **108** (3), 927 (1998).
[16] R. Velotta, P. Digirolamo, V. Berardi, N. Spinelli, and M. Armenante, J. Phys. B-At. Mol. Opt. Phys. **27** (10), 2051 (1994).
[17] R. G. Cooks, Terwilli.Dt, and J. H. Beynon, J. Chem. Phys. **61** (3), 1208 (1974).
[18] D. M. Curtis and J. H. D. Eland, Int. J. Mass Spectrom. Ion Process. **63** (2-3), 241 (1985).
[19] G. Dujardin and D. Winkoun, J. Chem. Phys. **83** (12), 6222 (1985).
[20] R. Locht, M. Davister, W. Denzer, H. W. Jochims, and H. Baumgartel, Chem. Phys. **138** (2-3), 433 (1989).

21 T. Masuoka, Journal Of Electron Spectroscopy And Related Phenomena **103**, 53 (1999).

22 T. Masuoka, Phys. Rev. A **50** (5), 3886 (1994).

23 T. Masuoka, E. Nakamura, and A. Hiraya, J. Chem. Phys. **104** (16), 6200 (1996).

24 P. Millie, I. Nenner, P. Archirel, P. Lablanquie, P. Fournier, and J. H. D. Eland, J. Chem. Phys. **84** (3), 1259 (1986).

25 B. P. Tsai and J. H. D. Eland, Int. J. Mass Spectrom. Ion Process. **36** (2), 143 (1980).

26 R. Bombach, J. Dannacher, J. P. Stadelmann, and J. C. Lorquet, J. Chem. Phys. **79** (9), 4214 (1983).

27 J. H. D. Eland and J. Berkowitz, J. Chem. Phys. **67** (6), 2782 (1977).

28 R. Frey, B. Gotchev, O. F. Kalman, W. B. Peatman, H. Pollak, and E. W. Schlag, Chem. Phys. **21** (1), 89 (1977).

29 R. Locht, Int. J. Mass Spectrom. Ion Process. **148** (1-2), L17 (1995).

30 H. Bluhme, N. P. Frandsen, F. M. Jacobsen, H. Knudsen, J. P. Merrison, R. Mitchell, K. Paludan, and M. R. Poulsen, J. Phys. B-At. Mol. Opt. Phys. **32** (24), 5825 (1999).

31 J. H. Sanderson, T. Nishide, H. Shiromaru, Y. Achiba, and N. Kobayashi, Phys. Rev. A **59** (6), 4817 (1999).

32 J. P. Brichta, S. J. Walker, R. Helsten, and J. H. Sanderson, J. Phys. B-At. Mol. Opt. Phys. **40** (1), 117 (2007).

33 A. E. Slattery, T. A. Field, M. Ahmad, R. I. Hall, J. Lambourne, F. Penent, P. Lablanquie, and J. H. D. Eland, J. Chem. Phys. **122** (8) (2005).

34 K. Furuya, A. Matsuo, and T. Ogawa, J. Phys. B-At. Mol. Opt. Phys. **35** (14), 3077 (2002).

35 S. Taylor and J. H. D. Eland, Chem. Phys. **315** (1-2), 8 (2005).

36 J. H. D. Eland, Chem. Phys. **294** (2), 171 (2003).

37 R. I. Hall, L. Avaldi, G. Dawber, A. G. McConkey, M. A. Macdonald, and G. C. King, Chem. Phys. **187** (1-2), 125 (1994).

38 M. L. Langford, F. M. Harris, C. J. Reid, J. A. Ballantine, and D. E. Parry, Chem. Phys. **149** (3), 445 (1991).

39 M. Hochlaf, F. R. Bennett, G. Chambaud, and P. Rosmus, J. Phys. B-At. Mol. Opt. Phys. **31** (10), 2163 (1998).

40 H. Hogreve, J. Phys. B-At. Mol. Opt. Phys. **28** (8), L263 (1995).

41 D. Schroder and H. Schwarz, J. Phys. Chem. A **103** (37), 7385 (1999).

42 J. H. D. Eland, Molecular Physics **61** (3), 725 (1987).

43 H. Y. Afeety, J. F. Liebman, and S. E. Stein, *"Neutral Thermochemical Data"*. (National Institute of Standards and Technology, Gaithersburg MD, 20899 (http://webbook.nist.gov), June 2005).

44 S. G. Lias, *"Ion Energetics Data"*. (National Institute of Standards and Technology, Gaithersburg MD, 20899 (http://webbook.nist.gov), June 2005).

45 D. Mathur, Physics Reports-Review Section of Physics Letters **391** (1-2), 1 (2004).

46 J. H. D. Eland, in *Vacuum Ultraviolet Photonionization and Photodissociation of Molecules and Clusters*, edited by C. Y. Ng (World Scientific, Singapore, 1991).

47 S. Hsieh and J. H. D. Eland, J. Chem. Phys. **103** (3), 1006 (1995).

48 Z. Herman, International Reviews in Physical Chemistry **15** (1), 299 (1996).

49 S. D. Price, Journal Of The Chemical Society-Faraday Transactions **93** (15), 2451 (1997).

Chapter 8 Electron Ionization of H_2O

8.1 Introduction

Ionization of H_2O is a process of importance in planetary atmospheres[1] and comets[2]. In addition, the emission of slow secondary electrons following dissociative ionization of water present in biological tissue, plays a crucial role in DNA damage following radiolysis[3]. A detailed understanding of such processes requires, among other factors, accurate and reliable data on the partial ionization cross sections (PICS) for forming both the parent ion and the various ionic fragments resulting from single and multiple ionization.

8.1.1 Partial Ionization Cross Sections of H_2O

The PICS following electron ionization of water vapour have been the subject of a number of previous experimental investigations. Schutten *et al.*[4] measured PICS for the formation of all singly and doubly charged ions using a mass spectrometer designed to measure ion currents, in the energy range 20-2000 eV. PICS for the formation of H_2O^+, OH^+, O^+ and H^+ have been measured using a quadrupole mass spectrometer (QMS) by Orient and Srivastava[5], up to an ionizing energy of 400 eV. This work was later supplanted by the data of Rao *et al.*[6], who, using a QMS with an improved ion extraction technique, measured PICS for the formation of ions with up to 5 eV of initial kinetic energy, at ionizing energies below 1000 eV. Interestingly, Rao *et al.*[6] reported the direct observation of H_2O^{2+} ions in their mass spectra, although this assignment has recently been questioned[7]. Straub *et al.*[7] measured PICS for the formation of singly and doubly charged ions for both H_2O and D_2O up to 1000 eV, using a time of flight mass spectrometer coupled with position sensitive detection. In this way Straub *et al.*[7] were able to demonstrate the complete collection of all ionic fragments, including those formed with considerable translational kinetic energy. However, despite the wealth of available experimental data concerning the PICS of water vapour, very few studies have investigated the multiple ionization of H_2O due to electron impact. Frémont *et al.*[8] measured the fragment energy distributions of ions formed by single, double and triple ionization, in the ionizing energy range 20-200 eV. Most recently, Montenegro *et al.*[9] measured cross sections for the formation of $H^+ + O^+$ and $H^+ + OH^+$ ion pairs, in addition to all single ions, at electron energies between 45 and 1500 eV. To date, complete sets of measurements on the formation

ion pairs and ion triples, following dissociative multiple ionization of H_2O, are confined to studies involving collisions with fast ions[10,11].

In this study the electron ionization of H_2O is investigated in the energy range 30-200 eV, using time-of-flight mass spectrometry coupled with a 2-D ion coincidence technique. Relative PICS $\sigma_r[X^{m+}]$ are reported for the formation of H^+, H_2^+, O^{2+}, O^+, and OH^+ ions, expressed relative to the formation of H_2O^+, as a function of ionizing electron energy in the range 30-200 eV. The data are shown to be in excellent agreement with the existing PICS of Straub *et al.*[7] Precursor-specific relative PICS $\sigma_n[X^{m+}]$ are then derived for the formation of these fragment ions, which quantify the contribution to the yield of each fragment ion from single (n=1), double (n=2) and triple (n=3) ionization. These measurements represent the first complete description of the single and multiple ionization of H_2O due to electron impact.

8.1.2 The Water Dication H_2O^{2+}

The 2-D ion coincidence technique used in this work provides information on the energetics of the dissociation of the H_2O dication. The energies of the electronic states of H_2O^{2+} have been studied using a variety of techniques, including photoion-photion coincidence (PIPICO) spectroscopy[12,13], photoelectron-photoelectron coincidence (PEPECO) spectroscopy[14], double charge transfer (DCT) spectroscopy[15], Auger electron spectroscopy (AES)[16], and theoretical methods[17-19]. In this study, simulations of the peaks appearing in the coincidence spectra are performed to determine the kinetic energy release involved in ion pair formation following dissociative double ionization of H_2O. These measurements are then used to provide estimates of the precursor state energies of H_2O^{2+} involved in forming various ion pairs, and provide further evidence that the formation of H^+ + OH^+ ion pairs proceeds *via* indirect processes below the vertical double ionization potential[14].

8.2 Experimental Procedures

All experiments in this study were performed using a TOF mass spectrometer of Wiley-McLaren design, as has been described in detail in Section 2.3. Distilled water which was thoroughly degassed prior to the experiment by a sequence of freezing, pumping and thawing cycles, was held at a temperature of 273 K using a water-ice bath. The vapour above this sample was introduced to the apparatus *via* a hypodermic needle to form a continuous effusive beam of H_2O in the source region. The operating conditions of the apparatus involve target gas pressures less than 10^{-6} Torr, and low electron flux, thus ensuring that on average much less than one ionization event occurs per pulse of ionizing electrons. As described in previous chapters, this methodology greatly reduces the number of 'false coincidences' that contribute to the coincidence spectra recorded. The voltage conditions used in this study are those described in Section 2.3 and permit the efficient collection of ions formed initially with up to 11 eV of translational energy.

8.3 Data Analysis

8.3.1 Singles Mass Spectra

A representative singles mass spectrum of H_2O recorded at an ionizing electron energy of 200 eV is shown in Figure 8.1. The intensities of individual ion peaks, $I_1[X^+]$ for monocations and $I_2[X^{2+}]$ for dications, appearing in the singles mass spectrum, are extracted using the analysis procedure described in Section 3.2.1. Small corrections were made to the intensity of O^+ ions and O^{2+} ions measured in each mass spectrum, to account for the contributions to these peaks from the ionization of background O_2 gas present in the vacuum chamber. These minor contributions are subtracted, using the procedure outlined in Section 3.2.1.2, by normalization to the O_2^+ peak intensity. Typically contributions to the raw O^+ peak intensity from background gas are much less than 2 %.

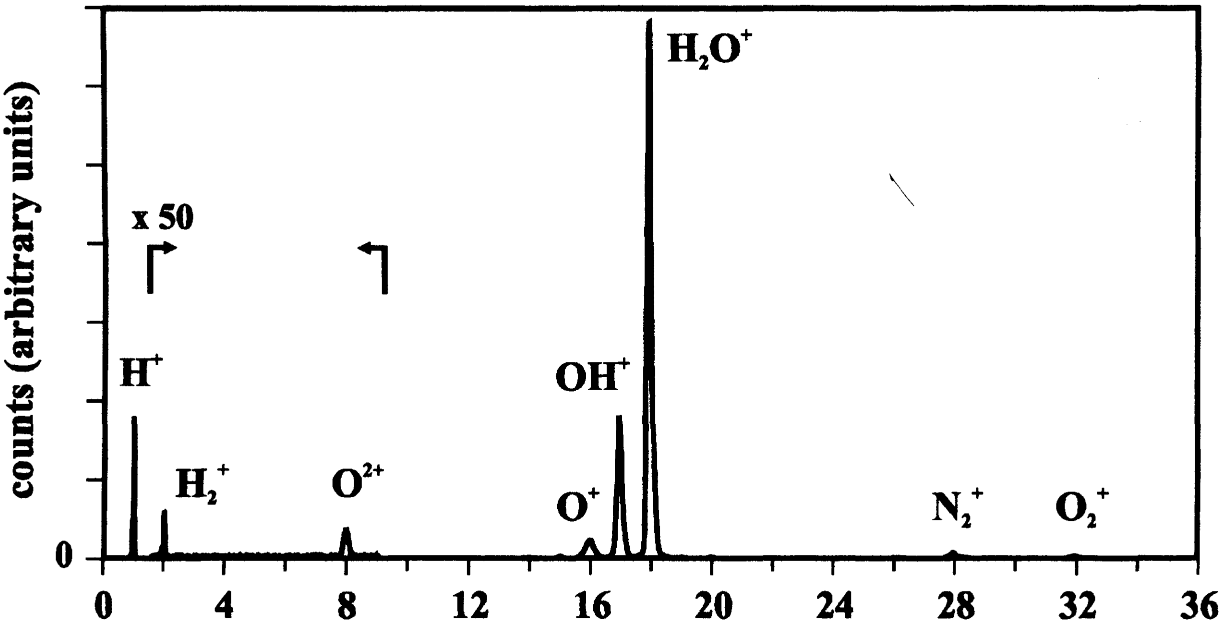

Figure 8.1 A characteristic (singles) mass spectrum of H_2O following electron ionization at 200 eV.

8.3.2 Ion Coincidence Spectra

A representative pairs mass spectrum of H_2O recorded at an ionizing electron energy of 200 eV is shown in Figure 8.2. The intensities of the various ion peaks are extracted, using the procedure described in Section 3.2.2, to yield the overall contribution of each individual fragment ion to the pairs spectrum $P[X^+]$. In this work a distinction is made between the ion counts in pairs which must be formed *via* dissociative triple ionization $P_3[X^+]$, for example $H^+ + O^{2+}$, and ion pairs that may have contributions from both double and triple ionization $P_2[X^+]$, such as $H^+ + O^+$. Contributions from triple ionization to the intensities of such monocation pairs may arise when only two ions of an ion triple are detected, due to the less than unit efficiency of the apparatus. The number of false coincidences that contribute to each ion pair peak is evaluated manually using an ion-autocorrelation function (Section 3.2.2.1), typically 1-2% of the raw peak intensity at higher ionizing electron energy, which is then subtracted. In the experiment no ion pairs are recorded if the second ion arrives at the detector within 32 ns of the first ion, due to the 'deadtime' of the discrimination circuitry. Such deadtime losses significantly affect the number of counts recorded in the $H^+ + H^+$ peak in the pairs spectra. To estimate the number of ions lost, a separate one-dimensional (t_2-t_1) spectrum is constructed from the $H^+ + H^+$ coincidence data which is then appropriately extrapolated to the limit t_1=t_2, using simple geometry, to correct for the losses (Section 3.2.2.3).

As described above, ions may reach the detector provided they have a translational energy component of less than 11 eV perpendicular to the TOF axis. However, if the total KER involved in ion pair formation exceeds this value, a small proportion of ions forming coincident ion pairs may be 'missed'. Any such losses most commonly arise for ion pairs comprising H^+ in coincidence with an ion of greater mass, since conservation of linear momentum dictates that most of the energy released in the dissociation process is partitioned to the lighter H^+ ion. These losses are evidenced by a small hollowing of the corresponding (t_2-t_1) plot for a particular ion peak, as has been demonstrated in previous PIPICO studies where low ion drawout fields are used[12,20]. In this study small losses of energetic $H^+ + O^+$ ion pairs are observed at ionizing energies above 100 eV, which are again evaluated and corrected in each pairs spectrum using simple geometry (Section 3.2.2.2). The size of this correction does not exceed 10% of the raw $H^+ + O^+$ pairs peak intensity in the ionizing energy range investigated in this study. It is noted, however, that corrections cannot be made for any losses of energetic monocations from single ionization, or dications from double ionization, if such fragment ions are formed with a kinetic energy greater than 11 eV.

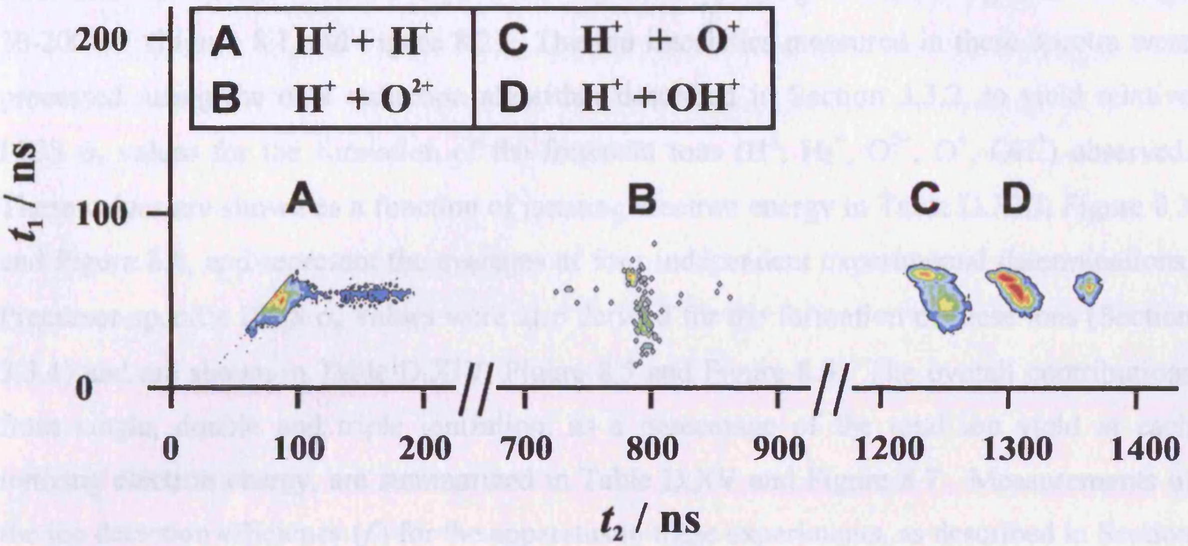

Figure 8.2 Representative 'pairs' mass spectrum of H_2O recorded at 200 eV showing observed ion pairs formed *via* charge-separating dissociation of H_2O^{2+} and H_2O^{3+}.

Ion triples are processed by specifying a time-of-flight range for a particular ion (O^+), and then extracting all ion triples containing at least one ion whose arrival time t_1 lies within this specified range. Once extracted, the respective flight times of the two remaining ions ($H^+ + H^+$) forming an ion triple are plotted as a two-dimensional histogram (t_2 *vs.* t_3). The contribution of a fragment ion $T[X^+]$ is then obtained from the number of counts in the $H^+ + H^+$ peak, after applying a small geometric correction to account for losses due to the 'deadtime', as described above. Only the formation of $H^+ + H^+ + O^{q+}$ ion triples *via* dissociative triple ionization (q=1) are considered, since the number of ion triples detected for quadruple or higher order ionization ($q \geq 2$) are too small to be quantified in this work. False triple coincidences that contribute to the $H^+ + H^+ + O^+$ counts are subtracted using the procedure outlined in Section 3.2.3.1.

All ion intensities measured in this work were corrected numerically using the natural isotopic distributions.

8.4 Relative Partial Ionization Cross Sections

8.4.1 Results

Mass and coincidence spectra of H_2O were recorded at ionizing electron energies in the range 30-200 eV (Figure 8.1 and Figure 8.2). The ion intensities measured in these spectra were processed, using the data reduction algorithm described in Section 3.3.2, to yield relative PICS σ_r values for the formation of the fragment ions (H^+, H_2^+, O^{2+}, O^+, OH^+) observed. These values are shown as a function of ionizing electron energy in Table D.XIII, Figure 8.3 and Figure 8.4, and represent the averages of four independent experimental determinations. Precursor-specific PICS σ_n values were also derived for the formation of these ions (Section 3.3.4) and are shown in Table D.XIV, Figure 8.5 and Figure 8.6. The overall contributions from single, double and triple ionization, as a percentage of the total ion yield at each ionizing electron energy, are summarized in Table D.XV and Figure 8.7. Measurements of the ion detection efficiency (f_i) for the apparatus in these experiments, as described in Section 3.3.3, resulted in a value of $f_i = 0.19 \pm 0.01$.

In the pairs spectra three dissociation channels of H_2O^{2+} are observed: $H^+ + OH^+$, $H^+ + O^+ + H$ and $H^+ + H^+ + O$. At electron energies above 85 eV one additional ion pair and one ion triple, resulting from dissociation of H_2O^{3+}, are observed in the ion coincidence spectra: $H^+ + O^{2+} + H$ and $H^+ + H^+ + O^+$. The conclusions drawn from these coincidence signals concerning the energetics of dissociative double ionization of H_2O^{2+} are discussed below.

8.4.2 Discussion

8.4.2.1. Relative PICS (σ_r) Values

The values of σ_r determined in this work for formation of H^+, H_2^+, O^{2+}, O^+ and OH^+ ions are shown in Figure 8.3 and Figure 8.4 respectively. Where appropriate, these values are compared with values of relative PICS derived from the H_2O data of Rao *et al.*[6] and Montenegro *et al.*[9], and the data of Straub *et al.*[7] One notes that a direct comparison with the H_2O data of Straub *et al.*[7] for the formation of O^+, OH^+ and H_2O^+, is not possible as these authors report only combined cross-sections for the formation of these ions. However, Straub *et al.*[7] deduced from their data that the PICS for forming O^+, OH^+ and H_2O^+ ions are the same, within experimental error, as the PICS for forming O^+, OD^+ and D_2O^+. Therefore a comparison is made between the σ_r values derived in this work for forming O^+ and OH^+, with the data from Straub *et al.*[7] for the corresponding ions formed from D_2O. For H^+ and H_2^+ ions the σ_r values derived in this work are compared with values extracted from the data of Straub *et al.*[7], obtained by normalizing the absolute PICS for forming H^+ and H_2^+ to the corresponding values reported for forming D_2O^+. As shown in Figure 8.3 and Figure 8.4, over the entire ionizing energy range there is excellent agreement between the present σ_r values and these values derived from Straub *et al.*[7]

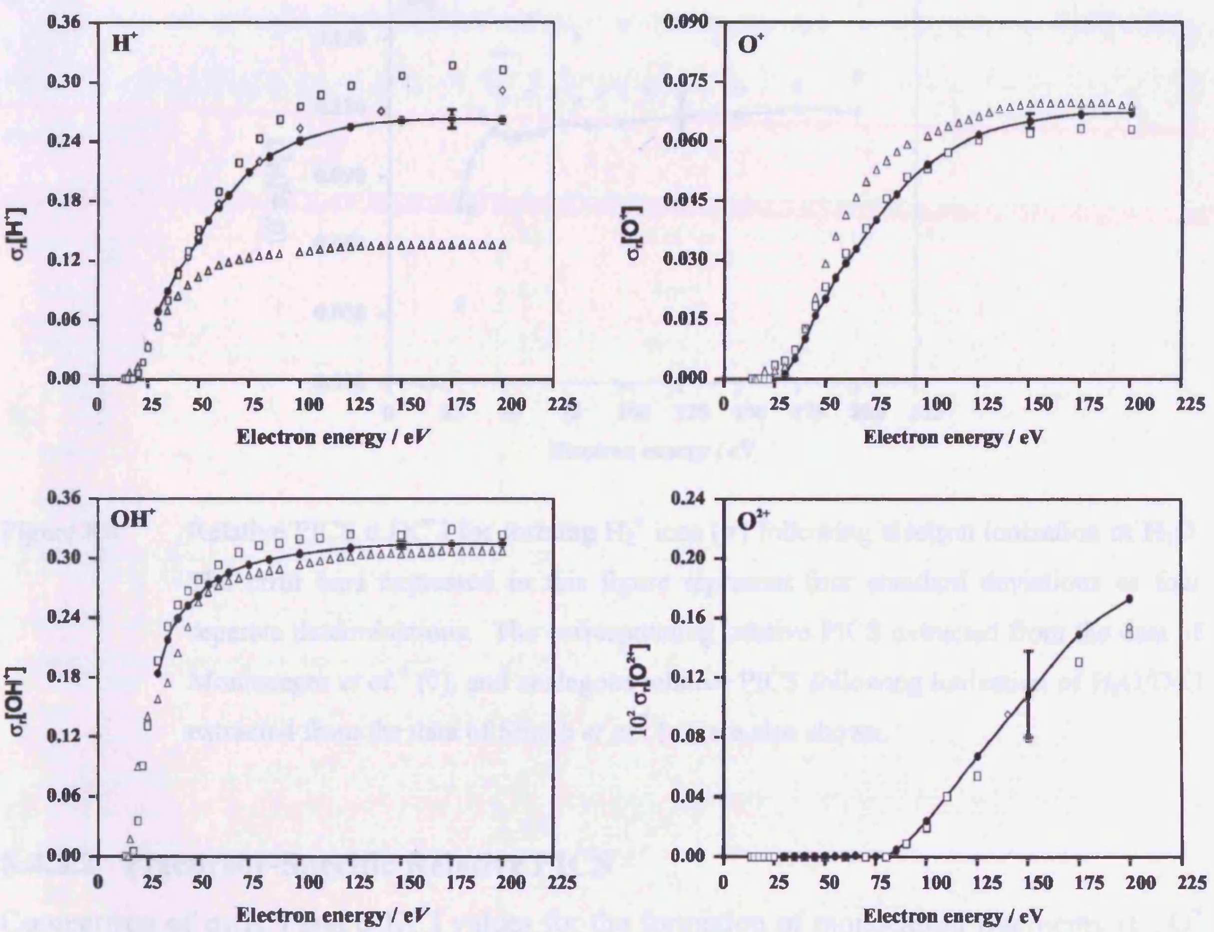

Figure 8.3 Relative PICS $\sigma_r[X^{n+}]$ for forming fragment ions (●) following electron ionization of H_2O. The error bars expressed in this figure represent four standard deviations of four separate determinations. The corresponding relative PICS extracted from the data of Rao *et al.*[6] (△), Montenegro *et al.*[9] (◊), and analagous relative PICS following ionization of H_2O/D_2O extracted from the data of Straub *et al.*[7] (□), are also shown.

A comparison of the $\sigma_r[X^+]$ values derived in this work to the data of Montenegro *et al.*[9], not shown for the formation of monocation fragments in Figure 8.3 for clarity, similarly reveal an excellent agreement between the two data sets. By contrast, the $\sigma_r[H^+]$ values derived from the data of Rao *et al.*[6] lie considerably lower than these data sets, and these differences can be explained by the inefficient collection of H^+ ions formed with significant translational energy in this earlier work. All singles spectra recorded exhibit no discernible peaks attributable to H_2O^{2+} formation and an upper limit of 0.00005 is placed on the values of $\sigma_r[H_2O^{2+}]$.

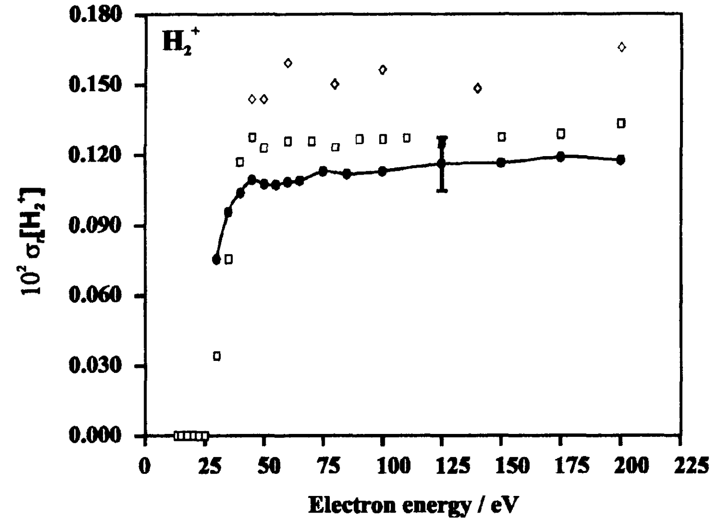

Figure 8.4 Relative PICS $\sigma_r[X^{n+}]$ for forming H_2^+ ions (●) following electron ionization of H_2O. The error bars expressed in this figure represent four standard deviations of four separate determinations. The corresponding relative PICS extracted from the data of Montenegro *et al.*[9] (◊), and analagous relative PICS following ionization of H_2O/D_2O extracted from the data of Straub *et al.*[7] (□), are also shown.

8.4.2.2. Precursor-Specific Relative PICS

Comparison of $\sigma_1[X^+]$ and $\sigma_2[X^+]$ values for the formation of monocation fragments H^+, O^+ and OH^+ (Figure 8.5), reveal that contributions to the yields of these ions from dissociative double ionization are small compared to contributions from dissociative single ionization. The σ_n values derived in this work also show that contributions to the O^{2+} ion yield are from both double and triple ionization, although the $\sigma_3[O^{2+}]$ values are an order of magnitude lower than the corresponding $\sigma_2[O^{2+}]$ values in this ionizing energy range. Contributions to the yield of H^+ ions and O^+ ions from dissociative triple ionization (Figure 8.6) are similarly at least an order of magnitude smaller than the corresponding $\sigma_2[X^+]$ values. If this minor contribution from triple ionization is neglected, a comparison can be made between the $\sigma_2[O^+]$ and $\sigma_2[OH^+]$ values with the cross section measurements of Montenegro *et al.*[9] for forming $H^+ + O^+$ and $H^+ + OH^+$ ion pairs. Such a comparison reveals a less satisfactory agreement between the data sets. For example, at 100 eV the present $\sigma_2[O^+]$ and $\sigma_2[OH^+]$ values are both around 40% lower than the corresponding values extracted from the data of Montenegro *et al.*[9], while at 200 eV this difference is 59% and 48%, respectively. The origin of these discrepancies is not readily apparent. In the pairs spectra recorded at 200 eV over a longer time period, evidence of a weak peak corresponding to $H_2^+ + O^+$ formation is observed (not shown in Figure 8.2). Measurements suggest that the intensity of this minor ion pair peak at 200 eV is only 0.12% of the intensity of the major ion pair peak $H^+ + OH^+$. This value concurs with an upper limit of 0.2% proposed in the PIPICO study of Richardson *et al.* at 40.8 eV.[12]

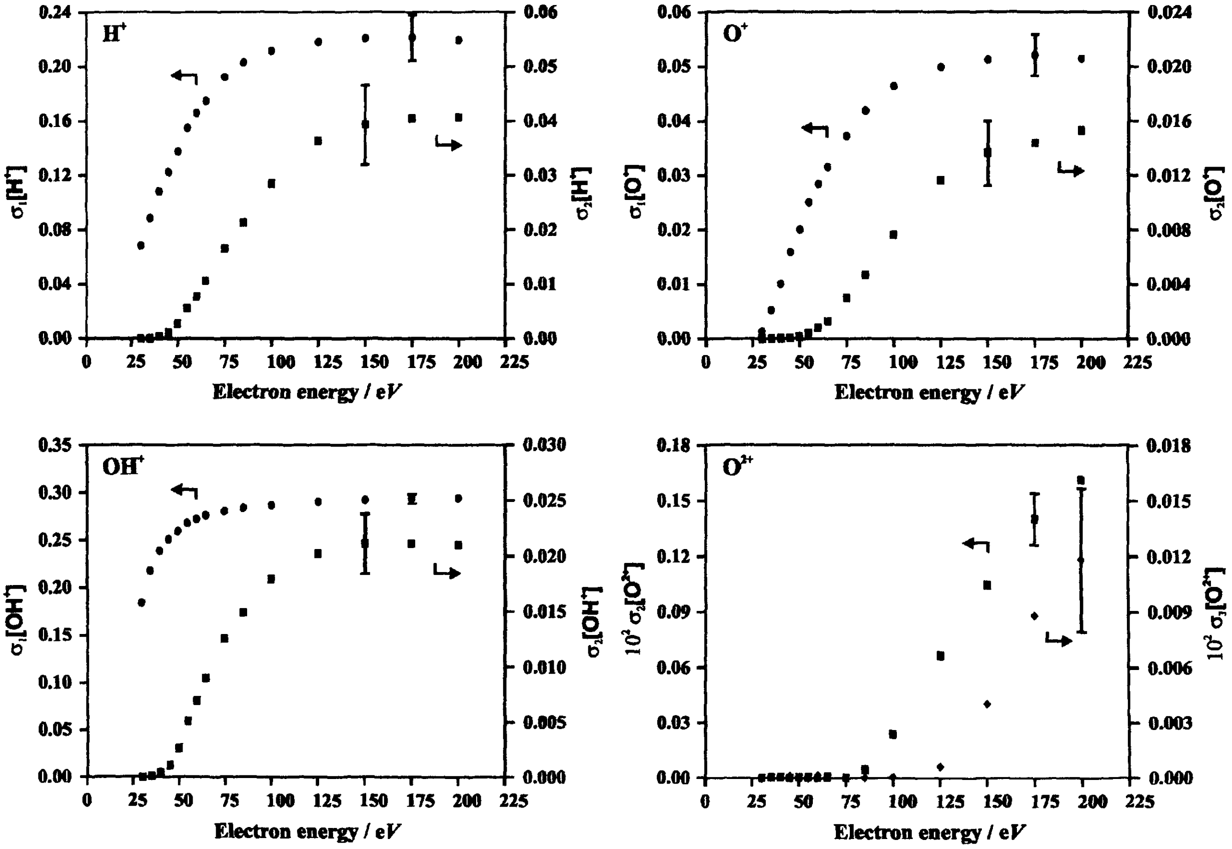

Figure 8.5 Relative precursor specific PICS for forming ion fragments *via* single ionization (●), *via* double ionization (■), and *via* triple ionization (♦), following electron ionization of H_2O. The representative error bars show four standard deviations of four separate determinations.

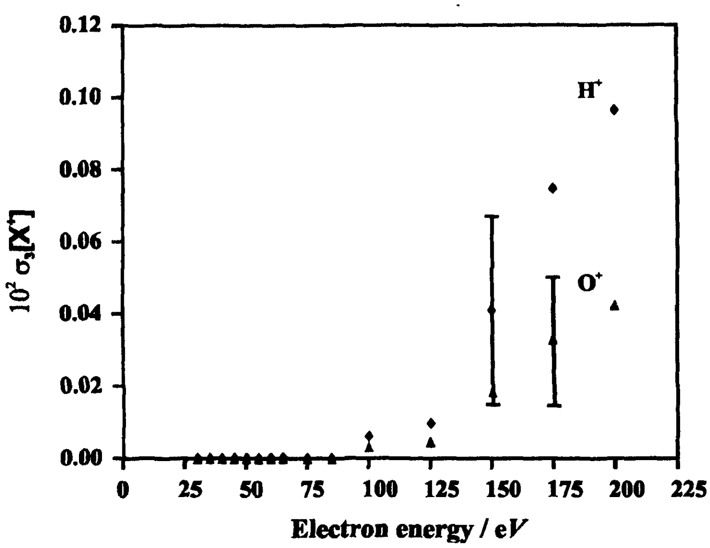

Figure 8.6 Relative precursor specific PICS for forming monocation fragments H^+ (♦) and O^+ (▲) *via* triple ionization, following electron ionization of H_2O. The representative error bars show four standard deviations of four separate determinations.

In Table D.XV and Figure 8.7 it is shown that contributions to the total ion yield from double ionization increase slowly to 4.8% at 200 eV. This value lies higher than the value of 1% proposed by Frémont *et al.*[8], based on conclusions drawn from the KER distribution of all ions formed at 200 eV. One can compare the maximum in the ion yield from double ionization for H_2O (4.8%) to the corresponding yields for other small molecules C_2H_2 (11%)[21], HC*l* (11%)[22], CH_4 (12%) and CO_2 (17%)[23] recorded using this apparatus. Such a comparison shows that in the ionizing electron energy range 30-200 eV the yield of dissociative double ionization for H_2O is low. Indeed, a low quantum yield of double ionization for H_2O has been reported previously by Eland[14] using TOF-PEPECO measurements. Recent theoretical work on the water dication[18] H_2O^{2+} indicated that the potential curves for a number of low-lying dication states were almost 'flat' over a range of internuclear distances. Such "flat" potential energy surfaces may delay the dissociation of H_2O^{2+}, but, of course, they cannot account for a low yield of dissociative double ionization if long-lived dications are not observed experimentally. Hence, it seems clear that, in the experimental energy regime, the intrinsic probability for removing two electrons from H_2O is small, perhaps due to some underlying feature of the electron-correlation in the molecule.

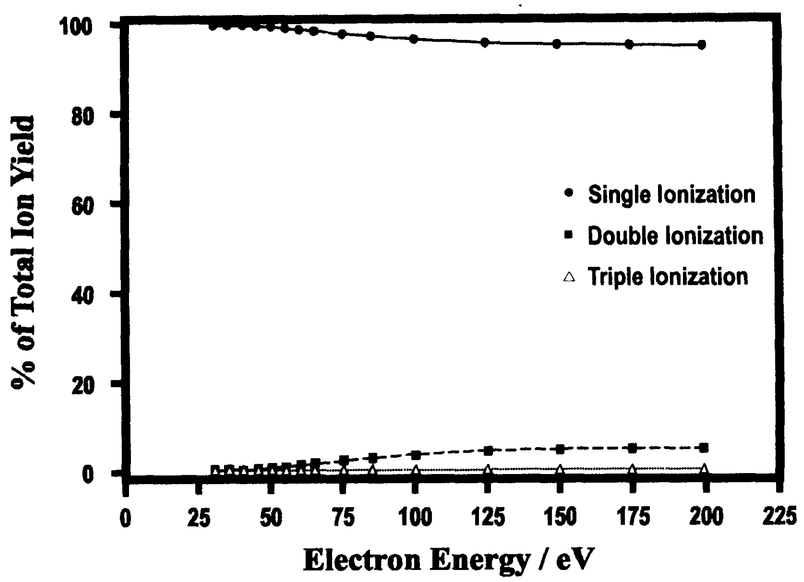

Figure 8.7 Contributions to the total ion yield from single, double, and triple ionization, following electron ionization of H_2O.

8.5 The Energetics of Dissociative Double Ionization

The kinetic energy of the ion pairs formed by dissociation of the H_2O^{2+} dication have been determined using Monte Carlo simulations of the peaks observed in the pairs spectrum, as described in Section 3.5. KER determinations for the formation of $H^+ + OH^+$ and $H^+ + O^+$ ion pairs were made from data recorded at electron energies above 50 eV and 75 eV respectively, as the coincidence spectra recorded at electron energies lower than these values contained insufficient coincidence signals to produce statistically significant results. In these simulations all KER components were modelled using a Gaussian distribution with a width of 1.2 eV at FWHM. In the sections that follow these KER measurements are compared with available experimental data.

$H^+ + OH^+$

The formation of $H^+ + OH^+$ ion pairs is the dominant dication dissociation channel at all ionizing energies investigated in this study above the double ionization threshold. For this ion pair at 50 eV two KER components are determined with a near equal weighting, the first centred at 3.6 ± 0.4 eV and a second larger KER of 9.2 ± 0.5 eV, suggesting an average KER of around 6.4 eV ± 0.5 eV. This smaller KER component rises steadily to a value of 5.2 ± 0.4 eV above 75 eV, while the second KER component remains as 9.2 eV with an increased weighting of 60%. The values of the KER determined in the ionizing energy range 50-75 eV agree only partially with corresponding data from earlier PIPICO measurements of Richardson *et al.*[12], who determined an average KER of 4.5 ± 0.5 eV at a photon energy of 40.8 eV. In a separate PIPICO study, Winkoun *et al.*[13] observed two KER components for $H^+ + OH^+$ formation at 41 eV, 3.0 ± 0.3 eV and 5.5 ± 0.5 eV, respectively. Of these values, only the smaller component of KER agrees with the present observations, within experimental error, at an ionizing electron energy of 50 eV.

The kinetic energy release of 3.6 ± 0.4 eV obtained in this work at 50 eV suggests a dissociative precursor state lying at 35.4 ± 0.4 eV, assuming the formation of ground state products $H^+ + OH^+$ ($^3\Sigma^-$), a dissociation limit which lies at 31.78 eV [24,25] with respect to the ground state of H_2O (X $^2B_1$). This value lies considerably lower than measurements of the vertical double ionization energy 39.6 eV, obtained by double charge transfer experiments[15]. Thus, additional evidence is provided here for the formation of $H^+ + OH^+$ ion pairs *via* an indirect two-step process, involving an autoionization step well outside of the vertical Franck-Condon region, as shown in the recent PEPECO study of Eland[14].

Previous KER determinations performed using this apparatus[21] have been shown to produce reliable KER values for dicationic dissociation processes which form an H^+ ion (see also Chapter 6). Thus, the discrepancy between the present KER values and those from the previous photoionization studies is most likely due to higher energy dication states being accessed in these experiments using 50 eV electrons than in experiments employing lower energy photons.

$H^+ + O^+ + H$

From a Monte Carlo simulation of the coincidence data for $H^+ + O^+ + H$ formation at 75 eV a single-valued kinetic energy release of 11.5 ± 0.5 eV is determined. In addition, at ionizing electron energies in excess of 75 eV the growth of a second single-valued KER component is observed of around 17 eV. These simulations assume that this ion pair is formed *via* a instantaneous explosion[26] (Section 3.4.3.1), although it is noted that simulations performed assuming a sequential dissociation process yield nearly identical energy releases. Therefore these determinations of the KER represent a lower limit for the total KER release involved in $H^+ + O^+ + H$ formation, as a small additional amount of translational energy may be partitioned to the neutral H atom that is not detected by the apparatus. The corresponding photoionization measurements of Richardson *et al.*[12] (5 ± 0.5 eV) (41.8 eV), and Winkoun *et al.*[13] (4.7 ± 0.3 eV) (46 eV), obtained from PIPICO measurements significantly closer to the double ionization threshold, are considerably smaller than the KER values determined in this work for $H^+ + O^+ + H$ formation with 75 eV electrons. A likely explanation for this discrepancy is that the present experiments are dominated by the dissociation of excited states lying high in the electronic state manifold of H_2O^{2+}, which were not accessed in the earlier photoionization experiments. The identity of these excited states is unknown, as the electronic structure of the water dication high above the double ionization potential has not been investigated.

8.6 Conclusions

Time-of flight mass spectrometry coupled with a 2-D ion coincidence technique has been used to measure relative partial ionization cross sections for the formation of positively charged ions following electron ionization of H_2O in the energy range 30-200 eV. Relative precursor-specific PICS have also been derived for the formation of these ions, which quantify the contribution to the yield of each fragment ion from single, double and triple ionization. These measurements include, for the first time, contributions from all positive ion pairs and ion triples formed by dissociative electron ionization.

Excellent agreement is found between the present data and a recent determination of the PICS of H_2O[7], in which the efficient collection of all ion fragments with considerable translational energy was demonstrated. The precursor-specific relative PICS reveal that contributions to the yield of all fragment monocations are dominated by single ionization up to an ionizing electron energy of 200 eV. In this ionizing energy regime, the overall contributions from dissociative double ionization to the total ion yield for H_2O are shown to be less than 5%, significantly lower than for other small molecules studied using this apparatus. Fragment ions formed *via* dissociative triple ionization are shown to comprise less than 0.1% of the total ion yield at 200 eV. Measurements of the kinetic energy release involved in ion pair formation following dissociative double ionization of H_2O reveal that indirect processes contribute significantly to the yield of $H^+ + OH^+$ ion pairs below the vertical double ionization threshold.

8.7 References

[1] D. E. Shemansky and D. T. Hall, J. Geophys. Res-Space Phys. **97** (A4), 4143 (1992).

[2] R. M. Haberli, M. R. Combi, T. I. Gombosi, D. L. De Zeeuw, and K. G. Powell, Icarus **130** (2), 373 (1997).

[3] B. Boudaiffa, P. Cloutier, D. Hunting, M. A. Huels, and L. Sanche, Science **287** (5458), 1658 (2000).

[4] J. Schutten, F. J. Deheer, H. R. Moustafa, A. J. Boerboom, and Kistemak.J, J. Chem. Phys. **44** (10), 3924 (1966).

[5] O. J. Orient and S. K. Srivastava, J. Phys. B-At. Mol. Opt. Phys. **20** (15), 3923 (1987).

[6] M. Rao, I. Iga, and S. K. Srivastava, J. Geophys. Res.-Planets **100** (E12), 26421 (1995).

[7] H. C. Straub, B. G. Lindsay, K. A. Smith, and R. F. Stebbings, J. Chem. Phys. **108** (1), 109 (1998).

[8] F. Fremont, C. Leclercq, A. Hajaji, A. Naja, P. Lemennais, S. Boulbain, V. Broquin, and J. Y. Chesnel, Phys. Rev. A **72** (4) (2005).

[9] E. C. Montenegro, S. W. J. Scully, J. A. Wyer, V. Senthil, and M. B. Shah, Journal of Electron Spectroscopy and Related Phenomena **155** (1-3), 81 (2007).

[10] B. Siegmann, U. Werner, H. O. Lutz, and R. Mann, J. Phys. B-At. Mol. Opt. Phys. **34** (18), L587 (2001).

[11] U. Werner, K. Beckord, J. Becker, and H. O. Lutz, Phys. Rev. Lett. **74** (11), 1962 (1995).

[12] P. J. Richardson, J. H. D. Eland, P. G. Fournier, and D. L. Cooper, J. Chem. Phys. **84** (6), 3189 (1986).

[13] D. Winkoun, G. Dujardin, L. Hellner, and M. J. Besnard, J. Phys. B-At. Mol. Opt. Phys. **21** (8), 1385 (1988).

[14] J. H. D. Eland, Chem. Phys. **323** (2-3), 391 (2006).

[15] J. C. Severs, F. M. Harris, S. R. Andrews, and D. E. Parry, Chem. Phys. **175** (2-3), 467 (1993).

[16] W. E. Moddeman, T. A. Carlson, M. O. Krause, B. P. Pullen, W. E. Bull, and Schweitz.Gk, J. Chem. Phys. **55** (5), 2317 (1971).

[17] P. R. Bunker, O. Bludsky, P. Jensen, S. S. Wesolowski, T. J. Van Huis, Y. Yamaguchi, and H. F. Schaefer, J. Molecular Spectroscopy **198** (2), 371 (1999).

[18] K. Nobusada and K. Tanaka, J. Chem. Phys. **112** (17), 7437 (2000).

[19] T. J. Van Huis, S. S. Wesolowski, Y. Yamaguchi, and H. F. Schaefer, J. Chem. Phys. **110** (24), 11856 (1999).

[20] P. Millie, I. Nenner, P. Archirel, P. Lablanquie, P. Fournier, and J. H. D. Eland, J. Chem. Phys. **84** (3), 1259 (1986).

[21] S. J. King and S. D. Price, J. Chem. Phys. **127**, 174307 (2007).

[22] S. Harper, P. Calandra, and S. D. Price, Phys. Chem. Chem. Phys. **3** (5), 741 (2001).

[23] S. J. King and S. D. Price, Int. J. Mass Spectrom. **272** (2-3), 154 (2008).

[24] H. Y. Afeety, J. F. Liebman, and S. E. Stein, *"Neutral Thermochemical Data"*. (National Institute of Standards and Technology, Gaithersburg MD, 20899 (http://webbook.nist.gov), June 2005).

[25] S. G. Lias, *"Ion Energetics Data"*. (National Institute of Standards and Technology, Gaithersburg MD, 20899 (http://webbook.nist.gov), June 2005).

[26] J. H. D. Eland, Molecular Physics **61** (3), 725 (1987).

Chapter 9 Concluding Remarks

In this thesis a variety of experimental data has been presented describing the formation of single product ions, ion pairs and ion triples, following the electron ionization of a selection of gaseous target molecules. The systems investigated range from the larger halogenated molecules C_2F_6 and $SiCl_4$ (Chapters 4-5), which have important applications in plasma processing technologies, through to the smaller molecular systems C_2H_2, CO_2 and H_2O (Chapters 6-8), which are components of a number of planetary atmospheres. In this section some overall conclusions are made in relation to the partial ionization cross sections that have been derived for these molecules. The conclusions drawn from the PICS data and 2-D ion coincidence data, are then combined with the results of existing studies of the dissociation of gaseous molecular ions, to address the more general question of whether non-statistical processes play an important role in the fragmentations of small molecular dications.

9.1 Partial Ionization Cross Sections

For each of the target molecules listed above, relative PICS have been derived for the formation of positively charged ions, following electron ionization in the energy range 30-200 eV. Comparisons of the present PICS data with existing values of the PICS for these molecules have shown, in many cases, major discrepancies between the available data for the formation of the lighter ion fragments. In general, these differences were attributed to losses of translationally energetic fragment ions in the earlier studies, often involving quadrupoles or magnetic sector mass spectrometers. As expected, an excellent agreement was found between the present PICS data and the absolute PICS data of Tian and Vidal (C_2H_2 [1], CO_2 [2,3]), and Straub *et al.* (CO_2 [4], H_2O [5]). Indeed, both the apparatus used for the present investigations (Chapter 2), and the apparatus of Tian and Vidal, and Straub *et al.* (Section 1.4.4), permit the efficient collection of energetic fragment ions. A good overall agreement was also found between the present PICS data and the corresponding PICS data of Basner *et al.*, measured using the fast-neutral beam method (Section 1.4.4), for the electron ionization of C_2F_6 [6] and $SiCl_4$ [7], respectively.

For the five target molecules investigated in this thesis, precursor specific relative PICS have been derived, which quantify the yield of each product ion from single, double and triple ionization, respectively. Such precursor specific relative PICS have been interpreted for each molecule, to provide a highly detailed chemical description of the dissociations of singly and multiply charged precursor ions formed by electron ionization. A common feature of the data for all of the molecules studied is that the contributions to the yields of the smaller monatomic and diatomic ion fragments from dissociative double ionization, are often comparable to the corresponding contributions from dissociative single ionization, above 100 eV. Interestingly, it was shown that dissociative double ionization forms the major contribution to the yields of the halogen ions X^+, following electron ionization of C_2F_6 (F^+), and $SiCl_4$ (Cl^+, Cl_2^+), respectively, at ionizing energies moderately in excess of the double ionization potential. Indeed, a closer inspection of the precursor specific relative PICS for these two molecules, and the corresponding relative PICS for ion pair formation, show that the corresponding molecular dications exhibit a propensity for a high degree of fragmentation, involving a number of bond cleavages. As will be explained below, such data may be interpreted as further evidence in support of the impulsive nature of the dissociations of these molecular dications. Of course, the propensity for forming such halogen ions X^+ *via* dissociative double ionization of these molecules may also reflect the large number of channels that are accessible on the dicationic potential energy surface that lead to the formation of ion pairs comprising and X^+ ion. Nevertheless, the precursor specific relative PICS data described in this thesis highlight the important role of dissociative multiple ionization processes to the yields of many fragment ions observed for these molecules. As was shown by simulations of the ion coincidence data, such fragment ions comprising ion pairs typically have a translational kinetic energy in excess of a few electron Volts. Therefore, such data is of considerable importance in the development of reliable models of the ion-molecule chemistry occurring in planetary atmospheres, and for the understanding of the chemical processes that take place in industrial plasmas. On a more fundamental level, the shapes of the relative PICS and precursor specific relative PICS curves can also provide further insight into the nature of the ionization processes that contribute to the fragment ion yields. Specifically, for $SiCl_4$ it was shown that the narrow low energy maxima observed in the existing PICS curves for $SiCl_x^+$ formation[7] (x=1-3), correlate with a maximum in the ion yield from dissociative single ionization. The respective shapes of the precursor specific relative PICS curves derived in the present work support the view that indirect single ionization processes, resonant near 30 eV, dominate the yield of $SiCl_x^+$ ions at low energy, while direct double ionization processes contribute significantly to the yield of these ions at higher electron energies.

9.2 Statistical and Non-Statistical Dissociations of Singly and Multiply Charged Ions

An important question to arise from any study of the dissociative ionization of gaseous molecules is: 'Does the parent ion decay in a statistical manner, or do non-statistical processes operate in the dissociation of the parent ion to form product ion fragments'?[8-10] In this section this question is extended to include the dissociation dynamics of small gaseous dications. As was described in Section 1.3.1, if the parent ion is long-lived on a time period of internal motion (vibration and rotation), then the excess internal energy of the ion is partitioned statistically among all available modes prior to dissociation. Thus, the fractional abundances of product ions appearing in the mass spectrum can be predicted using RRKM/QET theory[9] (Eqn 1.6), and, hence, the decay of the parent ion is described as statistical. Fine examples of the statistical decay of polyatomic ions have been observed experimentally for a number of large organic monocations. In addition, the dications of many large open-chain and aromatic hydrocarbons show a propensity for forming product ion pairs which correlate qualitatively with product thermodynamic stability, as described in Section 4.5.1.1. By contrast, if the molecular ion dissociates on a timescale that is comparable to, or faster than, a time period of internal molecular motion, then the decay is described as non-statistical, or impulsive.[11,12] In its simplest form, the impulsive decay of one or a number of electronic states of the parent molecular ion gives rise to a non-statistical distribution of ion fractional abundances.

A number of state selective studies of the dissociations of molecular ions have been reported in the literature, many of which were performed using the (threshold) photoelectron-photoion coincidence ((T)PEPICO) technique (Section 1.2.2).[11-28] Measurements of the fragment ion yields as a function of the ion energy may then be compared with theoretical predictions, thereby providing a rigorous test of the statistical models used to describe the fragmentation of polyatomic gaseous ions. Such measurements may also be compared with the corresponding threshold photoelectron spectra, to identify whether the formation of each ion of interest correlates with one or a number of electronic states of the parent monocation. Evidence of such 'isolated state' behaviour is, typically, only observed for the smaller polyatomic ions comprising less than 10 atoms, whereas statistical processes are of greater importance in the dissociations of the larger polyatomic ions.[8,11,12,15-28]

The molecular systems investigated in this thesis range from eight atoms (C_2F_6), through five atoms ($SiCl_4$) and four atoms (C_2H_2), to only three atoms (CO_2, H_2O). Given the above analysis, one might, perhaps, expect the hexafluoroethane dication $C_2F_6^{2+}$ to fragment in a more statistical manner than, for example, the smaller acetylene dication $C_2H_2^{2+}$. In the present studies of the electron ionization of these molecules, the energy distributions of the parent ions (monocations and dications) formed at each ionizing electron energy, are unknown. However, despite this limitation, dication branching ratios and PICS for ion pair formation derived from the experimental data have been analysed qualitatively, to establish whether non-statistical processes are prevalent in the dissociations of these small molecular dications.

In the study of hexafluoroethane it was shown that the major dissociation channels of the $C_2F_6^{2+}$ dication do not correlate with thermodynamic stability of the ion pair products that are energetically accessible. Through a detailed analysis of the peak slope data extracted from the 2-D ion coincidence spectra, fast sequential decay mechanisms were proposed for the formation of a number of ion pairs. These impulsive mechanisms involve C-F bond fission prior to any subsequent dissociation steps, thereby offering an explanation of the low propensity for forming $CF_3^+ + CF_3^+$ ion pairs (involving only C-C bond fission), the lowest energy dissociation asymptote of the hexafluoroethane dication. On the basis of this experimental evidence, it was concluded that non-statistical processes play a significant role in the dissociations of $C_2F_6^{2+}$ dications formed *via* electron ionization in the energy range 30-200 eV. By contrast, the comparison of the experimental branching ratios for charge-separating dissociation of the $C_2H_2^{2+}$ dication with corresponding *ab initio*/RRKM calculations[29], suggests that dissociation occurs predominantly on the ground triplet potential energy surface, with a much smaller contribution from dissociation *via* the lowest singlet potential energy surface, and perhaps higher electronic states. In summary, the present work shows that statistical processes are dominant in fragmentation of the acetylene dication, despite the fact that the C_2H_2 molecule contains only four atoms.

The broader implication of the above results is that the number of atoms is not the only factor that influences whether non-statistical processes are important in the dissociations of polyatomic (di)cations. Indeed, existing studies have shown that the identity of the atoms within a molecule play a significant role in the dissociation dynamics of gaseous ions. For example, in a series of TPEPICO studies Tuckett and co-workers investigated the dissociations of state-selected cations of the fluoroethanes[25-28] $C_2F_xH_{6-x}^+$ (x=5,4,3,1) and the perfluorocarbons[16,24] $C_2F_6^+$, $C_3F_8^+$, n-$C_4F_{10}^+$, and c-$C_4F_8^+$. Interestingly, for all of these fluorinated molecules isolated state behaviour was observed for the low-lying electronic states of the parent monocation. Specifically, these electronic states yield selectively fragment ions formed *via* C-F (or C-H) bond fission, as opposed to those ions formed *via* C-C bond fission or intramolecular rearrangement. Complementary molecular electronic structure calculations show that for lower ion internal energies, the product fragment ions formed correlate strongly with the type of electron removed upon ionization of the neutral molecule.[25-28] That is, the removal of an electron from a valence molecular orbital with strong C-F σ bonding or C-H σ bonding character gives rise to rapid non-statistical dissociation processes involving C-F or C-H bond fission. As described above, such processes were observed in the present work for the fragmentations of the $C_2F_6^{2+}$ dication. As expected, the importance of these non-statistical processes decreases among the perfluorocarbon cations as the number of atoms in the system increases.[16,24] However, a similar comparison of the TPEPICO data for the $C_2F_xH_{6-x}^+$ ions reveals that the extent of isolated state behaviour also decreases among the fluoroethanes as the number of hydrogen atoms increases.[25-28] Clearly, the small size and the lability of H-atoms has an important effect on the potential energy surfaces (PES) of small gaseous polyatomic ions, such that non-statistical processes become less important for these ions as the number of H-atoms increases. One may speculate that the presence of H-atoms increases the density of states of a molecular ion and may enhance the vibronic coupling of these states. As a result, molecules containing a larger number of H-atoms have access to a large manifold of states following ionization, and therefore dissociate predominantly *via* statistical processes. In the present work, the different influences of H-atoms and halogen atoms, respectively, on the various ion potential energy surfaces, may explain why the dissociations of the acetylene dication are largely statistical, while for the larger halogenated dications, $C_2F_6^{2+}$ and $SiCl_4^{2+}$, the dissociations are largely impulsive in nature.

9.3 The Energetics of Dication Dissociation

For each of the five molecular systems investigated in this thesis, simulations of the 2-D ion coincidence data were performed to determine the kinetic energy release (KER) involved in ion pair formation. These KER measurements have been used to provide estimates of the precursor state energies of the corresponding molecular dications, for forming ion pairs. For the $C_2F_6^{2+}$ and $SiCl_4^{2+}$ dications, these estimates represent the first estimates of the dicationic electronic state energies, therefore highlighting the need for further experimental and theoretical studies into the properties and energetics of these species. For the remaining dications investigated in the present work, $C_2H_2^{2+}$, CO_2^{2+}, and H_2O^{2+}, the determinations of the KER involved in ion pair formation, and dication precursor state energies, were shown to be in good overall agreement with existing experimental and theoretical data. As described above, such measurements are of importance to developing our understanding of the chemical processes take place in highly energised media, including industrial plasmas, planetary atmospheres and comets.

9.4 References

[1] C. C. Tian and C. R. Vidal, Journal Of Physics B-Atomic Molecular And Optical Physics **31** (4), 895 (1998).

[2] C. C. Tian and C. R. Vidal, Physical Review A **58** (5), 3783 (1998).

[3] C. C. Tian and C. R. Vidal, Journal Of Chemical Physics **108** (3), 927 (1998).

[4] H. C. Straub, B. G. Lindsay, K. A. Smith, and R. F. Stebbings, Journal Of Chemical Physics **105** (10), 4015 (1996).

[5] H. C. Straub, B. G. Lindsay, K. A. Smith, and R. F. Stebbings, Journal Of Chemical Physics **108** (1), 109 (1998).

[6] R. Basner, M. Schmidt, E. Denisov, P. Lopata, K. Becker, and H. Deutsch, International Journal of Mass Spectrometry **214** (3), 365 (2002).

[7] R. Basner, M. Gutkin, J. Mahoney, V. Tarnovsky, H. Deutsch, and K. Becker, Journal of Chemical Physics **123** (5) (2005).

[8] P. A. Hatherly, D. M. Smith, and R. P. Tuckett, Zeitschrift Fur Physikalische Chemie-International Journal of Research in Physical Chemistry & Chemical Physics **195**, 97 (1996).

[9] T. Baer and P. M. Mayer, Journal of the American Society for Mass Spectrometry **8** (2), 103 (1997).

[10] T. Baer, International Journal of Mass Spectrometry **200** (1-3), 443 (2000).

[11] J. C. Creasey, D. M. Smith, R. P. Tuckett, K. R. Yoxall, K. Codling, and P. A. Hatherly, Journal of Physical Chemistry **100** (11), 4350 (1996).

[12] D. P. Seccombe, R. Y. L. Chim, G. K. Jarvis, and R. P. Tuckett, Physical Chemistry Chemical Physics **2** (4), 769 (2000).

[13] T. A. Field and J. H. D. Eland, Journal of Electron Spectroscopy and Related Phenomena **73** (2), 209 (1995).

[14] D. Aitchison and J. H. D. Eland, Chemical Physics **263** (2-3), 449 (2001).

[15] K. J. Boyle, G. K. Jarvis, and R. P. Tuckett, Journal of the Chemical Society-Faraday Transactions **94** (8), 1045 (1998).

[16] G. K. Jarvis, K. J. Boyle, C. A. Mayhew, and R. P. Tuckett, Journal of Physical Chemistry A **102** (19), 3230 (1998).

[17] D. P. Seccombe, G. K. Jarvis, B. O. Fisher, and R. P. Tuckett, Chemical Physics **250** (3), 335 (1999).

[18] D. P. Seccombe, R. P. Tuckett, and B. O. Fisher, Journal of Chemical Physics **114** (9), 4074 (2001).

[19] C. R. Howle, R. Y. L. Chim, R. P. Tuckett, and A. E. R. Malins, Chemical Physics **303** (1-2), 227 (2004).

[20] C. R. Howle, D. J. Collins, R. P. Tuckett, and A. E. R. Malins, Physical Chemistry Chemical Physics **7** (11), 2287 (2005).

[21] M. A. Parkes, R. Y. L. Chim, C. A. Mayhew, V. A. Mikhailov, and R. P. Tuckett, Molecular Physics **104** (2), 263 (2006).

[22] M. A. Parkes, S. Ali, C. R. Howle, R. P. Tuckett, and A. E. R. Malins, Molecular Physics **105** (5-7), 907 (2007).

[23] M. A. Parkes, S. Ali, M. J. Simpson, R. P. Tuckett, and A. E. R. Malins, Molecular Physics **106** (14), 1739 (2008).

[24] G. K. Jarvis, K. J. Boyle, C. A. Mayhew, and R. P. Tuckett, Journal of Physical Chemistry A **102** (19), 3219 (1998).

[25] W. D. Zhou, D. P. Seccombe, R. P. Tuckett, and M. K. Thomas, Chemical Physics **283** (3), 419 (2002).

[26] W. D. Zhou, D. P. Seccombe, and R. P. Tuckett, Physical Chemistry Chemical Physics **4** (19), 4623 (2002).

[27] W. D. Zhou, D. J. Collins, R. Y. L. Chim, D. P. Seccombe, and R. P. Tuckett, Physical Chemistry Chemical Physics **6** (12), 3081 (2004).

[28] W. D. Zhou, D. J. Collins, R. Y. L. Chim, and R. P. Tuckett, New Journal of Physics **9** (4), 104 (2007).

[29] T. S. Zyubina, Y. A. Dyakov, S. H. Lin, A. D. Bandrauk, and A. M. Mebel, Journal Of Chemical Physics **123** (13) (2005).

Appendix A

Time-of-Flight Mass Spectrometry

The TOF mass spectrometer (TOFMS) used in this thesis is based upon the standard Wiley-McLaren[1] two-field design, shown schematically in Figure 2.1. In this appendix two important aspects of the design are discussed. Firstly, the relationship between the ion flight time and ion mass is derived, thereby providing a means for the calibration of all mass spectra recorded. Secondly, the conditions for space-focusing are derived for ions formed in the source, to first order.[1] These conditions are conveniently expressed in terms of a single parameter defined by the source field and acceleration field. This parameter enables voltage conditions to be selected which provide good spatial resolution whilst optimising the collection efficiency of energetic ions.

Derivation of Ion Flight Times for a Two-Field TOFMS

The flight time of an ion formed in the centre of the source region in the TOFMS can be derived using Newtonian mechanics and elementary electrostatic equations. This flight time (t_{tof}) can be divided into three individual time components, namely the time taken for an ion to traverse the source (t_s), acceleration (t_d) and drift (t_D) region, respectively:

$$t_{tof} = t_s + t_d + t_D \qquad \text{A.1}$$

t_s: The time taken for an ion to traverse the source region of length $2s$ can be expressed in terms of the initial ion velocity upon formation (v_0), the final ion velocity leaving the source (v_s), and the ion acceleration a:

$$t_s = \frac{v_s - v_0}{a} \qquad \text{where} \qquad v_s^2 = v_0^2 + 2as \qquad \text{A.2}$$

In these equations the acceleration of an ion of mass m and charge q is given by:

$$a = \frac{qE_s}{m} \qquad \text{A.3}$$

where E_s is the electric field strength in the source region.

The initial velocity of an ion formed with kinetic energy U_0 is defined as:

$$v_0 = \left(\frac{2U_0}{m}\right)^{1/2} \qquad \text{A.4}$$

Substitution of these expressions for a and v_0 into A.2 yields:

$$v_s = \left(\frac{2}{m}\right)^{1/2} [U_0 + qE_s s]^{1/2} \qquad \text{A.5}$$

and hence:

$$t_s = \frac{(2m)^{1/2}}{qE_s}\left[(U_0 + qE_s s)^{1/2} - U_0{}^{1/2}\right] \qquad \text{A.6}$$

t_d: The time taken for an ion to traverse the acceleration region of length d can similarly be found using the above method:

$$t_d = \frac{v_d - v_s}{a} \qquad \text{A.7}$$

where, for an acceleration field E_d:

$$a = \frac{qE_d}{m} \quad \text{and} \quad v_d = \left(\frac{2}{m}\right)^{1/2} [U_0 + qE_s s + qE_d d]^{1/2} \qquad \text{A.8}$$

and hence, by substitution:

$$t_d = \frac{(2m)^{1/2}}{qE_d}\left\{U^{1/2} - [U_0 + qE_s s]^{1/2}\right\} \qquad \text{A.9}$$

where U is defined as the final kinetic energy of the ion that impacts on the MCP detector:

$$U = U_0 + qE_s s + qE_d d \qquad \text{A.10}$$

t_D: Ions pass through the field-free drift tube with a constant velocity:

$$v_D = v_d = \left(\frac{2}{m}\right)^{1/2} U^{1/2} \qquad \text{A.11}$$

Therefore the time taken to traverse the drift length D is given by:

$$t_D = \frac{D}{v_D} = (2m)^{1/2}\frac{D}{2U^{1/2}} \qquad \text{A.12}$$

The combination of Eqns A.1, A.6, A.9 and A.12 yields an expression for the total flight time of an ion of mass *m* in the TOFMS:

$$t_{tof} = (2m)^{1/2}\left\{\left[\frac{(U_0 + qE_s s)^{1/2} - U_0^{1/2}}{qE_s}\right] + \left[\frac{U^{1/2} - (U_0 + qE_s s)^{1/2}}{qE_d}\right] + \frac{D}{2U^{1/2}}\right\} \qquad \text{A.13}$$

which can be simplified to:

$$t_{tof} = k\sqrt{m} + c \qquad \text{A.14}$$

where *k* are *c* are constants. The value of *k* is dependent on the geometry of the apparatus and voltage conditions used, while *c* is a constant that quantifies the time delay arising due to the timing electronics. An obvious consequence of this relationship is that flight times of at least two ions of known mass must be measured, and the resulting set of simultaneous equations solved for *k* and *c*, in order to calibrate the mass scale of each spectrum recorded.

Space Focusing

Due to the finite spatial width of the ionizing pulse of electrons, ions of identical mass and same initial kinetic energy are formed within a narrow range of initial positions about the plane, perpendicular to the TOF axis, that defines the centre of the source region. Such ions formed in different positions in the source may give rise to different flight times, thereby limiting the spectral resolution achieved by the apparatus. This problem was surmounted, in part, by Wiley and McLaren[1] in their development of a two-field TOFMS offering improved spatial and energy resolution. The improvement in spatial resolution utilises the fact that the above ions formed towards the back of the source region (further away from the detector) are accelerated for a longer time period and hence reach a higher kinetic energy than the ions formed towards the front of the source (closer to the detector). Therefore, although ions formed towards the back of the source arrive at the drift region after a longer time period, they traverse the drift region with a greater velocity. Within the drift region there exists a plane, defined as a space focus plane, where the ions formed initially further from the detector 'catch up' with the ions formed initially closer to the detector. This situation is shown schematically in Figure A.1. If the ion detector is positioned at this space focusing plane, the spatial resolution of the mass spectra obtained is greatly enhanced.

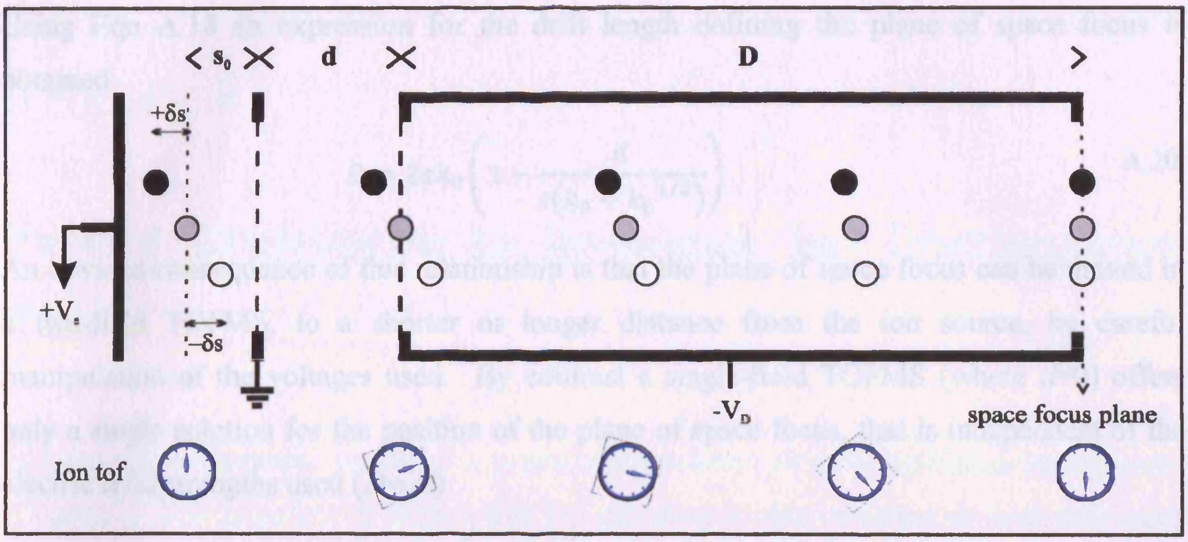

Figure A.1 Space focusing in a two-field TOFMS of Wiley-McLaren[1] design.

Wiley and McLaren defined a new parameter k_0:

$$k_0 = \frac{sE_s + dE_d}{sE_s} \qquad \text{A.15}$$

which, in combination with Eqn A.10 for the total ion KE *U*, provides the useful relations:

$$qsE_s = \frac{U}{k_0} \qquad \text{and} \qquad qdE_d = \frac{U(k_0 - 1)}{k_0} \qquad \text{A.16}$$

Substituting Eqns A.16 into Eqn A.13 yields an expression for the flight time for an ion with mass *m* and initial kinetic energy $U_0=0$ (chosen for simplicity), formed in the source region at a position defined by s_0:

$$t(0, s_0) = (2m)^{1/2}\left[\frac{{k_0}^{1/2}s_0}{U^{1/2}} + \frac{U^{1/2}(1 - {k_0}^{-1/2})kd}{U(k-1)} + \frac{D}{2U^{1/2}}\right] \qquad \text{A.17}$$

which, using the identity $(k\text{-}1)=(k^{1/2}\text{-}1)(k^{1/2}+1)$, gives:

$$t(0, s_0) = \left(\frac{m}{2U}\right)^{1/2}\left[2{k_0}^{1/2}s_0 + \frac{2{k_0}^{1/2}d}{({k_0}^{1/2} + 1)} + D\right] \qquad \text{A.18}$$

The condition for space focusing requires that ions formed in the source with an initial position $s=s_0\pm\delta s$ give rise to identical ion flight times at the space focusing plane. To first order, this condition requires that:

$$\left(\frac{\partial t}{\partial s}\right)_{U_0=0,s} = 0 \qquad \text{A.19}$$

Using Eqn A.18 an expression for the drift length defining the plane of space focus is obtained:

$$D = 2sk_0\left(1 - \frac{d}{s\left(k_0 + k_0^{1/2}\right)}\right) \qquad \text{A.20}$$

An obvious consequence of this relationship is that the plane of space focus can be moved in a two-field TOFMS, to a shorter or longer distance from the ion source, by careful manipulation of the voltages used. By contrast a single-field TOFMS (where $d=0$) offers only a single solution for the position of the plane of space focus, that is independent of the electric field strengths used ($D=2s$).

References

[1] W. C. Wiley and I. H. McLaren, Review Of Scientific Instruments **26** (12), 1150 (1955).

Appendix B

Further Experiments to Investigate Ion Discrimination Effects

In extracting quantitative data from a pulsed electron-beam time-of-flight mass spectrometer (Chapter 2) it is important to ensure that the apparatus is able to detect all ions with equal efficiency, regardless of their mass or initial kinetic energy.[1] Bruce and Bonham[2] have investigated a number of experimental parameters that may give rise to such discrimination effects through the careful measurement of the Ar^{2+}/Ar^+ ratio following electron ionization of argon. In this previous work, experimental parameters were termed 'dependent' if, upon variation within a specified range, a significant change (>3%) in the Ar^{2+}/Ar^+ ratio was observed. By contrast, experimental parameters that did not significantly affect this ratio were termed 'independent'. The results of this previous study are summarised in Table B.I. It must be noted, however, that both Ar^{2+} and Ar^+ ions detected in these experiments are formed initially with only thermal kinetic energies. Therefore the work of Bruce and Bonham[2] does not consider the effects of such experimental parameters on the collection efficiency of ions formed initially with greater-than-thermal kinetic energy. Translationally energetic ions may escape detection where, under the voltage conditions used, such ions are inefficiently collected at the detector. Losses of translationally energetic ions may also occur through collisions with the walls of the apparatus in the source region. As described in Section 6.2.1, any energy dependent discrimination effects in the mass spectrometer are particularly pertinent when studying fragmentation processes which generate H^+.[3] This is because if a dissociation event forms a proton, conservation of linear momentum dictates that most of the energy released in the dissociation process is partitioned to the lighter H^+ fragment ion. Therefore, further experiments are required to ensure that under the operating parameters used in this thesis, energy-dependent discrimination effects do not influence the ion yields measured.

In this section experiments are described whereby the intensities of singly charged fragment ions are measured following electron impact ionization of acetylene at 100 eV, whilst systematically changing a number of the experimental parameters highlighted in the important work of Bruce and Bonham. The intensities of these fragment ions, which may be formed with considerable kinetic energy[4-9], are processed to yield relative PICS values using the data reduction procedure described in Section 3.3.2. These values are expressed relative to the cross section for forming the parent monocation $C_2H_2^+$, formed with only thermal kinetic energy.

Independent Parameters		Dependent Parameters	
Parameter	Range varied	Parameter	Range varied
Electron beam current	0.1pA-5nA	Background gas pressure	1-30μTorr
Electron pulse duration	40ns-1μs	Ion impact E on MCP	1-5keV
Grids (defining the electric fields) in the TOFMS	2-5	Threshold setting on CFD	25-500mV
Drift Tube Potential	300-1000V		
Ion Extraction Potential	10-100V		
Time delay between electron pulse (end) and ion extraction	10ns-1μs		

Table B.I A summary of the experimental parameters investigated by Bruce and Bonham[2] in a study of the electron ionization of argon. Parameters denoted 'dependent' were shown to give rise to a ≥ 3% change in the Ar^{2+}/Ar^+ ratio measured using a pulsed electron-beam TOFMS.

MCP Detector Bias Voltage

Relative PICS values for formation of H^+, C^+, CH^+, C_2^+ and C_2H^+ ions, shown as a function of MCP detector bias voltage, are displayed in Figure B.1. No significant changes in the σ_r values for these ion fragments are observed within the narrow range of the detector bias voltage investigated. In addition the yields of these fragment ions are shown to be in good agreement with the 'recommended' PICS data of Tian and Vidal[10]. Thus, the results suggest that the values of the detector bias voltage used throughout this thesis (2150-2250 V), in combination with the discriminator threshold setting (~50 mV), do not give rise to ion discrimination effects. Under the typical operating conditions used in the TOFMS (Section 2.3) singly charged ions impinge on the detector with an energy in excess of 2 keV. Straub *et* *al.*[11] have shown previously that the detection efficiency of such ions with mass ≤ 131 Da approaches unity as the MCP detector bias is increased above 2000 V. Therefore, this previous work also implies that the detector bias voltage used in this thesis permits the detection of fragment ions with equal efficiency.

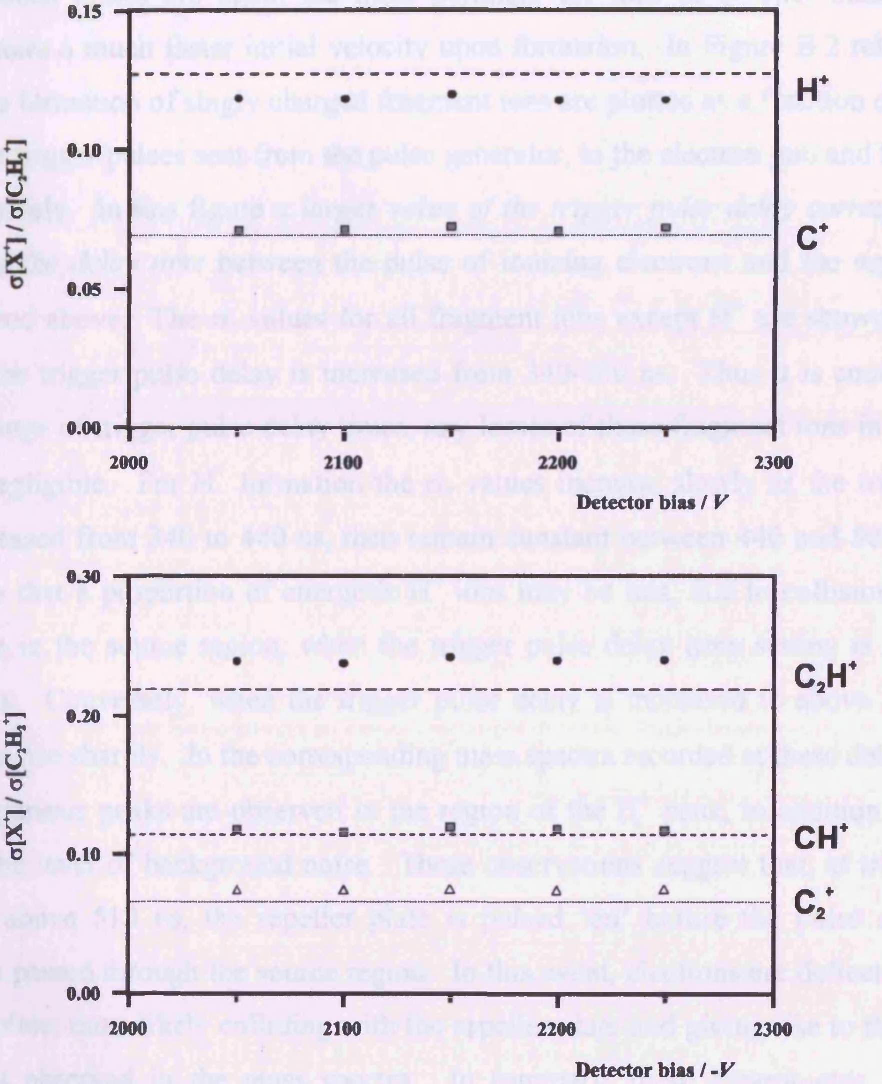

Figure B.1 Relative PICS for forming fragment ions following electron ionization of acetylene at 100 eV (solid shapes) as a function of MCP detector bias voltage. The dashed lines represent the relative PICS for each ion fragment derived from the 'recommended' data of Tian and Vidal[10].

Electron Pulse-Repeller Pulse Delay Time

In the source region of the TOFMS a short time delay exists between the passage of a pulse of ionizing electrons through the source and the pulsing of the repeller plate to extract any ions formed. During this time delay energetic fragment ions will traverse the source region and may escape detection through collisions with the repeller plate or the walls of the apparatus. Such losses are again the most pertinent for ions of smaller mass, as these typically acquire a much faster initial velocity upon formation. In Figure B.2 relative PICS values for the formation of singly charged fragment ions are plotted as a function of the delay time between trigger pulses sent from the pulse generator, to the electron gun and the repeller plate, respectively. In this figure *a larger value of the trigger pulse delay corresponds to a shortening of the delay time* between the pulse of ionizing electrons and the repeller plate pulse described above. The σ_r values for all fragment ions except H^+ are shown to remain constant as the trigger pulse delay is increased from 340-500 ns. Thus it is concluded that within this range of trigger pulse delay times, any losses of these fragment ions in the source region are negligible. For H^+ formation the σ_r values increase slowly as the trigger pulse delay is increased from 340 to 440 ns, then remain constant between 440 and 500 ns. This data suggests that a proportion of energetic H^+ ions may be lost, due to collisions with the repeller plate in the source region, when the trigger pulse delay time setting is reduced to below 440 ns. Conversely, when the trigger pulse delay is increased to above 510 ns the $\sigma_r[H^+]$ values rise sharply. In the corresponding mass spectra recorded at these delay times, a number of spurious peaks are observed in the region of the H^+ peak, in addition to a sharp increase in the level of background noise. These observations suggest that, at trigger pulse delay times above 510 ns, the repeller plate is pulsed 'on' before the pulse of ionizing electrons has passed through the source region. In this event, electrons are deflected towards the repeller plate, most likely colliding with the repeller plate and giving rise to the irregular noise signals observed in the mass spectra. In summary, these experiments suggest an optimum trigger pulse delay time of around 500 ns, while losses of energetic fragment ions are shown to be negligible for trigger pulse delay times between 440 and 500 ns. Thus for all experiments performed in this thesis, the delay time setting used for trigger pulses sent from the pulse generator to the electron gun and repeller plate (Table B.II), respectively, does not give rise to any significant losses of energetic ions.

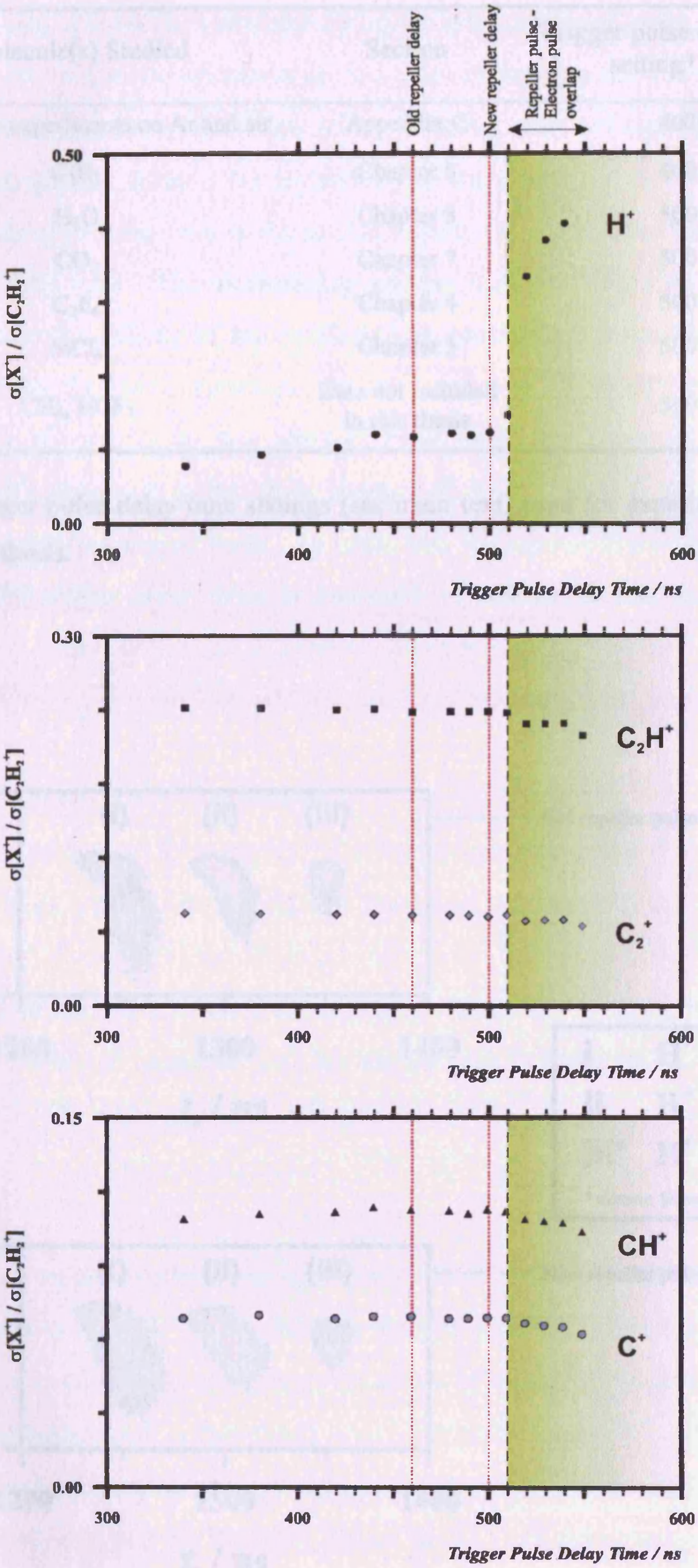

Figure B.2 Relative PICS for forming fragment ions following electron ionization of acetylene at 100 eV as a function of the delay time setting between trigger pulses sent to the electron gun and repeller plate, respectively.

Molecule(s) Studied	Section	Trigger pulse delay time setting* / ns
Preliminary experiments on Ar and air	Appendix C	460
C_2H_2	Chapter 6	460
H_2O	Chapter 8	500
CO_2	Chapter 7	500
C_2F_6	Chapter 4	500
$SiCl_4$	Chapter 5	500
CH_4, HCF_3	Data not included in this thesis	500

Table B.II Trigger pulse delay time settings (see main text) used for experiments performed in this thesis.

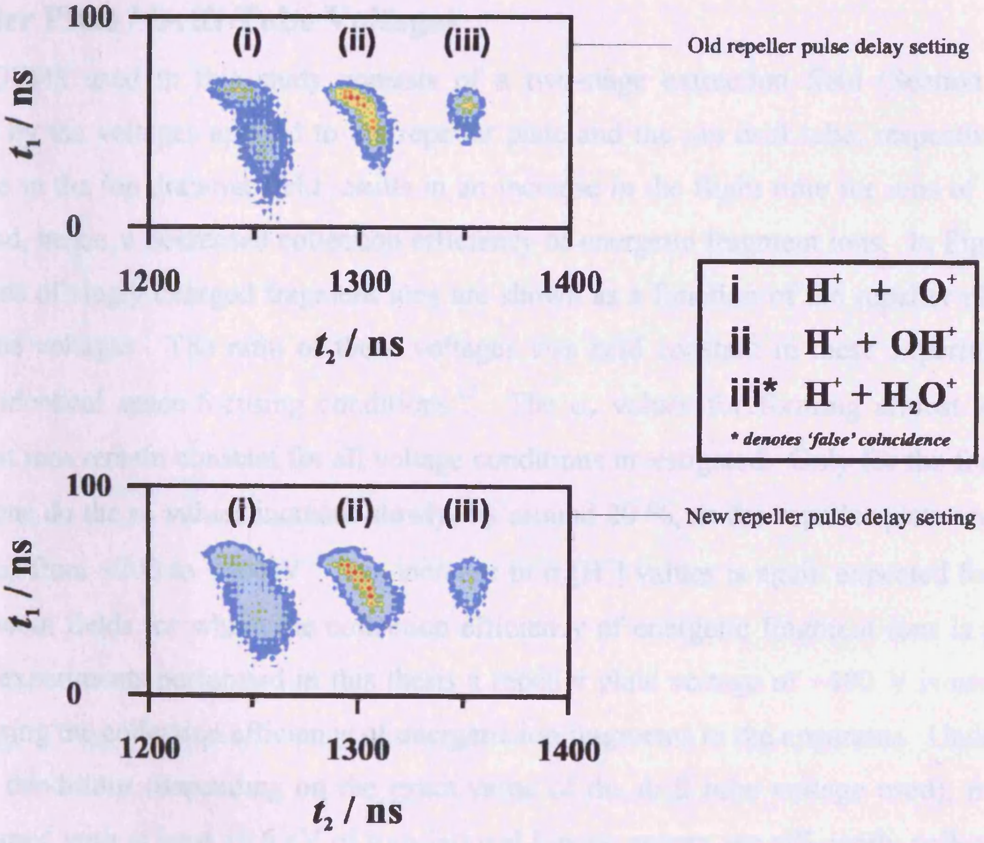

Figure B.3 Representative pairs mass spectra following electron ionization of H_2O at 200 eV. The top spectrum was recorded using a trigger pulse delay of 460 ns whereas the lower spectrum was recorded using the 'optimum' trigger pulse delay of 500 ns.

In all 2-D coincidence spectra for acetylene recorded using a trigger pulse delay time setting of 460 ns, asymmetric peaks are observed for ion pairs containing an H^+ ion (Section 6.2.1). The experiments described above show that this asymmetry does not signify any major losses of protons in the apparatus. Rather, the asymmetry of these peaks involving H^+ is due to the effects of a penetrating electric field in the source region, caused by the constant high voltage applied to the ion drift tube. This penetrating electric field partially extracts ions from the source region prior to the pulsing of the repeller plate, resulting in a reduction in the average flight time through the TOFMS. However, this effect is only observable in the mass spectra for peaks involving H^+ due to the low mass of these ions. In Figure B.3 a comparison is made between peaks observed in the pairs spectra of H_2O, recorded using a trigger pulse delay of 460 ns and 500 ns, respectively. As expected, the asymmetry of peaks involving H^+ is reduced when the trigger pulse delay is increased to 500 ns, as this minimises the delay between the time of ion formation and the repeller plate pulse.

Repeller Plate / Drift Tube Voltages

The TOFMS used in this study consists of a two-stage extraction field (Section 2.2.1), defined by the voltages applied to the repeller plate and the ion drift tube, respectively. A decrease in the ion drawout field results in an increase in the flight time for ions of a given mass and, hence, a decreased collection efficiency of energetic fragment ions. In Figure B.4 the yields of singly charged fragment ions are shown as a function of the repeller plate and drift tube voltages. The ratio of these voltages was held constant in these experiments to ensure identical space-focusing conditions.[12] The σ_r values for forming almost all such fragment ions remain constant for all voltage conditions investigated. Only for the formation of H^+ ions do the σ_r values increase slowly, by around 20 %, as the repeller plate voltage is increased from +200 to +400 V. This increase in $\sigma_r[H^+]$ values is again expected for larger ion drawout fields for which the collection efficiency of energetic fragment ions is greater. For all experiments performed in this thesis a repeller plate voltage of +400 V is used, thus maximising the collection efficiency of energetic ion fragments in the apparatus. Under these voltage conditions (depending on the exact value of the drift tube voltage used), fragment ions formed with at least 10.6 eV of translational kinetic energy are efficiently collected and detected (Section 2.3.2).

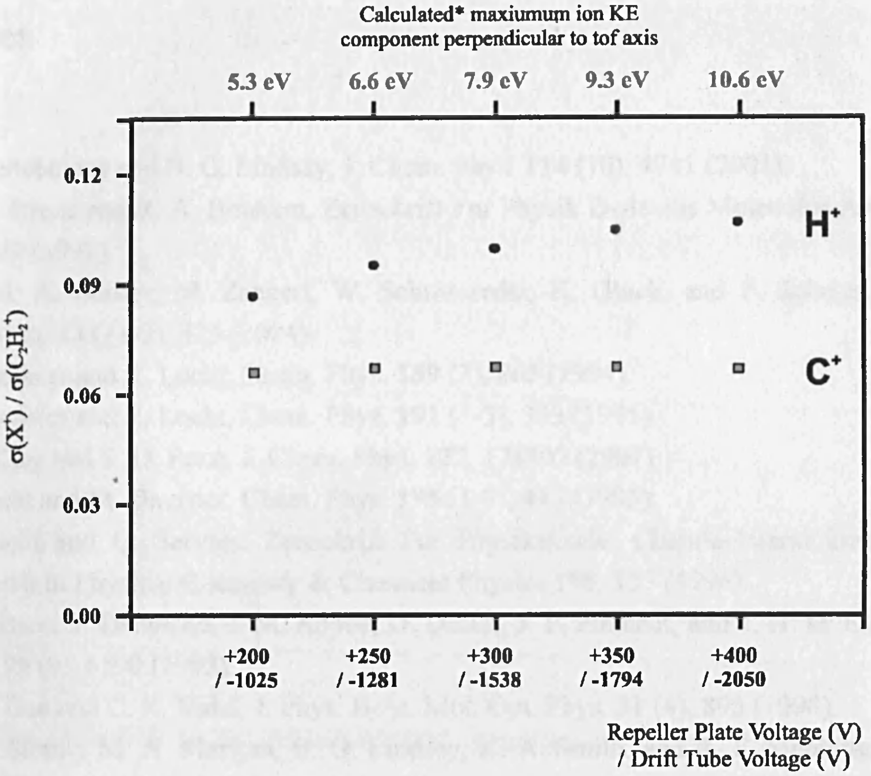

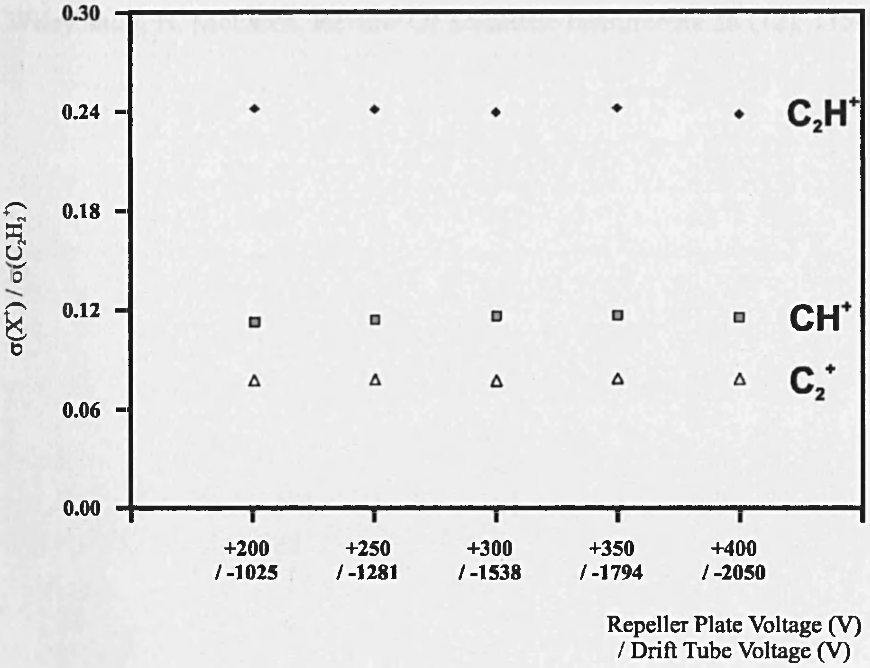

Figure B.4 Relative PICS for forming fragment ions following electron ionization of acetylene at 100 eV as a function of the repeller plate and drift tube voltage.

References

[1] R. F. Stebbings and B. G. Lindsay, J. Chem. Phys. **114** (10), 4741 (2001).

[2] M. R. Bruce and R. A. Bonham, Zeitschrift Fur Physik D-Atoms Molecules And Clusters **24** (2), 149 (1992).

[3] S. Feil, A. Bacher, M. Zangerl, W. Schustereder, K. Gluch, and P. Scheier, Int. J. Mass Spectrom. **233** (1-3), 325 (2004).

[4] M. Davister and R. Locht, Chem. Phys. **189** (3), 805 (1994).

[5] M. Davister and R. Locht, Chem. Phys. **191** (1-3), 333 (1995).

[6] S. J. King and S. D. Price, J. Chem. Phys. **127**, 174307 (2007).

[7] R. Locht and M. Davister, Chem. Phys. **195** (1-3), 443 (1995).

[8] R. Locht and C. Servais, Zeitschrift Fur Physikalische Chemie-International Journal Of Research In Physical Chemistry & Chemical Physics **195**, 153 (1996).

[9] R. Thissen, J. Delwiche, J. M. Robbe, D. Duflot, J. P. Flament, and J. H. D. Eland, J. Chem. Phys. **99** (9), 6590 (1993).

[10] C. C. Tian and C. R. Vidal, J. Phys. B-At. Mol. Opt. Phys. **31** (4), 895 (1998).

[11] H. C. Straub, M. A. Mangan, B. G. Lindsay, K. A. Smith, and R. F. Stebbings, Review Of Scientific Instruments **70** (11), 4238 (1999).

[12] W. C. Wiley and I. H. McLaren, Review Of Scientific Instruments **26** (12), 1150 (1955).

Appendix C

PICS of Ar, N_2 and O_2: Preliminary Experiments on the Electron Ionization of Argon and of Air

In this section the results of preliminary experiments on the electron ionization of argon and air are reported. All experiments were performed using the TOF mass spectrometer described in Section 2.2.1 using the operating parameters shown in Table 2.I. The argon gas was a commercial sample (>99%) and was used without further purification. The PICS of Ar^{2+} are expressed relative to the formation of Ar^+, while the PICS of N^{q+} and O^{q+} fragment ions are expressed relative to the formation of N_2^+ and O_2^+, respectively.

E / eV	$\sigma_r[Ar^{2+}]$	$10\,\sigma_r[N^{2+}]$	$\sigma_r[N^+/N_2^{2+}]$	$10\,\sigma_r[O^{2+}]$	$\sigma_r[O^+/O_2^{2+}]$
200	0.000	0.090	0.347	0.147	0.615
175	0.000	0.082	0.351	0.124	0.615
150	0.000	0.073	0.359	0.104	0.613
125	0.001	0.054	0.357	0.073	0.603
100	0.008	0.029	0.345	0.035	0.564
85	0.022	0.012	0.325	0.017	0.522
75	0.037	0.004	0.307	0.006	0.491
65	0.050	0.000	0.270	0.000	0.437
60	0.065	0.000	0.249	0.001	0.408
55	0.073	0.000	0.223	0.000	0.381
50	0.079	0.000	0.192	0.000	0.346
45	0.080	0.000	0.160	0.001	0.317
40	0.079	0.000	0.120	0.000	0.285
35	0.077	0.000	0.087	0.000	0.248
30	0.075	0.000	0.042	0.000	0.179

Table C.I Relative PICS for forming ions following electron ionization of argon and air, respectively. All values represent the averages of at least two separate experimental determinations.

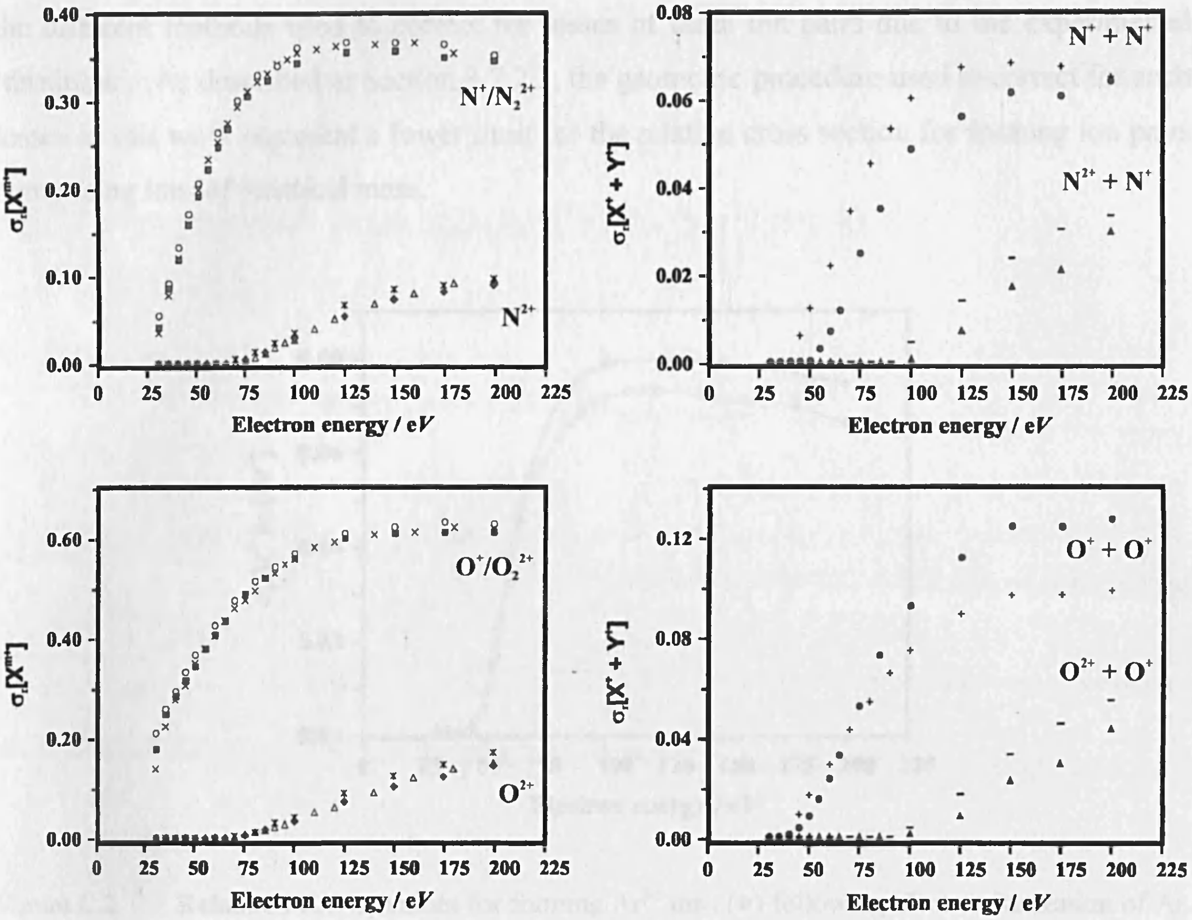

Figure C.1 Relative PICS $\sigma_r[X^{n+}]$ for forming fragment ions and ion pairs (filled symbols) following electron ionization of N_2 and O_2 (air). The estimated errors for these σ_r values are 10% for the formation of single ion fragments, and 15% for the formation of ion pairs. The corresponding relative PICS extracted from the data of Straub *et al.*[1] (hollow symbols), and Tian and Vidal[2] (lined-symbols), are also shown.

As shown in Figure C.1, the relative PICS values for forming single ions following electron ionization of air are in excellent agreement with the corresponding values derived from the data of Straub *et al.*[1] and Tian and Vidal[2]. In both of these previous studies the efficient collection of fragment ions formed with considerable initial kinetic energy has been demonstrated (Section 1.4.4). Therefore, the good agreement found between all three data sets suggests that under the operating conditions used in this thesis, energy dependent discrimination effects do not influence the ion yields measured. Only for the formation of N^+ + N^+ ion pairs are the σ_r values measured in this work significantly lower than the corresponding values of Tian and Vidal[2]. The origin of this discrepancy is most likely due to the different methods used to correct for losses of these ion pairs due to the experimental 'deadtime'. As described in Section 3.2.2.3, the geometric procedure used to correct for such losses in this work represent a lower limit for the relative cross section for forming ion pairs comprising ions of identical mass.

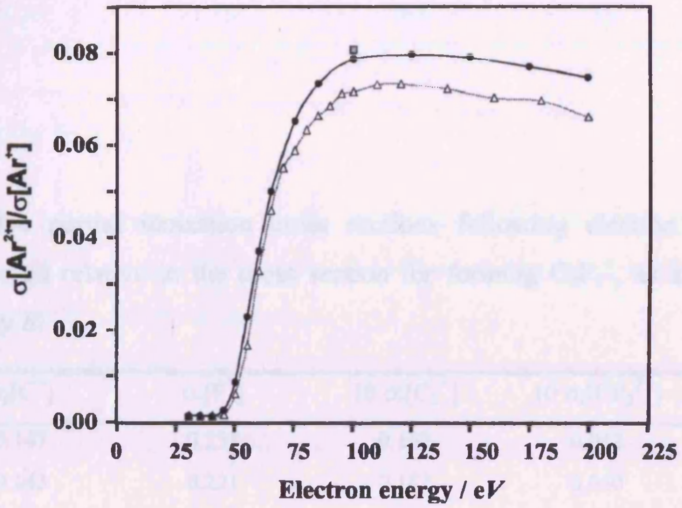

Figure C.2 Relative PICS σ_r values for forming Ar^{2+} ions (●) following electron ionization of Ar. The errors for these σ_r values are estimated as ±10%. The corresponding relative PICS extracted from the data of Bruce and Bonham[3] (□), and Straub *et al.*[4] (△), are also shown.

References

[1] H. C. Straub, P. Renault, B. G. Lindsay, K. A. Smith, and R. F. Stebbings, Phys. Rev. A **54** (3), 2146 (1996).

[2] C. Tian and C. R. Vidal, J. Phys. B-At. Mol. Opt. Phys. **31** (24), 5369 (1998).

[3] M. R. Bruce and R. A. Bonham, Zeitschrift Fur Physik D-Atoms Molecules And Clusters **24** (2), 149 (1992).

[4] H. C. Straub, P. Renault, B. G. Lindsay, K. A. Smith, and R. F. Stebbings, Phys. Rev. A **52** (2), 1115 (1995).

Appendix D

Relative Partial Ionization Cross Section Data

C_2F_6

Relative PICS

Table D.I Relative partial ionization cross sections following electron ionization of C_2F_6, expressed relative to the cross section for forming $C_2F_5^+$, as a function of electron energy *E*.

E / eV	$\sigma_r[C^+]$	$\sigma_r[F^+]$	$10\ \sigma_r[C_2^+]$	$10\ \sigma_r[CF_2^{2+}]$	$\sigma_r[CF^+]$
200	0.147	0.235	0.162	0.042	0.741
175	0.143	0.221	0.162	0.040	0.749
150	0.133	0.195	0.148	0.035	0.748
125	0.113	0.154	0.131	0.025	0.723
100	0.081	0.099	0.093	0.012	0.656
85	0.056	0.064	0.068	0.006	0.580
75	0.040	0.045	0.052	0.003	0.513
65	0.023	0.026	0.033	0.001	0.429
60	0.017	0.020	0.022	0.000	0.385
55	0.012	0.015	0.011	0.000	0.346
50	0.008	0.010	0.002	0.000	0.300
45	0.004	0.007	0.001	0.000	0.236
40	0.001	0.003	0.001	0.000	0.154
35	0.000	0.001	0.000	0.000	0.085
30	0.000	0.000	0.001	0.000	0.053

E / eV	$10\ \sigma_r[C_2F^+]$	$\sigma_r[CF_2^+]$	$10\ \sigma_r[C_2F_2^+]$	$\sigma_r[CF_3^+]$	$10\ \sigma_r[C_2F_4^+]$
200	0.148	0.480	0.025	1.613	0.078
175	0.155	0.486	0.026	1.625	0.078
150	0.154	0.488	0.026	1.635	0.079
125	0.154	0.481	0.028	1.645	0.078
100	0.136	0.448	0.029	1.647	0.080
85	0.122	0.406	0.029	1.635	0.079
75	0.109	0.366	0.030	1.613	0.079
65	0.093	0.310	0.030	1.582	0.078
60	0.083	0.280	0.029	1.567	0.077

E / eV	$10\,\sigma_r[C_2F^+]$	$\sigma_r[CF_2^+]$	$10\,\sigma_r[C_2F_2^+]$	$\sigma_r[CF_3^+]$	$10\,\sigma_r[C_2F_4^+]$
55	0.075	0.251	0.027	1.556	0.077
50	0.056	0.218	0.026	1.549	0.077
45	0.030	0.177	0.018	1.530	0.073
40	0.008	0.131	0.009	1.500	0.069
35	0.002	0.093	0.001	1.488	0.068
30	0.001	0.062	0.000	1.501	0.058

Precursor-Specific PICS

Table D.II Relative *precursor-specific* PICS for forming fragment ions following dissociative electron ionization of C_2F_6, expressed relative to the cross section for forming $C_2F_5^+$, as a function of electron energy *E*.

E / eV	$10\,\sigma_1[C^+]$	$\sigma_2[C^+]$	$10\,\sigma_3[C^+]$	$10\,\sigma_1[F^+]$	$\sigma_2[F^+]$
200	0.171	0.109	0.213	0.020	0.164
175	0.211	0.106	0.155	0.058	0.162
150	0.234	0.099	0.099	0.132	0.145
125	0.279	0.082	0.025	0.229	0.116
100	0.333	0.047	0.002	0.299	0.066
85	0.322	0.024	0.000	0.298	0.034
75	0.284	0.011	0.000	0.268	0.018
65	0.204	0.003	0.000	0.196	0.007
60	0.158	0.001	0.000	0.160	0.004
55	0.116	0.000	0.000	0.128	0.002
50	0.075	0.000	0.000	0.096	0.001
45	0.040	0.000	0.000	0.064	0.000
40	0.012	0.000	0.000	0.032	0.000
35	0.002	0.000	0.000	0.008	0.000
30	0.001	0.000	0.000	0.002	0.000

E / eV	$10\,\sigma_3[F^+]$	$10\,\sigma_1[C_2^+]$	$10\,\sigma_2[C_2^+]$	$10^2\,\sigma_2[CF_2^{2+}]$	$10\,\sigma_3[CF_2^{2+}]$
200	0.694	0.032	0.130	0.009	0.041
175	0.526	0.045	0.117	0.013	0.038
150	0.372	0.052	0.096	0.021	0.033
125	0.148	0.066	0.065	0.042	0.021
100	0.031	0.067	0.026	0.046	0.008
85	0.004	0.062	0.006	0.046	0.001
75	0.000	0.052	0.001	0.029	0.000
65	0.000	0.033	0.000	0.013	0.000
60	0.000	0.022	0.000	0.000	0.000

E / eV	10 $\sigma_3[\mathrm{F}^+]$	10 $\sigma_1[\mathrm{C_2}^+]$	10 $\sigma_2[\mathrm{C_2}^+]$	10^2 $\sigma_2[\mathrm{CF_2}^{2+}]$	10 $\sigma_3[\mathrm{CF_2}^{2+}]$
55	0.000	0.011	0.000	-0.002	0.000
50	0.000	0.002	0.000	0.000	0.000
45	0.000	0.001	0.000	0.000	0.000
40	0.000	0.001	0.000	0.000	0.000
35	0.000	0.000	0.000	0.000	0.000
30	0.000	0.001	0.000	0.000	0.000

E / eV	$\sigma_1[\mathrm{CF}^+]$	$\sigma_2[\mathrm{CF}^+]$	10 $\sigma_3[\mathrm{CF}^+]$	10 $\sigma_1[\mathrm{C_2F}^+]$	10 $\sigma_2[\mathrm{C_2F}^+]$
200	0.279	0.409	0.534	0.087	0.060
175	0.294	0.408	0.474	0.098	0.057
150	0.308	0.403	0.375	0.101	0.053
125	0.334	0.371	0.174	0.110	0.044
100	0.369	0.283	0.041	0.110	0.026
85	0.381	0.199	0.004	0.110	0.013
75	0.378	0.136	0.000	0.104	0.005
65	0.361	0.067	0.000	0.093	0.000
60	0.341	0.045	0.000	0.083	0.000
55	0.320	0.025	0.000	0.075	0.000
50	0.289	0.011	0.000	0.056	0.000
45	0.231	0.005	0.000	0.030	0.000
40	0.153	0.001	0.000	0.008	0.000
35	0.085	0.000	0.000	0.002	0.000
30	0.053	0.000	0.000	0.001	0.000

E / eV	$\sigma_1[\mathrm{CF_2}^+]$	$\sigma_2[\mathrm{CF_2}^+]$	10 $\sigma_3[\mathrm{CF_2}^+]$	10 $\sigma_1[\mathrm{C_2F_2}^+]$	10^2 $\sigma_2[\mathrm{C_2F_2}^+]$
200	0.120	0.346	0.142	0.021	0.040
175	0.126	0.348	0.125	0.022	0.038
150	0.132	0.345	0.104	0.023	0.038
125	0.143	0.331	0.061	0.025	0.031
100	0.162	0.285	0.018	0.026	0.024
85	0.176	0.229	0.004	0.028	0.017
75	0.179	0.186	0.000	0.030	0.009
65	0.183	0.127	0.000	0.030	0.003
60	0.183	0.097	0.000	0.029	0.001
55	0.181	0.070	0.000	0.027	0.000
50	0.177	0.040	0.000	0.026	0.000
45	0.158	0.019	0.000	0.018	0.000
40	0.127	0.004	0.000	0.009	0.000
35	0.092	0.001	0.000	0.001	0.000
30	0.062	0.000	0.000	0.000	0.000

E / eV	$\sigma_1[CF_3^+]$	$\sigma_2[CF_3^+]$	10 $\sigma_3[CF_3^+]$	10 $\sigma_1[C_2F_4^+]$	10^2 $\sigma_2[C_2F_4^+]$
200	1.428	0.181	0.033	0.076	0.020
175	1.439	0.182	0.032	0.076	0.021
150	1.451	0.181	0.028	0.077	0.018
125	1.471	0.172	0.020	0.076	0.018
100	1.496	0.150	0.008	0.078	0.017
85	1.509	0.125	0.002	0.078	0.010
75	1.509	0.104	0.000	0.078	0.008
65	1.510	0.072	0.000	0.077	0.005
60	1.510	0.057	0.000	0.077	0.003
55	1.513	0.042	0.000	0.077	0.001
50	1.523	0.026	0.000	0.077	0.001
45	1.516	0.013	0.000	0.073	0.000
40	1.497	0.003	0.000	0.069	0.000
35	1.488	0.000	0.000	0.068	0.000
30	1.501	0.000	0.000	0.058	0.000

Total Ion Yield from Each Level of Ionization

Table D.III Contributions to the total ion yield from single, double, and triple ionization, following electron ionization of C_2F_6, as a function of electron energy *E*.

E / eV	Single Ionization / %	Double Ionization / %	Triple Ionization / %
200	67.3	28.8	3.9
175	68.1	28.7	3.2
150	69.6	28.0	2.4
125	72.8	26.1	1.1
100	78.6	21.1	0.3
85	83.7	16.3	0.0
75	87.3	12.7	0.0
65	91.9	8.1	0.0
60	93.8	6.2	0.0
55	95.6	4.4	0.0
50	97.5	2.5	0.0
45	98.8	1.2	0.0
40	99.7	0.3	0.0
35	100.0	0.0	0.0
30	100.0	0.0	0.0

$SiCl_4$

Relative PICS

Table D.IV Relative partial ionization cross sections following electron ionization of $SiCl_4$, expressed relative to the cross section for forming $SiCl_4^+$, as a function of electron energy *E*.

E / eV	$10^2\ \sigma_r[Si^{2+}]$	$10^2\ \sigma_r[Cl^{2+}]$	$\sigma_r[Si^+]$	$10^2\ \sigma_r[SiCl^{2+}]$	$\sigma_r[Cl^+]$
200	0.185	0.145	0.259	0.902	1.113
175	0.215	0.153	0.277	0.983	1.176
150	0.188	0.143	0.295	1.014	1.260
125	0.205	0.129	0.316	1.079	1.329
100	0.185	0.097	0.336	1.207	1.386
85	0.125	0.069	0.339	1.196	1.368
75	0.097	0.049	0.342	1.078	1.354
65	0.077	0.033	0.334	1.097	1.271
60	0.063	0.000	0.322	1.068	1.200
55	0.024	0.000	0.308	1.019	1.125
50	0.006	0.000	0.289	0.710	0.983
45	0.000	0.000	0.278	0.283	0.829
40	0.000	0.000	0.249	0.106	0.592
35	0.000	0.000	0.177	0.003	0.302
30	0.000	0.000	0.076	-0.052	0.125

E / eV	$10^2\ \sigma_r[SiCl_2^{2+}]$	$\sigma_r[SiCl^+]$	$10\ \sigma_r[Cl_2^+]$	$\sigma_r[SiCl_2^+]$	$\sigma_r[SiCl_3^+]$
200	0.392	0.600	0.311	0.147	1.737
175	0.373	0.633	0.326	0.151	1.746
150	0.423	0.671	0.341	0.157	1.758
125	0.415	0.714	0.359	0.161	1.765
100	0.459	0.771	0.373	0.167	1.774
85	0.420	0.810	0.392	0.172	1.774
75	0.423	0.841	0.383	0.175	1.783
65	0.366	0.881	0.389	0.179	1.786
60	0.364	0.908	0.391	0.180	1.786
55	0.350	0.940	0.407	0.184	1.789
50	0.316	0.983	0.396	0.188	1.791
45	0.203	1.003	0.354	0.187	1.778
40	0.061	0.989	0.247	0.180	1.731
35	-0.010	0.952	0.111	0.181	1.649
30	-0.006	0.779	0.045	0.189	1.585

Precursor-Specific PICS

Table D.V Relative *precursor-specific* PICS for forming fragment ions following dissociative electron ionization of $SiCl_4$, expressed relative to the cross section for forming $SiCl_4^+$, as a function of electron energy E.

E / eV	$10^2\,\sigma_2[\mathrm{Si}^{2+}]$	$10^2\,\sigma_3[\mathrm{Si}^{2+}]$	$10^2\,\sigma_2[\mathrm{Cl}^{2+}]$	$10^2\,\sigma_3[\mathrm{Cl}^{2+}]$	$\sigma_1[\mathrm{Si}^+]$	$\sigma_2[\mathrm{Si}^+]$
200	-0.004	0.189	0.047	0.097	0.114	0.082
175	0.069	0.147	0.071	0.082	0.119	0.099
150	0.066	0.122	0.078	0.065	0.125	0.108
125	0.105	0.100	0.073	0.056	0.137	0.119
100	0.134	0.051	0.064	0.033	0.149	0.143
85	0.090	0.035	0.063	0.006	0.156	0.158
75	0.089	0.007	0.050	-0.001	0.162	0.168
65	0.079	-0.002	0.033	0.000	0.184	0.148
60	0.061	0.002	0.000	0.000	0.200	0.122
55	0.024	0.000	0.000	0.000	0.219	0.089
50	0.007	-0.001	0.000	0.000	0.256	0.033
45	0.001	-0.001	0.000	0.000	0.270	0.008
40	0.000	-0.001	0.000	0.000	0.247	0.002
35	0.000	0.000	0.000	0.000	0.177	0.000
30	0.000	0.000	0.000	0.000	0.076	0.000

E / eV	$\sigma_3[\mathrm{Si}^+]$	$10^2\,\sigma_2[\mathrm{SiCl}^{2+}]$	$10^2\,\sigma_3[\mathrm{SiCl}^{2+}]$	$\sigma_1[\mathrm{Cl}^+]$	$\sigma_2[\mathrm{Cl}^+]$	$\sigma_3[\mathrm{Cl}^+]$
200	0.063	0.403	0.499	0.037	0.876	0.201
175	0.060	0.475	0.509	0.036	0.942	0.198
150	0.062	0.481	0.533	0.050	1.001	0.209
125	0.060	0.552	0.527	0.064	1.056	0.208
100	0.044	0.667	0.541	0.108	1.105	0.173
85	0.025	0.736	0.460	0.142	1.099	0.127
75	0.012	0.779	0.299	0.179	1.095	0.079
65	0.002	1.046	0.051	0.233	1.022	0.016
60	0.000	1.064	0.004	0.271	0.929	0.000
55	0.000	1.019	0.000	0.327	0.798	0.000
50	0.000	0.710	0.000	0.403	0.580	0.000
45	0.000	0.283	0.000	0.421	0.408	0.000
40	0.000	0.106	0.000	0.372	0.220	0.000
35	0.000	0.003	0.000	0.235	0.067	0.000
30	0.000	-0.052	0.000	0.111	0.014	0.000

E / eV	$10^2\,\sigma_2[\mathrm{SiCl_2}^{2+}]$	$\sigma_1[\mathrm{SiCl}^+]$	$\sigma_2[\mathrm{SiCl}^+]$	$\sigma_3[\mathrm{SiCl}^+]$	$10^2\,\sigma_1[\mathrm{Cl_2}^+]$	$10\,\sigma_2[\mathrm{Cl_2}^+]$
200	0.392	0.377	0.188	0.035	0.164	0.289
175	0.373	0.396	0.201	0.037	0.163	0.304
150	0.423	0.416	0.215	0.040	0.198	0.316
125	0.415	0.440	0.233	0.041	0.206	0.332
100	0.459	0.479	0.252	0.040	0.206	0.346
85	0.420	0.505	0.268	0.036	0.293	0.358
75	0.423	0.529	0.286	0.026	0.379	0.341
65	0.366	0.558	0.316	0.006	0.477	0.340
60	0.364	0.584	0.324	0.000	0.482	0.343
55	0.350	0.623	0.317	0.000	0.684	0.338
50	0.316	0.739	0.244	0.000	0.797	0.317
45	0.203	0.858	0.145	0.000	1.041	0.250
40	0.061	0.941	0.048	0.000	1.020	0.145
35	-0.010	0.947	0.005	0.000	0.750	0.036
30	-0.006	0.777	0.001	0.000	0.410	0.004

E / eV	$10^2\,\sigma_3[\mathrm{Cl_2}^+]$	$10\,\sigma_1[\mathrm{SiCl_2}^+]$	$10\,\sigma_2[\mathrm{SiCl_2}^+]$	$\sigma_1[\mathrm{SiCl_3}^+]$	$\sigma_2[\mathrm{SiCl_3}^+]$
200	0.055	0.716	0.757	1.554	0.183
175	0.058	0.722	0.785	1.554	0.191
150	0.058	0.747	0.820	1.556	0.202
125	0.063	0.755	0.855	1.551	0.214
100	0.064	0.792	0.883	1.551	0.223
85	0.048	0.816	0.900	1.548	0.225
75	0.041	0.849	0.902	1.555	0.228
65	0.015	0.930	0.857	1.556	0.230
60	0.003	0.947	0.852	1.553	0.233
55	0.001	0.992	0.843	1.553	0.236
50	0.000	1.106	0.771	1.556	0.235
45	0.000	1.287	0.580	1.565	0.213
40	0.000	1.504	0.295	1.582	0.149
35	0.000	1.756	0.050	1.592	0.057
30	0.000	1.877	0.010	1.575	0.010

Total Ion Yield from Each Level of Ionization

Table D.VI Contributions to the total ion yield from single, double, and triple ionization, following electron ionization of $SiCl_4$, as a function of electron energy *E*.

E / eV	Single Ionization / %	Double Ionization / %	Triple Ionization / %
200	64.3	29.4	6.3
175	63.1	30.8	6.0
150	62.1	31.8	6.1
125	61.2	32.8	5.9
100	61.3	33.8	4.8
85	62.3	34.2	3.5
75	63.3	34.5	2.2
65	65.9	33.6	0.5
60	68.0	32.0	0.0
55	70.9	29.1	0.0
50	77.1	22.9	0.0
45	83.1	16.9	0.0
40	90.3	9.7	0.0
35	96.8	3.2	0.0
30	99.3	0.7	0.0

C_2H_2

Relative PICS

Table D.VII Relative partial ionization cross sections following electron ionization of C_2H_2, expressed relative to the cross section for forming $C_2H_2^+$, as a function of electron energy *E*. The value in parenthesis indicates the standard deviation in the last figure.

E / eV	$\sigma_r[H^+]$	$10^3\ \sigma_r[H_2^+]$	$10^3\ \sigma_r[C^{2+}]$	$\sigma_r[C^+/C_2^{2+}]$
200	0.102(4)	0.36(6)	0.20(3)	0.071(1)
175	0.110(6)	0.45(13)	0.17(2)	0.074(1)
150	0.115(3)	0.44(6)	0.16(2)	0.076(1)
125	0.117(5)	0.41(3)	0.11(3)	0.077(1)
100	0.117(6)	0.41(6)	0.07(2)	0.075(1)
85	0.113(4)	0.39(7)	0.03(2)	0.071(1)
75	0.104(4)	0.37(7)	0.02(1)	0.065(3)
65	0.100(13)	0.47(11)	-0.01(2)	0.059(2)
60	0.089(4)	0.41(4)	-0.01(1)	0.054(1)
55	0.087(5)	0.45(10)	0.00(2)	0.050(2)

E / eV	$\sigma_r[H^+]$	$10^3\ \sigma_r[H_2^+]$	$10^3\ \sigma_r[C^{2+}]$	$\sigma_r[C^+/C_2^{2+}]$
50	0.076(1)	0.39(2)	-0.01(1)	0.042(1)
45	0.066(2)	0.39(3)		0.035(2)
40	0.051(5)	0.36(3)		0.026(3)
35	0.035(9)	0.32(7)		0.015(3)
30	0.017(4)	0.25(6)		0.006(2)

E / eV	$\sigma_r[CH^+/C_2H_2^{2+}]$	$10^3\ \sigma_r[CH_2^+]$	$\sigma_r[C_2^+]$	$\sigma_r[C_2H^+]$
200	0.107(1)	2.4(9)	0.066(2)	0.237(2)
175	0.111(1)	2.9(3)	0.066(2)	0.236(2)
150	0.115(1)	2.4(4)	0.070(1)	0.242(2)
125	0.119(2)	2.2(9)	0.072(3)	0.242(3)
100	0.122(2)	2.5(8)	0.076(1)	0.247(3)
85	0.122(1)	3.2(6)	0.077(1)	0.246(2)
75	0.119(3)	3.2(5)	0.077(1)	0.245(1)
65	0.116(6)	4.0(14)	0.077(1)	0.246(1)
60	0.110(2)	3.7(3)	0.075(1)	0.246(2)
55	0.105(4)	3.9(4)	0.075(1)	0.246(1)
50	0.090(4)	3.5(10)	0.067(4)	0.226(11)
45	0.079(3)	3.7(6)	0.063(5)	0.215(21)
40	0.066(5)	4.1(7)	0.056(6)	0.19(11)
35	0.051(7)	3.5(5)	0.046(5)	0.184(13)
30	0.032(5)	3.5(3)	0.035(6)	0.173(30)

Precursor-Specific PICS

Table D.VIII Relative *precursor-specific* PICS for forming cationic fragments following dissociative electron ionization of C_2H_2, expressed relative to the cross section for forming $C_2H_2^+$, as a function of electron energy *E*. The value in parenthesis indicates the standard deviation in the last figure.

E / eV	$\sigma_1[H^+]$	$\sigma_2[H^+]$	$10^3\ \sigma_3[H^+]$	$10^3\ \sigma_2[C^{2+}]$	$10^3\ \sigma_3[C^{2+}]$	$\sigma_1[C^+]$
200	0.038(4)	0.062(4)	0.83(7)	0.14(4)	0.14(4)	0.034(2)
175	0.045(10)	0.064(4)	0.92(7)	0.12(3)	0.12(3)	0.036(3)
150	0.050(3)	0.064(3)	0.73(10)	0.14(3)	0.14(3)	0.039(3)
125	0.053(5)	0.063(4)	0.27(10)	0.10(2)	0.10(4)	0.043(3)
100	0.058(7)	0.059(4)	0.13(3)	0.07(2)	0.07(2)	0.047(2)
85	0.064(5)	0.049(1)		0.03(3)	0.03(3)	0.048(2)
75	0.062(4)	0.0423(4)		0.02(1)		0.048(3)
65	0.069(14)	0.031(2)		-0.01(2)		0.050(3)
60	0.063(4)	0.025(1)		-0.01(1)		0.048(1)

E / eV	$\sigma_1[H^+]$	$\sigma_2[H^+]$	$10^3\ \sigma_3[H^+]$	$10^3\ \sigma_2[C^{2+}]$	$10^3\ \sigma_3[C^{2+}]$	$\sigma_1[C^+]$
55	0.069(6)	0.018(1)		0.00(2)		0.047(2)
50	0.065(2)	0.010(1)		-0.01(1)		0.040(1)
45	0.061(2)	0.0048(4)		0.14(4)		0.035(2)
40	0.050(5)	0.0012(3)		0.12(3)		0.026(3)
35	0.035(9)	0.0001(1)		0.14(3)		0.015(3)
30	0.017(4)	0.0000(1)		0.10(2)		0.006(2)

E / eV	$\sigma_2[C^+]$	$10^3\ \sigma_3[C^+]$	$\sigma_1[CH^+]$	$\sigma_2[CH^+]$	$10^3\ \sigma_3[CH^+]$	$\sigma_1[CH_2^+]$
200	0.036(2)	0.98(5)	0.068(4)	0.038(3)	0.34(2)	0.0014(9)
175	0.036(3)	1.2(17)	0.069(5)	0.041(5)	0.39(8)	0.0019(3)
150	0.036(3)	1.0(15)	0.073(5)	0.042(5)	0.29(4)	0.00134(4)
125	0.034(2)	0.33(14)	0.079(8)	0.040(6)	0.23(2)	0.0011(9)
100	0.029(1)	0.18(4)	0.082(5)	0.040(3)	0.10(4)	0.0015(8)
85	0.022(2)		0.084(5)	0.038(4)		0.0022(7)
75	0.017(1)		0.085(4)	0.034(4)		0.0022(5)
65	0.009(2)		0.092(10)	0.024(5)		0.0031(15)
60	0.0056(7)		0.091(6)	0.019(4)		0.0029(4)
55	0.0032(5)		0.091(7)	0.014(4)		0.0032(4)
50	0.0011(1)		0.082(5)	0.007(1)		0.0030(10)
45	0.0004(1)		0.076(3)	0.0026(4)		0.0035(6)
40	0.00012(2)		0.066(5)	0.0006(1)		0.0040(7)
35	0.00003(1)		0.051(7)	0.00007(6)		0.0035(5)
30	0.00001(1)		0.032(5)	0.000002(2)		0.0035(4)

E / eV	$\sigma_2[CH_2^+]$	$\sigma_1[C_2^+]$	$\sigma_2[C_2^+]$	$\sigma_1[C_2H^+]$	$\sigma_2[C_2H^+]$
200	0.00099(11)	0.051(2)	0.0143(13)	0.212(1)	0.0250(12)
175	0.00097(6)	0.052(2)	0.0147(12)	0.211(2)	0.0260(15)
150	0.00104(6)	0.055(2)	0.0149(11)	0.215(3)	0.0263(9)
125	0.00104(6)	0.057(4)	0.0147(15)	0.215(3)	0.0270(16)
100	0.00104(6)	0.062(1)	0.0140(6)	0.221(2)	0.0267(20)
85	0.00103(9)	0.065(1)	0.0115(5)	0.222(2)	0.0242(7)
75	0.00104(1)	0.067(1)	0.0101(3)	0.223(2)	0.0220(4)
65	0.00084(11)	0.069(1)	0.0070(8)	0.227(2)	0.0188(9)
60	0.00080(13)	0.070(1)	0.0056(4)	0.229(2)	0.0167(6)
55	0.00067(9)	0.071(1)	0.0036(4)	0.234(3)	0.0127(10)
50	0.00043(2)	0.066(4)	0.00148(9)	0.218(12)	0.0085(5)
45	0.00025(3)	0.063(5)	0.00042(6)	0.211(21)	0.0044(4)
40	0.00007(2)	0.056(7)	0.00006(2)	0.192(11)	0.0011(3)
35	0.000010(3)	0.046(5)	0.00002(2)	0.184(13)	0.0001(1)
30	0.000000(0)	0.035(6)	0.00001(2)	0.173(31)	-0.00001(1)

Total Ion Yield from Each Level of Ionization

Table D.IX Contributions to the total ion yield from single, double, and triple ionization, following electron ionization of C_2H_2, as a function of electron energy *E*.

E / eV	Single Ionization / %	Double Ionization / %	Triple Ionization / %
200	88.7	11.2	0.14
175	88.4	11.4	0.16
150	88.5	11.4	0.13
125	88.9	11.0	0.05
100	89.7	10.3	0.02
85	91.0	9.0	0.00
75	92.1	7.9	0.00
65	94.4	5.6	0.00
60	95.4	4.6	0.00
55	96.7	3.3	0.00
50	98.1	1.9	0.00
45	99.1	0.9	0.00
40	99.8	0.2	0.00
35	100.0	0.0	0.00
30	100.0	0.0	0.00

CO_2

Relative PICS

Table D.X Relative partial ionization cross sections following electron ionization of CO_2, expressed relative to the cross section for forming CO_2^+, as a function of electron energy *E*. The value in parenthesis indicates the standard deviation in the last figure.

E / eV	$10^2\ \sigma_r[C^{2+}]$	$10^2\ \sigma_r[O^{2+}]$	$\sigma_r[C^+]$	$\sigma_r[O^+]$	$\sigma_r[CO_2^{2+}]$	$\sigma_r[CO^+]$
200	0.1387 (12)	0.0981 (37)	0.1517 (14)	0.3135 (22)	0.01448 (6)	0.1716 (14)
175	0.1218 (38)	0.0790 (65)	0.1528 (10)	0.3157 (17)	0.01444 (36)	0.1767 (24)
150	0.0941 (66)	0.0629 (72)	0.1533 (6)	0.3139 (15)	0.01452 (44)	0.1802 (21)
125	0.0629 (36)	0.0307 (54)	0.1498 (6)	0.3071 (8)	0.01399 (15)	0.1842 (15)
100	0.0289 (24)	0.0110 (32)	0.1415 (13)	0.2863 (7)	0.01275 (28)	0.1877 (13)
85	0.0117 (5)	0.0053 (16)	0.1326 (10)	0.2639 (23)	0.01102 (21)	0.1890 (14)
75	0.0043 (8)	0.0006 (12)	0.1239 (9)	0.2427 (9)	0.00934 (4)	0.1872 (19)
65	0.0004 (3)	0.0002 (2)	0.1110 (5)	0.2132 (13)	0.00678 (13)	0.1831 (6)
60	0.0000 (1)	-0.0002 (4)	0.1022 (1)	0.1947 (26)	0.00530 (3)	0.1806 (6)
55	0.0000 (5)		0.0920 (9)	0.1775 (5)	0.00394 (3)	0.1733 (13)

E / eV	$10^2\ \sigma_r[C^{2+}]$	$10^2\ \sigma_r[O^{2+}]$	$\sigma_r[C^+]$	$\sigma_r[O^+]$	$\sigma_r[CO_2^{2+}]$	$\sigma_r[CO^+]$
50			0.0762 (1)	0.1498 (10)	0.00221 (5)	0.1645 (12)
45			0.0645 (5)	0.1324 (13)	0.00106 (2)	0.1614 (1)
40			0.0473 (15)	0.1161 (7)	0.00028 (3)	0.1633 (18)
35			0.0233 (10)	0.0985 (12)	0.00001 (1)	0.1576 (33)
30			0.0068 (3)	0.0788 (13)	-0.00000 (1)	0.1192 (44)

Precursor-Specific PICS

Table D.XI Relative *precursor-specific* PICS for forming ion fragments following dissociative electron ionization of CO_2, expressed relative to the cross section for forming CO_2^+, as a function of electron energy *E*. The value in parenthesis indicates the standard deviation in the last figure

E / eV	$10^3\ \sigma_2[C^{2+}]$	$10^3\ \sigma_3[C^{2+}]$	$10^3\ \sigma_2[O^{2+}]$	$10^3\ \sigma_3[O^{2+}]$	$\sigma_1[C^+]$
200	0.741 (120)	0.646 (124)	0.309 (35)	0.672 (69)	0.0979 (26)
175	0.782 (76)	0.436 (48)	0.362 (75)	0.428 (80)	0.0994 (15)
150	0.635 (104)	0.305 (48)	0.367 (111)	0.262 (52)	0.1017 (24)
125	0.585 (40)	0.045 (15)	0.246 (64)	0.062 (25)	0.1039 (7)
100	0.286 (27)	0.003 (4)	0.106 (26)	0.004 (6)	0.1063 (17)
85	0.117 (4)	0.000 (2)	0.050 (10)	0.004 (6)	0.1080 (12)
75	0.044 (8)		0.006 (9)	-0.001 (4)	0.1079 (12)
65	0.003 (2)		0.003 (4)		0.1037 (5)
60	0.000 (3)		-0.002 (2)		0.0984 (0)
55					0.0904 (8)
50					0.0759 (1)
45					0.0645 (5)
40					0.0472 (15)
35					0.0232 (10)
30					0.0067 (3)

E / eV	$\sigma_2[C^+]$	$\sigma_3[C^+]$	$\sigma_1[O^+]$	$\sigma_2[O^+]$
200	0.0444 (14)	0.00944 (44)	0.1480 (54)	0.1461 (33)
175	0.0453 (2)	0.00814 (65)	0.1504 (30)	0.1487 (15)
150	0.0452 (12)	0.00651 (84)	0.1522 (27)	0.1484 (27)
125	0.0413 (5)	0.00459 (18)	0.1583 (26)	0.1394 (23)
100	0.0341 (5)	0.00108 (18)	0.1647 (26)	0.1194 (20)
85	0.0245 (4)	0.00020 (10)	0.1701 (29)	0.0935 (17)
75	0.0161 (4)	-0.00003 (3)	0.1734 (18)	0.0693 (10)
65	0.0073 (2)		0.1710 (15)	0.0422 (3)
60	0.0038 (1)		0.1656 (28)	0.0291 (2)
55	0.0016 (1)		0.1590 (2)	0.0185 (3)

E / eV	$\sigma_2[C^+]$	$\sigma_3[C^+]$	$\sigma_1[O^+]$	$\sigma_2[O^+]$
50	0.00029 (3)		0.1429 (13)	0.0070 (4)
45	0.00005 (1)		0.1305 (12)	0.0019 (3)
40	0.00007 (3)		0.1159 (5)	0.0002 (2)
35	0.00005 (3)		0.0985 (13)	0.0000 (1)
30	0.00007 (2)		0.0787 (15)	0.0001 (2)

E / eV	$\sigma_3[O^+]$	$\sigma_1[CO^+]$	$\sigma_2[CO^+]$	$\sigma_3[CO^+]$
200	0.0194 (11)	0.0934 (24)	0.0781 (12)	0.00007 (1)
175	0.0167 (15)	0.0966 (35)	0.0800 (13)	0.00003 (1)
150	0.0134 (17)	0.1003 (30)	0.0799 (9)	0.00003 (2)
125	0.0093 (3)	0.1068 (22)	0.0774 (8)	0.00002 (2)
100	0.0022 (4)	0.1175 (16)	0.0703 (3)	0.00000 (1)
85	0.0004 (2)	0.1283 (21)	0.0607 (9)	
75	-0.0001 (1)	0.1370 (23)	0.0502 (4)	
65		0.1485 (7)	0.0346 (2)	
60		0.1548 (8)	0.0258 (2)	
55		0.1555 (14)	0.0178 (2)	
50		0.1572 (13)	0.0072 (2)	
45		0.1589 (4)	0.0025 (2)	
40		0.1627 (19)	0.00065 (15)	
35		0.1574 (34)	0.00019 (10)	
30		0.1190 (45)	0.00023 (13)	

Total Ion Yield from Each Level of Ionization

Table D.XII Contributions to the total ion yield from single, double, and triple ionization, following electron ionization of CO_2, as a function of electron energy *E*.

E / eV	Single Ionization / %	Double Ionization / %	Triple Ionization / %
200	81.0	17.2	1.8
175	81.0	17.4	1.5
150	81.4	17.4	1.2
125	82.7	16.5	0.8
100	85.2	14.5	0.2
85	88.1	11.9	0.0
75	90.7	9.3	0.0
65	94.0	6.0	0.0
60	95.7	4.3	0.0
55	97.1	2.9	0.0
50	98.8	1.2	0.0

E / eV	Single Ionization / %	Double Ionization / %	Triple Ionization / %
45	99.6	0.4	0.0
40	99.9	0.1	0.0
35	100.0	0.0	0.0
30	100.0	0.0	0.0

H_2O

Relative PICS

Table D.XIII Relative partial ionization cross sections following electron ionization of H_2O, expressed relative to the cross section for forming H_2O^+, as a function of electron energy *E*. The value in parenthesis indicates two standard deviations in the last figure.

E / eV	$\sigma_r[H^+]$	$10^2\ \sigma_r[H_2^+]$	$10^2\ \sigma_r[O^{2+}]$	$\sigma_r[O^+]$	$\sigma_r[OH^+]$
200	0.261 (11)	0.118 (6)	0.173 (30)	0.0671 (18)	0.315 (3)
175	0.263 (9)	0.119 (18)	0.149 (20)	0.0667 (14)	0.315 (1)
150	0.261 (12)	0.117 (10)	0.109 (11)	0.0651 (18)	0.313 (3)
125	0.255 (12)	0.116 (11)	0.067 (17)	0.0615 (15)	0.310 (2)
100	0.240 (11)	0.113 (8)	0.024 (3)	0.0540 (13)	0.305 (3)
85	0.225 (12)	0.112 (5)	0.005 (3)	0.0466 (17)	0.299 (2)
75	0.209 (9)	0.113 (12)	0.000 (3)	0.0402 (15)	0.293 (3)
65	0.185 (8)	0.109 (8)	0.001 (1)	0.0328 (11)	0.285 (2)
60	0.174 (8)	0.109 (16)	0.000 (1)	0.0292 (18)	0.279 (2)
55	0.160 (8)	0.107 (12)	0.000 (1)	0.0255 (16)	0.273 (2)
50	0.141 (8)	0.107 (12)	0.000 (1)	0.0202 (11)	0.262 (2)
45	0.124 (7)	0.109 (8)	0.000 (1)	0.0159 (10)	0.252 (4)
40	0.109 (6)	0.104 (11)	0.000 (1)	0.0101 (25)	0.239 (5)
35	0.089 (6)	0.096 (12)	0.000 (1)	0.0052 (8)	0.218 (3)
30	0.068 (5)	0.076 (5)	0.000 (1)	0.0013 (9)	0.184 (4)

Precursor-Specific PICS

Table D.XIV Relative *precursor-specific* PICS for forming fragment ions following dissociative electron ionization of H_2O, expressed relative to the cross section for forming H_2O^+, as a function of electron energy *E*. The value in parenthesis indicates two standard deviations in the last figure

E / eV	$\sigma_1[\mathrm{H}^+]$	$\sigma_2[\mathrm{H}^+]$	$10^2\,\sigma_3[\mathrm{H}^+]$	$10^2\,\sigma_2[\mathrm{O}^{2+}]$	$10^2\,\sigma_3[\mathrm{O}^{2+}]$
200	0.220 (19)	0.0407 (80)	0.096 (51)	0.161 (33)	0.0118 (40)
175	0.221 (17)	0.0405 (80)	0.075 (37)	0.140 (24)	0.0088 (50)
150	0.221 (19)	0.0394 (73)	0.041 (27)	0.105 (14)	0.0041 (27)
125	0.218 (18)	0.0364 (71)	0.010 (13)	0.067 (17)	0.0006 (16)
100	0.211 (17)	0.0285 (62)	0.006 (7)	0.024 (3)	0.0000 (2)
85	0.203 (16)	0.0214 (40)	0.000 (1)	0.005 (3)	0.0000 (1)
75	0.192 (13)	0.0166 (39)	0.000 (1)	0.000 (3)	0.0000 (1)
65	0.175 (10)	0.0106 (19)		0.001 (1)	
60	0.166 (9)	0.0078 (9)		0.000 (1)	
55	0.155 (9)	0.0056 (8)			
50	0.138 (9)	0.0028 (8)			
45	0.122 (7)	0.0011 (2)			
40	0.108 (6)	0.0004 (3)			
35	0.089 (7)	0.0001 (1)			
30	0.068 (5)	0.0000 (1)			

E / eV	$\sigma_1[\mathrm{O}^+]$	$\sigma_2[\mathrm{O}^+]$	$10^2\,\sigma_3[\mathrm{O}^+]$	$\sigma_1[\mathrm{OH}^+]$	$\sigma_2[\mathrm{OH}^+]$
200	0.0514 (50)	0.0153 (28)	0.042 (24)	0.294 (6)	0.0210 (16)
175	0.0520 (38)	0.0144 (24)	0.033 (18)	0.293 (5)	0.0211 (18)
150	0.0512 (40)	0.0136 (24)	0.018 (13)	0.292 (6)	0.0211 (13)
125	0.0499 (28)	0.0116 (17)	0.005 (6)	0.290 (5)	0.0202 (13)
100	0.0464 (23)	0.0076 (12)	0.003 (4)	0.287 (5)	0.0179 (13)
85	0.0419 (22)	0.0047 (6)	0.000 (1)	0.284 (5)	0.0149 (14)
75	0.0372 (18)	0.0030 (5)	0.000 (1)	0.281 (4)	0.0126 (10)
65	0.0315 (11)	0.0013 (1)		0.276 (2)	0.0090 (5)
60	0.0284 (19)	0.0008 (1)		0.272 (3)	0.0070 (4)
55	0.0250 (16)	0.0004 (1)		0.268 (3)	0.0051 (4)
50	0.0200 (11)	0.0001 (1)		0.259 (2)	0.0027 (4)
45	0.0159 (10)	0.0001 (1)		0.251 (4)	0.0011 (1)
40	0.0101 (25)	0.0000 (1)		0.239 (5)	0.0004 (1)
35	0.0052 (8)	0.0000 (1)		0.218 (4)	0.0001 (1)
30	0.0013 (9)	0.0000 (1)		0.184 (4)	0.0000 (1)

Total Ion Yield from Each Level of Ionization

Table D.XV Contributions to the total ion yield from single, double, and triple ionization, following electron ionization of H_2O, as a function of electron energy *E*.

E / eV	Single Ionization / %	Double Ionization / %	Triple Ionization / %
200	95.1	4.8	0.09
175	95.2	4.7	0.07
150	95.4	4.6	0.04
125	95.8	4.2	0.01
100	96.6	3.4	0.01
85	97.4	2.6	0.00
75	97.9	2.1	0.00
65	98.6	1.4	0.00
60	99.0	1.0	0.00
55	99.2	0.8	0.00
50	99.6	0.4	0.00
45	99.8	0.2	0.00
40	99.9	0.1	0.00
35	100.0	0.0	0.00
30	100.0	0.0	0.00

Relative PICS for Ion Pair Formation

C_2F_6

Table D.XVI Relative partial ionization cross sections for forming monocation-monocation pairs following electron ionization of C_2F_6, expressed relative to the cross section for forming $C_2F_5^+$, as a function of electron energy *E*. All values shown have been multiplied by a factor of 10.

E / eV	$\sigma_r[C_2F_5^+ + F^+]$	$\sigma_r[C_2F_4^+ + F^+]$	$\sigma_r[CF_3^+ + C^+]$	$\sigma_r[CF_3^+ + F^+]$	$\sigma_r[CF_3^+ + CF^+]$
200	0.005	0.002	0.093	0.144	0.950
175	0.006	0.002	0.090	0.143	0.960
150	0.004	0.002	0.088	0.135	0.953
125	0.004	0.002	0.078	0.125	0.903
100	0.003	0.002	0.059	0.104	0.771
85	0.003	0.001	0.041	0.082	0.627
75	0.002	0.001	0.027	0.062	0.507
65	0.002	0.000	0.011	0.037	0.332

E / eV	$\sigma_r[C_2F_5^+ + F^+]$	$\sigma_r[C_2F_4^+ + F^+]$	$\sigma_r[CF_3^+ + C^+]$	$\sigma_r[CF_3^+ + F^+]$	$\sigma_r[CF_3^+ + CF^+]$
60	0.001	0.000	0.006	0.026	0.252
55	0.001	0.000	0.002	0.016	0.177
50	0.000	0.000	0.001	0.007	0.094
45	0.000	0.000	0.000	0.002	0.036
40	0.000	0.000	0.000	0.000	0.005
35	0.000	0.000	0.000	0.000	0.001
30	0.000	0.000	0.000	0.000	0.000

E / eV	$\sigma_r[CF_3^+ + CF_2^+]$	$\sigma_r[CF_3^+ + CF_3^+]$	$\sigma_r[C_2F_2^+ + F^+]$	$\sigma_r[CF_2^+ + C^+]$	$\sigma_r[CF_2^+ + F^+]$
200	0.536	0.043	0.004	0.103	0.086
175	0.548	0.042	0.004	0.103	0.089
150	0.550	0.041	0.004	0.105	0.090
125	0.540	0.040	0.003	0.094	0.086
100	0.488	0.039	0.002	0.071	0.067
85	0.431	0.034	0.002	0.046	0.041
75	0.380	0.032	0.001	0.028	0.024
65	0.288	0.026	0.000	0.008	0.009
60	0.242	0.023	0.000	0.002	0.004
55	0.188	0.020	0.000	0.000	0.001
50	0.128	0.015	0.000	0.000	0.000
45	0.074	0.011	0.000	0.000	0.000
40	0.018	0.005	0.000	0.000	0.000
35	0.001	0.000	0.000	0.000	0.000
30	0.000	0.000	0.000	0.000	0.000

E / eV	$\sigma_r[CF_2^+ + CF^+]$	$\sigma_r[CF_2^+ + CF_2^+]$	$\sigma_r[C_2F^+ + F^+]$	$\sigma_r[CF^+ + C^+]$	$\sigma_r[CF^+ + F^+]$
200	0.772	0.981	0.060	0.433	0.624
175	0.773	0.985	0.057	0.427	0.625
150	0.754	0.977	0.053	0.414	0.599
125	0.697	0.949	0.044	0.359	0.531
100	0.556	0.832	0.026	0.230	0.328
85	0.415	0.681	0.013	0.119	0.168
75	0.302	0.566	0.005	0.052	0.075
65	0.158	0.402	0.000	0.008	0.017
60	0.099	0.311	0.000	0.001	0.005
55	0.050	0.232	0.000	0.000	0.001
50	0.013	0.131	0.000	0.000	0.000
45	0.002	0.054	0.000	0.000	0.000
40	0.000	0.010	0.000	0.000	0.000
35	0.000	0.002	0.000	0.000	0.000
30	0.000	0.000	0.000	0.000	0.000

E / eV	$\sigma_r[CF^+ + CF^+]$	$\sigma_r[C_2^+ + F^+]$	$\sigma_r[F^+ + C^+]$	$\sigma_r[F^+ + F^+]$	$\sigma_r[C^+ + C^+]$
200	0.657	0.130	0.260	0.161	0.101
175	0.648	0.117	0.257	0.162	0.091
150	0.653	0.096	0.219	0.123	0.083
125	0.612	0.065	0.153	0.073	0.070
100	0.470	0.026	0.053	0.022	0.029
85	0.331	0.006	0.012	0.006	0.009
75	0.210	0.001	0.002	0.002	0.001
65	0.080	0.000	0.000	0.000	0.000
60	0.044	0.000	0.000	0.000	0.000
55	0.013	0.000	0.000	0.000	0.000
50	0.001	0.000	0.000	0.000	0.000
45	0.005	0.000	0.000	0.000	0.000
40	0.002	0.000	0.000	0.000	0.000
35	0.000	0.000	0.000	0.000	0.000
30	0.000	0.000	0.000	0.000	0.000

$SiCl_4$

Table D.XVII Relative partial ionization cross sections for forming monocation-monocation pairs following electron ionization of $SiCl_4$, expressed relative to the cross section for forming $SiCl_4^+$, as a function of electron energy *E*.

E / eV	$\sigma_r[Cl^+ + Si^+]$	$\sigma_r[Cl^+ + Cl^+]$	$\sigma_r[SiCl^+ + Cl^+]$	$\sigma_r[SiCl^+ + Cl_2^+]$
200	0.082	0.188	0.167	0.021
175	0.099	0.202	0.179	0.022
150	0.108	0.213	0.192	0.023
125	0.119	0.219	0.209	0.024
100	0.143	0.217	0.227	0.025
85	0.158	0.197	0.243	0.025
75	0.168	0.179	0.261	0.025
65	0.148	0.137	0.292	0.024
60	0.122	0.100	0.300	0.024
55	0.089	0.053	0.293	0.024
50	0.033	0.011	0.223	0.021
45	0.008	0.005	0.128	0.017
40	0.002	0.003	0.039	0.009
35	0.000	0.001	0.004	0.002
30	0.000	0.001	0.001	0.000

E / eV	$\sigma_r[SiCl_2^+ + Cl^+]$	$\sigma_r[SiCl_2^+ + Cl_2^+]$	$\sigma_r[SiCl_3^+ + Cl^+]$
200	0.068	0.008	0.183
175	0.070	0.009	0.191
150	0.073	0.009	0.202
125	0.076	0.009	0.214
100	0.078	0.010	0.223
85	0.080	0.010	0.225
75	0.081	0.009	0.228
65	0.076	0.010	0.230
60	0.075	0.010	0.233
55	0.074	0.010	0.236
50	0.067	0.010	0.235
45	0.050	0.008	0.213
40	0.024	0.005	0.149
35	0.003	0.002	0.057
30	0.001	0.000	0.010

C_2H_2

Table D.XVIII Relative partial ionization cross sections for forming monocation-monocation pairs following electron ionization of C_2H_2, expressed relative to the cross section for forming $C_2H_2^+$, as a function of electron energy *E*. All values shown have been multiplied by a factor of 10.

E / eV	$\sigma_r[H^+ + H^+]$	$\sigma_r[H^+ + C^+]$	$\sigma_r[H^+ + CH^+]$	$\sigma_r[H^+ + C_2^+]$	$\sigma_r[H^+ + C_2H^+]$
200	0.012	0.163	0.043	0.143	0.250
175	0.012	0.164	0.047	0.147	0.260
150	0.011	0.159	0.045	0.149	0.263
125	0.007	0.157	0.045	0.147	0.270
100	0.007	0.129	0.044	0.139	0.267
85	0.000	0.093	0.038	0.115	0.242
75	0.000	0.069	0.033	0.101	0.220
65	0.000	0.028	0.021	0.070	0.188
60	0.000	0.014	0.015	0.056	0.167
55	0.000	0.005	0.008	0.036	0.127
50	0.000	0.001	0.003	0.015	0.085
45	0.000	0.000	0.000	0.004	0.044
40	0.000	0.000	0.000	0.001	0.011
35	0.000	0.000	0.000	0.000	0.001
30	0.000	0.000	0.000	0.000	0.000

E / eV	$\sigma_r[C^+ + C^+]$	$\sigma_r[C^+ + CH^+]$	$\sigma_r[CH^+ + CH^+]$	$\sigma_r[C^+ + CH_2^+]$
200	0.054	0.080	0.128	0.010
175	0.050	0.084	0.140	0.010
150	0.051	0.087	0.144	0.010
125	0.044	0.082	0.136	0.010
100	0.035	0.077	0.139	0.010
85	0.025	0.071	0.137	0.010
75	0.017	0.061	0.122	0.010
65	0.006	0.038	0.090	0.008
60	0.003	0.029	0.073	0.008
55	0.001	0.018	0.055	0.007
50	0.000	0.006	0.031	0.004
45	0.000	0.001	0.012	0.002
40	0.000	0.000	0.003	0.001
35	0.000	0.000	0.000	0.000
30	0.000	0.000	0.000	0.000

CO_2

Table D.XIX Relative partial ionization cross sections for forming monocation-monocation pairs following electron ionization of CO_2, expressed relative to the cross section for forming CO_2^+, as a function of electron energy *E*. All values shown have been multiplied by a factor of 10.

E / eV	$\sigma_r[O^+ + C^+]$	$\sigma_r[CO^+ + O^+]$	$\sigma_r[O^+ + O^+]$
200	0.444	0.781	0.118
175	0.453	0.800	0.117
150	0.452	0.799	0.117
125	0.413	0.774	0.104
100	0.341	0.703	0.075
85	0.245	0.607	0.042
75	0.161	0.502	0.015
65	0.073	0.346	0.002
60	0.038	0.258	-0.002
55	0.016	0.178	-0.005
50	0.003	0.072	-0.003
45	0.001	0.025	-0.003
40	0.001	0.007	-0.002
35	0.000	0.002	-0.001
30	0.001	0.002	-0.001

I_2O

Table D.XX Relative partial ionization cross sections for forming monocation-monocation pairs following electron ionization of C_2H_2, expressed relative to the cross section for forming $C_2H_2^+$, as a function of electron energy *E*. All values shown have been multiplied by a factor of 10.

E / eV	$\sigma_r[H^+ + H^+]$	$\sigma_r[H^+ + O^+]$	$\sigma_r[H^+ + OH^+]$
200	0.022	0.153	0.210
175	0.025	0.144	0.211
150	0.023	0.136	0.211
125	0.023	0.116	0.202
100	0.015	0.076	0.179
85	0.009	0.047	0.149
75	0.005	0.030	0.126
65	0.002	0.013	0.090
60	0.000	0.008	0.070
55	0.000	0.004	0.051
50	0.000	0.001	0.027
45	0.000	0.001	0.011
40	0.000	0.000	0.004
35	0.000	0.000	0.001
30	0.000	0.000	0.000